Part III

Textile–body interactions and modelling issues

13

Heat and moisture transfer in fibrous clothing insulation

Y. B. LI and J. FAN, The Hong Kong Polytechnic University, Hong Kong

13.1 Introduction

Heat and moisture transfer with phase change in porous media is a very important topic in a wide range of scientific and engineering fields, such as civil engineering, energy storage and conservation, as well as functional clothing design, etc. Such processes have therefore been extensively studied by experimental investigation and numerical modeling.[1–10]

For clothing systems used in subzero climates, heat and moisture transfer is complicated by various factors. Heat transfer takes place through conduction in all of the phases, radiation through the highly porous fibrous insulation, and convection of moist air. Mass transport occurs not only through diffusion and convection, but also through moist absorption or desorption between the fibres and the surrounding air as well as the movement of condensed liquid water as a result of external forces, such as capillary pressure and gravity. The moisture absorption or desorption and phase change within the fibrous insulation absorbs or releases heat, which further complicates the heat transfer process. The difficulty in studying these processes is further aggravated by the fact that the transport properties of the material involved vary considerably with the moisture or liquid water content.

In this chapter, past literature and our recent work will be reviewed and discussed, which include experimental investigations and development of theoretical models, as well as numerical simulation of the effects of material properties and environmental parameters.

13.2 Experimental investigations

13.2.1 Experimental methods

Thomas *et al*.[11] studied the diffusion of heat and mass through wetted fibrous insulation of medium density. The experiment consisted of uniformly wetting six layers of insulation and stacking them together to form a continuous slab.

The slab was then heat-sealed in a plastic film. The test sample was inserted into a protected hot plate apparatus and subjected to one-dimensional temperature gradients. The temperature profile inside the slab was monitored with thermocouples and the liquid content was measured at regular intervals through disassembling the slab and measuring the weight of each of the six layers. Farnworth[12] reported the use of a sweating hot plate, by which water is fed into the hot side of the fibrous insulation using a syringe pump. The temperature and heat loss was measured during one sweating on and off cycle. Shapiro and Motakef[13] conducted an experiment in which a fiberglass test sample with a known liquid content distribution was placed inside a hot–cold box, and the cold side of the specimen was covered by a vapor barrier. The hot–cold box consists of two temperature- and humidity-controlled chambers, connected through the specimen. The temperature profile in the sample at different times and the final liquid content distribution were measured. Wijeysundera *et al.*[14] conducted two series of experiments in which a heat flow meter apparatus based on the ASTM guidelines was built. In the first series, water was sprayed on the hot face of the slab and, in the second series, the hot face was directly exposed to a moist airflow. Transient temperature changes were monitored and the total amount of moisture absorption and/or condensation after a period of time was measured. A similar experiment to Wijeysundera's second series was conducted by Tao *et al.*[15] except that the cold side was subjected to the temperature below the triple point of water. Murata[16] built an apparatus in which mixture of dry air and distilled water vapor was preheated to desired temperature (89 °C), then the mixture was blown through the fibrous insulation and stopped by an impermeable glass plate at a low temperature (24–62 °C). The temperature and heat flux were monitored during the testing.

In order to resemble many practical situations where the fibrous insulation is sandwiched in between two layers of moisture retarders, such as is the case in clothing and building insulation, Fan[17,18] and his coworkers investigated coupled heat and moisture transfer through fibrous insulations sandwiched between two covering lining fabrics, using a sweating guarded hot plate under a low temperature condition. The details of this experiment will be elaborated in the following sections.

13.2.2 Instrumentation

The sweating guarded hot plate specified in the ISO 11092:1993(E) was improved for use under frozen conditions. The device is shown schematically in Fig. 13.1. The device had a shallow water container 1 with a porous plate 3 at the top. The container was covered by a man-made skin 2 made of a waterproof, but moisture permeable (breathable) fabric. The edge of the breathable fabric was sealed with the container to avoid water leakage. Water

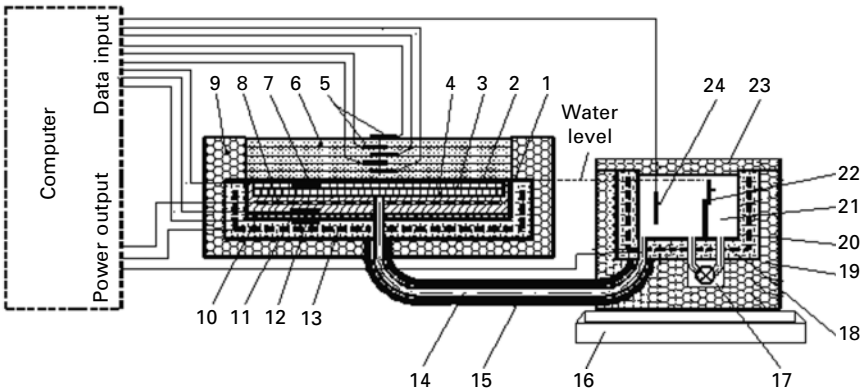

1. Shallow water container
2. Menmade skin
3. Porous plate
4. Water
5. Measuring sensor
6. Layers of specimen
7. Temperature sensor
8. Heating element
9. Insulation foam
10. Insulation pad
11. Temperature sensor
12. Temperature sensor
13. Heating element
14. Water supply pipe
15. Insulation layer
16. Electronic balance
17. Water pump
18. Water tank
19. Insulation foam
20. Heating element
21. Warm water
22. Water level adjustor
23. Cover
24. Temperature sensor

13.1 Schematic drawing of the sweating hot-plate.

was supplied to the container from a water tank 16 through an insulated pipe 14. The water in the water tank was pre-heated to 35 °C. The water level in the water tank was maintained by a pump 17 which circulated the water between the two halves of tank. Between the two halves was a separator 22 whose height could be adjusted to ensure that the water was in full contact with the breathable skin at the top of the container. The water temperature in the container 1 was controlled at 35 °C, simulating the human skin temperature. The amount of water supplied to the water container was measured by the electronic balance 16. To prevent heat loss from directions other than the upper right direction, the water container was surrounded with a guard having a heating element 13. The temperature of the guard was controlled so that its temperature difference from that of the bottom of the container was less than 0.2 °C. The whole device was further covered by a thick layer of insulation foam.

All temperatures were measured using RTD sensors (conforming to BS 1904 and DIN43760, 100 Ω at 100 °C) and the heating elements were made of thermal resistant wires. Temperature control was achieved by regulating the heat supply according to a Proportional–Integral–Derivative (PID) control algorithm[19]. To ensure the accuracy in the measurement of heat supply and stability of the system, the power supply was in DC and was stabilized using a voltage stabilizer.

13.2.3 Experimental procedure

The samples in the experiment consisted of several thin layers of fibrous battings sandwiched with inner and outer layers of covering fabric, simulating the construction of a 'down' jacket. Two types of covering fabrics and fibrous battings were used in the testing, and their properties are listed in Tables 13.1 and 13.2: The resistance to air penetration was tested using a KES -F8-AP1 Air Permeability Tester.[20] The moisture absorption and condensation under cold condition was measured according to the following instructions:

(i) Condition the covering fabric and the fibrous battings in an air-conditioned room, with temperature at 25.0 ± 0.5 °C and humidity at 65 ± 5%, for at least 24 hours.
(ii) Start the temperature control and measurement system of the sweating hot plate in the same conditioned room until the temperature and power supply is stabilized.
(iii) Weigh and record the weights of each layer of fibrous battings.
(iv) Sandwich multiple layers of fibrous batting with top and bottom layers of covering fabric, and place the ensemble on top of the man-made skin of the instrument. Immediately place the sweating guarded hot plate in a cold chamber with the temperature controlled at –20 ± 1 °C.
(v) After a pre-set time (e.g. 8, 16 or 24 hours), take out each layer of the fibrous battings and weigh them immediately using an electronic balance.
(vi) Record the temperatures, consumed water and power supply with time, continuously and automatically.

Table 13.1 Properties of covering fabric

Composition	Nylon	Three-layer laminated fabric
Construction	Woven	Woven + membrane + warp knit
Weight (kg/m^2)	0.108	0.22
Thickness (m)	2.73E-04	5.15E-04
Thermal resistance (Km^2/W)	3.15E-02	3.16E-02
Water vapour resistance (s/m)	64.99	143.79
Resistance to air penetration (kPa.s/m)	0.524	Impermeable

Table 13.2 Properties of fibrous batting

Composition	Viscose	Polyester
Weight (kg/m^2)	0.145	0.051
Thickness (m)	1.94E–03	4.92E–03
Fibre density (kg/m^3)	1.53E+03	1.39E+03
Porosity	9.51E–01	9.93E–01
Resistance to air penetration (kPa.s/m)	0.062	0.0061

(vii) Calculate the percentage of moisture or water accumulation due to absorption or condensation on each layer of fibrous battings by

$$Wc_i = \frac{W_{ai} - W_{oi}}{W_{oi}} \times 100\%$$

13.2.4 Experimental findings and discussion

Temperature distribution. The temperature distributions within the fibrous battings are plotted against the thickness from the inner layer of the covering fabric in Figs. 13.2–13.5 for two types of fibrous battings and covering fabrics. In general, the temperature of the inner battings next to the warm 'skin' increases quickly in the first few minutes and may even exceed the 'skin' temperature of 35 °C before it drops to a stable value. However, the temperature at the outer battings close to the cold environment reduces gradually. Most of the changes of temperature distribution occurred within about 0.5 hour, unrelated to the type of battings and covering fabrics.

Comparing Figs. 13.2 and 13.3, which are for the same non-hygroscopic polyester battings but with differing covering fabrics, there is no significant difference in the stabilized temperature distribution, but the one with the more permeable nylon covering fabric reached stabilization faster. As for the hygroscopic viscose batting (see Figs. 13.4 and 13.5), a significant difference

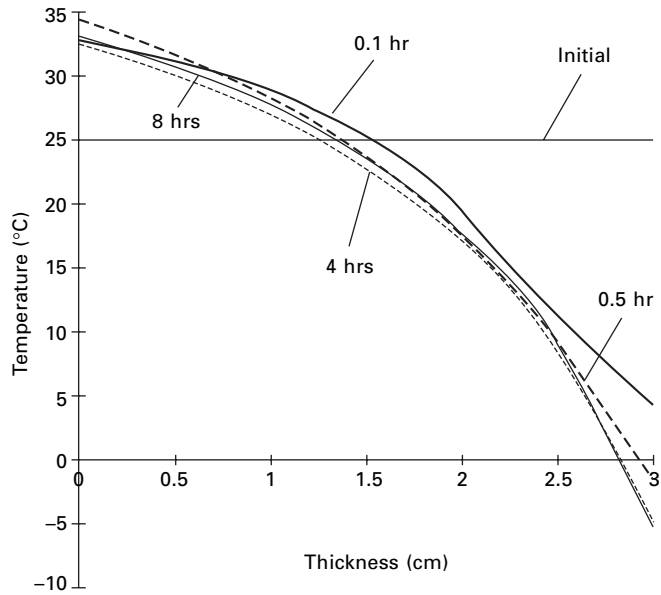

13.2 Temperature distribution for 6 plies polyester batting sandwiched by two layers of nylon fabric.

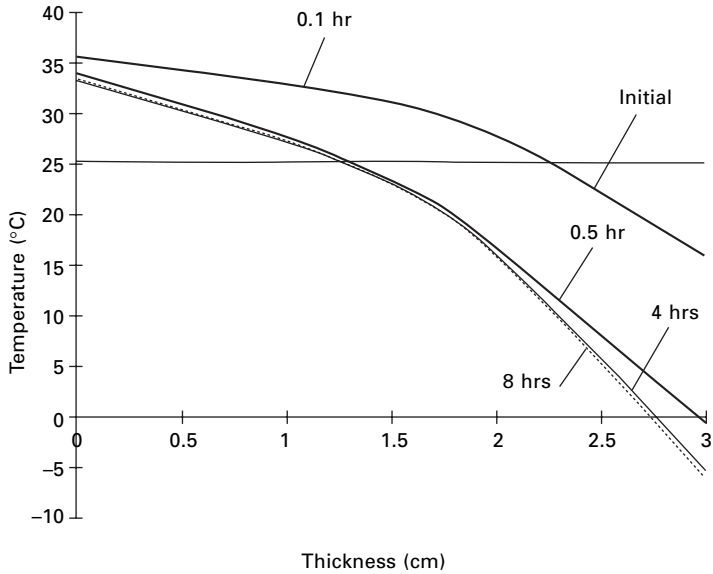

13.3 Temperature distribution for 6 plies polyester batting sandwiched by two layers of laminated fabric.

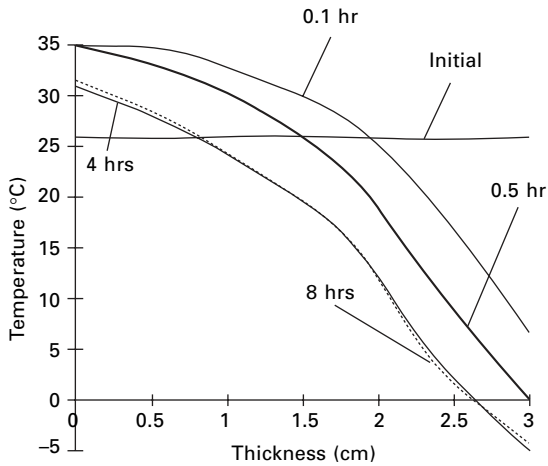

13.4 Temperature distribution for 15 plies viscose batting sandwiched by two layers of nylon fabric.

in temperature was found in the middle of the battings. This was caused by the differences in the moisture absorption within the fibrous battings. When covered with the highly permeable nylon fabric, more moisture was transmitted into the viscose battings within the same period and a greater rate of moisture absorption took place in the initial period, which released a greater amount

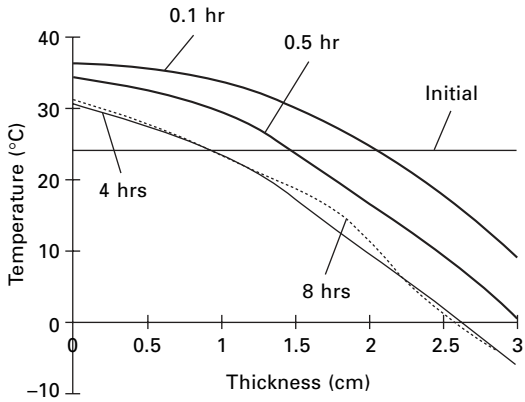

13.5 Temperature distribution for 15 plies viscose batting sandwiched by two layers of laminated fabric.

of heat during moisture absorption and consequently caused a higher temperature. After about 4 hours, the viscose battings covered with either the nylon fabric or the laminated fabric was almost saturated, resulting in a smaller temperature difference.

Heat loss. The changes of power supply or heat loss with time for the two types of battings and covering fabrics are shown in Fig. 13.6. The initial fluctuation of the curves is understandably due to the PID adjustment used for controlling the temperature of the water within the shallow container. It is clear from Fig. 13.6 that the heat loss after stabilization through the polyester battings covered with the more permeable nylon fabric was about 5% greater than that through the battings covered with the less permeable laminated fabric, which may be attributed to the greater loss in latent heat of moisture transmission. It can also be seen from Fig. 13.6 that the heat losses through the viscose battings are similar, irrespective of whether they are covered with the nylon or laminated fabric. Moreover, it can be seen that clothing assemblies with hygroscopic viscose batting will lose more heat than those with non-hygroscopic polyester batting after stabilization. When condensation takes place, hygroscopic batting may not be as warm as non-hygroscopic batting at the same thickness.

Water content distribution. Figures 13.7 and 13.8 show the distribution of water content within the fibrous battings after 8 and 24 hours for the two types of battings and covering fabrics, respectively. Here water content within the fibrous battings is a combination of moisture absorption and condensation. As can be seen, the water content in the batting next to the 'skin' was nearly zero for the non-hygroscopic polyester and about 18% for the hygroscopic viscose. It remained almost unchanged from after 8 hours to after 24 hours

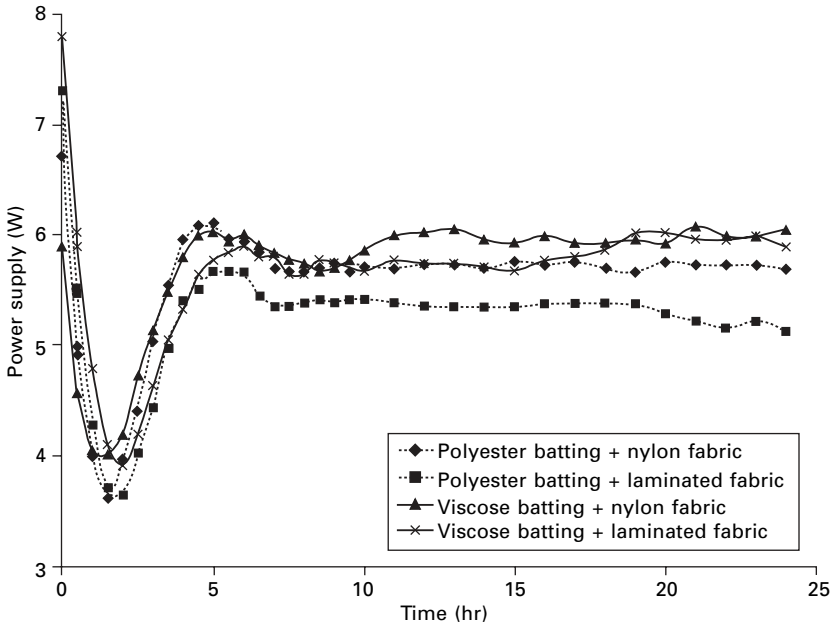

13.6 Power supply for different configurations of battings and cover fabrics.

for the polyester batting and only increased slightly for the viscose batting. It is therefore reasonable to believe that there was no condensation in the batting next to the 'skin', and the accumulation of water was only because of moisture absorption. Polyester batting absorbs little moisture and hence its water content remained zero. However, viscose batting absorbs much moisture at the beginning because the saturated water content is about 30% in a 95% RH environment.

The water content increases from the inner region to the outer region of the batting due to the increased amount of condensation. The water content also accumulates with time. At the outer region, the water content after 24 hours is about 4 times that after 8 hours for the polyester batting, and about 2 times that after 8 hours for viscose batting. The possible reason is that the polyester batting is more porous and permeable, thus allowing more moist air to be transmitted or diffuse from its inner region to the outer region, where condensation takes place. Another reason is that viscose is hydrophilic and polyester is hydrophobic. The condensed water on the hydrophilic fibre surface tends to wick to regions where the water content is lower.

It can also been seen from the graphs that, although the water content at the outer region was greater, the greatest water content may not occur at the outermost layer of the battings. This may be due to the complex interaction of heat and moisture transfer in the battings. Condensation within the fibrous

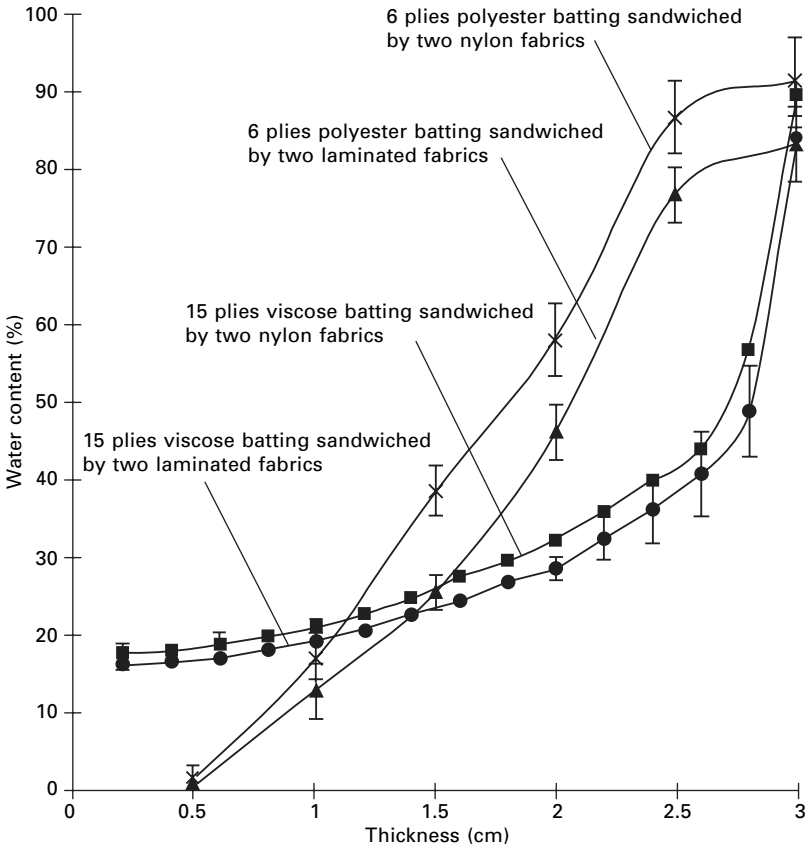

13.7 Water content distribution within the fibrous batting after 8 hours at –20 °C environment temperature.

battings is a result of the moisture content within the air space exceeding the saturated moisture content, which is a function of temperature. As the temperature reduces from the inner region to the outer regions, the saturated moisture content initially reduces sharply and then more gradually from the inner region to the outer region (because the effect of temperature on the saturated moisture content is less pronounced at lower temperatures). On the other hand, from the inner region to the outer region, the moisture content reduces at an increasing rate due to increased condensation in the outer region. The greatest difference between the moisture content of the fibers and the saturated moisture content of the air in the void space may not occur at the outermost boundary of the battings.

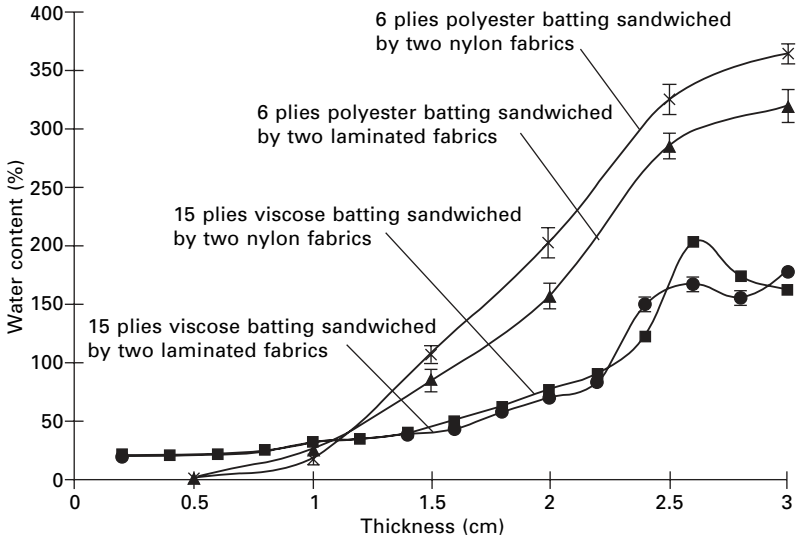

13.8 Water content distribution within the fibrous batting after 24 hours at –20 °C environment temperature.

13.3 Theoretical models

Apart from experimental study, a number of theoretical models have been proposed to simulate the coupled heat and moisture transfer in fibrous insulations. Henry[21] first established a model of coupled heat and moisture transfer with sorption/desorption in cotton bales. Phase change was, however, not considered in this early model. Since then, little progress was made in terms of rigorous theoretical modeling until Ogniewicz and Tien[22] proposed a model, assuming that heat is transported by conduction and convection and that the condensate is in a pendular state. The analysis was limited to a quasi-steady state, viz. the temperature and vapor concentration remained almost unchanged with time before the condensates became mobile. Motakef and El-Masri[23] first considered the quasi-steady state corresponding to mobile condensate, under which the condensate diffuses towards the wet zone's boundaries, as liquid, and re-evaporates at these boundaries leaving the time-invariant temperature, vapor concentration and liquid content profiles. This theoretical model was later extended by Shapiro and Motakef[13] to analyze the unsteady heat and moisture transport processes and compare the analytical results with experimental ones under some very limited circumstances. This analysis was only valid when the time scale for the motion of the dry–wet boundary in porous media is much larger than the thermal diffusion time scale, which may, however, not be the case with frosting and small moisture accumulation.[15]

The first dynamic model of coupled heat and moisture transfer with sorption and condensation was presented by Farnworth.[24] This model was rather simplified and only appropriate for multi-layered clothing, as it was assumed that the temperature and moisture content in each clothing layer were uniform. Vafai and Sarkar[25] first modeled the transient heat and moisture transfer with condensation rigorously. For the first time, the interface between the dry and wet zones was found directly from the solution of the transient governing equations. In this work, the effects of boundary conditions, and of the Peclet number and the Lewis Number, on the condensation process were numerically analyzed. Later, Vafai and Tien[26] extended the analysis to two-dimensional heat and mass transport, accounting for phase change in a porous matrix. Tao *et al.*[15] first analyzed the frosting effect in an insulation slab by applying Vafai and Sarker's model to the case with a temperature below the triple point of water. Tao *et al*.[27] also for the first time, considered the hygroscopic effects of insulation materials in the modeling. Murata[16] first considered the falling of condensate under gravity and built the phenomena into his steady-state model.

Fan and his co-workers[28,29] first combined the dynamic moisture absorption process and radiative heat transfer as well as the movement of liquid condensates in their transient models. These models were further improved by introducing moisture bulk flow, which is caused by the vapor pressure gradients and super-saturation state.[30–32] The following description is based on Fan's theoretical model and is combined with Finite Volume Method (FVM) for the numerical solution.

13.3.1 Model formulation

In modeling the heat and moisture transfer within a clothing system, we assume that

(i) The porous fibrous batting is isotropic in fiber arrangement and material properties.
(ii) Volume changes of the fibers due to changing moisture and water content can be neglected.
(iii) Local thermal equilibrium exists among all phases and, as a consequence, only sublimation or ablimation is considered in the frozen region.
(iv) The moisture content at the fiber surface is in sorptive equilibrium with that of the surrounding air.

The mass conservation equation for the water vapor in the inter-fiber void can be given by

$$\varepsilon \frac{\partial C_a}{\partial t} = -\varepsilon u \frac{\partial C_a}{\partial x} + \frac{D_a \varepsilon}{\tau} \frac{\partial^2 C_a}{\partial x^2} - \Gamma(x, t) \qquad [13.1]$$

where u is the bulk movement speed of moist air, which is calculated by Darcy's law:

$$u = -\frac{K_x}{\mu}\frac{\partial p}{\partial x} \qquad [13.2]$$

where p is the pressure of water vapor in the inter-fiber void, calculated by $p = p_{sat} \cdot Rhf$.

Even when there is no condensation on the surface of a fiber in the porous batting (i.e. the relative humidity is less than 100%), fibers absorb or desorb moisture; the absorption or desorption rate is of the form:

$$\Gamma_s(x,t) = \rho(1-\varepsilon)\frac{\partial C_f(x,t)}{\partial t} \qquad [13.3]$$

where $C_f(x, t)$ is the moisture content within the fiber, which can be integrated by[33]

$$C_f(x,t) = \{2/(\rho R_f^2)\}\int_0^{R_f} C_f' r dr \qquad [13.4]$$

where R_f is the radius of the fiber. C_f' is the volumetric moisture concentration in the fiber, which can be determined by the Fickian diffusion law[11]

$$\frac{\partial C_f'}{\partial t} = \frac{1}{r}\frac{\partial}{\partial r}\left(d_r\frac{\partial C_f'}{\partial r}\right) \qquad [13.5]$$

Water condensation and evaporation are modeled using the Hertz–Knudsen equation.[34] The condensation or evaporation rate per unit surface area of fiber covered with condensate (liquid water or ice) is

$$\Gamma_{sce}(x,t) = -E\sqrt{M/2\pi R}\,(P_{sat}/\sqrt{T_s} - P_v/\sqrt{T_v}) \qquad [13.6]$$

From Equation [13.6], we can get

$$\Gamma_{sce}(x,t) = -E\sqrt{M/2\pi R}\,(1-Rhf)\,P_{sat}/\sqrt{T} \qquad [13.7]$$

since the surface area of the fiber covered by condensate in the control volume is $\frac{2\sqrt{(1-\dot{\varepsilon})(1-\varepsilon)}}{R_f}$. Therefore, the condensation or evaporation rate per unit volume is

$$\Gamma_{ce}(x,t) = -\frac{2E\sqrt{(1-\dot{\varepsilon})(1-\varepsilon)}}{R_f}\sqrt{M/2\pi R}\,(1-Rhf)\,P_{sat}/\sqrt{T} \qquad [13.8]$$

Therefore, the total water accumulation rate $\Gamma(x, t)$ is

$$\Gamma = \Gamma_s + \Gamma_{ce} \quad [13.9]$$

The free water, i.e. the water on the fiber surface, may diffuse when it is in liquid form and its content exceeds a critical value. According to the mass conservation, we have

$$\rho(1-\varepsilon)\frac{\partial \tilde{W}}{\partial t} = \rho(1-\varepsilon)d_l\frac{\partial^2 \tilde{W}}{\partial x^2} + \Gamma_{ce}(x,t) \quad [13.10]$$

where $\tilde{W} = W(x, t) - W_f(x, t)$ is the free water content. $W_f(x, t) = C_f(x, t)/\rho$ is the water absorbed within the fiber; $W(x,t) = \frac{1}{\rho}\int_0^t \Gamma_{ce}(x,t)dt$ is the total water content including that absorbed by the fibers and on the fiber surface. d_l is defined phenomenologically, and depends on water content, temperature and properties of the fiber batting. $d_l = 0$ when the condensate is immobile, which is the case when the water content is less than a critical value W_c, or when the free water is frozen.

Based on the conservation of heat energy and applying the two-flux model of radiative heat transfer, at position x and time t, we obtain the heat transfer equation

$$C_v(x,t)\frac{\partial T}{\partial t} = -\varepsilon u C_{va}(x,t)\frac{\partial T}{\partial x} + \frac{\partial}{\partial x}\left(k(x,t)\frac{\partial T}{\partial x}\right) + \frac{\partial F_L}{\partial x} - \frac{\partial F_R}{\partial x} + \lambda(x,t)\Gamma(x,t) \quad [13.11]$$

where $$\frac{\partial F_L}{\partial x} = \beta(x)F_L - \beta(x)\sigma T^4(x,t) \quad [13.12]$$

$$\frac{\partial F_R}{\partial x} = -\beta(x)F_R + \beta(x)\sigma T^4(x,t) \quad [13.13]$$

where the effective thermal conductivity $k(x, t)$ is a volumetric average calculated by $k(x, t) = \varepsilon k_a + (1 - \varepsilon)(k_f + \rho W k_w)$, the effective volumetric heat capacity of the fibrous batting is calculated by $C_v = \varepsilon C_{va}\ (1 - \varepsilon)(C_{vf} + \rho W C_{vw})$, and the porosity of fiber plus condensates (liquid water, or ice) is calculated by $\varepsilon = \varepsilon' - (\rho/\rho_w)W(1 - \varepsilon')$.

Since the conductive heat transfer and moisture transport at the interfaces between the inner covering fabric and the batting, as well as between the batting and the outer covering fabric, should be continuous, we have

$$k(0,t)\left.\frac{\partial T}{\partial x}\right|_{x=0} = \frac{1}{R_{t0}}(T|_{x=0} - T_0) \quad [13.14]$$

$$k(L,t)\left.\frac{\partial T}{\partial x}\right|_{x=L} = \frac{T_1 - T|_{x=L}}{R_{t1} + (1/h_t)} \quad [13.15]$$

$$\left.\frac{D_a\varepsilon}{\tau}\frac{\partial Ca}{\partial x}\right|_{x=0} = \frac{Ca|_{x=0} - Ca_0}{R_{d0}} \quad [13.16]$$

$$\left.\frac{D_a\varepsilon}{\tau}\frac{\partial Ca}{\partial x}\right|_{x=L} = \frac{Ca_1 - Ca|_{x=L}}{R_{d1} + (1/h_c)} \quad [13.17]$$

Considering the radiative heat transfer at the interface between the inner thin fabric and the fibrous batting and that between the outer thin fabric and the fibrous batting, we have initial conditions for Equations [13.12] and [13.13] as follows:

$$(1 - \zeta_1)F_L(0, t) + \zeta_1\sigma T^4(0, t) = F_R(0, t) \quad [13.18]$$

$$(1 - \zeta_2)F_R(L, t) + \zeta_2\sigma T^4(L, t) = F_L(L, t) \quad [13.19]$$

13.3.2 Numerical solution with finite volume method (FVM)

Due to the natural formulation of the FVM, the integral conservation of quantities such as mass, momentum and energy is exactly satisfied over any group of control volumes and, definitely, over the whole calculation domain.[35] Therefore, in the FVM, the mass conservation exists for any number of grid points; even the coarse-grid solution exhibits exact integral balances. Moreover, it is easier to handle the mass transfer over the boundary of control volumes with many different properties such as variable porosities and media materials.

For each control element, as shown in Fig. 13.9, the vector quantities, such as moisture flow speed, heat resistance, vapor resistance and Darcy flow resistance, are placed on the boundary; the scalar quantities, such as energy, temperature, moisture pressure and vapor concentration, are on the center of the element. This treatment leads to a clear physical interpretation of the moisture and heat transport.

From Fig. 13.9, it is easy to derive the discretized formulation for the moisture mass conservation equation. In order to make the calculation more efficiently, an upstream method for the convection item is also introduced

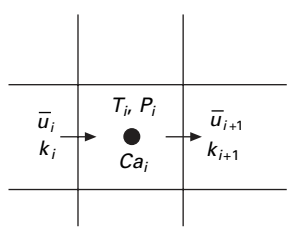

13.9 Location of element properties.

into the numerical formation. This means that the physical properties transferred along the convection flow are dominated by the donating element's physical properties. Therefore, the discretized convection item in Equation [13.1] can be written as follows:

$$\varepsilon u \frac{\partial Ca_i}{\partial x_i} = \frac{1}{\Delta xi}\{Min\{\varepsilon_i, \varepsilon_{i+1}) \times (Ca_i^{n+1} \times Max(u_{i+1}, 0) - Ca_{i+1}^{n+1} \times Max(-u_{i+1}, 0)) - Min\{\varepsilon_i, \varepsilon_{i-1}) \times (Ca_{i-1}^{n+1} \times Max(u_i, 0) - Ca_i^{n+1} \times Max(-u_i, 0))\} \quad [13.20]$$

where symbol *Min* means the minimum value of the two parameters and *Max* means the maximum value. *Min*() ensures that the lower porosity of the neighboring elements is chosen to calculate the moisture flow between the two neighboring elements. *Max*() identifies whether the moisture flow is moving out or into the element. Such treatment ensures the mass transport over the entire calculation domain is conserved, viz. no mass is lost during calculation.

For calculation of u by Darcy's law, if we use K to replace K_x/μ, then Darcy's law can be expressed as

$$u = K\frac{\Delta P}{\Delta x} = \frac{\Delta P}{\frac{\Delta x}{K}} \quad [13.21]$$

Then $\frac{\Delta x}{K}$ can be regarded as the Darcy flow resistance R_D. This resistance on the element boundary between element i and $i + 1$ can be calculated:

$$R_D = \frac{1}{2}\left(\frac{\Delta x_i}{K_i} + \frac{\Delta x_{i+1}}{K_{i+1}}\right) \quad [13.22]$$

where Δx_i is the dimension for ith element.

We can take advantage of the FVM and introduce a diffusion resistance R_d, which is located on the element boundary, and we have

$$Rd_i = \frac{\frac{1}{2}\Delta x_i \tau}{Da_i \varepsilon_i} + \frac{\frac{1}{2}\Delta x_{i-1}\tau}{Da_{i-1}\varepsilon_{i-1}} \quad [13.23]$$

Then the diffusion item in Equation [13.1] can be described as:

$$\frac{D_a \varepsilon}{\tau}\frac{\partial^2 C_a}{\partial x^2} = \frac{1}{\Delta x_i}\left(\frac{Ca_{i+1}^{n+1} - Ca_i^{n+1}}{Rd_{i+1}} - \frac{Ca_i^{n+1} - Ca_{i-1}^{n+1}}{Rd_i}\right) \quad [13.24]$$

Using the implicit scheme over the time step, we have:

$$\frac{\partial Ca_i}{\partial t} = \frac{Ca_i^{n+1} - Ca_i^n}{\Delta t} \quad [13.25]$$

Submit Equations [13.20], [13.24] and [13.25] into Equation [13.1], and we get the following discretization formation for the mass conservation equation:

$$\tilde{A}_i^n Ca_{i-1}^{n+1} + \tilde{B}_i^n Ca_i^{n+1} + \tilde{C}_i^n Ca_{i+1}^{n+1} = \tilde{D}_i^n \quad (i = 1, 2, \ldots, N-1) \quad [13.26]$$

where

$$\tilde{A}_i^n = -\frac{1}{\Delta x_i \cdot R_{di}} - \frac{Min(\varepsilon_{i-1}, \varepsilon_i)}{\Delta x_i} \cdot Max(u_i, 0)$$

$$\tilde{B}_i^n = \frac{\varepsilon_i}{\Delta t} + \frac{1}{\Delta x_i \cdot Rd_i} + \frac{1}{\Delta x_i \cdot Rd_{i+1}} + \frac{Min(\varepsilon_{i-1}, \varepsilon_i)}{\Delta x_i} \cdot Max(-u_i, 0) + \frac{Min(\varepsilon_i, \varepsilon_{i+1})}{\Delta x_i} \cdot Max(-u_{i+1}, 0)$$

$$\tilde{C}_i^n = -\frac{1}{\Delta x_i \cdot Rd_{i+1}} - \frac{Min(\varepsilon_i, \varepsilon_{i+1})}{\Delta x_i} \cdot Max(-u_{i+1}, 0)$$

$$\tilde{D}_i^n = \frac{\varepsilon_i}{\Delta t} Ca_i^n - \Gamma_i^n$$

Next, the discretized formation of Equation [13.11] will be discussed. It is believed that heat radiation inside the batting plays an important role in the total heat transfer because of the high porosity. From Equations [13.12] and [13.13], we get

$$F_L(x,t) = -\beta\sigma e^{\beta x}\left[\int_0^x e^{-\beta x} T^4(x,t)\,dx + c_2\right] \quad [13.27]$$

$$F_R(x,t) = -\beta\sigma e^{-\beta x}\left[\int_0^x e^{\beta x} T^4(x,t)\,dx + c_1\right] \quad [13.28]$$

Submit Equations [13.27] and [13.28] into Equations [13.12] and [13.13], and we have

$$\frac{\partial F_L}{\partial x} = -\beta^2\sigma e^{\beta x}\left[\int_0^x e^{-\beta x} T^4(x,t)\,dx + c_2\right] - \beta\sigma T^4(x,t) \quad [13.29]$$

$$\frac{\partial F_R}{\partial x} = -\beta^2\sigma e^{-\beta x}\left[\int_0^x e^{\beta x} T^4(x,t)\,dx + c_1\right] + \beta\sigma T^4(x,t) \quad [13.30]$$

By using Equations [13.27] and [13.28] and the initial conditions [13.18] and [13.19], we obtain

$$c_1 = \frac{\zeta_1}{\beta} T^4(0, t) - (1 - \zeta_1) c_2 \qquad [13.31]$$

$$c_2 = \frac{1}{(1-\xi_2)\beta(1-\zeta_1)e^{-\beta L} - \beta e^{\beta L}} \left((1-\zeta_2)\beta e^{-\beta L} \int_0^L e^{\beta k} T^4(k,t)\, dk \right.$$

$$\left. + \beta e^{\beta L} \int_0^L e^{-\beta k} T^4(k,t)\, dk + (1-\xi_2)\zeta_1 e^{-\beta L} T^4(0,t) + \zeta_2 T^4(L,t) \right) \qquad [13.32]$$

Submit Equations [13.29] and [13.30] into Equation [13.11], and we obtain

$$C_v(x, t)\frac{\partial T}{\partial t} = -\varepsilon u C_{va}(x, t)\frac{\partial T}{\partial x} + \frac{\partial}{\partial x}\left(k_e(x, t)\frac{\partial T}{\partial x} \right) + \Theta \qquad [13.33]$$

where $$\Theta = \beta^2 \sigma e^{\beta x} \left[\int_0^x e^{-\beta x} T^4(x, t)\, dx + c_2 \right]$$

$$- \beta^2 \sigma e^{-\beta x} \left[\int_0^x e^{\beta x} T^4(x, t)\, dx + c_1 \right]$$

$$+ 2\beta\sigma T^4(x, t) + \lambda(x, t)\Gamma(x, t)$$

A positive integer N is selected, and inscribed into the strip such that $\{(x, t): x \in [0, L], t \geq 0\}$. The values of the temperature in x_i at time $n\Delta t$ are denoted by T_i^n. Since Θ appears in nonlinear form, we replace it by the corresponding value at the previous time step Θ_i^n. Consequently, at each time step we only need to solve a linear tri-diagonal system.

The same manipulation can be used in discretizing the energy equation. The moisture concentration Ca is replaced with temperature T and diffusion resistance is replaced with thermal resistance R_t:

$$R_{ti} = \frac{\frac{1}{2}\Delta x_i}{k(x, t)_i} + \frac{\frac{1}{2}\Delta x_{i-1}}{k(x, t)_{i-1}} \qquad [13.34]$$

Similarly, the discretized formation for Equation [13.11] is derived:

$$A_i^n T_{i-1}^{n+1} + B_i^n T_i^{n+1} + C_i^n T_{i+1}^{n+1} = D_i^n \quad (i = 1, 2, \ldots, N-1) \qquad [13.35]$$

where

$$A_i^n = -\frac{1}{\Delta x_i \cdot R_{ti}} - \frac{Min(\varepsilon_i, \varepsilon_{i-1})}{\Delta x_i} C_{vai-1} Max(u_i, 0)$$

$$B_i^n = \frac{C_{vi}^n}{\Delta t} + \frac{C_{vai}}{\Delta x_i}[Min(\varepsilon_i, \varepsilon_{i-1}) \cdot Max(u_{i+1}, 0) + Min(\varepsilon_i, \varepsilon_{i-1}) \cdot Max(-u_i, 0)] + \frac{1}{\Delta x_i \cdot R_{ti+1}} + \frac{1}{\Delta x_i \cdot R_{ti}}$$

$$C_i^n = -\frac{1}{\Delta x_i \cdot R_{ti+1}} - \frac{Min(\varepsilon_i, \varepsilon_{i+1})}{\Delta x_i} C_{vai+1} Max(-u_{i+1}, 0)$$

$$C_i^n = \frac{C_{vi}^n}{\Delta t} T_i^n + \Theta_i^n$$

13.4 Numerical simulation

Numerical simulation has been applied to investigate the effects of material properties and environmental conditions on heat and moisture transfer through fibrous clothing insulations.[30,31] In this section, the simulation results of Fan's model solved with a finite volume scheme are presented.

The initial condition is 25°C and 65% RH for the clothing assembly. The numerical values used as boundary conditions are given as follows:

$$T_0 = 35\,^{\circ}\text{C}, \text{RH}_0 = 96\%$$

$$T_1 = -25\,^{\circ}\text{C}, \text{RH}_1 = 90\%$$

The numerical values of the other physical parameters used in the calculation are shown in Tables 13.2 and 13.3. The numerical results of temperature and water content distribution in fibrous battings are plotted in Figs. 13.10–13.13, with comparison to experimental data. As can be seen, there is generally good agreement between the numerical results and the experimental ones. The theoretical model can provide a good mapping of the mechanisms involved in the coupled heat transfer through clothing assemblies with moisture absorption and phase change.

Table 13.3 Common properties used in calculation for two kinds of battings

ρ_{ice}	λ			h_c	k_a	k_f	k_w
	Dry region	Wet region	Freezing region				
920.0	2522.0	2260.0	2593.0	0.1149	0.025	0.1	0.57
β	h_t	D_a		R	C_{va}	C_{vf}	C_{vw}
2.5	12.7	$2.16 \times 10^{-5} \times \left(\frac{T_i}{273.15}\right)^{1.8}$		8.31	1.169	1300	4200
W_c	ζ_1	ζ_2	σ	RH_0	RH_1	T_0	T_1
0.5	0.9	0.9	5.672×0^{-8}	99%	90%	308	253

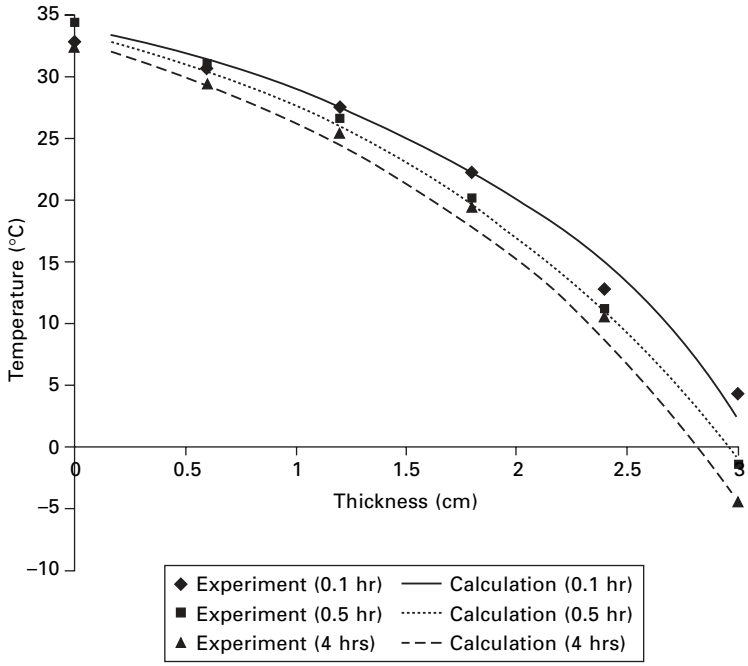

13.10 Comparison of temperature distribution between simulation and experiment (6 plies polyester batting sandwiched by two layers of nylon fabric).

In this section, the effects of various material properties on condensation within the fibrous battings are investigated through numerical simulation. This is important for the optimization of clothing design for thermal comfort. The following simulations are conducted based on the configuration of the viscose batting and two layers of nylon covering fabrics. In Tables 13.1–13.3, one parameter is considered as a changing variable and the rest are kept unchanged.

13.4.1 Effect of radiative sorption constant of the fibers β

The effect of radiative sorption constant of the fibers β on the water content distribution in the batting is shown in Fig. 13.14. The water content reduces with increase of β, but the reduction at the outermost region is less than that in the inner and middle regions. From the view of thermal comfort of clothing wearers, sweating occurs when the human body cannot release its heat through dry heat loss alone. During sweating, less accumulation of water in clothing is desirable, and hence a greater value of β is preferred.

β is related to the fractional fiber volume, fiber emissivity and fiber radius:[36]

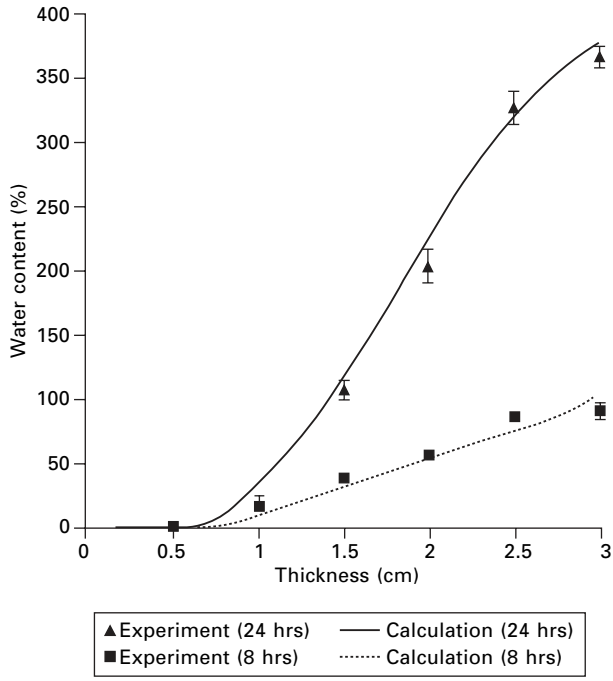

13.11 Comparison of water content distribution between simulation and experiment (6 plies polyester batting sandwiched by two layers of laminated fabric).

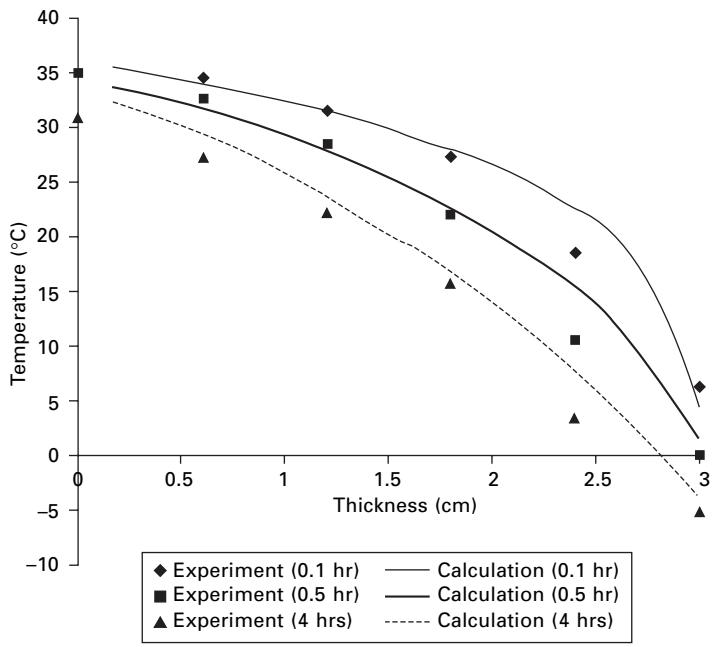

13.12 Comparison of temperature distribution between simulation and experiment (15 plies viscose batting sandwiched by two layers of nylon fabric).

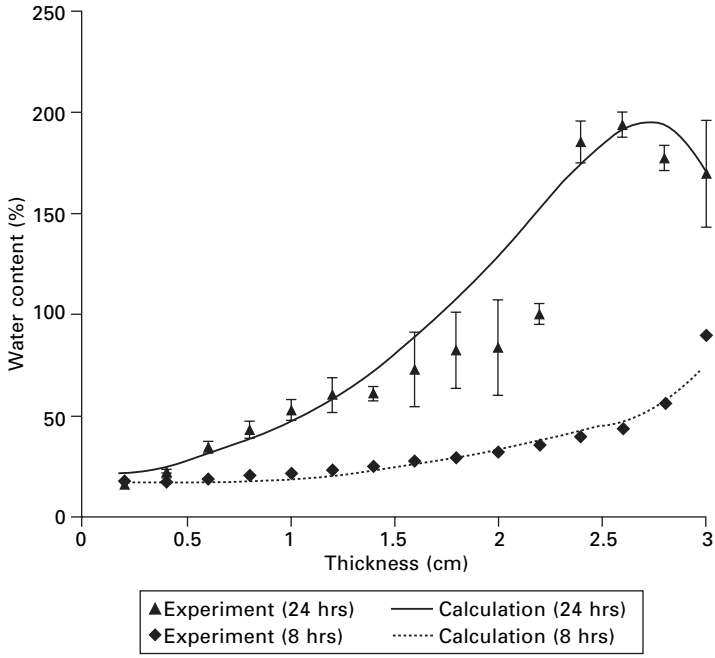

13.13 Comparison of water content distribution between simulation and experiment (15 plies viscose batting sandwiched by two layers of laminated fabric).

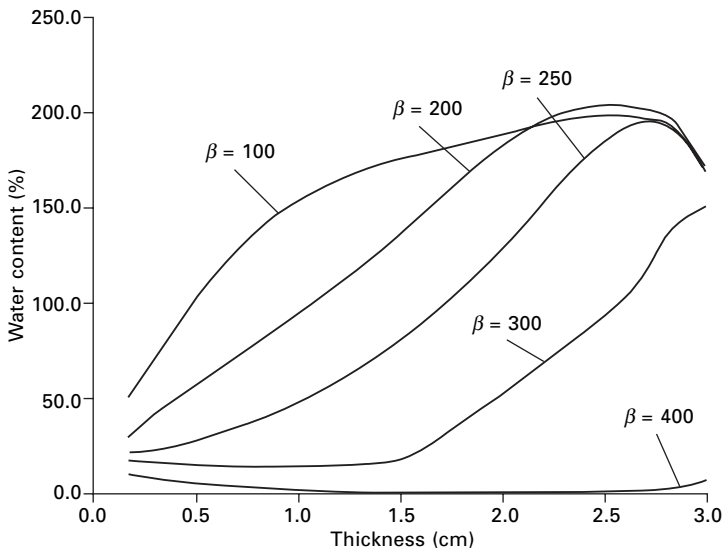

13.14 Water content distribution within the batting thickness after 24 hours while having different radiative sorption constants of the fibers.

$$\beta = \frac{(1 - \varepsilon)\zeta_f}{R_f}$$

where R_f is the fiber radius, ε porosity of the batting and ζ_f the emissivity of fiber. Therefore, higher fiber content, finer fiber, and greater emissivity of fiber are preferred for less condensation within the fibrous batting.

13.4.2 Effect of diffusion coefficient of moisture in the fiber d_f

As can be seen from Fig. 13.15, water content increases with increasing d_f. However, the increase is limited by the saturation of moisture regain within the fibres. Therefore, when the diffusion coefficient is greater than 1.512×10^{-16} m^2/s, there is little further increase in water content, even if the coefficient increases 100 times (see Fig. 13.15). These results indicate that hygroscopic fibers with hydrophilic surfaces having a high value of d_f (e.g. viscose) may be detrimental to thermal comfort in cold conditions because, when exercising and sweating, there is more and quicker accumulation of water within clothing. The accumulated water content may be a source of 'after-chill' discomfort when the wearer stops exercising.

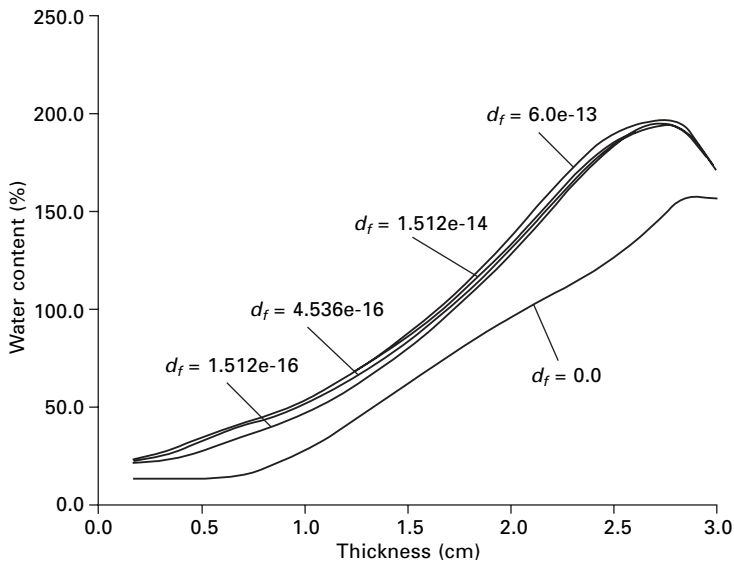

13.15 Water content distribution within the batting thickness after 24 hours while having different diffusion coefficients of moisture (unit: m^2/s) in the fiber.

13.4.3 Effect of disperse coefficient of free water in the fibrous batting, d_l

The effect of the disperse coefficient of free water in the fibrous batting d_l on the water content distribution is shown in Fig. 13.16. When d_l is small or approaches zero (corresponding to a hydrophobic fiber or ice condensate), there is no movement of liquid water on the fiber surface, and the water content will accumulate at the outer region of batting. With an increase of d_l, when the amount of liquid condensate exceeds a certain value, the liquid water overcomes the surface tension and moves to the region with a lower water content. When $d_l = 5.4 \times 10^{-8}$ m^2s^{-1}, the distribution of water content is almost even, except the outmost part, because its temperature is below zero and the condensed water is in a frozen state.

13.4.4 Effect of air permeability of fibrous batting, k_x

The effect of the air permeability of the fibrous batting (i.e. coefficient of Darcy's Law $k_x = \frac{K_x}{\mu}$) on the water content distribution, assuming the porosity of the batting has not changed, is shown in Fig. 13.17. When $k_x = 0.0$ (i.e. there is no flow of moist air within the fibrous batting, which may be achieved

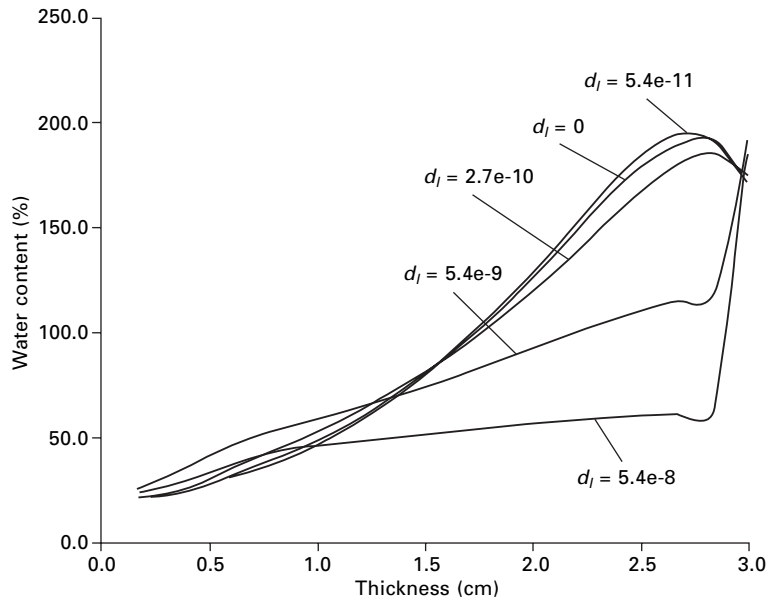

13.16 Water content distribution within the batting thickness after 24 hours while having different disperse coefficients of free water (unit: m^2/s) in the fibrous batting.

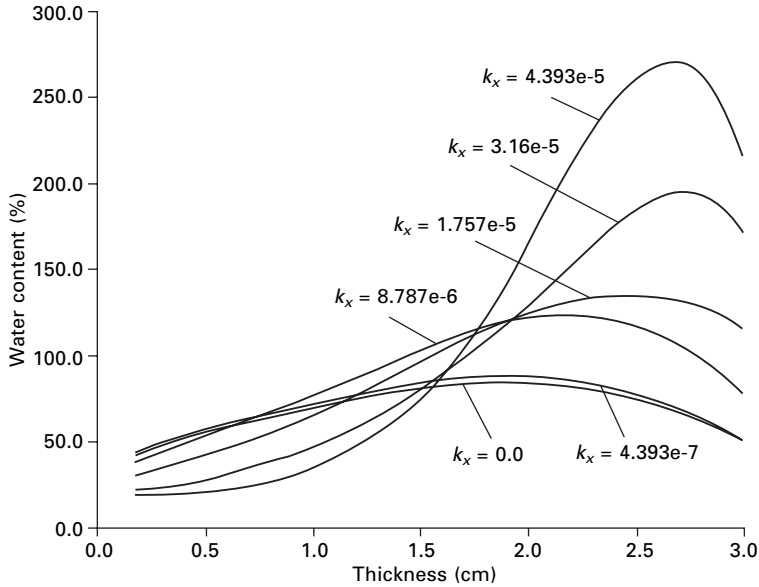

13.17 Water content distribution within the batting thickness after 24 hours while having different coefficients of Darcy's Law k_x (unit: $m^2/(Pa\ s)$.

by interlacing the layers of battings with air-impermeable fabrics), the distribution of water content is convex. With increase of k_x, the shape of the distribution is gradually changed to concave. It is clear that a higher k_x can cause a greater difference between the water content at the inner region and that at the outer region of the batting. The reduction of the air permeability k_x, achieved as indicated by interlacing the layers of the battings with less permeable fabrics or by using finer fibres with greater surface area to volume ratio, can create more even distribution of water content.

13.4.5 Effect of moisture vapor resistance of inner covering fabric

When the moisture vapor resistance of the inner covering fabric is varied from 64.7 to 2087.0 $s\ m^{-1}$, its effect on the water content distribution within the fibrous batting can be seen from Fig. 13.18. Obviously, the moisture vapor resistance of the inner covering fabric has a significant influence on the water content within the batting. This is due to the fact that fabric having a higher vapor resistance will retard the moisture entering the batting, hence resulting in less condensation. This, however, will cause discomfort to the wearer, as perspiration cannot be dissipated from the body effectively. The

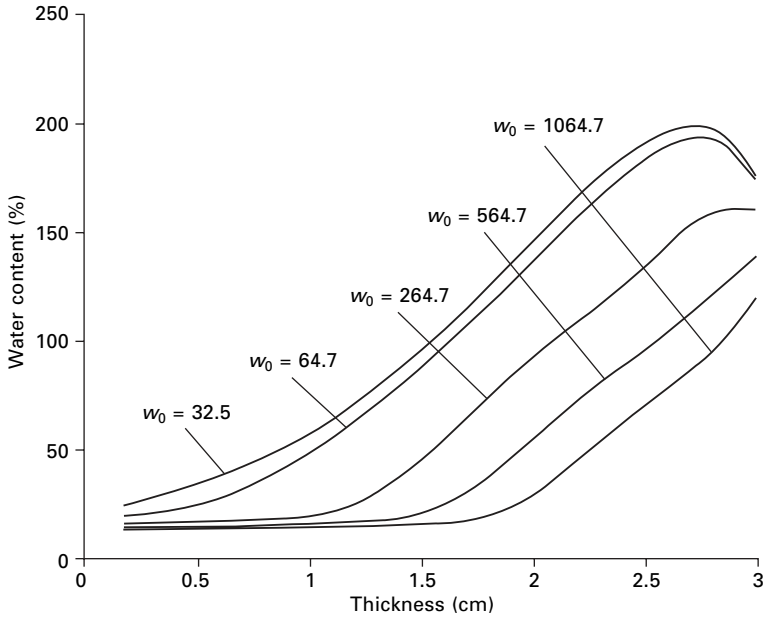

13.18 Effect of moisture vapor resistance (unit: s/m) of inner covering fabric on water content distribution after 24 hours.

increase of moisture vapor resistance of the inner covering fabric as a method for reducing condensation is hence not recommended.

13.4.6 Effect of moisture vapor resistance of outer covering fabric

The water content distribution within the batting is also significantly affected by the moisture vapor resistance of the outer covering fabric, as shown in Fig. 13.19. With an outer covering fabric of lower moisture vapor resistance, less condensation will take place within the batting. This is because more moisture will be transmitted by convection or diffusion into the environment through a more permeable outer covering fabric. The vapor permeability of the outer fabric is therefore critical and should be maximized while meeting the requirements of protection.

13.5 Conclusions

From experiments at –20 °C using a novel sweating guarded hot plate, it was found that most of the changes in temperature distribution within fibrous battings sandwiched by an inner and outer layer of thin covering fabric took place within 1/2 hour of exposure to the cold condition. The distributions of

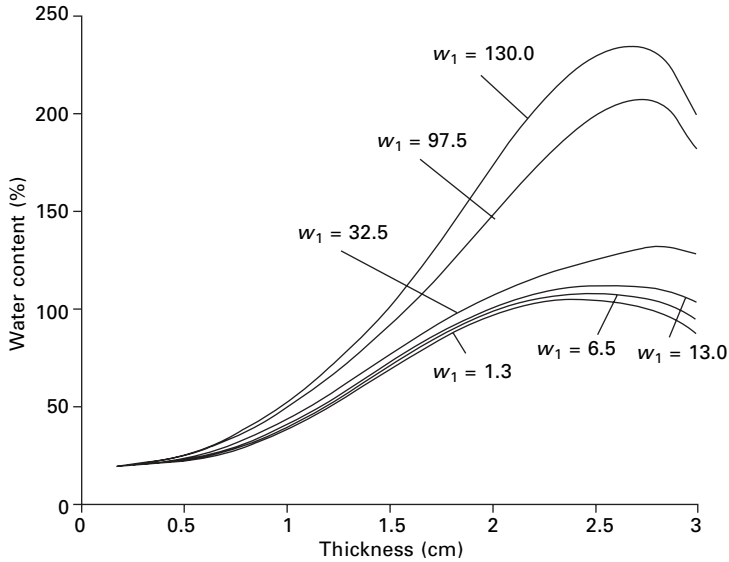

13.19 Effect of moisture vapor resistance (unit: s/m) of outer covering fabric on water content distribution after 24 hours.

temperature and water content within the battings are affected by the moisture absorption properties of the fibers and the density or porosity of the battings. Moisture absorption of the fibers increases the temperature in the battings. And greater permeability of the battings results in greater accumulation of condensed water in the outer region of the battings.

A theoretical model of coupled heat and moisture transfer within clothing assemblies considering moisture absorption, phase change, moisture bulk flow, radiative heat transfer and mobile condensates has been presented. Numerical solution was accomplished by using the Finite Volume Method. The theoretical results were compared with the experimental ones and found good agreement.

Numerical simulation was conducted to investigate the effects of various clothing parameters on the condensation and moisture absorption within clothing. Based on the numerical analysis, it is believed that, for clothing consisting of fibrous battings sandwiched by two layers of thin fabrics, inner fibrous battings having higher fiber content, finer fiber, greater fiber emissivity, higher air permeability, lower disperse coefficient of surface free water, and lower moisture absorption rate would cause less condensation and moisture absorption, which is beneficial to thermal comfort during and after exercising in cold weather conditions. It is also shown that covering fabrics have a significant influence on the water content within the fibrous batting.

13.6 Nomenclature

C_a water vapor concentration in the inter-fiber void space (kg m^{-3})
C_f mean water vapor concentration in the fiber (kg m^{-3})
C'_f volumetric moisture concentration in the fiber (it varies over the radius of the fibers) (kg m^{-3})
C_v effective volumetric heat capacity of the fibrous batting (kJ m^{-3} K^{-1})
C_{va} volumetric heat capacity of dry air (kJ m^{-3} K^{-1})
C_{vf} effective volumetric heat capacity of the fiber (kJ m^{-3} K^{-1})
C_{vw} volumetric heat capacity of water (kJ m^{-3} K^{-1})
D_a diffusion coefficient of water vapor in the air (m^2 s^{-1})
d_f diffusion coefficient of moisture in the fiber (m^2 s^{-1})
d_l disperse coefficient of free water in the fibrous batting (m^2 s^{-1})
E condensation or evaporation coefficient, dimensionless
F_L total thermal radiation incident traveling to the left (W)
F_R total thermal radiation incident traveling to the right (W)
h_c convective mass transfer coefficient (m s^{-1})
h_t convective thermal transfer coefficient (W m^{-2} K^{-1})
k effective thermal conductivity of the fibrous batting (W m^{-1} K^{-1})
K_x permeability of porous batting (m^2)
K_{rx} relative permeability of porous batting (m^2)
k_x coefficient of Darcy's Law (m^2 $(Pa.s)^{-1}$)
L thickness of the fabric batting (m)
L_i thickness of the inner and outer covering fabrics (m) (i = 0: inner fabric; i = 1: outer fabric)
M molecular weight of the evaporating substance, M = 18.0152 ($g.mol^{-1}$) for water
p pressure of water vapor in the inter-fiber void (Pa)
p_{sat} saturated water vapor pressure at temperature T_s (Pa)
p_v vapor pressure in vapor region at T_v (Pa)
R the universal gas constant, R = 8.31 (J K^{-1} mol^{-1})
R_f radius of fibers (m)
R_{ti} resistance to heat transfer of inner or outer covering fabric (Km^2 W^{-1}) (i.e. i = 0: inner fabric, i = 1: outer fabric)
R_{wi} resistance to water vapor (i.e. i = 0: inner fabric, i = 1: outer fabric) (s m^{-1})
R_{di} diffusion resistance to water vapor
r radial distance (m)
RH_i relative humidity of the surroundings (%) (i.e. i = 0: surface next to human body, i = 1: surrounding air)
Rhf relative humidity of the air space within the porous batting (%)
T temperature (K)
T_i temperature of the boundaries (K) (i.e. i = 0: surface next to human body, i = 1: surrounding air)

T_s temperature at the interface of condensates and vapor (K)
T_v temperature in the vapor region (K)
t time (s)
u velocity of water vapor (m s^{-1})
W water content of the fibrous batting (%), which is defined as the weight of water divided by the weight of the dry fibrous batting, and may be greater than 100%
W_{ai} weight of the ith layer of the batting after placing on the instrument in the cold chamber (g)
W_{0i} weight of the ith layer of the batting before placing on the instrument in the cold chamber (g)
W_c critical level of water content above which the liquid water becomes mobile (%)
W_f water content of the fibers in the porous batting (%)
WC_i water content of the ith layer of the batting (%)
x distance from the inner covering fabric (the warm side) (m)
β radiative sorption constant of the fibers (m^{-1})
ε porosity of fibrous batting considering condensates (liquid water, or ice) in the batting
ε' porosity of the dry fibrous batting (ε = cubic volume of interfiber space/total cubic volume of batting space)
λ latent heat of (de)sorption of fibers or condensation of water vapor (kJ kg^{-1})
μ dynamic viscosity of dry water vapor (kg $m^{-1}s^{-1}$)
ρ density of the fibers (kg m^{-3})
ρ_w density of liquid water or ice (kg m^{-3})
σ Boltzmann constant $\sigma = 5.6705 \times 10^{-8}$ (W K^{-4} m^{-2})
τ effective tortuosity of the fibrous batting. The degree of bending or twist of the passage of moisture diffusion due to the bending or twist of fibers in the fibrous insulation. It normally changes between 1.0 and 1.2, depending on the fiber arrangements.
Γ total rate of (de)sorption, condensation, freezing and/or evaporation (kg s^{-1} m^{-3})
Γ_{ce} rate of condensation, freezing and/or evaporation (kg s^{-1} m^{-3})
Γ_s rate of (de)sorption (kg s^{-1} m^{-3})

13.7 References

1. Spencer-Smith J L, 'The Physical Basis of Clothing Comfort. Part 6: Application of the Principles of the Design of Clothing for Special Conditions', *Clothing Res. J.*, 1978.
2. De Vries D A, 'The theory of heat and moisture transfer in porous media revisited', *Int. J. Heat Mass Transfer* 1987 **30** (7) 1343–1350.

3. Fan J, *A Study of Heat Transfer through Clothing Assemblies*, Ph.D Thesis, The University of Leeds, 1989.
4. Fan J and Keighley J H, 'A theoretical and experimental study of the thermal insulation of clothing in windy conditions', *International Journal of Clothing Science and Technology* 1989 **1** (1) 21–29.
5. Fan J and Keighley J H, 'The design of effective clothing for use in windy conditions', *International Journal of Clothing Science and Technology* 1989 **2**(1) 28–32.
6. Chen Z., *Primary Driving Force in Wood Vacuum Drying*, Ph.D Thesis, Virginia Polytechnic Institute and State University, 1997.
7. Bouddour A, Auriault J L and Mhamdi-Alaoui M, 'Heat and mass transfer in wet porous media in presence of evaporation-condensation', *Int. J. Heat Mass Transfer* 1998 **41** (15) 2263–2277.
8. Langlais C, Hyrien M and Karlsfeld S, 'Moisture migration in fibrous insulating material under the influence of a thermal gradient and its effect on thermal resistance', *ASTM Special Technical Publications* 779, 1982, 191–206.
9. Slegel D L and Davis L R, 'Transient heat and mass transfer in soils in the vicinity of heated porous pipe', *J. Heat Transfer* 1977 **99** 541–546.
10. Saito H and Seki N, 'Mass transfer and pressure rise in moist porous material subjected to sudden heating', *J. Heat Transfer* 1977 **99** 105–112.
11. Thomas W C, Bal G P and Onega R J, 'Heat and Moisture Transfer in a Glass Roof-insulating Material', *ASTM STP* 1983, **789**, 582–601.
12. Farnworth B, 'Mechanics of heat flow through clothing insulation', *Textile Research Journal* 1983 717–725.
13. Shapiro A P and Motakef S, 'Unsteady heat and mass transfer with phase change in porous slab: analytical solutions and experimental results', *J. Heat Mass Transfer* 1990 **33**(1) 163–173.
14. Wijeysundera N E, Hawlader M N A and Tan Y T, 'Water vapor diffusion and condensation in fibrous insulations', *Int. J. Heat Mass Transfer* 1989 **32**(10) 1865–1878.
15. Tao Y X, Besant R W and Rezkallah K S, 'Unsteady heat and mass transfer with phase changes in an insulation slab: frosting effects', *Int. J. Heat Mass Transfer* 1991 **34** (7) 1593–1603.
16. Murata K, 'Heat and mass transfer with condensation in a fibrous insulation slab bounded on one side by a cold surface', *Int. J. Heat Mass Transfer* 1995 **38**(17) 3253–3262.
17. Fan J, Cheng X Y and Chen Y S, 'An experimental investigation of moisture absorption and condensation in fibrous insulations under low temperature', *Experimental Thermal and Fluid Science* 2003 **27** 723–729.
18. Fan J and Cheng X Y, 'Heat and Moisture Transfer with Sorption and Phase Change Through Clothing Assemblies: Part I: Experimental Investigation', *Textile Research Journal* 2005 **75**(2) 99–105.
19. Corripio A B, *Tuning of Industrial Control System (2nd ed.)*, North Carolina, ISA, The Instrumentation, Systems, and Automation Society, 2001, 7–32.
20. Instruction Manual for KES-F8-AP1 Air Permeability Tester, Kyoto, Kato Tech Co. Ltd.
21. Henry P S H, 'Diffusion in absorbing media', *Proceedings of the Royal Society of London*, Series A, 1939 **171** 215–241.
22. Ogniewicz Y and Tien C L, 'Analysis of condensation in porous insulation', *J. Heat Mass Transfer* 1981 **24** (4) 421–429.

23. Motakef S and El-Masri M A, 'Simultaneous heat and mass transfer with phase change in a porous slab', *J. Heat Mass Transfer* 1986 **29**(10) 1503–1512.
24. Farnworth B, 'A numerical model of the combined diffusion of heat and water vapor through clothing', *Tex. Res. J.* 1986 **56** (11) 653–665.
25. Vafai K and Sarkar S, 'Condensation effects in a fibrous insulation slab', *J. Heat Transfer* 1986 **108** (8) 667–675.
26. Vafai K and Tien H C, 'A numerical investigation of phase change effects in porous materials', *Int. J. Heat Mass Transfer* 1989 **32** (7) 1261–1277.
27. Tao Y X, Besant R W and Rezkallah K S, 'The transient thermal response of a glass-fiber insulation slab with hygroscopic effects', *Int. J. Heat Mass Transfer* 1992 **35** (5) 1155–1167.
28. Fan J, Luo Z and Li Y, 'Heat and moisture transfer with sorption and condensation in porous clothing assemblies and numerical simulation', *Int. J. Heat Mass Transfer* 2000 **43** (12) 2989–3000.
29. Fan J and Wen X, 'Modelling heat and moisture transfer through fibrous insulation with phase change and mobile condensates', *Int. J. Heat Mass Transfer* 2002 **45** 4045–4055.
30. Cheng X Y and Fan J, 'Simulation of heat and moisture transfer with phase change and mobile condensates in fibrous insulation', *Int. J. of Thermal Sciences* 2004 **43** 665–676.
31. Fan J, Cheng X Y, Wen X and Sun W, 'An improved model of heat and moisture transfer with phase change and mobile condensates in fibrous insulation and comparison with experimental results', *Int. J. of Heat and Mass Transfer* 2004 **47** 2343–2352.
32. Fan J and Cheng X Y, 'Heat and moisture transfer with sorption and phase change through clothing assemblies: Part II: Theoretical modeling, simulation, and comparison with experimental results', *Textile Research Journal* 2005 **75** (3) 187–196.
33. Gibson P W and Charmchi M, 'Modeling convection/diffusion processes in porous textiles with inclusion of humidity-dependent air permeability', *International Comm. Heat Mass Transfer* 1997 **24**(5) 709–724.
34. Jones E F, *Evaporation of Water – With Emphasis on Application and Measurements*, Michigan, Lewis Publishers, 1992, 25–43.
35. Patankar S V, *Numerical Heat Transfer and Fluid Flow*, Levittown, Taylor & Francis, 1980, 31–40.
36. Ghali K, Ghaddar N and Jones B, 'Modeling of heat and moisture transport by periodic ventilation of thin cotton fibrous media', *International Journal of Heat and Mass Transfer* 2002 **45** 3703–3714.

14

Computer simulation of moisture transport in fibrous materials

D. LUKAS, E. KOSTAKOVA and A. SARKAR
Technical University of Liberec, Czech Republic

The present chapter is oriented towards the field of computer simulation of some selected transport phenomena associated with fibrous materials. Particularly, the phenomena covered here are transportation of liquid and moisture along individual fibres, fibre bundles, and in fibrous masses. A unified approach to describe these physical processes, based on stochastic processes in the lattices with spatial interactions amongst the lattice cells, has been sought. Unlike the classical fashion of analysis, generally incorporating dynamics of heat and fluids with an application of differential calculus in continuum, this method is characterised by discrete cells that represent nibbles of solid fibres, liquids and gases, mutually bonded together with various types of interactions. Unfortunately, this distinctive endeavour has not covered the phenomena associated with liquid viscosity in detail, but has created an excellent theoretical base, reflecting manifold structural aspects of fibrous masses.

Briefly, the first section, 14.1, will be primarily concerned with a description of random fields and Markov random fields, following a short introduction to one of the most famous spatial schemes used for computer simulations, known as the Ising model. These mathematical objects will be illustrated with a few elementary examples. As will be explained there, random and Markov random fields delineate the richness of manifold configurations, which mutate with time and exhibit the properties of their constituent cells, thus demonstrating the net geometry of their interactions. Subsequently, the remarkable proposition of Besag will be formulated in Section 14.2 to bridge the gap between joint and local conditional probabilities of random fields. The mathematical conceptualisation of the Besag proposition will then serve as the general equation encompassing all kinds of spatial interactions in the model. The interactions dealt with there will be described using the notions of 'neighbourhood' and 'clan'. In the process of finding a general solution for the Besag proposition, the theorem of Hammersley and Clifford that will form, thenceforth, the foundation to categorise stochastic models with spatial

interactions, will be encountered. Amongst them, the auto-model will be of prime concern here and will be used for computer simulation of wetting phenomena. The fact that the Hammersley and Clifford theorem rationalises an additive nature of energies in physical systems, which are well explained with the concept of random fields, is also estimable. The dynamics of the stochastic processes and their time evolution in the domain of random fields will be managed by Markov chains, based on various exchange dynamics. Eventually, constraints associated with the Besag proposition, from the viewpoint of conservation laws of canonical systems, will be mentioned.

Unlike the preceding sections, which mainly concentrate on the theoretical concepts of stochastic spatial processes, Section 14.3 contains three case studies of computer simulation used for reproducing wetting phenomena in a fibre mass. To begin with, individual fibres will be chosen to use a well-established fact pertaining to interfacial fluid dynamics, called 'Rayleigh instability', to explain the behaviour of liquid films coating individual fibres. This instability has a significant influence on the processes of fibre spinning from polymer solutions or melts. The theory justifies the spontaneous creation of equidistantly spaced droplets from liquid films covering individual cylindrical fibres, and the detachment of liquid jets into drops. The description will be prolonged thereafter, describing morphological transitions of shapes of the liquid body within bundles of parallel fibres with various inter-fibre distances. In addition, transition from long cylindrical to unduloid structures of liquids for pairs of parallel fibres, will be dealt with. The third case study of this section is related to the behaviour of moisture imbibitions in disordered fibrous material.

14.1 Introduction

The random evolution of spatial systems with spatially interacting variables has attracted the attention of numerous disciplines, viz. plant ecology (Besag, 1974), chemistry (van Kampen, 1992), physics (Swishchuk, 1997), cybernetics (Korolyuk and Swishchuk), 1995; Ermakov and Nekrakin, 1989), and modelling of images and textures (Chen and Dubes, 1989). Probably, the first physical model built on a spatial concept was the Ising model. It was introduced by Lenz (1920) and Ising (1925) at the beginning of the twentieth century. A more recent survey of this classic model has been given by Prum and Fort (1991).

The Ising model consists of a periodic lattice of cells wherein are situated elementary magnets with either 'up' or 'down' orientation with respect to a preferred direction. Physically, two neighbouring magnets require less energy to be orientated in the same orientation as compared to a mutually opposite one. It was primarily assumed that each magnet was sensitive only to the orientation of its nearest neighbouring magnets. So the first spatial scheme

was created, having a lattice with spatially interacting elements represented by magnets at each of the lattice cells, defined by random variables also known as the Ising variables, ascribed with values +1 and –1. The basic concept of the Ising model is displayed in Fig. 14.1. This model was developed to explain the thermal dependence of magnetism. Such dependence originates due to thermal fluctuations causing, for instance, magnets to be flipped randomly and subsequently to new orientations in discrete steps. The new local configuration of an elementary magnet in a cell is then determined by comparison of the values of 'local conditional probabilities'. Although this notion will be detailed subsequently, for the time being, it can be mentioned that the first 'local conditional probability' refers to the probability of the original configuration of the chosen elementary magnet with respect to a certain configuration of its neighbours, i.e. the configuration of its neighbouring elementary magnets creates the condition. The last local conditional probability belongs to a newer orientation of the magnet under consideration, subjected to the same condition. Both the local conditional probabilities depend on the sum of the interaction energies between the elementary magnet having a certain orientation, and its neighbours, and, of course, on the temperature.

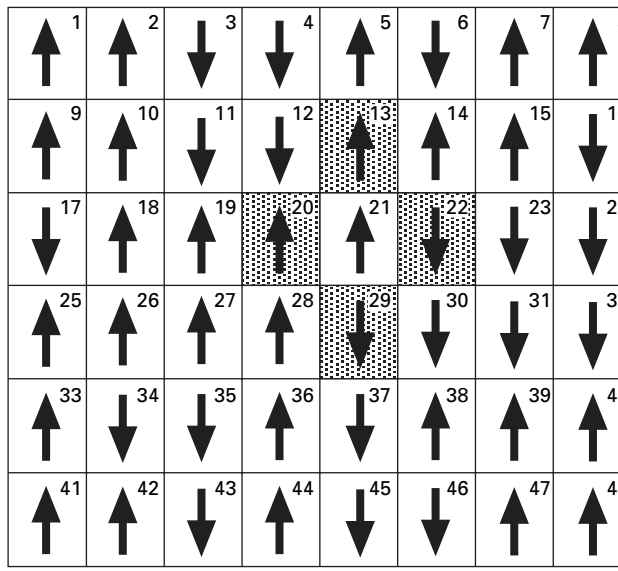

14.1 Up or down orientated magnets in the two-dimensional Ising model. The lattice consists of 48 cells. Each of them contains an elementary magnet. The up magnet orientation is assigned the value +1 of the random variable while the down orientation is coded as –1. Each cell in the classic Ising model interacts only with its nearest neighbours. The particular cell s_{21} neighbourhood consists of cells $\{s_{13}, s_{20}, s_{22}, s_{29}\}$.

The lower the interaction energy of a configuration, the higher is the probability of its occurrence. Temperature also influences these transitional probabilities of flipping. An elevated temperature causes the system to resist a shift towards a higher ordered configuration of its array of elementary magnets. The Ising model was designed for studying the phase transition between the ferro- and para-magnetic state of metals.

Spatial schemes, built on approaches more generalised than that of the Ising model (having random variables attributable by more than two values, representing spatial dislocation of various materials, such as, gas, liquid, and solid fibre in the case of wetting and liquid transport phenomena) will be employed. The Ising model was designed chiefly for a thorough investigation of phase transitions such as the previously mentioned transition between ferro- and para-magnetic states. As opposed to that approach, this chapter emphasises the pertinence of the spatial schemes, namely auto-models, to analyse phenomena far away from a threshold of phase transition given by a critical temperature. The present attempt is mainly aimed at an investigation of the influence of the boundary conditions on the system configuration. As an example, an interaction of a fibre surface with a binary mixture of a liquid and a gas to evoke wetting and a subsequent transfer of the liquid into the fibrous material may be thought of. The liquid starts to take conformations of films and droplets to coat the solid fibres. The manifold morphology of liquid bodies, interacting with fibres and fibrous masses, hence conforms to the complexity of the superficial geometry of fibrous matters. In this chapter, an elaborate microscopic account of such complex structure-based phenomena, using computer simulation, is presented.

14.1.1 Random fields

Two fundamental mathematical concepts of random field and Markov random field, significantly involved in the context of the present chapter, will be described in this subsection. The concept of 'random field' forms the foundations of the Besag proposition. The construct of Markov random field facilitates 'knowing the ropes' in a quantum of existing and unrealized interactions between elements/cells belonging to a random field, thus simplifying procedural aspects of model design with all the required essence kept intact for explaining the physics of the phenomena.

The notations for random fields used in this chapter will be kept as it was used by Geman (1991) and Paget (1999). Spatial schemes, which will be dealt with, consist of a set S of cells, denoted by s_i where i is an index identifying each of the cells individually. Set S is represented as $S = \{s_1, s_2, \ldots, s_n\}$, where n is the total number of cells in a particular system. For any of the cells s_i belongs a random variable X_i assigned with values x_i from a local configuration state space Λ_i. Any particular configuration of a lattice

composed of those elementary cells is given by a set of values of related random variables, conveniently represented as $\vec{x}$ with elements $\{x_1, x_2,\ldots, x_n\}$ and mostly referred to as the 'configuration vector'. The global configuration space of the system Ω is then created by the product of all the local configuration state spaces Λ_i's.

$$\Omega = \prod_{1\le i\le n} \Lambda_i \qquad [14.1]$$

Thus, the geometry of a random field has been presented. To make it more vivid, let it be illustrated with some more examples, such as a bed of carrot plants in a yard. Using a plant peg, the bed is divided into areas, each of which represents a cell. The cells of this system need not be regular. A usable variable X_i to evaluate a horticultural achievement may be considered to be assigned with the number of plants $x_{i,}$ in a cell s_i. The number of plants x_i may vary stochastically with time, i.e. over various seasons. Here, the number x_i is a particular value of the random variable X_i. The local configuration space Λ_i is directly connected to the number n_i of seeds embedded in a cell s_i as the random variable X_i may have values $\{0, 1, 2, \ldots, n_i\}$, ranging from an absolute failure or, 'zero success', i.e. when none of the seeds germinate, to an entire success, i.e. when all n_i seeds germinate. Here, the global configuration space Ω represents all the eventualities of carrot plant distributions, for instance $\vec{x} = (3, 0_2, 5_3, \ldots, 2_n)$ as given by the local fertility of the bed and the interactions among plants. Over a series of seasons, the variable X_i behaves randomly because of the fact that the yield depends on contingencies such as weather, activity of pests, intensity of sunlight and competition among all the carrots for water, mainly dependent on watering and weeding of the bed.

The next example of a random field is more close to the subject of our interest. Envisage that a three-dimensional space in the vicinity of a fibre, coated with a liquid film, is divided into regular cubic cells. The set of cubes in a lattice, in this case, may be related to the set S of cells, as defined before. Local variable X_i in a cell s_i is then considered to acquire three possible values $\{0, 1, 2\}$ i.e. $x_i \in \{0, 1, 2\}$, depending on the prevailing material in it, viz. a gas, a liquid, or a solid fibre. The related local configuration state space Λ_i then either consists of values $\{0, 1\}$ for areas with liquid–gas binary mixture, or is composed of a value of 2, signifying a solid fibre, considered fixed in space and stationary over time. The global configuration space Ω is then made up of all the possible configurations given by redistribution of gas and liquid cells within a fixed fibrous mass. The concept of this type of random field is pictorially depicted in Fig. 14.4 of Section 14.1.2, which will follow the forthcoming discussion concerning intercellular interactions of a system.

With the random fields are consorted two generic notions of 'joint' and 'local conditional' probabilities. The joint probability is associated with the

appearance of a particular configuration $P(\vec{x})$ of a system as a whole, and the 'local conditional probability' concerns that of a local value x_i in a cell, s_i, conditional to a certain fixed configuration to which the remaining cells are tuned up. A local conditional probability will be denoted as $p(x_i|\ x_1, x_2,\ldots, x_{i-1}, x_{i+1},\ldots, x_n)$, wherein the part of the argument of p before the partition represents the concern about the probability of an appearance of x_i in the cell s_i, while the set of concrete random variable values $\{x_1, x_2,\ldots, x_{i-1}, x_{i+1},\ldots, x_n\}$, beyond the partition, appropriately expresses the fixed configuration of all the remaining cells of the system that represents the condition.

Now, to explain vividly the concept of global, i.e. joint and local conditional probabilities, a modified Ising model will be utilised. Let a part of a regular two-dimensional square lattice, comprising nine cells arranged in a square array, be as shown in Fig. 14.2. In each of the cells is embedded an elementary magnet. It may be supposed that this random field of magnets is not influenced by any external magnetic field and so configurations involve, exclusively, mutual interaction among the elementary magnets. Deviating from the classic Ising model, it is further assumed that the mutual interactions exist among all the nine elementary magnets. Now, if the temperature of the system is

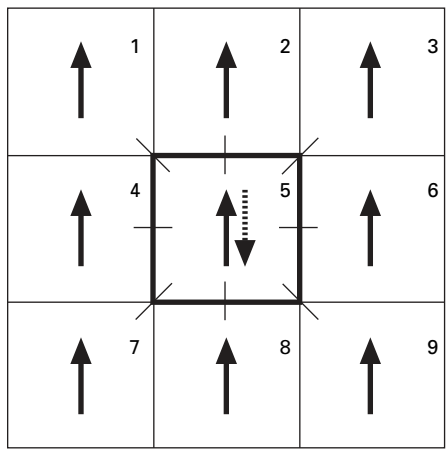

14.2 The modified two-dimensional Ising model with the neighbourhood of the central cell s_5 composed of eight cells. Interaction exists between the cells s_5 and all its neighbours from the set of cells $S = \{ s_1, s_2, s_3, s_4, s_5, s_6, s_7, s_8, s_9\}$ as is indicated using pieces of the lines outgoing from the cell s_5. We suppose the ambient temperature is very low and hence the fully coherent orientation of all elementary magnets is extremely probable. Without an external magnetic field, the joint probability value of the configuration with all magnets up is 0.5, while the joint probability of the configuration with only the central magnet down and the rest up is zero.

very low, i.e. if it tends towards absolute zero, the joint probability for the total order in the system becomes very high due to identical orientations of the elementary magnets. There exist two such completely unified configurations, characterised by all the elementary magnets orientated either upwards or downwards. It is due to the choice of a temperature close to absolute zero that the two entirely ordered arrangements of the random field of nine magnets share a unitary value of the total probability of appearance of all possible configurations having identical cellular orientations. Denoting the upward orientation of an elementary magnet in a cell s_i with a value of the random variable (x_i) as +1 and the downward orientation as –1, the joint probabilities pertaining to two different instances when all the magnets simultaneously point upwards or downwards are represented as $P(+1_1, +1_2, +1_3, +1_4, +1_5, +1_6, +1_7, +1_8, +1_9)$ and $P(-1_1, -1_2, -1_3, -1_4, -1_5, -1_6, -1_7, -1_8, -1_9)$, respectively, each having a value of 0.5. It is quite obvious that any other configuration, with at least one magnet oppositely orientated with respect to the others, will certainly have a joint probability nearly equal to zero. For instance, an alternately orientated array of elementary magnets, $P(+1_1, -1_2, +1_3, -1_4, +1_5, -1_6, +1_7, -1_8, +1_9)$, has a value equalling zero.

Let a chosen local probability of an elementary magnet in the field, be considered keeping the rest of the eight unaltered. First of all, appropriate conditions are selected to evaluate the local probabilities of its two possible orientations. In this process the elementary magnet at the centre of the array in the cell s_5 will be attended. Considering an upward orientation of all the other elementary magnets, the set of eight variables, as stated before, may be arranged as $\{+1_1, +1_2, +1_3, +1_4, +1_6, +1_7, +1_8, +1_9\}$. The upward orientation of the central magnet, under this condition, will be highly probable, i.e. it can be written that $p(+1_5| +1_1, +1_2, +1_3, +1_4, +1_6, +1_7, +1_8, +1_9)$ has a value of 1. It should be noted here that the state of the central magnet is not the condition of itself. Accordingly, the index 5 with its assigned variable x_5 is excluded from the conditional part of the argument of the aforementioned local conditional probability p. For the same system there exists another instance of the local conditional probability related to the cell at the fifth position under the same condition. It refers to the downward orientation of the central magnet. For this particular configuration, the local conditional probability, $p(-1_5| +1_1, +1_2, +1_3, +1_4, +1_6, +1_7, +1_8, +1_9)$ diminishes as the temperature approaches absolute zero.

An upward or downward orientation of the central elementary magnet may be chosen for quite an improbable configuration, such as the one having an alternate arrangement of upwards and downwards orientations of the rest of its eight elementary magnets, represented as $\{+1_1, -1_2, +1_3, -1_4, -1_6, +1_7, -1_8, +1_9\}$. The relevant local conditional probability, $p(+1_5| +1_1, -1_2, +1_3, -1_4, -1_6, +1_7, -1_8, +1_9)$ for the upward orientation of the central magnet then attains a value of 0.5, as the central elementary magnet, acted upon by

equally numerous groups of neighbours, has an equal chance to be orientated either upwards or downwards. A similar result is obtained for the downward orientation of the central magnet, i.e. $p(-1_5|\,+1_1, -1_2, +1_3, -1_4, -1_6, +1_7, -1_8, +1_9)$ too has a value of 0.5. Hence, the sum of the local conditional probabilities associated with two possible local configurations of the cell s_5 under the same condition is equal to one.

Obviously, the sum of local conditional probabilities for all nodes s_i of the random field for a particular system configuration is not normalised and so may be, occasionally, greater than unity. This is well exemplified, when a coordinated upward orientation of all the magnets with a joint probability value of 0.5 is considered. Each of the local conditional probabilities with x_i having a value of +1, i.e. $p(x_i|\,+1_1, \ldots +1_{i-1}, \ldots, +1_9)$ then approaches a value of 1, mainly due to the interaction of the elementary magnet in the observed cell s_i having an orientation identical to the predominant orientation of the system. Hence, the sum of all local conditional probabilities for an entire upward orientation, i.e. $\sum_{1\le i\le 9} p(x_i|+1_1, \ldots, +1_{i-1}, \ldots, +1_9)$ is 9.

Interactions between all the members of the set S are permitted in random fields, whereas restrictions in this regard are exerted in Markov random fields, as will be described in the next subsection.

14.1.2 Markov random fields

A Markov random field is a random field with a slightly modified characteristic concerning the condition that influences the value x_i attributed to the variable X_i at a cell s_i. The value of x_i may be any one from a local state space Λ_i, but the probability that X_i assumes a value x_i is strictly conditional to the values x_j of the neighbouring cells of s_i. This assumption, as a rule, causes that random field to have independent regions, at least by groups of two. In other words, a random field is composed of groups of cells wherein local probabilities are not conditioned by the configurations in the independent regions. This condition is referred to as the Markovian condition and the pertinent field is known as the Markov random field. Moussouris (1973) mentioned that this Markovian assumption resembles the definition of the famous Markov random chains in which the likelihood of a particular configuration of a system at any instant depends on the state of its immediate past only and not on any other of its historical details (Van Kampen, 1991). Markov chains will be involved more deeply later in Section 14.2.5 to inspire dynamics in some models. A Markov random field is, therefore, a space–time analogy of a Markov chain where some events, characterised by a certain space, depend on chosen spatial neighbours only at the same instant of time and not on the whole spatial array of other events. This comparison has a slight limp with time, having a constantly grooving value, while on the other hand, interactions in space schemes are distributed in three dimensions and are, as a rule,

bilateral. Nevertheless, the analogy with their preceding spatial distribution of interactions has caused these random fields to be named Markov random fields.

The notion of a Markov random field is documented here taking support from the following example. Resurrecting the previous example of a carrot bed and selecting one plant in it, let it be indexed with '*i*' for denoting its cell. The system of cells consists, at this moment, of individual plants. As is seen from Fig. 14.3, the plant in this concrete Markov random field has just five close neighbours with whom it competes for water and sunshine. Here, a mutual independence between growth of the chosen plant in the cell s_i and the plants situated further on may be considered as a supposition, i.e. the development of the plant in question and its 'non-neighbours' are independent of each other. To be more precise, for the Markov random field model of the bed, the corresponding local conditional probabilities of 'non-neighbours' are independent of each other.

The last illustration underlines that a neighbourhood does not necessarily mean a group of cells from the vicinity of a chosen one. Considering a dissociated liquid wetting a fibre and subsequently treating this system as a Markov random field, two kinds of interactions of a cell have to be accounted for. Short-range intermolecular interaction, caused by van der Waals forces is one. The other involves long-range interaction caused by Coulomb

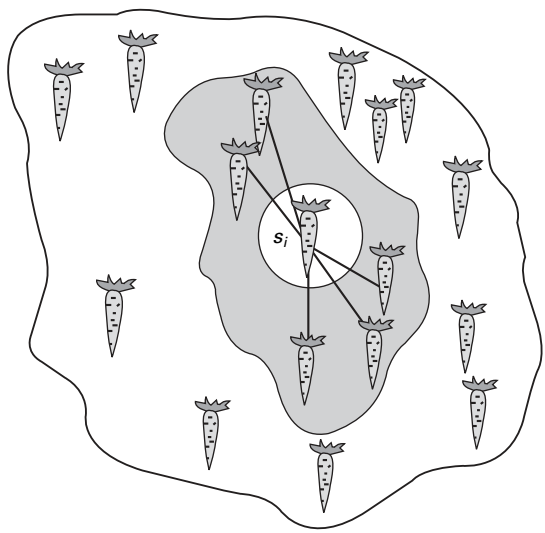

14.3 A Markov field of an irregular bed of carrot plants: The carrot plant denoted with the index *i* has five neighbours. This neighbourhood lies in the greyish area of the bed. In the white area behind this neighbourhood are located plants that are not able to influence the growth of the *i*-th one. That is why the local conditional probability concerning the *i*-th carrot does not depend on them.

electrostatic forces between charged particles, i.e. between dissociated ions. Such a neighbourhood is sketched in Fig. 14.4.

Undoubtedly, mathematical objects of random and Markov random fields are so universal that they can be used widely to model systems, especially those concerning many-body issues. On the other hand, random and Markov random field are such general objects that it seems no massive and special rules govern them, but the contrary is surprisingly true, as will be shown in the next section.

14.2 Auto-models

To demonstrate the rules and laws governing random fields and Markov random fields, let the Besag proposition, introduced in the first half of the 1970s by Besag (1974), be considered. Besag's speech, read before the Royal Statistical Society in the year 1974, had been inspired by the area of plant ecology, which was then supposed to benefit from the potential applications of this newly developed theory. As a typical illustration of a stochastic spatial situation in plant ecology, it had been mentioned beforehand in Cochran's work (1936) on patterns of infection in an array of tomato

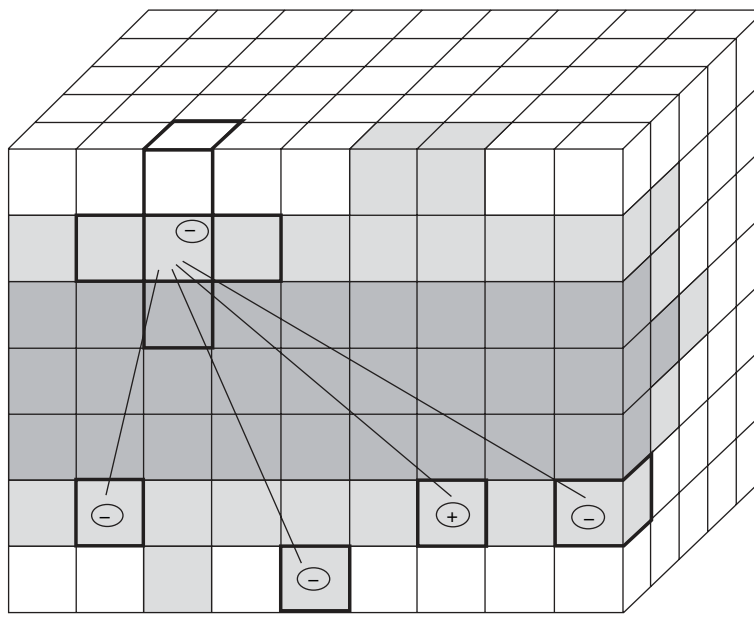

14.4 A neighbourhood of the charged liquid particle in the cell s_i is composed of particles in its vicinity interacting through van der Waals interactions and of all charged particles in the Markov random field that possess the long-range Coulomb interaction.

plants. It is due to the general nature of random fields that the Besag proposition, has recently become useful for versatile applications. As will be shown later in this section, there lies a strong link between the Besag proposition, its consequences, and some substantial ideas of statistical physics that are further employed to simulate cooperative wetting phenomena in fibrous masses.

14.2.1 The Besag proposition

It was only in the 1960s that the relationship between joint and local conditional probabilities of random fields was purely realized. White (1963) remarked that equilibrium processes in statistical mechanics have a natural construction in terms of joint probabilities rather than in local probability formulations. Again, it was found in the process of formulating the Ising model of ferromagnetism that the conditional probabilities completely generated its joint probabilities. This could well be explained by the fact that Markov chains were designed merely on the basis of the local conditional probabilities related to the local changes in Hamiltonian, as will be shown in Section 14.2.5. But, as has already been shown, the original Ising model considered exclusively the interactions with the nearest neighbours. At the start of the 1970s, two works (Spitzer, 1971; Besag, 1972) threw light on the joint-local conditional probability relationship for Markov random fields for systems based on concept of nearest neighbour in *k*-dimensional finite cubic lattices. The scope, consequently, was restricted neither to the nearest neighbour interactions nor to the lattice schemes. In fact, the Besag proposition is even valid for fairly arbitrary systems with the cells distributed randomly in space. The Basag proposition was formulated for random fields, without any limitation on the opulence of the intercellular interactions. As will be seen immediately, the Besag proposition is a direct consequence of Bayes' theorem.

$$p(x_i|\, x_1, x_2, \ldots, x_{i-1}, x_{i+1}, \ldots, x_n = \frac{P(x_1, x_2, \ldots, x_n)}{\Pi(x_1, x_2, \ldots, x_{i-1}, x_{i+1}, \ldots, x_n)} \qquad [14.2]$$

More information about Bayes' theorem is provided by Van Kampen (1992) in the section 'Multivariate distributions'. Two terms of Bayes' rule, i.e. in Equation [14.2], are frequently encountered, viz. the conditional probability p on the left-hand side and the joint probability P in the numerator of the right-hand side of the equation. The probability $\Pi(x_1, x_2, \ldots, x_{i-1}, x_{i+1}, \ldots, x_n)$ in the denominator is, according to Van Kampen (1991), referred to as the 'marginal probability', which is the sum of the joint probabilities for all the possible variable values x_i in a chosen cell s_i, keeping the variable values in all the remaining cells unchanged.

$$\Pi(x_1, x_2,\ldots, x_{i-1}, x_{i+1},\ldots, x_n) = \sum_{x_i \in \Lambda_i} P(x_1, x_2,\ldots, x_{i-1}, x_i, x_{i+1},\ldots, x_n) \quad [14.3]$$

where $(x_1, x_2,\ldots, x_{i-1}, x_{i+1},\ldots, x_1)$ are fixed and only x_i changes.

The above-cited Bayes' rule may be verified using the example connected to the modified Ising model consisting of nine cells, as described earlier in Section 14.1.1. Previously, the joint and the local conditional probabilities for a temperature approaching absolute zero were evaluated. Recalling that the calculated joint probabilities for the coordinated orientation of all the magnets constituting the lattice, directed either upwards or downwards, were 0.5 separately, the joint probability of the configuration with the downwards orientation solely being associated to the central magnet, i.e. $P(+1_1, +1_2, +1_3, +1_4, -1_5, +1_6, +1_7, +1_8, +1_9)$ has to have a value close to zero, as is evident from the normalisation condition $\sum_{\vec{x}\in\Omega} P(\vec{x}) = 1$. Consequently, the marginal probability, according to Eq. [14.3], comes out to be

$$\Pi(+1_1, +1_2, +1_3, +1_4, +1_6, +1_7, +1_8, +1_9) = 0.5 + 0 = 0.5 \quad [14.4]$$

It is notable at this juncture that the local configuration space Λ_5, related to the cell s_5, comprises only two possible configurations of upward and downward orientations. Accordingly, Bayes' rule furnishes identical values of the local conditional probabilities for the cell s_5 when the remaining magnets point upwards. It can also be seen that the local conditional probability p for $x_5 = +1$ is, in agreement with Eq. [14.2], equal to

$$p(+1_5 | +1_1, +1_2, +1_3, +1_4, +1_6, +1_7, +1_8, +1_9) = \frac{0.5}{0.5} = 1 \quad [14.5]$$

while, under the same condition, the local conditional probability p with the central magnet pointing downwards, i.e. $x_5 = -1$, appears to be

$$p(-1_5 | +1_1, +1_2, +1_3, +1_4, +1_6, +1_7, +1_8, +1_9) = \frac{0}{0.5} = 0 \quad [14.6]$$

The above results, Equations [14.5] and [14.6], are in agreement with those obtained previously in Section 14.1.1.

The derivation of the Besag proposition begins with a trivial mathematical manipulation of Bayes' rule to enable one to rewrite the joint probability $P(\vec{x})$ of the system, taking into account events relating to cell s_1, as given below:

$$P(\vec{x}) = p(x_1 \mid x_2, x_3,\ldots, x_n)\ \Pi\ (x_2, x_3,\ldots, x_n) \quad [14.7]$$

Let another value, y_1, of the variable X_1 in the same cell s_1 be conceived, such that $x_1, y_1 \in \Lambda_1$. This means that the local state space Λ_1 is composed of at least two local configurations with two values of its local variable $X_1 = x_1$

or $X_1 = y_1$. Using this notion, Bayes' rule for random variable value y_1 in the cell s_1 may be written as

$$P(y_1, x_2, x_3,\ldots, x_n) = P(y_1 \mid x_2, x_3,\ldots, x_n)\ \Pi(x_2, x_3,\ldots, x_n) \qquad [14.8]$$

The marginal probability Π in Equation [14.8] is identical with the one in Eq. [14.7]. Hence these two equations may be used to obtain the following relation:

$$P(\vec{x}) = \frac{p(x_1 \mid x_2, x_3, \ldots, x_n)}{p(y_1 \mid x_2, x_3, \ldots, x_n)}\, P(y_1, x_2, x_3, \ldots, x_n) \qquad [14.9]$$

Therefore, the Bayes' rules for the joint probabilities $P(y_1, x_2, x_3,\ldots, x_n)$ and $P(y_1, y_2, x_3,\ldots, x_n)$, having marginal probabilities identical to the one obtained, when cell s_2 is attended $\Pi(y_1, x_3, x_4,\ldots, x_n)$, take the following forms:

$$P(y_1, x_2, x_3, \ldots, x_n) = \frac{p(x_2 \mid y_1, x_3, x_4, \ldots, x_n)}{\Pi(y_1, x_3, x_4 \ldots, x_n)},$$

$$P(y_1, y_2, x_3, \ldots, x_n) = \frac{p(y_2 \mid y_1, x_3, x_4, \ldots, x_n)}{\Pi(y_1, x_3, x_4 \ldots, x_n)} \qquad [14.10]$$

Implementing substitutions successively for $P(y_1, x_2, x_3,\ldots, x_n)$ in Eq. [14.9] from the first relation in Eq. [14.10] and then for the marginal probability $\Pi(y_1, x_3, x_4,\ldots, x_n)$ from the second relation in Eq. [14.10], the following relation is derived:

$$P(\vec{x}) = \frac{p(x_1 \mid x_2, x_3, \ldots, x_n)\, p(x_2 \mid y_1, x_3, x_4, \ldots, x_n)}{p(y_1 \mid x_2, x_3, \ldots, x_n)\, p(y_2 \mid y_1, x_3, x_4, \ldots, x_n)} \times P(y_1, x_2, x_3, x_4,\ldots, x_n) \qquad [14.11]$$

Undoubtedly, after 'n' such substitutions, the right-hand side of Equation [14.11] will have all the values of x_i replaced by new y_i values in the argument of the joint probability P as well as in arguments of the last fraction of conditional probabilities p, to take an ultimate form as exhibited in Eq. [14.12]. The most vital role played by the chain of substitutions is that the marginal probabilities, crucial in Bayes' rule, disappear from the Besag proposition. Therefore, the shape of the final relation can be predicted as

$$P(\vec{x}) = \frac{p(x_1 \mid x_2, x_3, \ldots, x_n)\, p(x_2 \mid y_1, x_3, x_4, \ldots, x_n)}{p(y_1 \mid x_2, x_3, \ldots, x_n)\, p(y_2 \mid y_1, x_3, x_4, \ldots, x_n)} \times \frac{p(x_3 \mid y_1, x_2, x_4, \ldots, x_n)}{p(y_3 \mid y_1, y_2, x_4, \ldots, x_n)} \times \ldots \frac{p(x_n \mid y_1, y_2, y_3, \ldots, y_{n-1})}{p(y_n \mid y_1, y_2, y_3, \ldots, y_{n-1})}\, P(\vec{y}) \qquad [14.12]$$

Arranging and concisely writing the terms of the above obtained relation, the Besag proposition is framed in the following way:

$$\frac{P(\vec{x})}{P(\vec{y})} = \prod_{1 \le i \le n} \frac{p(x_i \mid y_1, y_2, \ldots, y_{i-1}, x_{i+1}, x_{i+2}, \ldots, x_n)}{p(y_i \mid y_1, y_2, \ldots, y_{i-1}, x_{i+1}, x_{i+2}, \ldots, x_n)} \qquad [14.13]$$

where the symbol $\prod_{1 \le i \le n}$ denotes the product of all the fractional terms having indices ranging from 1 to n. The Besag proposition states that the joint probability distribution $P(\vec{x})$ of random variables X_i is uniquely determined by its local conditional probabilities p. It is quite obvious that each conditional probability appearing in the denominator of Equation [14.13] has to be non-zero. It implies that each configuration of the system has to have the chance to appear, i.e. $P(\vec{y}) > 0$ for each $(\vec{y}) \in \Omega$. This assumption was referred to as the 'positivity condition' by Hammersley and Clifford (1971). It will be seen later that the positivity condition gives a number of problems when dealing with some constraints imposed by using canonical and micro-canonical systems that conserve the numbers of particles and/or energy.

To comment on the mathematical formalism involved above, it may be observed that all the equations used there are basic algebraic equations constructed with ordinary operations of multiplication and division. The richness of these relations is, however, hidden in manifold forms of the joint and the local configurations that echo in complex forms of the arguments of joint and local conditional probabilities. To 'know the ropes' in an intricate juxtaposition of conditions caused by numerous intercellular interactions in the models aimed at in the present chapter, application of appropriate tools becomes indispensable. The next sub-section will include an elaborate account of such tools. For the time being, it can merely be said that the tools will conceptually encompass the forms of 'neighbourhoods' and 'clans'. These tools will be instrumental in the formulation of the Hammersley and Clifford theorem, which, in turn, will give birth to generalised 'energy functions'. The Hammersley and Clifford theorem will be formulated through the general solution of the Besag proposition.

14.2.2 Neighbourhoods and clans

The fundamental aspect of Markov random fields, demarcating the domain of interactions among cells in random fields, has already been described. Local probabilities for Markov random fields are conditional only on the values of x_j's referring to the predefined cells neighbouring to a selected cell s_i. As a supposition, N_i may be considered as the set of all the s_j cells that construct the neighbourhood of the cell s_i. Representing the relational facet of the neighbourhood N_i, formed by s_j cells having a set of random variables x_j, the notation $\{x_j;\ s_j \in N_i\}$ is applied. Using this notation, a more concise representation of conditional probabilities of either Markov random fields or random fields is accomplishable:

$$p(x_i|\, x_1, x_2, \ldots, x_n) = p(x_i|x_j;\, s_j \in N_i) \qquad [14.14]$$

Accordingly, the argument of the conditional probability on the right-hand side of Equation [14.14] is read in the following manner. Conditional probability that belongs to the appearance of a random variable X_i, assigned with a value x_i and associated to a referred cell s_i, depends on the condition that the cells $\{s_j;\, s_j \in N_i\}$ create a neighbourhood N_i of the cell at reference with a definite configuration $\{x_j;\, s_j \in N_i\}$. A set of all the existing neighbourhoods in a set of S cells make the neighbourhood system N. Drawing an analogy with the classic physical principle of action and reaction, the models will involve, hereafter, only symmetric neighbourhoods which adhere to the following criteria:

$$\text{(i) } s_i \notin N_i \quad \text{(ii) } s_j \in N_i \Leftrightarrow s_i \in N_j \qquad [14.15]$$

The first criterion claims that a cell s_i is not its own neighbour and the last one alleges that, if a cell s_j is an element of the neighbourhood N_i of the cell s_i then the cell s_i belongs to the neighbourhood N_j of the cell s_j, and vice versa. An example each of a symmetrical and an unsymmetrical neighbourhood is depicted in Fig. 14.5. On regular lattices, some symmetrical neighbourhoods have translational symmetry. The geometrical shape of such a neighbourhood N_i coalescences with that of a N_j after a translation, i.e., $\vec{t} : s_i \rightarrow s_j$, as also shown in Fig. 14.5. In this chapter, symmetric neighbourhoods will be predominantly dealt with.

An important property pertaining to the idea of neighbourhoods is the order 'o', introduced by Geman and Geman (1984) and Geman (1991) while dealing with the recognition of pictures. In the process, these authors sought appropriate symmetric as well as translational symmetric neighbourhoods. They chose an integer 'o' as the order of neighbourhood and constructed a neighbourhood N_i^o of order 'o', associated to a cell s_i as the set of cells s_k's fulfilling the condition

$$N_i^o = \{s_k \in S;\, 0 < /s_i - s_k/^2 \leq o\} \qquad [14.16]$$

The mathematical representation of the definition of a neighbourhood N_i^o of a cell s_i, having an order o, is interpreted as follows. The neighbourhood N_i^o of a cell s_i, having an order of o, is the set of cells s_k that belong to the set S of all cells, where the square of the distance between the cells s_i and s_k, abbreviated as $/s_i – s_k/^2$, is equal to or less than the neighbourhood order o. The first-order neighbourhood is also called the 'nearest neighbour neighbourhood'. The neighbourhoods of different orders are shown in Fig. 14.6. Generally, distances in regular lattices are measured in lattice units, l.u. One lattice unit is the distance between the nearest neighbouring cells.

In physical systems, the scope of inter-particle forces predefines the neighbourhood order. The order o is then the second power of the distance over which interaction energies are non-negligible. Moreover, various kinds

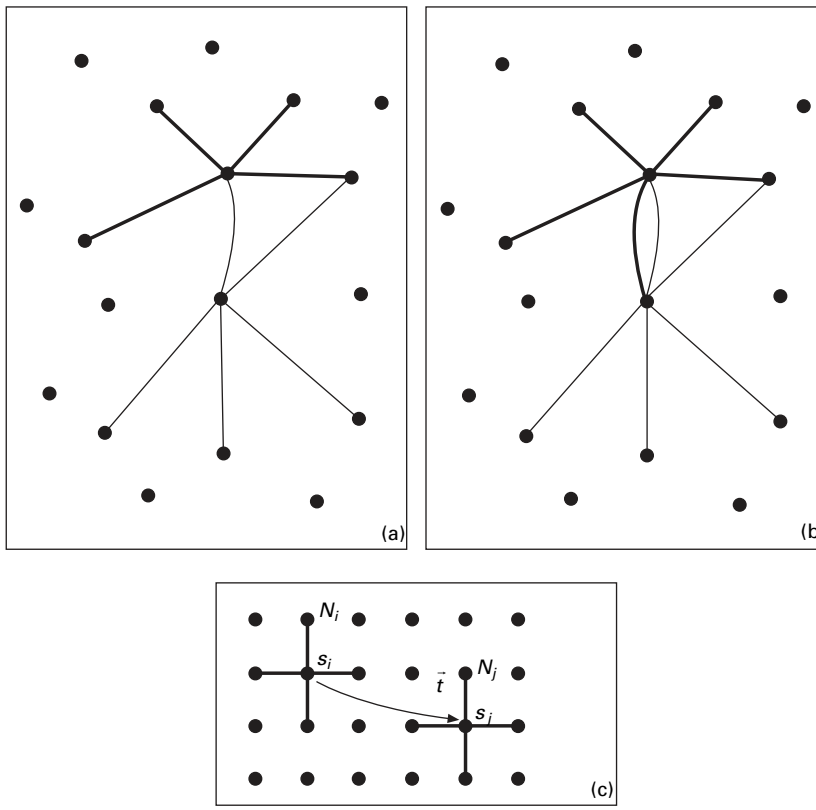

14.5 Symmetrical (a) and unsymmetrical (b) neighbourhoods of cells *i* and *j* in a Markov random field. Interactions of the cell s_i are depicted with a bold line while neighbouring cells of the cell s_j interact with it via thin bonds. On regular lattices, some symmetrical neighbourhoods have translational symmetry. The geometrical shape of neighbourhood N_i coalesces with N_j after the translation $\vec{t} : s_i \rightarrow s_j$.

of physical interaction, such as short-distance intermolecular forces together with long-distance selective Coulomb forces, can render sparseness to-neighbourhood. As an eventuality, the neighbourhood system loses the translational symmetry and so ceases to obey the relation [14.16], mainly accounted for by some uncharged cells at a distance D with magnitude less than that of the square root of the order o, i.e. $\sqrt{o}$ from the 'central' charged one s_i, characterised by either not having any long-range electrical interaction with the cell s_i or being beyond the reach of any short-distance forces from the referred cell to act upon. For a graphical interpretation of this kind of neighbourhood, Fig. 14.6(b) is presented.

A general solution of the Besag proposition will be sought in the next section, where the notion of a clan will be instrumental in accomplishing the

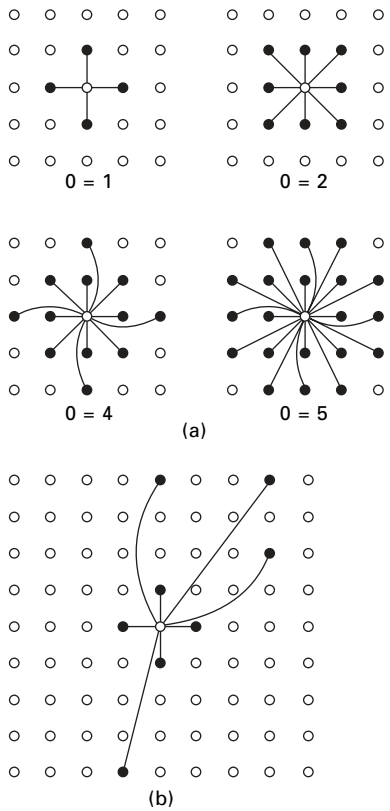

14.6 Neighbourhoods of the order o = 1, 2, 4, and 5 (a) are sketched, together with a Markov random field that contains a combination of short- and long-range interactions (b). Distances in regular lattices are measured, as a rule, in lattice units, l.u. One lattice unit is the distance between the nearest neighbouring cells.

present target. Clans are uniquely determined by a system of neighbourhoods N on a set S of all cells. According to Paget (1999), a 'clan' in a given a neighbourhood system N is a set 'c' of cells, where $c \subset S$. Every couple of distinct cells in the set c are mutual neighbours. That is, for each couple of cells s_i and s_j belonging to the set c, i.e. $s_i, s_j \in c$ such that, $s_i \neq s_j$, the relation $s_i \in N_j$ implies $s_j \in N_i$. As opposed to the definition of a neighbourhood, where the cell at reference s_i is excluded from its own neighbourhood, the definition of a clan says that a cell s_i creates its own clan, known as one-clan. Henceforth, the set of all possible clans in S with respect to the system of neighbourhoods N will be defined by C, while C_i will refer to the local set of the clans of a cell s_i, i.e. it will include all the clans where a cell s_i participates.

The number of clans grows almost exponentially with an increase in the order o of neighbourhoods in regular lattices of cells, as has been shown by

Paget (1999). In other papers and works, clans are called 'cliques' (Paget, 1999; Besag, 1974; Geman and Geman, 1984), but here will be used the notion of Moussoris (1973), who argued that the term clique is generally used in the graph theory for maximal complete sub-graphs, whereas clans are not only complete sub-graphs but, at times, are single sites and even empty sets, too. The count of cells in a clan will be introduced here as v, to denote a zero-clan – an empty clan; one-clan – a clan containing one cell only; two-clan – a clan containing two cells; and a v-clan for a clan consisting of v cells.

Being equipped with all the essential prerequisites, it is now time to seek the general solution of the Besag proposition. It will be realised in the next subsection with the endeavour perceived through the attainment of the Hammersley and Clifford theorem.

14.2.3 Hammersley and Clifford theorem

The Besag proposition [14.13], derived earlier in Section 14.2.1, has the striking feature of being independent of labelling of individual cells. This has rendered the flexibility to jumble up wildly the indices of the cells with the variable values assigned to them unaltered and retain the original form of the Besag proposition. Arbitrary labelling of cells evidently justifies the existence of severe restriction on the functional form of joint probabilities, as was asserted by Besag (1974). It is here that the functional form is looked for. The functional form is based on an expansion of functions having arguments comprising random variable values, assigned to the cells of v-clans, where $v = 1, 2, 3, \ldots, n$. To realise this idea, let a Markov random field, characterised by the sole existence of one-clans, be conceived. In the present enterprise, an ideal gas-like system with various particles (or cells) will be dealt with. These particles are, in the parlance of physics, considered not to interact mutually. The probability of the appearance of a particle in a certain part of a space, then, depends merely on external fields, for instance, gravitation.

The existence of exclusively one-clans in the system under consideration, i.e. in the Markov random field, considerably simplifies the conditional part of local conditional probabilities appearing in the Besag proposition. For one-clans in Markov random fields, the term $p(x_i|x_1, x_2, \ldots, x_{i-1}, x_{i+1}, \ldots, x_n)$ reduces to $p(x_i|\emptyset) = p(x_i)$, where $\emptyset$ denotes an empty set of variables. The Besag proposition for one-clan systems is hence simplified to

$$\frac{P(\vec{x})}{P(\vec{y})} = \prod_{1 \le i \le n} \frac{p(x_i)}{p(y_i)} \qquad [14.17]$$

with a trivial solution

$$P(\vec{x}) = \prod_{1 \le i \le n} p(x_i) \qquad [14.18]$$

This result is in accord with the familiar statement about the probability of an event composed of mutually exclusive sub-events. Stimulated by the above trivial solution, an attempt to solve the Besag proposition for a Markov random field comprising only of two-clans will be made.

The Besag proposition is a simple algebraic equation with complex arguments ascertained by combinations of configurations $(\vec{x}, \vec{y})$ from a joint configuration space, defined by $\vec{x}, \vec{y} \in \Omega$. Moreover, this proposition is valid for each labelling of cells. While exploring a general solution of the Besag proposition, attainment of a more physically realisable form of the arguments of the joint and the local conditional probabilities in Eq. [14.13] by a systematic approach, would be emphasised. Structurally, the Besag proposition is quite similar to that of the functional equations in which the arguments play a vital role also. Let a simple and well-known instance of an equation of the following functional form be considered:

$$f(x) = f(x + a),\ 0 < a = \text{const.} \qquad [14.19]$$

The above equation, for a particular function f, is satisfied only for certain discrete values of a in the argument, as the function f repeats its value with steps of a in the argument. Hence, the solution of Eq. [14.19] is a set of all the functions with a periodicity of a. One can anticipate a similar inference drawn from the prospective solution of the Besag proposition. In fact, as will be revealed, not only a sole concrete function but a family of functions accomplishing it will surface as a consequence. Similar qualitative information was incurred while solving the one-clan Markov field, Eq. [14.18]. At the onset of the forthcoming exercise to bring out a solution to the Besag proposition for a two-clan system with the backdrop of the Markov random field (used to describe a stochastic process involving spatial interactions), an intention towards designing graphical tools rather than the commonly encountered mathematical formalism, to simplify the procedural aspect of seeking the solution, is thought to be beneficial.

The relevant model here is supposed to be composed of six cells with six bonds or interactions between the couples of neighbouring cells, i.e. for the neighbourhood order, o of 1. Cells are, solely for convenience, arranged on a fraction of a square lattice as shown in Fig. 14.7. The figure demonstrates the system of neighbourhoods N of this Markov random field, and the set C of all the two-clans with the same elements. The variable X_i, here, is connected to the number of entities, such as carrots, in the cell s_i. Two different joint configurations of systems having configuration vectors $\vec{x}$ and $\vec{y}$ will be dealt with. The elements of these vectors are not considered to be under any compulsion to be uniquely assigned to individual cells. Two such configurations are portrayed in Fig. 14.7. It will be appropriate for further graphical interpretation of the Besag proposition to express the $\vec{x}$ configuration with black cells and that of the $\vec{y}$ with white ones. It is now time to draw

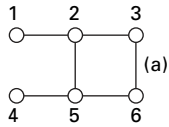

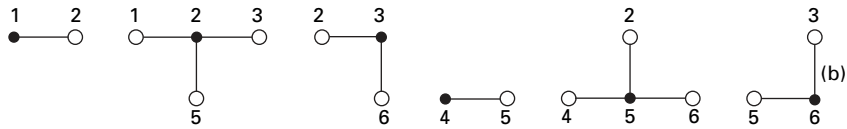

The set of all neighbourhoods *N*.

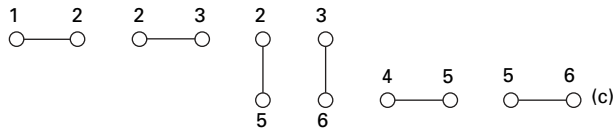

The set *C* of all two-clans.

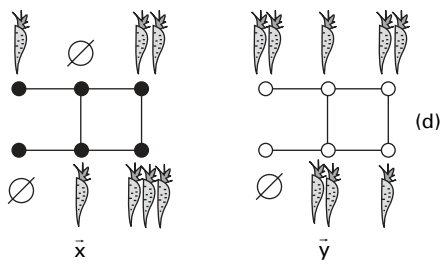

14.7 A fraction of a square lattice with six cells where bonds among cells represent mutual, i.e. symmetrical, cell interactions (a). The set *N* of all neighbourhoods in the Markov random field is depicted in (b). Neighbours of particular cells are depicted here as empty circles. The set *C* of all two-clans is sketched at in (c). The meaning of the random variable in a node s_i can be the number of carrot plants growing in a cell. Two various configurations $\vec{x}$ and $\vec{y}$ of a carrot bed that represents the Markov random field are shown in (d). The random field with the complete set of interactions/bonds is depicted in (e).

a graphical scheme for the representation and solution of the Besag proposition.

The pertinent Markov random field, comprising solely two-clans, has a significant reduction of the number of cells remaining in the conditional part of the local conditional probabilities. Instead of the notation $p(x_1|x_2, x_3, x_4, x_5, x_6)$, typical for random fields with all the possible intercellular bonds, as displayed in Fig. 14.7, the local conditional probabilities for particular configurations of the chosen Markov random field will be presented through notations that look like $p(x_1|x_2)$, $p(y_2|\ y_1, y_3, x_5)$ or $p(x_6|x_3, x_5)$. Thus, in this context, the part of the argument revealing the condition of a local conditional probability merely constitutes all the neighbours of the referred cell to which the local conditional probability applies. On the right-hand side of the Besag proposition [14.13] appear local conditional probabilities with 'mixed' conditions, contributed by local configurations from the configuration vector $\vec{y}$ to an index i–1, then followed by local states from the configuration vector $\vec{x}$ starting with an index $i + 1$. To exemplify, let $p(x_3|y_1, y_2, x_4, x_5, x_6)$ for a particular cell with an index, i of 3, belonging to the random field, as shown in Fig. 14.7, be considered. The analogous argument for the local conditional probability is reduced to $p(x_3 \mid y_2, x_6)$ in the case of a Markov random field with two-clans and a system of neighbourhoods with order o of 1. In this chapter, the argument of these local conditional probabilities pertaining to configuration vectors $\vec{x}$ and $\vec{y}$ is symbolised by black and white cells, respectively. An instance of a particular distribution of interactions is illustrated in Fig. 14.8. In the same figure are sketched schemes for some local conditional probabilities, such as $p(x_3|y_2, x_6)\ p(x_1|x_2)$ from the numerator, and $p(y_5|y_2, x_4, x_6)$ from the denominator of the Besag proposition. Subsequently, an effort is made to extend the aforementioned procedure of graphical interpretation of local conditional probabilities to depict the entire right-hand side of the Besag proposition. In Fig. 14.9, the multiplication operator is denoted by a little 'ex' and the dividing line is sketched as a long horizontal line separating elementary pictures derived from the numerator of the Besag proposition from those depicting representing terms from the denominator. The condition in the local conditional probability belonging to a cell s_i, defines all two-

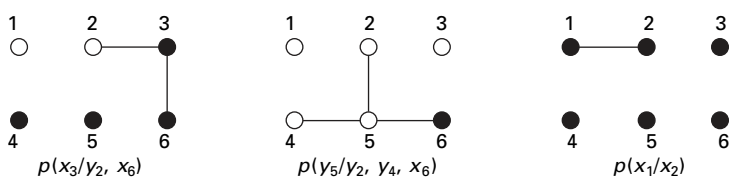

14.8 Schemes for local conditional probabilities: $p(x_3|y_2, x_6)$ and $p(x_1|x_2)$ are from the numerator of the Besag proposition, while $p(y_5|y_2, y_4, x_6)$ belongs to its denominator.

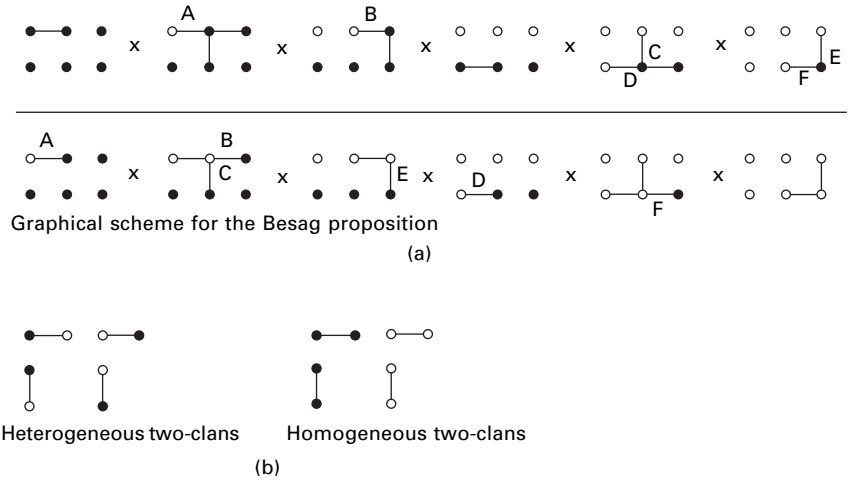

14.9 A graphical scheme of the Besag proposition depicted using the particular Markov random field and its two configurations black and white (a). Heterogeneous and homogeneous two-clans are sketched in (b).

clans containing the cell s_i. The clans in Figs. [14.7], [14.8] and [14.9] are couples of neighbouring cells interconnected to each other. Two-clans may be classified into two groups. The first will be called here 'homogeneous' two-clans consisting either completely of variable values from the configuration vector $\vec{x}$, i.e. the black cells or from that of the configuration vector $\vec{y}$, i.e. the white cells. The last class of the two-clans consists of the 'heterogeneous' one, which is characterised by a combination of a black and a white cell. These heterogeneous two-clans are of prime interest. They are distinguished in Fig. 14.9 with capital letters and, as is it evident from the figure that they appear with the same frequency in the numerator and in the denominator, the heterogeneous terms share a high risk of getting wiped out. Consequently, with the prospect of having only the homogeneous terms left behind, the analysis of two-clan Markov Random field may be deemed to have been simplified. In fact, then, the homogeneous clans consisting of black cells and white cells will correspond to the joint probabilities $P(\vec{x})$ and $P(\vec{y})$, respectively. Before moving on to the final stage of the present analysis, it is worth recalling, that Eq. [14.17] had expressions for joint probabilities of one-clan system as $P(\vec{x}) = \prod_{1 \le i \le n} p(x_i)$ and $P(\vec{y}) = \prod_{1 \le i \le n} p(y_i)$, located in the numerator and denominator, respectively.

To understand the two-clan affair, it should be said beforehand that homogeneous two-clan functions may be mathematically laid out as $g(x_i, x_j)$, $g(y_i, y_j)$. Incidentally, it is notable that such a convention, when applied to heterogeneous clans, reveals a symmetry between the functions $g(y_i, x_j)$ and

$g(x_j, y_i)$. Using these g-functions, each of the local conditional probabilities may be factorised, e.g. $p(y_5|y_2, y_4, y_6) = g(y_5, y_2)g(y_5, y_4)\, g(y_5, x_6)$ and $p(x_6|y_3, y_5) = g(x_6, y_3)g(x_6, y_5)$. It is unnecessary to substitute the entire graphical scheme of Fig. 14.9 by such factors; such step would cause nothing but confusion. It is sufficient to have in one's mind that each of the two-clans is a factor of the Besag proposition. Heterogeneous clans, being symmetric and appearing with the same frequency in the numerator and the denominator, cancel out altogether. After removal of all the heterogeneous clans, denoted by capital letters in Fig. 14.9, only homogeneous two-clan g-functions remain. Moreover, all those appearing in the numerator are black homogeneous clans and those appearing in the denominator are white ones. Accordingly, the ultimate form of the Besag proposition is delivered as:

$$\frac{P(\vec{x})}{P(\vec{y})} = \prod_{1\le i\le n} \frac{g(x_i, x_j)}{g(y_i, y_j)} \qquad [14.20]$$

where the product notation runs over all the pairs of cells interconnected with a bond, i.e. over all two-clans. Structurally, the terms in the numerator associated with the configuration vector $\vec{x}$ are identical to that of the denominator belonging to the configuration vector $\vec{y}$ in Equation [14.20]. Hence, it follows that the general solution of the Besag proposition for a two-clan Markov random field can be constructed as $P(\vec{x}) = \prod_{1\le i\le n} g(x_i, x_j)$. This result is, however, not a general one to represent instances where various v-clans $v \in \{1, 2, \ldots, z\}$ are juxtaposed. The freedom in the choice of the g-function allows one to write the solution, accompanied by an arbitrary multiplication factor F:

$$P(\vec{x}) = F \prod_{1\le i\le n} g(x_i, x_j) \qquad [14.21]$$

Apparently, the normalisation condition $\sum_{\vec{x}\in\Omega} P(\vec{x}) = 1$ implies that the g-functions in Eq. [14.21] have values different from those in Eq. [14.20], but they will not be denoted by any other notation. The physical illustration of a one-clan Markov random field is, for instance, given by the system of an ideal gas, as has already been mentioned. A pure two-clan system may be conceived as a system composed of elements, particles or groups of particles interacting in pairs, where the individual cells are not influenced by any external field. Let, now, the above-obtained solutions for a one-clan and a two-clan Markov random field on a regular lattice with a neighbourhood order, o, of 1 be merged.

Having a Markov random field with one and two-clans, it is quite meaningful to see if the solutions [14.20] and [14.21], corresponding to a one-clan and a two-clan system, contribute in constructing a solution for a mixed system containing both types of clans. The factor F from Eq. [14.21] will be instrumental for this purpose. It is meaningful, too, to assume the solutions

of the systems concerning each of the clan types, derived on independent platforms, will be useful to solve the Besag proposition for a mixed system, when $\prod_{|\leq i\leq n} p(x_i)$ from Eq. [14.18] is substituted for F in Eq. [14.21]. The coexistence of one- and two-clans in a mixed system does not interfere with arriving at the solution [14.21], i.e. one-clans do not affect factorisation of the local probabilities using two-clan g-functions. The only way to express the factor F is to use the one-clan probabilities $p(x_i)$ from Eq. [14.18] and to divide them by a constant value to fulfil the normalisation condition $\sum_{\vec{x}\in\Omega} P(\vec{x}) = 1$. These functions will, subsequently, be denoted as one-clan g functions. To differentiate between one- and two-clan g-functions, corresponding symbols will be indexed as g_1 and g_2. After substituting the factor F with multiple g_1 functions, the long-awaited solution for the Besag proposition, applicable for systems with one and two-clans, is realised.

$$p(\vec{x}) = F \prod_{1\leq i\leq n} g_2(x_i, x_j) = \prod_{1\leq i\leq n} g_1(x_i) \prod_{1\leq i\leq n} g_2(x_i, x_j) \qquad [14.22]$$

Returning to the primitive idea of drawing the simplest picture of a complex situation, an instance of a Markov random field solely occupied by three-clans with an order of neighbourhoods, o, of 2, is now considered in the present context. It would be apposite now to highlight the fact that a three-clan system, even with fewer cells, is far richer than a pure two-clan system. Presently, a Markov random field comprising only four cells with two mutually independent cells s_3 and s_4, as is shown in Fig. 14.10, will serve the purpose. In the said field, a local conditional probability, p, is presented in terms of three-clan g functions. This has been demonstrated in the same figure with the local conditional probability of the cell s_2 to establish $p(x_2|y_1, x_3, x_4) = g_3(y_1, x_2, x_3)\, g_3(y_1, x_2, x_4)$. Functions of g_3, such as $g_3(y_i, x_j, x_k)$ and $g_3(x_k, x_j, y_i)$, maintain a symmetry among themselves for all permutations of their arguments. Unlike Fig. 14.9, where two-clans are easily visible from one picture belonging to the local conditional probability, the g_3 functions in Fig. 14.10 are individualised to show their joint correspondence with the local conditional probabilities.

Concerning the heterogeneous clans, identical configurations with the same frequency appear in the numerator and the denominator, and are marked with the same upper-case letters in Fig. 14.10. Accordingly, the Besag proposition [14.13] for a purely three-clan system reduces to:

$$\frac{P(\vec{x})}{P(\vec{y})} = \prod_{1\leq i<j<k\leq n} \frac{g_3(x_i, x_j, x_k)}{g_3(y_i, y_j, y_k)} \qquad [14.23]$$

with the solution

$$P(\vec{x}) = \prod_{1\leq i<j<k\leq n} g_3(x_i, x_j, x_k) \qquad [14.24]$$

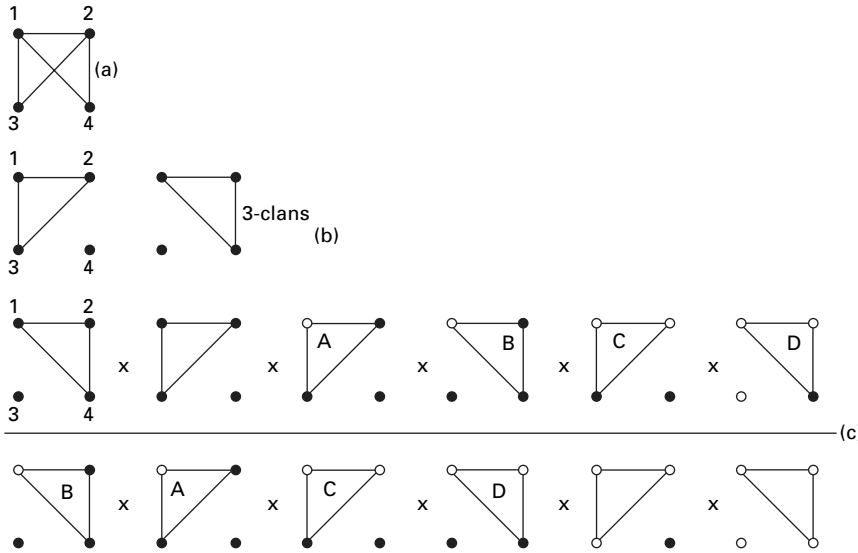

14.10 A graphical scheme of the Besag proposition for a purely three-clan system: The Markov random field (a). There exist only two three-clans in it (b). All local conditional probabilities of the type $p(x_i|y_j, x_k)$ are depicted in (c) The symbol $\times$ represents multiplication and the horizontal line the division of the right-hand side of the Besag proposition [14.23].

where, the nodes $\{s_i, s_j, s_k\}$ create clans. The solution of the Besag proposition for a system composed of a mixture of one, two, and three-clans will be brought about in a way dissimilar to the one previously used for the construction of Equation [14.22]. A Markov random field with a mixture of one-, two- and three-clans has local conditional probabilities typically represented as $p(x_2|x_1)$, $p(x_2|x_1, x_3)$, and $p(x_2|x_1, x_3, x_4)$, i.e. conversely, the associated local conditional probabilities can be factorised with the help of those clans, as is shown in Fig. 14.10. Such a factorisation, when carried out in the node s_2, attributed with a random variable x_2 and a local set of clans C_2, acquires a form of $p(x_2|y_1, x_3) = g_1(x_2)g_2(x_2, y_1)g_2(x_2, x_3)g_3(y_1, x_2, x_3)g_3(y_1, x_2, x_4)$. Complete nullification of all the heterogeneous two-and three-clans causes the Besag proposition to be expressed as:

$$P(\vec{x}) = \prod_{1\le i\le n} g_1(x_i) \prod_{1\le i<j\le n} g_2(x_i, x_{j_k}) \prod_{1\le i<j<k\le n} g_3(x_i, x_j, x_k) \qquad [14.25]$$

The above multiplicative expansion may be further extended to any arbitrary count ν of nodes of a clan in a Markov random field, as will be encountered in Eq. [14.26].

Now let the formulation of the Hammersley and Clifford theorem be initiated. This theorem is indispensable to the construction of valid spatial schemes through conditional probability. As the original methodology of its proof was rather circuitous and necessitated development of an operational calculus, the 'blackening algebra', the theorem was never published by its authors, Hammersley and Clifford (1971). An alternative approach was brought about by Besag (1974) and the formulation of Hammersley and Clifford theorem could be found in the work of Paget (1999). A great deal of work, preparatory to the present study, regarding the formulation of this theorem, was carried out to achieve the general solution of the Besag proposition. As a result, the first part of the Hammersley and Clifford theorem, as stated below, will be fully apprehensible.

(i) *Consider a random field or a Markov random field with a given neighbourhood of each cell that predetermines the set C of all its clans. Then there exists an observation that any joint probability* $P(\vec{x})$ *of the system can be written down as the multiplicative expansion [14.26], subject to the 'positivity condition'.*

$$P(\vec{x}) = \prod_{1\le i\le n} g_1(x_i) \prod_{1\le i<j\le n} g_2(x_i, x_j) \prod_{1\le i<j<k\le n} g_3(x_i, x_j, x_k) \times \ldots \prod_{1\le i<j<k<\ldots<l\le n} g_\nu(x_i, x_j, x_k, \ldots, x_l) \qquad [14.26]$$

The previous results of Eq. [14.18], [14.22], and [14.25] are particular examples of the above multiplicative expansion for $P(\vec{x})$.

The second part of the theorem considers the effect of sets of cells that do not create a clan. To get a clear picture of the situation, Fig. 14.10, where the members of the set of cells $\{s_1, s_3, s_4\}$ do not construct a three-clan, may be consulted. The next question, evidently, arises about the appropriate value of the relevant g_3-function $g_3\{x_1, x_3, x_4\}$, when a multiplicative expansion as in Eq. [14.26] is applied. The only way to assign such a value without affecting $P(\vec{x})$ is to assume $g_3(x_1, x_3, x_4) = 1$. The second part of the Hammersley and Clifford theorem declares:

(ii) *For indexes* $1 \le i < j < \nu \le n$, *the function* $g_\nu(x_i, x_j, \ldots, x_\nu)$ *in [14.26] may be different from one if, and only if, the sites i, j, k,..., n form a clan. Subjected to this restriction, the g-functions may be chosen arbitrarily.*

Finally, it is highlighted that the Hammersley and Clifford expansion is commonly written as a sum and not as a multiplicative expansion. One obtains the summation expansion directly from Eq. [14.26] by employing a logarithmic function.

$$Q(\vec{x}) = \sum_{1\le i\le n} q_1(x_i) + \sum_{1\le i<j\le n} q_2(x_i, x_j) + \sum_{1\le i<j<k\le n} q_3(x_i, x_j, x_k) + \ldots + \sum_{1\le i<j<k<\ldots<l\le n} q_\nu(x_i, x_j, x_k, \ldots, x_l) \qquad [14.27]$$

where

$$Q(\vec{x}) = \ln(P(\vec{x})) \qquad [14.28]$$

The q functions are logarithms of g functions, e.g. $q_3(x_i, x_j, x_k) = \log q_3(x_i, x_j, x_k)$. As the sets of cells not creating clans have values of each of their g-functions as unity, the related values of their q-functions are zero. Function Q is called the 'energy function'.

The following endeavour will be characterised by an intention to relate the above-obtained results, framed basically on a mathematical approach, with statistical physics that identifies a system of interacting particles by its total energy/Hamiltonian $U(\vec{x})$, mainly composed of energies from intermolecular interactions and interactions with external fields. When such a concept is introduced in Markov random fields, the energies associated with the clans may be referred to as 'clan energies' and may be represented as $V_C(\vec{x})$, where the index c denotes a clan.

$$U(\vec{x}) = \sum_{c \subset c} V_C(\vec{x}) \qquad [14.29]$$

The summation in the relation [14.29] comprehends all the clans made out of elements of set C, i.e. it includes all individual clans of the system of all clans C. Here, clan energies are real energies of short as well as long chemical and physical interactions, and energies due to interactions of individual particles with external fields. They represent, for instance, interactions in physical terms, such as, $J\sigma_i\sigma_j$ and $H\sigma_i$ of the Ising model (Binder and Heermenn, 1997). Relations [14.35] and [14.36] in Section 14.2.4 may be referred to. Statistical physics mentions a joint probability, known as the 'Gibbs distribution', $P(\vec{x})$, related by the Boltzmann law as:

$$P(\vec{x}) = \frac{1}{Z} e^{-\frac{U(\vec{x})}{\tau}} \qquad [14.30]$$

where Z is a normalising factor, commonly referred to as the 'partition function', and τ stands for the statistical temperature (Kittel, 1980). As Equations [14.28] and [14.30] are comparable in terms of $P(\vec{x})$, it becomes discernible that the function $Q(\vec{x})$ of the Hammersley and Clifford theorem contains energy $U(\vec{x})$, the statistical temperature τ, and the partition function Z. It depends on a system of interacting particles in a framework of Markov random field and its structure is based on the contributions of all the individual clan energies. Briefly speaking, between the aforesaid relations [14.28] and [14.30], the partition function Z and the temperature τ are the factors that bring some disparity. This hindrance may be overcome in a way that is now described.

Energies in Eq. [14.29] have the flexibility of having an arbitrary additive factor. The arbitrary value of this additive factor gives the same distribution $P(\vec{x})$ with an appropriately chosen partition function Z. One such choice of

additive energy value causes Z to have a value of 1 due to Equations [14.28] and [14.30]. From these two equations the following relation crops up:

$$e^{Q(\vec{x})} = \frac{1}{Z} e^{-\frac{U(\vec{x})}{\tau}} \qquad [14.31]$$

Using a logarithmic function in Eq. [14.31] and rearranging the terms, the energy function $Q(\vec{x})$ and the Hamiltonian $U(\vec{x})$ are equated as:

$$Q(\vec{x}) = -\left(\frac{U(\vec{x})}{\tau} + \ln Z\right) = -\left(\frac{U(\vec{x}) + \tau \ln Z}{\tau}\right) \qquad [14.32]$$

As can be observed from the last equation, the term $\tau \ln Z$ symbolises an additive energy value that appropriately interprets the Hamiltonian in terms of the energy function. On the other hand, it is well known that the physical behaviour and properties of a system are not dependent on the choice of basic energy level. That is the reason behind the fact that physical models are uniquely governed by their Hamiltonians $U(\vec{x})$ at any chosen temperature τ. Accordingly, physical models will be described, henceforth, using Hamiltonians instead of energy functions $Q(\vec{x})$, keeping the relationship [14.32] in mind.

Before a family of energy functions is selected for computer simulation, as put forward in Section 14.3, some comments on the significance of the Hammersley and Clifford theorem are needed. To begin with, it is worth mentioning that the theorem shows how the general shape of an energy function looks in the realm of Markov random fields. This bears an enormous importance from the viewpoint that Markov random fields, as has already been indicated, are 'equivalent' to a distribution of configuration probabilities of various assemblies in statistical physics. More accounts of Markov random field – Gibbs distribution equivalence can be found in recent literature (Paget, 1999; Moussouris, 1973; Dubes and Jain, 1989; Prum and Fort, 1991).

The last remark underlines the significance of the Hammersley and Clifford theorem, serving as evidence for an additive nature of energy for all physical systems modelled with Markov random fields. This has a strong relevance to the superposition principle in electrostatics and that of the intermolecular forces in the molecular theories of cohesion and capillarity (Rowlinson, 2002). The next subsection is devoted to the classification of auto-models.

14.2.4 Particular auto-models

Auto-models, listed below, are used for the modelling of real physical systems, as well as for image analysis. They are introduced together to underline their common theoretical background.

Ideal gas model. To deal with the physical model, a prior step to distinguish energy functions $Q(\vec{x})$ and Hamiltonians $U(\vec{x})$ becomes essential. The

simplest physical model, equivalent to a Markov random field, is that of an ideal gas lattice with only one-clans. The interaction of identical molecules in a uniform mass m put into an external field of gravity with an acceleration g leads to the Hamiltonian

$$U(\vec{x}) = \sum_{1 \le i \le n} mgx_i h_i \qquad [14.33]$$

where h_i is the height of a layer of gas above a chosen basic position, and random variable x denotes the number of molecules in the layer, i.e. in the cell, s_i, as shown in Fig. 14.11.

The function mgx_ih_i is, indeed, a one–clan q_1-function appearing in the Hammersley and Clifford Equation [14.27], i.e. $q_1(x_i) \approx mgx_ih_i$.

Following the one-clan system, exemplified by the ideal gases, comes the two-clan system, represented by what are commonly known as 'auto-models' in the Hammersley and Clifford series. The second system permits one- and two-clans but prohibits the existence of any higher-order v-clans with $v \ge 3$. Their general energy function is given as:

$$U(\vec{x}) = \sum_{1 \le i \le n} q_1(x_i) + \sum_{1 \le i < j \le n} q_2(x_i, x_j) \qquad [14.34]$$

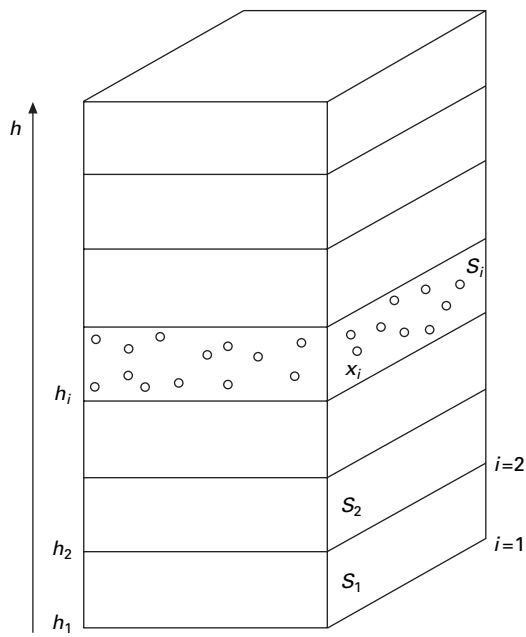

14.11 A column of an ideal gas is divided into layers representing non-interacting cells of a Markov random field. The random variable value X_i is equal to x_i, the number of particles in the cell s_i.

There exist different kinds of auto-models. The most common ones are listed below.

The Ising model. The most famous auto-model in physics is probably the Ising model with its total energy or Hamiltonian expressed as:

$$U(\vec{x}) = -J \sum_{1 \le i < j \le n} \sigma_i \sigma_j \qquad [14.35]$$

The Hamiltonian $U(\vec{x})$ of the above relation pertains to a system of interacting elementary magnets without any external magnetic field. The constant J is called the exchange energy and σ's are spins that are assigned values of +1 for an upwards orientation, or –1 for a downwards orientation. In fact, spin σ_i is a random variable value, analogous to previously mentioned x_i. The function q_2, i.e. the two-clan energy function of the Hammersley and Clifford expansion, is stated as $q_2(\sigma_i, \sigma_j) \approx -J\sigma_i\sigma_j$. If a uniform external magnetic field of an intensity H is introduced, the Hamiltonian takes the form:

$$U(\vec{x}) = -H \sum_{1 \le i \le n} \sigma_i - J \sum_{1 \le i < j \le n} \sigma_i \sigma_j \qquad [14.36]$$

In the above relation [14.36], interpretation of the g_2 functions remains the same as that of Eq. [14.35], while the q_1 functions are connected to the first Hamiltonian term $q_1(\sigma_i) \approx -H\sigma_i$. More information about the Ising and other related models may be seen in some previous works of Preston (1976) and Ruelle (1969). One can read the history of the problem, written by Brush (1967). The work of Dobrushin *et al.* (1978) provides applications of the Ising model in biology.

The auto-binary model. The auto-binary model was the first model, introduced by Cox (1970), with variables X_i having binary values (zero/one). The one- and two-clan q functions of the Hammersley and Clifford theorem are replaced by arbitrary parameters α's and β's multiplied by random variable values. The energy function of this model is given by

$$Q(\vec{x}) = \sum_{1 \le i \le n} \alpha_i x_i + \sum_{1 \le i < j \le n} \beta_{i,j} x_i x_j \qquad [14.37]$$

As opposed to the Ising model, where the only parameters are H and J, there exist $n + \dfrac{n!}{2(n-2)!}$ parameters in the auto-binary model. Contrary to the Hamiltonians introduced subsequently to simulate wetting phenomena, all the parameters of the present model are functions of cell indices and do not depend on x_i's in corresponding cells. Auto-binary models have been utilised for parametric estimation and model selection in image analysis, using Markov random fields (Paget, 1999; Seymour, 1993).

The auto-binomial model. Cross and Jain (1983) introduced a model, designed for pattern analysis, having the two-clan term of its energy function identical to that of the auto-binary model, i.e. the $q_2(x_i, x_j)$ functions of the Hammersley and Clifford expansion had the form of $\beta_{i,j}x_ix_j$. The one-clan energy function, $q_1(x_i)$, of the expansion contained a binomial term; $q_1(x_i) = \log\left(\frac{L!}{x_s!(L-x_s)!}\right) + \alpha_s x_s$. The common local configuration space Λ_i for a cell s_i of this model consisted of $L + 1$ states, where $\Lambda = \{0, 1, 2,\ldots, L\}$. Thus, the energy function of the auto-binomial model could be given as

$$Q(\vec{x}) = \sum_{1\le i\le n}\left[\log\left(\frac{L!}{x_s!(L-x_s)!}\right) + \alpha_i x_i\right] + \sum_{1\le i<j\le n}\beta_{i,j}x_ix_j \qquad [14.38]$$

The Derin–Elliott model. For modelling and segmentation of images and their parts, known as textures (Paget, 1999), a model configured by Derin and Elliott (1987) has an energy function of the following shape:

$$Q(\vec{x}) = \sum_{1\le i\le n}\alpha x_i + \sum_{1\le i<j\le n}\beta_{i,j}I(x_i, x_j) \qquad [14.39]$$

The one-clan term of this model is similar to the first term of the Hamiltonian Eq. [14.36] of the Ising model. The other term concerning two-clans consists of a function of two variables, $I(x_i, x_j)$. This function attains a value of 1 when x_i equals x_j, and otherwise a value of –1.

The auto-model for wetting phenomena. An auto-model for the computer simulation of wetting of a fibrous mass, introduced by Lukas *et al.* (2004), will be described in detail later, in Section 14.3. To physically interpret the auto-model, it is necessary to distinguish between the energy function and the Hamiltonian with an approach similar to the description of the Ising model. For a three-dimensional system wherein a simulation box is composed of cubic cells occupied by one of the three kinds of materials (values of x_i being 0, 1 and 2 to represent a gas, a liquid and a solid fibre, respectively), the Hamiltonian becomes

$$U(\vec{x}) = \sum_{1\le i\le n}C_g h(x_i) + \sum_{1\le i<j\le n}C(x_i, x_j) \qquad [14.40]$$

where C_g denotes a constant having the sense of the product of the gravity gradient and the mass of a liquid cell, and $h(x_i)$ is the height of a cell s_i above a chosen level. The function $h(x_i)$ has a non-zero value for liquid cells only, i.e. for value of x_i being 1. Sometimes the Hamiltonian of this auto-model is used without the first gravity term. The local configuration space Λ_i of a cell s_i is either a one-element set $\Lambda_i = \{2\}$, having a cell occupied by a fixed fibre element and assigned with a value x_i of 2, or a set of two elements $\Lambda_i = \{0, 1\}$

standing for a binary liquid–gas mixture corresponding to x_i values of 0 and 1, respectively. The two-clan term of this auto-model represents a cohesive interaction between neighbouring cells s_i and s_j, whenever x_i and x_j have the same values, and an adhesive one in other instances. The functions C's are interaction energies symmetric between the neighbouring cells, i.e. $C(x_i, x_j) = C(x_j, x_i)$. This Hamiltonian will be dealt in detail later on, in Section 14.3.

The other auto-models are auto-logistic, auto-normal, auto-Poisson, and auto-potential. The first two are mentioned by Paget (1999) and the other two by Besag (1974). Auto-models have been used by Liggett (1985) in sociology to study changes in a body of ideas. Prum and Fort (1991) described an auto-model for epidemics. Fricot (1985) introduced a model for a renewal process.

14.2.5 Markov chains

Markov chains may be regarded as tools used to impart liveliness to Markov random fields in simulation, in a way that is simple but retains most of the features relevant to real systems. A Markov chain acts as a pathfinder while 'travelling' in a joint configuration space Ω from one configuration $\vec{x}_m$ to the next $\vec{x}_{m+1}$, searching for an equilibrium distribution of the joint probabilities. The index m counts the jumps from a referred configuration (it is not the cell index as before), for which m is assigned a value of 0, and the terms $\vec{x}_m, \vec{x}_{m+1}$ are, as a convention, various succeeding configurations. Since a trajectory in a joint configuration space composed of chain elements is a function of time t, it is justifiable to connect a set of successive time moments to the set of successive jump indices, m, where $m \rightarrow t(m)$. In a Markov chain of configurations $(\vec{x}_{t(0)}, \vec{x}_{t(1)}, \vec{x}_{t(2)}, \ldots, \vec{x}_{t(m)})$, any successive configuration $\vec{x}_{t(m+1)}$ is constructed from the previous one, i.e. $\vec{x}_{t(m)}$, through a suitable transitional probability defined by $W(\vec{x}_{t(m)} \rightarrow \vec{x}_{t(m+1)})$. One should emphasise here that the transitional probability governing the jump $\vec{x}_{t(m)} \rightarrow \vec{x}_{t(m+1)}$ is uniquely determined by the two configurations encountered at proximate past and future instants of time. Hence, any event occurring at a time beyond the proximate limits does not influence the transitional probability. This time independence is similar to the space independence of local conditional probabilities in Markov random fields mentioned in Section 14.1.2.

Transitional probabilities are usually chosen in limit $M \rightarrow \infty$, where M is the total number of jumps. The trajectory of the Markov chain in Ω touches various configurations with the probabilities $P(\vec{x})$ close to the equilibrium probability $P_{eq}(\vec{x})$ of an investigated system. The distribution of the equilibrium probabilities, or briefly, the equilibrium distribution, is given by the Gauss distribution

$$P_{eq}(\vec{x}) = \frac{1}{Z} e^{\frac{-U(\vec{x})}{\tau}} \qquad [14.41]$$

where the total energy $U(\vec{x})$ has a serial additive structure comparable to that of the Hammersley and Clifford expansion in Eq. [14.27]. At equilibrium, the system under consideration is stationary and so its properties do not depend on time. Originally, the idea of applying Markov chains to estimate the equilibrium properties of Markov random fields was brought in and advanced by Metropolis *et al*. (1953). The example of a Markov chain of configurations, connected by trajectories in the global configuration space Ω, is shown in Fig. 14.12.

Transitional probabilities, *W*'s, may be chosen in various fashions, as was described by Binder and Heermenn (1997) and Binder (1986). They will be designed here on the foundation of the principle of detailed balance. The trajectory of a Markov chain in a joined configuration space Ω is complex, but the equilibrium distribution $P_{eq}(\vec{x})$ may be arrived at by justifying equal frequencies of to and fro jumps between each couple of configurations. Let two successive configurations $\vec{x}$ and $\vec{y}$ be chosen at random from a joined configuration space Ω. Jumps from $\vec{x}$ to $\vec{y}$ are characterised with a probability $P(\vec{x} \to \vec{y}) = P(\vec{x})W(\vec{x} \to \vec{y})$ and those in the reverse direction have a probability $P(\vec{y} \to \vec{x}) = P(\vec{y})W(\vec{y} \to \vec{x})$. The principle of detailed balance, then, claims that, in equilibrium, these transition probabilities are equal:

$$P_{eq}(\vec{x})W(\vec{x} \to \vec{y}) = P_{eq}(\vec{y})W(\vec{y} \to \vec{x}) \qquad [14.42]$$

Transitional probabilities $W(\vec{x} \to \vec{y})$, obeying the principle of the detailed balance, guarantee that every possible deviation from the equilibrium values, such as $P_{eq}(\vec{x})$ and $P_{eq}(\vec{y})$, will be quenched. Therefore, a Markov chain

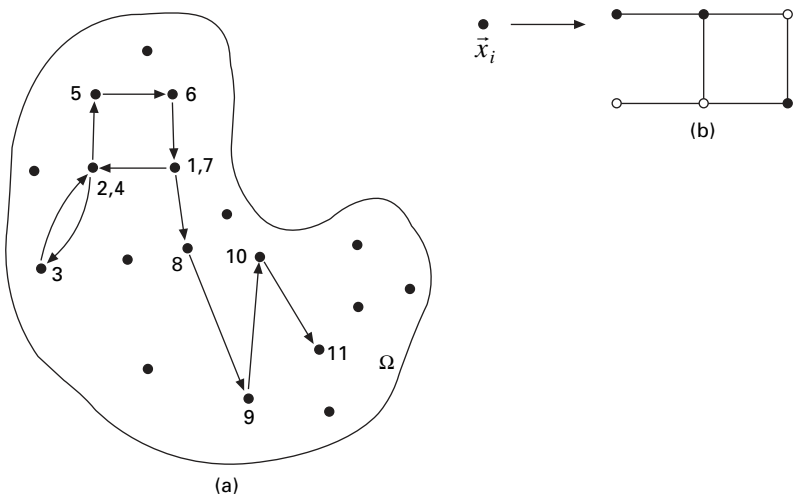

14.12 A configuration space Ω with its elements (a). These elements are particular configurations $\vec{x}$ of a system (b). Jumps between these configurations create the Markov chain.

satisfying the detailed balance will restore the equilibrium probability distribution $P_{eq}(\vec{x})$ after each distortion. To verify it, two non-equilibrium joint probabilities $P(\vec{x}), P(\vec{y})$, fulfilling the condition $P(\vec{x})/P(\vec{y}) > P_{eq}(\vec{x})/P_{eq}(\vec{y})$, may be conjectured. To re-establish the equilibrium, the value $P(\vec{x} \to \vec{y}) - P(\vec{y} \to \vec{x})$ of forward and backward jumps concerning $\vec{x}, \vec{y}$ has to be positive to nullify the redundant probabilistic value $P(\vec{x})$ and/or to compensate for the deficit of the probabilistic value $P(\vec{y})$. The above subtraction is invariably negative when the transitional probabilities, *W*, fulfil the said principle. The following series of relations draws a clearer picture:

$$\begin{aligned} 0 &< P(\vec{x} \to \vec{y}) - P(\vec{y} \to \vec{x}) \\ &= P(\vec{x})W(\vec{x} \to \vec{y}) - P(\vec{y})W(\vec{y} \to \vec{x}) \\ &= P(\vec{x})W(\vec{y} \to \vec{x})\left(\frac{W(\vec{x} \to \vec{y})}{W(\vec{y} \to \vec{x})} - \frac{P(\vec{y})}{P(\vec{x})}\right) \\ &= P(\vec{x})W(\vec{y} \to \vec{x})\left(\frac{P_{eq}(\vec{y})}{P_{eq}(\vec{x})} - \frac{P(\vec{y})}{P(\vec{x})}\right) \end{aligned} \quad [14.43]$$

The extreme right-hand term of Equation [14.43] is positive, as the product of the probabilities $P(\vec{x})$ and $W(\vec{y} \to \vec{x})$ is positive and the presumption $P(\vec{x})/P(\vec{y}) > P_{\text{eq}}(\vec{x})/P_{\text{eq}}(\vec{y})$ explains the rest.

Similarly, the situation $P(\vec{x})/P(\vec{y}) < P_{\text{eq}}(\vec{x})/P_{\text{eq}}(\vec{y})$ drives the joined probability $P(\vec{x})$ to demand a contribution from the joined probability $P(\vec{y})$ along a path of a Markov chain as the value $P(\vec{x} \to \vec{y}) - P(\vec{y} \to \vec{x})$ is negative whenever transitional probabilities are governed by detailed balance condition. Steps similar to those of Eq. [14.43] lead to the inequality

$$0 > P(\vec{x} \to \vec{y}) - P(\vec{y} \to \vec{x}) = P(\vec{x})W(\vec{y} \to \vec{x})\left(\frac{P_{\text{eq}}(\vec{y})}{P_{\text{eq}}(\vec{x})} - \frac{P(\vec{y})}{P(\vec{x})}\right) \quad [14.44]$$

Thus, transitional probabilities, *W*, that fulfil the detailed balance condition lead to the equilibrium distribution $P_{\text{eq}}(\vec{x})$ for both kinds of disturbance after a sufficiently long Markov chain is gone through.

Concrete functions for transition probabilities will be introduced later when dealing with Glauber and Kawasaki dynamics. Currently, an effort may be directed towards tracing out the set of configurations in configuration space Ω by altering single, couples or groups of random variable values, x_i, to realise a Markov chain. In practice, any one of the following procedures corresponding to various assemblies in statistical mechanics is used. The rate at which equilibrium configurations are arrived at depends on the choice

of a simulation procedure. This aspect demarcates the application of Markov chains to associate them with the kinetics or dynamics of a model.

The ability of Markov random fields and auto-models to interpret dynamics is also imparted by Markov chains. This aspect is described in detail in Section 14.3.3.

Besag coding. Besag proposed methods of coding intended for regular lattices with symmetric neighbourhoods, which began with the process of labelling the cells alternately as black and white (Besag, 1974). The white colour was meant for cells where configuration could be changed in a single step and the black colour belonged to their neighbourhoods. The black neighbourhood served as a separator in a homogenous and symmetric neighbourhood system (Moussouris, 1973). The notion of a separator is explained in general by Fig. 14.13(a), where two white nodes are quite independent. The scheme of a regular check-board-like pattern of white cells and their black separators owes much to the transitional symmetry of a lattice as well as to the symmetry and homogeneity of a neighbourhood system. The method is visualised in Fig. 14.13(b). A change of variables in the white cells depends only on the configurations of the cells in the separator. The white cells could adjust their value concurrently. Neighbouring configurations in the Markov chains differ by changes carried out on groups of cells having the same colour. Thereafter, the mask of white cells can be

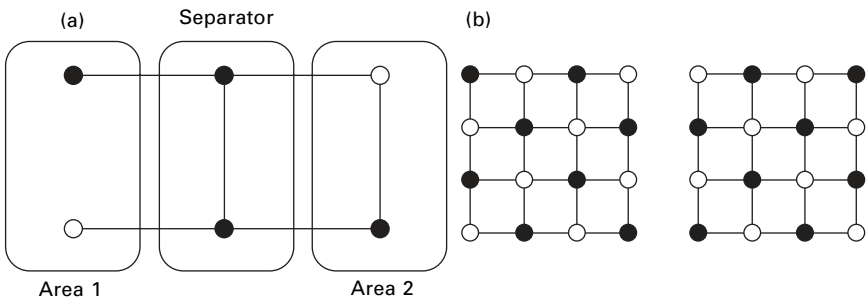

14.13 A Markov random field (a) where two areas of nodes are independent. They are isolated by a set of cells that is called a separator. Local conditional probabilities of the cells in one of these areas separated by the separator do not depend on the random variable values from the other area. The scheme of a regular check-board-like pattern of white cells and their black separators is depicted in (b). Changes of variables in the white cells depend only on the configurations of the cells in the black separator. So the white cells could adjust their values concurrently. The right-hand side of (b) depicts the shift of the mask of white cells with respect to the original white mask on the left.

shifted to a lattice either regularly or randomly, and changes for another group of coloured cells can be initiated.

Besag coding is more appropriate for Glauber dynamics than for Kawasaki dynamics because the latter can involve changes in the values of variables of both the black and white zones. Both of these dynamics will be detailed later.

Gibbs–Geman sampling. Prum and Fort (1991) gave Gibbs–Geman sampling as a method where a cell s_i, belonging to the set S of all cells, was chosen independently at each step in a uniform random manner. This procedure was directly suitable for Glauber dynamics. When dealing with Kawasaki dynamics, one has to find the next cell s_j with which the random variable value x_i may be exchanged.

Glauber dynamics. Glauber dynamics (Glauber, 1963) created a purely relaxation model without any conservation laws. Both energy as well as particles could be exchanged with a thermodynamic reservoir. In Glauber dynamics, a cell s_i was encountered at random. The local configuration x_i of the relevant cell was then passed to a new configuration y_i, keeping configuration of all the other cells intact. As a result, this dynamics could be represented by a single variable change, as shown in Fig. 14.14(a). The probability of the changeover to a new local configuration, i.e. the transitional probability, is given by:

$$W(\vec{x} \rightarrow \vec{y}) = \exp\left(-\frac{U(\vec{y}) - U(\vec{x})}{\tau}\right)$$

where
$$\begin{aligned} U(\vec{x}) &= U(x_1,\ldots, x_i,\ldots, x_j,\ldots, x_n) \leq U(\vec{y}) \\ &= U(x_1,\ldots, y_i,\ldots, x_j,\ldots, x_n); \end{aligned}$$

$$W(\vec{x} \rightarrow \vec{y}) = 1$$

when
$$\begin{aligned} U(\vec{x}) &= U(x_1,\ldots, x_i,\ldots, x_j,\ldots, x_n) > U(\vec{y}) \\ &= U(x_1,\ldots, y_i,\ldots, x_j,\ldots, x_n) \end{aligned} \qquad [14.45]$$

The terms $U(\vec{x}), U(\vec{y})$ are Hamiltonians of the configurations $\vec{x}$ and $\vec{y}$. Glauber dynamics were originally designed for a two-state Ising model.

Kawasaki dynamics. Kawasaki dynamics was initially proposed for a nearest-neighbour exchange procedure (Kawasaki, 1972), as shown in Fig. 14.14(b). Two neighbouring cells, s_i and s_j, which are allowed to commute their variable values, are chosen at random. With an original local configurations having variable values x_i and y_j and a subsequent trial carried out for destined values of y_i and x_j, the transition probability is typified as $W(x_i \leftrightarrow y_i)$, where

$$W(x_i \leftrightarrow y_j) = \exp\left(-\frac{U(\vec{y}) - U(\vec{x})}{\tau}\right)$$

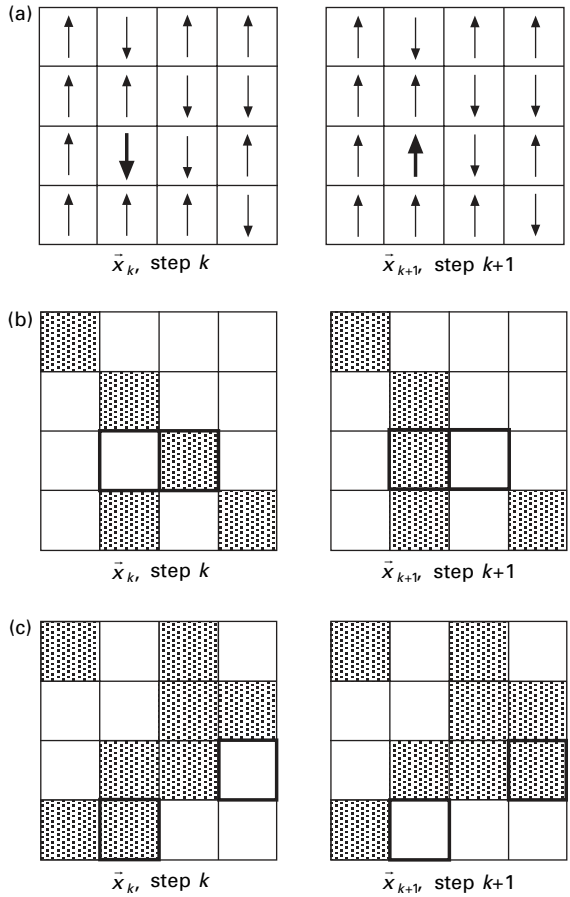

14.14 Glauber's dynamics (a) and Kawasaki's dynamics for short (b) and long (c) distance. All neighbourhoods are considered here of the order $o = 1$.

$$\text{where} \quad U(\vec{x}) = U(x_1,\ldots, x_i,\ldots, y_j,\ldots, x_n) \leq U(\vec{y})$$
$$= U(x_1,\ldots, y_i,\ldots, x_j,\ldots, x_n)$$
$$W(x_i \leftrightarrow y_j) = 1$$
$$\text{where} \quad U(\vec{x}) = U(x_1,\ldots, x_i,\ldots, y_j,\ldots, x_n) > U(\vec{y})$$
$$= U(x_1,\ldots, y_i,\ldots, x_j,\ldots, x_n) \qquad [14.46]$$

The terms $U(\vec{x})$, $U(\vec{y})$ are, respectively, the original and the final total energies/Hamiltonians for the global configurations $\vec{x}$ and $\vec{y}$.

Kawasaki dynamics have a version for long-distance exchange between a chosen pairs of cells. In that case s_i and s_j are not necessarily mutual neighbours as shown in Fig. 14.14.

14.2.6 Markov random fields with constraints

Positivity conditions postulated for deriving the Besag proposition and, consequently, for the Hammersley and Clifford theorem, seem awkward for some assemblies of statistical physics normally obeying conservation laws, such as canonical or micro-canonical assemblies, when some of the configurations, $\vec{x}$, of a system violate conservation laws to produce relevant joint probabilities, $P(\vec{x})$, and local conditional probabilities, $p(x_i|\ x_1,\ldots, x_{i-1}, x_{i+1},\ldots, x_n)$, with values equalling zero. It is also well established both from theory and experiments that the choice of a statistical assembly does not affect the additive structure of the corresponding Hamiltonians resembling the Hammersley and Clifford expansion [14.27]. Hence, there exists a possibility to preserve the newly introduced theory for physical systems, where violation of conservation laws works against the positivity condition.

As far as it can be traced back, pioneering work dealing with Markov random fields having non-zero joint probabilities assigned only to some subset Ω^+ of a configuration space Ω, were carried out by Moussouris (1973). Configurations in a configuration space Ω outside the region Ω^+, i.e. in the region $\Omega - \Omega^+$, were forbidden and so they were assigned zero probabilities. In those systems, Markov conditions, i.e. the independence of local probabilities in some areas of cells, still made sense but the positivity condition $P(\vec{x}) \neq 0$ for each configuration $\vec{x} \in \Omega$ was no longer conformed to. Moussouris suggested the treatment of systems with such constraints using a finite value of a continuous limit of an energy function for forbidden configurations

$$U(\vec{x}) \to \infty \quad \text{for} \quad \vec{x} \in \Omega - \Omega^+ \qquad [14.47]$$

Clan configurations that were energetically forbidden were called 'barriers' and all the configurations with zero probabilities created a 'barrier system'. More information about these considerations can be obtained from Moussouris's paper (1973).

The approach followed here will be based on the structures of the Besag proposition and the Hammersley and Clifford theorem. Initially it is worth pointing out that the Hammersley and Clifford expansion belonging to a joint probability $P(\vec{x})$ may also be expressed as an expansion of a certain chosen set of non-zero individual homogeneous clan functions, g. For this reason, the Hammersley and Clifford theorem is a statement about particular configurations and so works, even when configurations are chosen from Ω^+ without accounting for the whole configuration space Ω. These findings elevate the suitability of the described theory in analysing the Markov random fields also with constraints.

Nevertheless, the Hammersley and Clifford theorem was deduced from the Besag proposition, based on a metamorphosis of configurations, from $\vec{x}$ to $\vec{y}$, effected by change of some variable values at individual cells in

accordance with a chosen process to label the cells. It may be noted that the Besag proposition [14.3] was derived in a similar fashion from the Bayes' rule [14.7]. Some of the local conditional probabilities $p(y_i|y_1,\ldots, y_{i-1}, x_{i+1},\ldots, x_n)$, appearing in the Besag proposition may belong to forbidden configurations $\vec{x}$ and, therefore, violate conservation laws. It may be overambitious to safeguard the Besag proposition for each of the random fields, but may not be so for Markov random fields with a large number of total cells much greater than the count of the cells in its particular neighbourhoods. The energy content along with the spectrum of clans regarding random variable values outside the chosen neighbourhood and within Ω^+ will be supposed to be large as well as rich enough to buffer during manipulations of the local configurations, i.e. the local conditional probabilities $p(x_i|y_1,\ldots, y_{i-1}, x_{i+1},\ldots, x_n)$ in the Besag proposition, wherein $\{s_1,\ldots, s_{i-1}, s_{i+1},\ldots, s_n\} \in N_i$. Briefly speaking, a conservation of the total energy or the total particle number in a system of canonic or micro-canonic assemblies is not susceptible to manipulations with random variable values in a cell and its neighbourhood because beyond the separator the system configuration is rich enough to maintain the conservation laws. To be more specific, for each such local change, depending only on the configuration of the neighbourhood N_i of a cell s_i, there exists a configuration of cells outside N_i fulfilling the conservation laws of the whole system. The situation is sketched in Fig. 14.15. In other words, outside the neighbourhood N_i and among configurations of Ω^+, the joint configuration can be tuned up to meet the conservation laws.

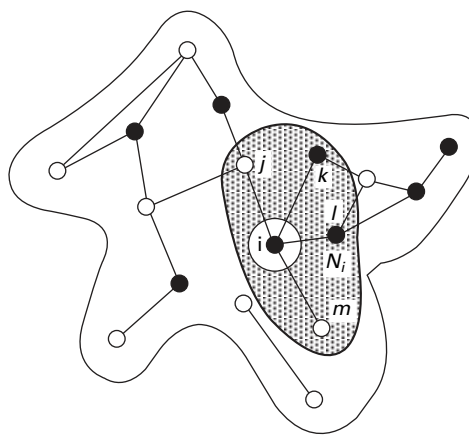

14.15 A local conditional probability $p(x_i|y_j, x_k, x_l, y_m)$ of a random node x_i with the neighbourhood $N_i = \{s_j, s_k, s_l, s_m\}$ does not depend on random variable values behind the separator. The separator is represented by the neighborhood N_i. Changes of random variable values in the cell s_i and its neighbourhood can be carried out if they belong to Ω^+.

For canonical assemblies having the total number of particles conserved, e.g. the total number of cells with a particular value of a random variable conserved, a more rigorous process may be undertaken. The dynamics of these systems are generally governed by Kawasaki dynamics. The modified Bayes' rule written for random variable values exchanged between two chosen cells s_i and s_j, takes the form:

$$\begin{aligned} &P(x_1,\ldots, x_i,\ldots, x_j,\ldots, x_n) \\ &= p(x_i, x_j|x_1,\ldots, x_{i-1}, x_{i+1},\ldots, x_{j-1}, x_{j+1},\ldots, x_1) \\ &\quad \times \Pi(x_1,\ldots, x_{i-1}, x_{i+1},\ldots, x_{j-1}, x_{j+1},\ldots, x_1) \end{aligned} \quad [14.48]$$

This is a modified form of the relation [14.7]. The local conditional probability of the appearance of random variable values x_i and x_j in corresponding cells s_i and s_j is denoted above as $p(x_i, x_j|x_1,\ldots, x_{i-1}, x_{i+1},\ldots, x_{j-1}, x_{j+1},\ldots, x_1)$. Permitted by the local configuration spaces Λ_i and Λ_j, an exchange of variable values $x_i \leftrightarrow x_j$ takes place to arrive at a final configuration $(x_1,\ldots, x_{i-1}, y_i, x_{i+1},\ldots, x_{j-1}, y_j\ x_{j+1},\ldots, x_1)$ from Ω^+. Following the exchange between the cells s_i and s_j , the new corresponding random variables are denoted here as y_i and y_j, respectively. The original configuration $\vec{x}$ starts to get transformed to the one comprised solely of $\vec{y}$ when the variables y_i and y_j gradually substitute the x_j and x_i, in the given order. The analogue of Equation [14.7], representing the modified Bayes' rule, just after the first exchange may be organised as:

$$\begin{aligned} &P(x_1,\ldots, x_{i-1}, y_i, x_{i+1},\ldots, x_{j-1}, y_j, x_{j+1},\ldots, x_n) \\ &= p(y_i, y_j|x_1,\ldots, x_{i-1}, x_{i+1},\ldots, x_{j-1}, x_{j+1},\ldots, x_1) \\ &\quad \times \Pi\,(x_1,\ldots, x_{i-1}, x_{i+1},\ldots, x_{j-1}, x_{j+1},\ldots, x_1) \end{aligned} \quad [14.49]$$

where $y_i = x_j$ and $y_j = x$. Marginal probabilities, Π, in both Equations [14.48] and [14.49], are identical. So, Eq. [14.48] and [14.49] may be used in a way very similar to that employed in Eq. [14.9] to get:

$$P(x_1, x_2,\ldots, x_n) = \frac{p(x_i, x_j|x_1,\ldots, x_{i-1}, x_{i+1},\ldots, x_{j-1}, x_{j+1},\ldots, x_n)}{p(y_i, y_j|x_1,\ldots, x_{i-1}, x_{i+1},\ldots, x_{j-1}, x_{j+1},\ldots, x_n)}$$

$$\times P(x_1, x_2,\ldots, x_{i-1}, y_i, x_{i+1},\ldots, x_{j-1}, y_j, x_{j+1},\ldots, x_n) \quad [14.50]$$

One may repeat the previous step for another pair of cells s_k and s_l to obtain an equation analogous to Eq. [14.11].

$$P(x_1, x_2, \ldots, x_n) = \frac{p(x_i, x_j | x_1, \ldots, x_{i-1}, x_{i+1}, \ldots, x_{j-1}, x_{j+1}, \ldots, x_n)}{p(y_i, y_j | x_1, \ldots, x_{i-1}, x_{i+1}, \ldots, x_{j-1}, x_{j+1}, \ldots, x_n)} \times$$

$$\times \frac{p(x_k, x_l | x_1, x_2, \ldots, x_{i-1}, y_i, x_{i+1}, \ldots, x_{k-1}, x_{k+1}, \ldots, x_{j-1}, x_j, y_{j+1}, \ldots, x_{l-1}, x_{l+1}, \ldots, x_n)}{p(y_k, y_l | x_1, x_2, \ldots, x_{i-1}, y_i, x_{i+1}, \ldots, x_{k-1}, x_{k+1}, \ldots, x_{j-1}, y_j, x_{j+1}, \ldots, x_{l-1}, x_{l+1}, \ldots, x_n)} \times$$

$$\times P(x_1, x_2, \ldots, x_{i-1}, y_j, x_{i+1}, \ldots, x_{k-1}, y_i, x_{k+1}, \ldots, x_{j-1}, y_j, x_{j+1}, \ldots, x_{l-1}, y_l, x_{l+1}, \ldots, x_n) \quad [14.51]$$

By continuing the process still further, a modified Besag proposition is framed

$$\frac{P(\vec{x})}{P(\vec{y})} = \overset{*}{\prod_{1 \le i \le n}} \frac{p(x_i, x_j | condition)}{p(y_i, y_j | condition)} \quad [14.52]$$

where $\vec{x}$ and $\vec{y}$ naturally belong to Ω^+. The symbol $\overset{*}{\Pi}$, standing for the product of all the fractional terms, runs only once over each pair of cells to ensure a transition from an original configuration $\vec{x}$ to a final configuration $\vec{y}$. A graphical representation of the modified Besag proposition for the chosen Markov random field is sketched in Fig. 14.16. It is shown that the heterogeneous two-clans cancel out from the right-hand side of the modified Besag proposition. Therefore, similar processes of factorisation with *g* functions and successive implementation of *q* functions to write in terms of the Hammersley and Clifford expansion, based on a change of variable values of a chosen pairs of cells, are made possible. Each of the exchange procedures fulfil the law of particle conservation and so a changeover from an original configuration to the next one obeys the constraints of a canonical assembly, i.e. using a sequence of configurations $\vec{x}$ from Ω^+. The procedure to factorise conditional probabilities $p(x_i, x_j \mid condition)$ with one-, two-, three- and other clans is the same as that for the local conditional probabilities $p(x_i, \mid condition)$.

The next section is devoted to applications of the Markov random field theory and the auto-models for computer simulation of the wetting of a fibrous mass.

14.3 Computer simulation

This section is divided into three parts. A computer simulation of the wetting phenomenon of individual fibres, describing Rayleigh instability of liquid jets and liquid films on a highly curved fibrous surface, is followed by a subsection devoted to the simulation of liquid columns in parallel fibrous bundles. The final subsection covers the simulation of liquid imbibition in a fibrous mass. The first two simulations study equilibrium or near equilibrium states of liquid bodies, while the final one concerns multiphase flows in fibrous materials.

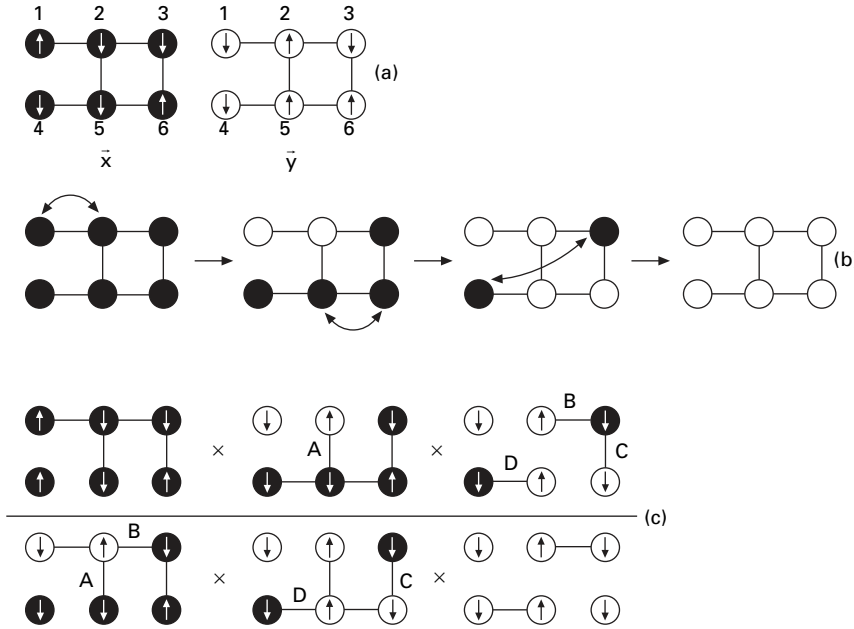

14.16 Graphical expression of the Besag proposition (c) for the Markov random field (a) composed purely of two-clans. Local conditional probabilities belong to pairs of cells that exchange their positions obeying Kawasaki dynamics (b).

Capillary phenomena associated with the presence of a liquid in a fibrous media, where the fibres are nearly cylindrical, are of great importance in a number of fields and products, such as wetting and wicking in textiles and paper. Out of these products, absorbents form a major category including baby diapers, training pants, sanitary napkins, tampons and incontinence products (White, 2001).

The interaction of liquids, polymer melts and solutions with fibrous systems of highly curved surfaces is critical in numerous industrial manufacturing processes, such as fibre formation by various spinning technologies, dyeing and finishing of fabrics, protective coating of wires, and non-woven fabrications. These interactions govern performance of the final products including baby diapers, surgical wipes, feminine hygiene products, hair cosmetics, and paper printings. Given such wide and common applications, it is puzzling to learn that the theoretical interpretation of the wetting of fibrous system is still in its early stage of development (Neimark, 1999).

14.3.1 Computer simulation of the Rayleigh instability

This section will attend to two physical processes, viz. the breaking down of a continuous liquid film covering a fibre and the detachment of a fragmented liquid film from a liquid jet.

Individual interactions of liquid with flat and cylindrical surfaces are dissimilar. When a fibre is covered with a thin, macroscopic liquid film, the film spontaneously breaks down into small droplets. Excepting extremely thin liquid films stabilised by intermolecular interactions like the van der Waals forces, the droplets have roughly uniform spacing along the fibre. The formation of such a droplet chain from an initially continuous liquid film occurs even in the case of a zero contact angle that favours a complete wetting of a surface, especially when it is plane (Roe, 1957). In other words, the wetting behaviour of fibres practically displays an instability or breakdown of liquid columns, crucial for all spinning technologies. This was first observed by Plateau (1873) and theoretically explained later by Rayleigh (1878), giving use to the term 'Rayleigh instability'.

In about 1870, Plateau experimented with oil-drops in water, mixed with alcohol, to form cylinders and found the instability to occur when the cylinder length, expressed as a wavelength λ, was between $1.99\pi r_o$ and $2.02\pi r_o$, where r_o is the radius of a cylindrical fibre with a liquid film. Several other theoretical as well as experimental studies on the same topic are traceable. Papers by deGennes *et al*. (2003) and Roe (1957) present a similar condition, $\lambda > 2\pi r_o$, for cylindrical liquid bodies. Here, two of such studies will be involved, viz. the ones by Tomotika (1935) and by Meister (1967).

The Rayleigh instability of long liquid jets is a consequence of a temporal development and intensification of original tiny perturbations, also known as capillary waves (Adamson and Gast, 1997; deGennes, 2003). The exact value of the Rayleigh wavelength is obtained by using Navier–Stokes equations. The Rayleigh wavelength λ has a value higher than the limiting value given in the aforementioned work of Plateau and according to the result obtained by Rayleigh (1878) has a value of $2.88\pi r_o$. Studies of de Gennes (2003) may be consulted for more details.

The well-known auto-model employed here to investigate the Rayleigh instability is composed of a three-dimensional simulation box of cuboid structure having n cells. The number of cells n is determined by the product of a chosen numbers of cells along the three axes x, y, and z, written as, $n_x * n_y * n_z$. The present simulation is connected to a particular value of n equalling $600 \times 20 \times 20 = 24 \times 10^4$ cells. In a cell s_i the random variable X_i is assigned the variable value x_i, equivalent to 0 for a gas, 1 for a liquid and 2 for a solid filling it. In the present context, function $U(\vec{x})$ is interpreted as the system Hamiltonian, i.e. the total system energy. This Hamiltonian is of the previously stated relation [14.40].

$$U(\vec{x}) = \sum_{1 \le i \le n} C(x_i, x_j) \qquad [14.53]$$

where $C(x_i, x_j)$ represents the interaction energies between the neighbouring cells s_i and s_j, having corresponding variable values x_i and x_j. τ is the statistical temperature, assigned a value of 50 e.u., where e.u. is the energy unit of the model. The values of C are provided in Table 14.1. One-clans do not contribute to energetic interactions because influences of the external gravitational field, the electrical field and other fields are presently neglected. Thus, the Hamiltonian [14.53] misses the first term of gravity of the auto-model, meant for describing the wetting phenomena. The freshly introduced Hamiltonian has a form similar to that of Eq. [14.40], mentioned earlier. For the current purpose, free boundary conditions (Binder, 1997) are engaged.

The neighbourhood of a cell, depicted in Fig. 14.17, is composed of 26 neighbouring cells that form a supercube of 27 cells, including the one at reference. So, the order o of this neighbourhood in a three-dimensional cuboid lattice is 2, according to the notation introduced in the Section 14.2.2

Table 14.1 Interaction energy values used for the simulation of the Rayleigh instability. Interaction energies are symmetric functions if their two variables $C(x_i, x_j) = C(x_j, x_i)$ and represent the energies belonging to the mutual interaction of neighbouring nodes i and j where random variables X_i and X_j have values x_i and x_j

Interaction energies in e.u. Rayleigh instability	Gas, $X_i = 0$	Liquid, $X_i = 1$	Fibre, $X_i = 2$
Gas, $X_j = 0$	$C(0, 0) = -40$	$C(0, 1) = -10$	$C(0, 2) = 20$
Liquid, $X_j = 1$	$C(1, 0) = -10$	$C(1, 1) = -26$	$C(1, 2) = -10$
Fibre, $X_j = 2$	$C(2, 0) = 20$	$C(2, 1) = -10$	$C(2, 2) = 0$

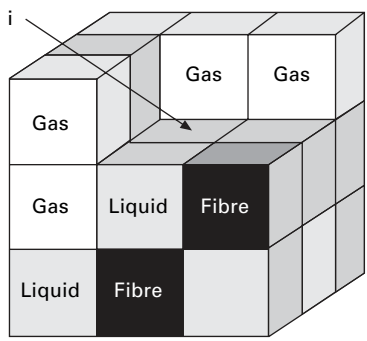

14.17 A cell i in the centre to form a supercube with its neighbouring cells. On the front surface can be seen various kinds of media that occupy the cells: the white colour denotes air, the grey color denotes liquid, and fibre cells are black.

and in Paget's paper (1999). Regarding the initial configurations of cylindrical liquid films and jets, all liquid and fibre cells are arranged in chains parallel to the x-axis so that their cross-sections perpendicular to the x-axis are nearly circular. Figure 14.18 may be consulted for an illustration of this. For simulations considering a liquid coating on a fibre, the central chain of cells represents a solid fibre with all x_i's of 2, and surrounded by chains of liquid cells with x_j's as 1. The cross-section of a studied system is also shown in Fig. 14.18.

The simulation in this chapter uses Monte Carlo dynamics, based on Gibbs–Geman sampling. The Markov chain is based on Kawasaki dynamics for short distances, described earlier in Section 14.2.5, where the proposed cells involved in an exchange are among the neighbours. In this method, a pair of cells is chosen at random using a random number generator. The

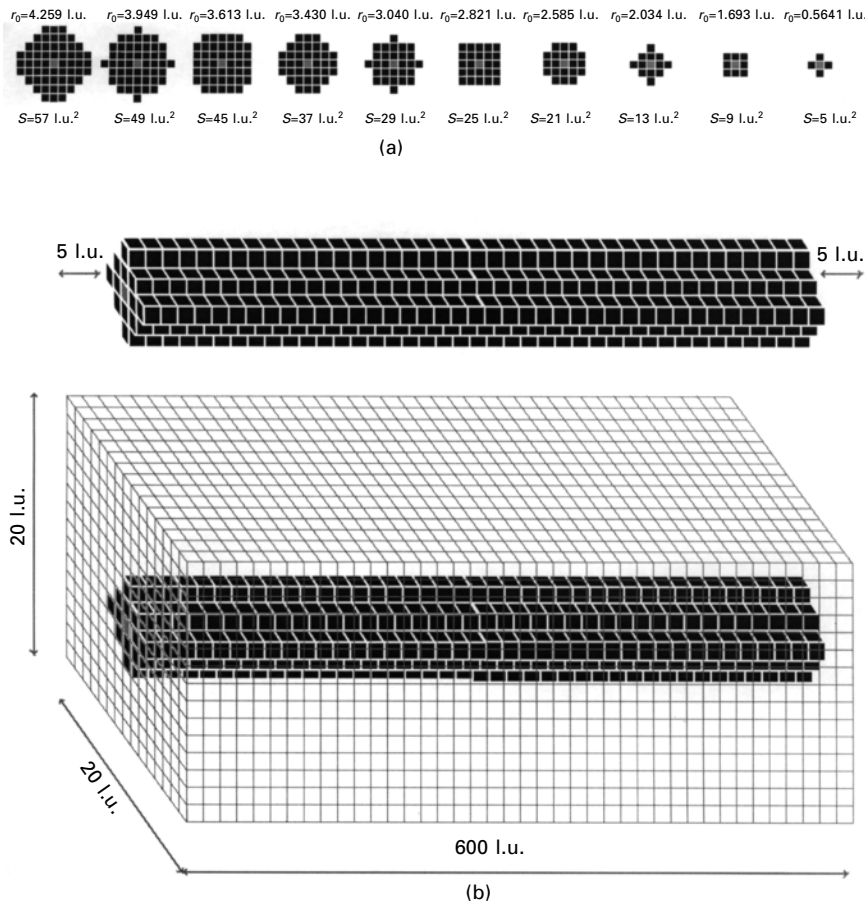

14.18 Initial configuration of a liquid film on a fibre.

random variables in a chosen pair of cells then exchange their positions to form a new configuration. The Hamiltonian values are calculated for the configurations both before and after the exchange. A configurational change from an original $\vec{x}$ to a new one $\vec{y}$ is accounted if it satisfies one of two conditions. One of the conditions, (A), is fulfilled, when the total energy for the new configuration $U(\vec{y})$ is lower than that of the original one $U(\vec{x})$. In that case the exchange probability $W(\vec{x} \rightarrow \vec{y})$ is equal to one. If it is otherwise, i.e. $U(\vec{y}) > U(\vec{x})$, the exchange is carried out only under condition (B), which postulates that claims the transition probability $W(\vec{x} \rightarrow \vec{y})$ allows such an exchange when $W(\vec{x} \rightarrow \vec{y}) = \exp[-(U(\vec{y}) - U(\vec{x}))/\tau]$. These values of transition probabilities are in accordance with [14.46] in Section 14.2.5. This probabilistic transition is realised by the generation of a random number z inside the uniform interval $\langle 0, 1 \rangle$ and the acceptance of a new system configuration meets the condition $z < W(\vec{x} \rightarrow \vec{y})$. More details about the model can be found in some recent work (Binder, 1997; Lukas *et al.*, 2004).

After creation of an initial joint system configuration, the simulation algorithm iterates the following steps to create the Markov chain of successive configurations of the system:

(i) Selecting at random two lattice cells s_i and s_j at which the random variables x_i and x_j are ascribed for the exchange $x_i \rightarrow x_j$ and $x_j \rightarrow x_i$. The cell s_i contains liquid, i.e. x_i has a value of 1, and s_j is filled by a gas. Moreover, as both the cells s_i and s_j are to be located in the interface between liquid and gas, the cell at the liquid interface is defined as the one whose neighbourhood of the order o is 2, consisting of at least one gas cell. Correspondingly, for the gaseous interface, the cell has at least one liquid cell in its neighbourhood. This type of random variable exchange between distant cells s_i and s_j is based on spin exchange of long-range Kawasaki kinetics (Kawasaki, 1972).

(ii) Computing the total energy change, ΔU, according to a chosen Hamiltonian associated with the exchange of the random variables. The values of the mass of the liquid cell, m, of unity, and the acceleration due to gravity, g, equalling 10 are considered here.

(iii) Calculating the transition probability $W(\vec{x} \rightarrow \vec{y})$ according to Equation [14.45]. In the present simulations, the value of the statistical temperature, τ, i.e. the product of the Boltzmann constant with the absolute temperature, is preset to 50 e.u.

(iv) Realising the probabilistic nature of the spin exchange by drawing a random number z, that is uniformly distributed in the interval $\langle 0, 1 \rangle$.

(v) Exchanging the spin cells, when $z < W(\vec{x} \rightarrow \vec{y})$.

(iv) The spin configuration obtained at the end of step (v) is counted as a new configuration after which the next iteration starts from step (i).

After an adequate number of repetitions, the registered set of simulated configurations is analysed both numerically and graphically to yield the shape of the liquid body as well as the sum of the total energy changes in the system.

The chain of succeeding configurations is broken as soon as the liquid film or jet disintegrates to independent droplets. The unit of time used in Monte Carlo dynamics is the Monte Carlo step per site (MCSPS), which corresponds, approximately, to one exchange trial for each cell in the simulation box. In the present case, one MCSPS is equivalent to 24×10^4 trials of cell exchange, since the simulation box of the dimensions $600 \times 20 \times 20$ [l.u.^{3}] has 24×10^4 cells.

One of the chosen original configurations of a liquid film coating a fibre is exhibited in Fig. 14.18. The system dynamics are nearly perpetual because the neighbouring droplets, detached from the original liquid film, communicate ceaselessly with others, resulting in exchange of liquid particles either via evaporation and condensation or via liquid films stabilised between droplets on a fibre. Accordingly, in spite of being a relatively sluggish process, substantial physical significance of the temporal system development draws one's attention in an attempt to observe the complete breakdown of the original cylindrical liquid bodies. Such an accomplishment is done through a series of graphs obtained at equal intervals on the MCSPS time scale. These graphs are obtained by plotting the count of liquid cells in the cross-sections perpendicular to the x-axis as a function of the corresponding x-axis coordinates. The liquid cells are counted at individual cross-sections, perpendicular to the x-axis, for every point on the x-axis. One such instance is given in Fig. 14.19.

Pertaining to the present simulation, time-dependent developments of droplet count both for a film covering a fibre surface and for a jet having a cross-section the same as that given in Fig. 14.20, are displayed in Fig. 14.21. It is quite discernible from the figure that the number of detached droplets experiences a temporal change propelled by minimisation of the total system energy. The system is dissipative and the released energy flows from it to a reservoir. Once the liquid jet is fragmented into droplets, the droplet number decreases as fusions of the neighbouring droplets take place. The time-dependent development of the droplet number, averaged from five computer simulations, is recorded in Fig. 14.20. It may be seen that the temporal

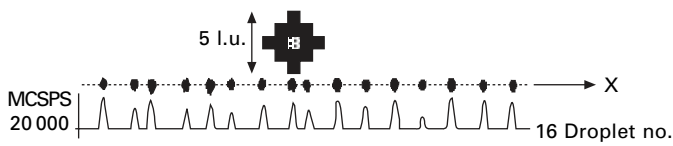

14.19 Liquid cell count inside individual cross-sections perpendicular to the *x*-axis.

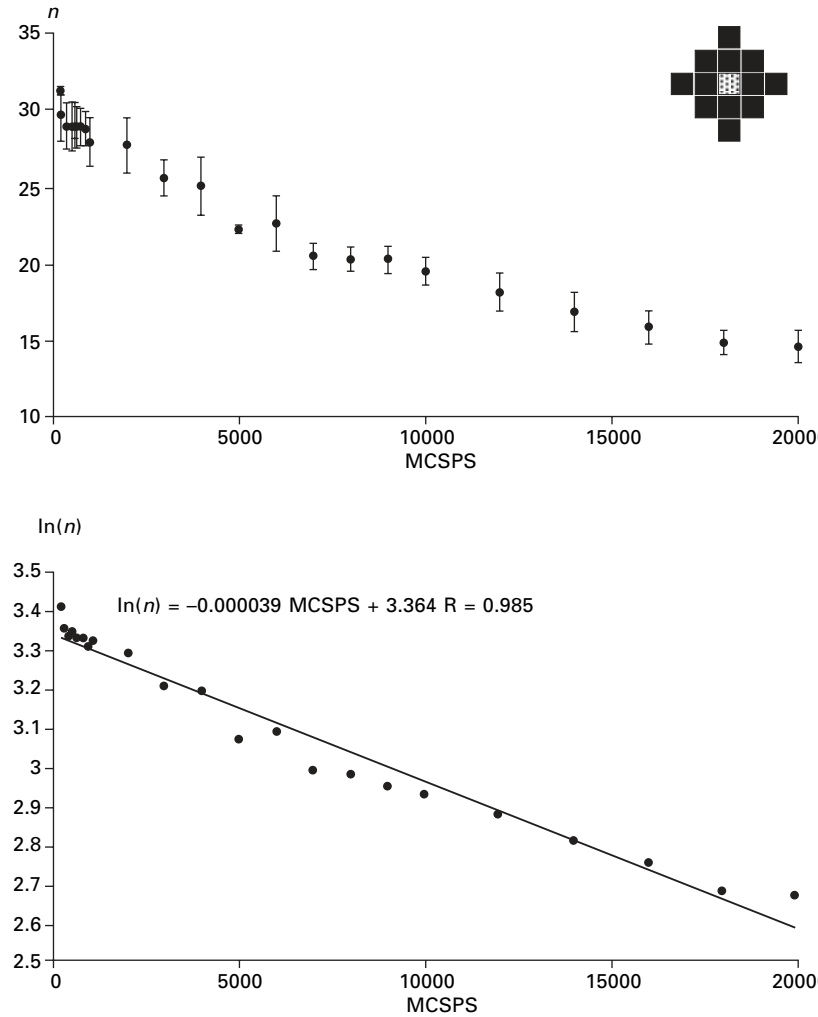

14.20 Temporal development of the droplet number is the consequence of a subsequent droplet fusing.

development of the droplet number, n_o, is well described by a logarithmic dependence ln $(n_o) = A \times \text{MCSPS} + B$, with a correlation coefficient, R, as high as 0.97.

For comparing the simulated results with the λ - r_o scaling for the Rayleigh instability, i.e. $\lambda = 2.88\pi r_o$, pertinent measurements from the computer-generated outputs are taken at the primary stages of the process of droplet detachment. The radii of the liquid film and of the liquid jet, both expressed as r_o, are varied. The original cross-sectional configurations of the films and the jets are shown in Fig. 14.18(a). The equivalent radii, r_o, of the circular

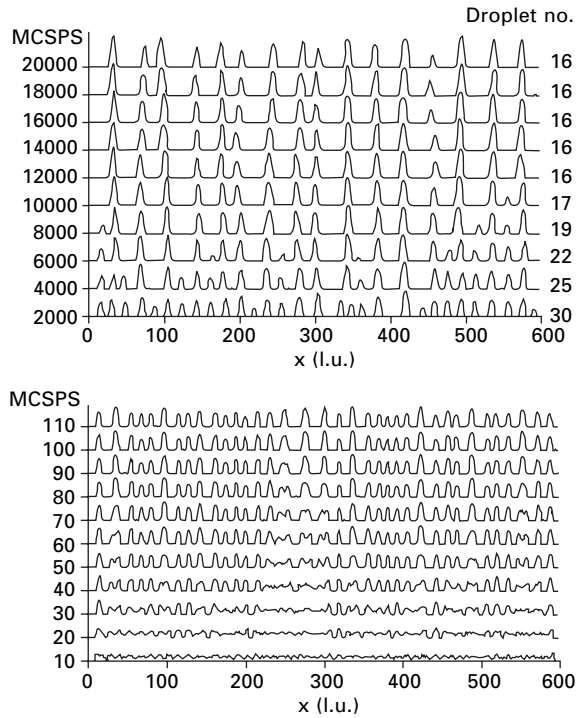

14.21 The perpetual dynamics of the system are caused by the coalescence of neighbouring droplets.

cross-sections are calculated from the equivalent cross-sectional areas, S, of the discrete models using the relation $r_o = \sqrt{S/\pi}$. The simulated systems maintain areas, S, in terms of the number of cells measured in $(\text{l.u.})^2$, where l.u. refers to a lattice unit, given by the distance between the nearest cells in the cubic lattice of the investigated model, as has been already mentioned in Section 14.2.2. One l.u. is also the natural length scale of the discrete lattice model under consideration. Cross-sectional areas S of the models and corresponding radii of the cylinders are also shown in Fig. 14.18(a).

Right from the primal phases of detachment of the liquid film or the jet, the number of droplets, formed n_o, is recorded. To estimate the Rayleigh wavelength, the initial length of the film or jet (590 l.u.) is divided by n_o. The wavelength obtained from the computer simulation is denoted as λ_{sim}. After averaging the set of values of the wavelength received from several successive executions of the computer program, it is compared with the analytical expression of λ as $2.88\pi r_o$. Each of the computer simulations is repeated five times for a chosen set of input data. Simulation results associated with liquid films and jets for various values of r_o are portrayed in Fig. 14.22. The slopes of both the curves are nearly the same.

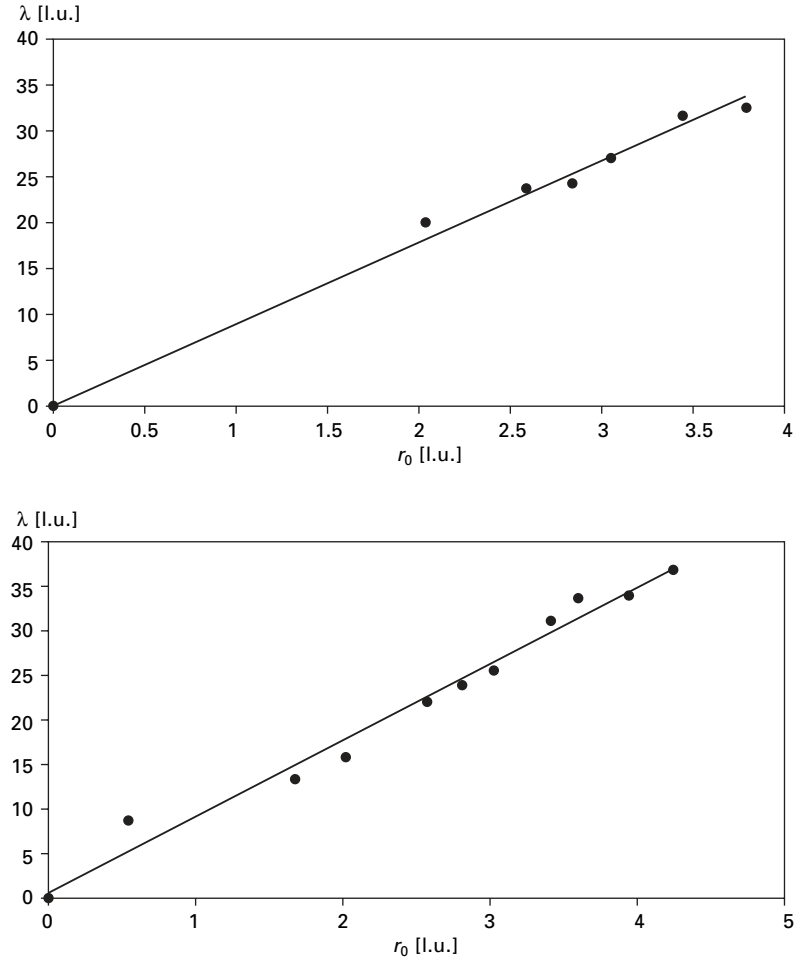

14.22 The dependence of the Rayleigh wavelength λ on the original radius of liquid films (a) and liquid jets (b).

Thus, it is established that the Monte Carlo method applied to an auto-model to examine the instability of liquid films and jets provides simulation outputs very similar to those of classic theoretical analysis. It may be anticipated that this kind of simulation will also imitate the behaviour of the soft mass in experimental arrangements under more complex conditions. It is highly probable that the auto-models are effective in describing liquid film and liquid jet instability even when the system loses its axial symmetry, i.e. for bent fibres. It may also be applicable to incorporate aspects of external fields, roughness and chemical inhomogeneity of fibre surfaces, mixtures of liquids, electrically charged liquids and polymer solutions, and so on. This

approach is not appropriate, however, for phenomena affected predominantly by momentum or viscosity.

A simple and straightforward approach to using an auto-model for accounting for the wetting of more complex fibrous structures will be shown in the next subsection. Interactions of liquids with fibre bundles will be taken up first.

14.3.2 Computer simulation of liquid columns in fibre bundles

Through a series of papers presented at the end of the 1960s, Princen (1969) considered a capillary rise between two vertical cylinders, and, subsequently, between three-, four-, and multi-cylinder systems (Princen, 1969a). The last paper in the series (Princen, 1970) was devoted to a study of equilibrium configurations of limited amounts of liquid in horizontal cylindrical assemblies, where gravitational effects were neglected. All of Princen's works were focused on contact angles ranging between 0° and 180°. Princen claimed in one of his works (Princen, 1970) that a liquid column between two closely separated horizontal cylinders ceased to maintain a uniform cross-section as soon as the distance between the cylinders increased to reach a certain critical value, and the liquid acquired a shape similar to that of an unduloid droplet on a single cylinder caused by Rayleigh instability, as described in the previous subsection. The abrupt change in the liquid body shape was mentioned as a morphological transition. The same literature (Princen, 1970) also maintained that liquid columns within a higher number of equidistantly placed cylinders exhibited other unusual features. The systems were then found to undergo morphological transitions, marked by two different changes in shape of the liquid phase, depending on the inter-cylinder separation. For a sufficiently small inter-cylinder distance, the liquid bridged only each pair of adjacent cylinders, with the central channel left open. Three separate columns were observed in the case concerned. Experiments and computer simulation for such morphological changes were carried out by Lukas and Chaloupek (2003a). When the distance was greater than a certain critical value, the liquid filled the inter-cylinder channel completely. The shape of the liquid body was termed the channel-filling column. A further increment of the distance between the cylinders carried the system to a second critical region, characterised by a transition of the channel-filling column to a state akin to the unduloid on a single cylinder. All these phenomena could be investigated using auto-models.

The cylinder system considered by Princen was simply a general geometrical model of fibrous bundles and fibrous materials. The venture to apply an auto-model to generate column morphological transitions, predicted previously by Princen for systems composed of pairs of parallel cylinders, will now be considered. The main focus will be on long liquid column–unduloid transitions

in bundles composed of two cylindrical fibres. Before the computer simulations are dealt with, an analytical description of the problem will be given.

Let a limited amount of a liquid, denoted as L, coexistent with another fluid phase represented for instance by a gas/vapour, say V, be considered. Air may be envisaged to constitute phase V. The liquid phase L is supposed to be located within the gap between two narrowly spaced cylinders S. Real wetting structures with dimensions in the order of microns will be involved, so as to neglect the line tension and the gravitational effects. It may be assumed that the liquid phase L forms a short bridge, the surface of which possesses a constant mean curvature $1/R$, as is sketched in Fig. 14.23. When the bridge contains a sufficient amount of the phase L, a long column with a constant cross-section, excluding the terminal menisci, will be constructed.

For convenience, the notations of various quantities used here are kept similar to those used by Princen (1970). The distance between the solid cylinders, having individual radii of r, is $2d$. Phases L (a liquid), V (a vapour) and S (a solid fibre) are characterised by a liquid contact angle θ. Referring to the cross-sectional geometry in Fig. 14.24, the angle between the line connecting the cylinder centres and the radial distance to the $L - V - S$ line is α, shown as the covering angle. The radius R represents the curvature of

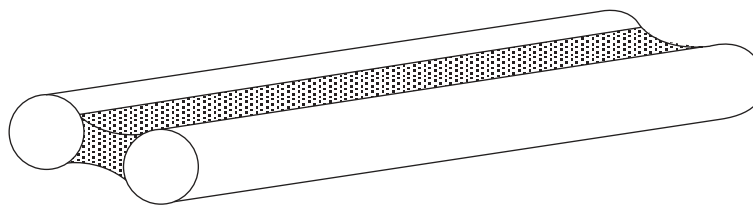

14.23 A liquid phase forms a short bridge between two cylindrical fibres.

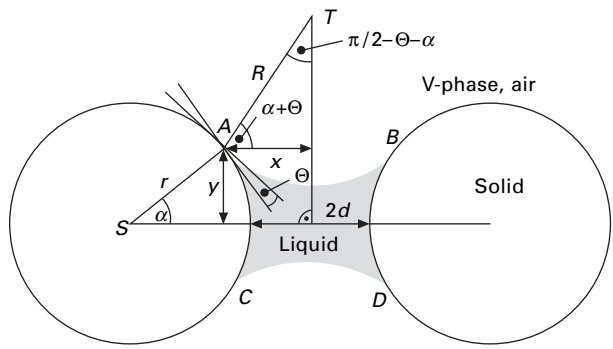

14.24 A cross-section of a long liquid column between two cylindrical fibres.

the liquid surface. Its value with respect to the Laplace pressure is considered positive if it has an outward concave surface; negative otherwise.

The present objective is to find the threshold value of the dimensionless ratio of the aforementioned quantities, d/r, at which the transition occurs. The complexity of the situation may be reduced by considering the contact angle θ tending to zero. To be more rigorous, the value of spreading, i.e. the Harkinson parameter $S = \gamma_{SV} - \gamma_{LS} - \gamma$ must approach zero, and so the transition to complete wetting is dealt with. Different shapes of cross-sections of the long liquid columns between the two cylinders/fibres are depicted in Fig. 14.25 for the case of θ having a value of 0°.

The forces, at equilibrium, on the front edge of liquid column are

$$F_{SV} = F_{LS} + F_{LV} + F_p \qquad [14.54]$$

where F_{SV} is the force of solid–vapour interface, generated by a corresponding surface tension γ_{SV}. This force acts outward in the liquid body and tends to spread the liquid along the cylinders. The force F_{SV} is also called the 'line force' as it is proportional to the length of the line along which γ_{SV} acts.

A transitional shape of the liquid body between the conformations of long column and unduloid is the cylindrical column as sketched in Fig. 14.25. For a circular cross-section of a long liquid column having an effective liquid area, responsible for Laplace pressure, of $A = \pi(R^2 - 2r^2)$, Equation [14.54] takes the following form:

$$4\gamma_{SV}r = 4\gamma_{SV}r + 2\gamma R - \frac{\gamma}{R}(R^2 - 2r^2) \qquad [14.55]$$

Using Young's equation, $\gamma_{SV} - \gamma_{SL} = \gamma\cos\theta$ and making the assumption that cos θ equals 1, a quadratic relationship for the dimensionless parameter,

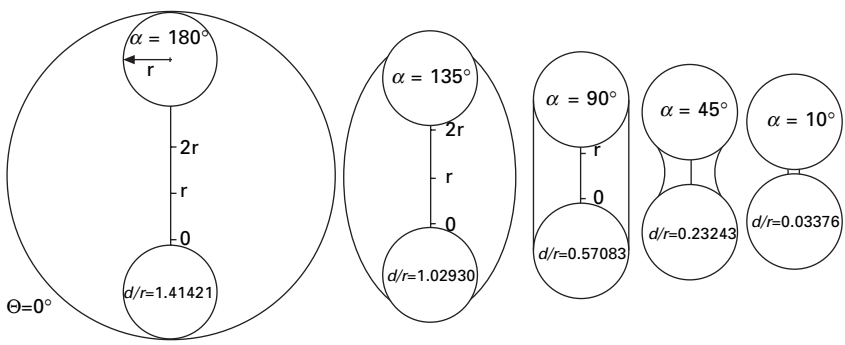

14.25 Various shapes of cross-sections of long liquid columns between two cylinders for spreading coefficient equal to zero, i.e. for contact angle just being equal to zero. The transitional shape between long columns and unduloids is the cylindrical long liquid column.

R/r, is obtained by multiplying Equation [14.55] by $\frac{R}{r^2\gamma}$. This is given below:

$$\left(\frac{R}{r}\right)^2 - 4\frac{R}{r} + 2 = 0 \qquad [14.56]$$

The solution for R/r in the above Equation [14.56] is $2 + \sqrt{2}$, arrived at with an omission of the other root $2 - \sqrt{2}$ to satisfy the relation between R and $2r$ as evident from Fig. 14.25. Particularly, the relation $R = 2r + d$ holds true. So the threshold of the dimensionless parameter d/r for the appearance of the long cylindrical liquid columns has the value $d/r = (R - 2r)/r = \sqrt{2} = 1.41421$.

The morphologies of a liquid body that are generated through computer simulation, built on the auto-model and Kawasaki dynamics identical to those described in the previous subsection, are depicted in Fig. 14.26. The

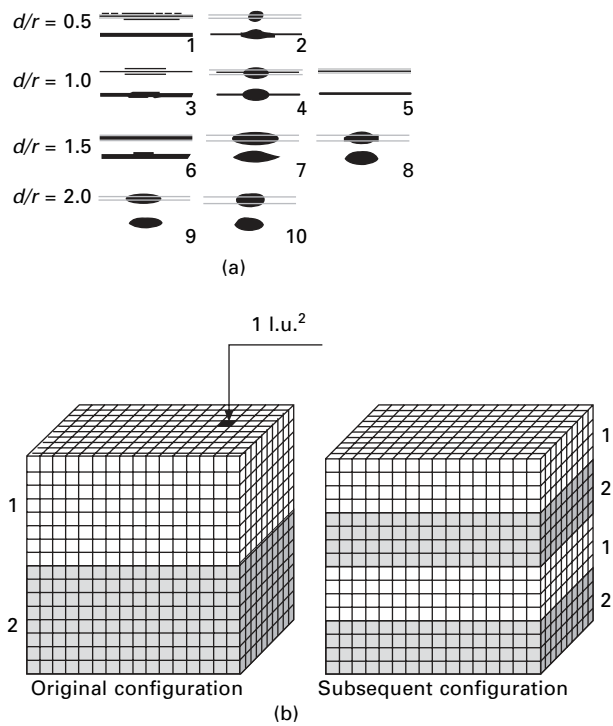

14.26 Long liquid column–unduloid transition. Computer simulation outputs carried out for zero contact angle θ and various values of dimensionless distance d/r between fibres (a) (courtesy of Jana Holubova, Technical University of Liberec). The original configuration and the subsequent one after the slab displacement are used for an estimation of surface tension values when the system temperature is low (b).

Table 14.2 Interaction energy values $C(x_i, x_j)$ used for the simulation of morphological transitions of liquid columns in a pair of parallel fibres. The choice of these values ensures the zero contact angle between the liquid and the solid fiber material since $E_{0,2} \geq E_{1,2} + E_{0,1}$, i.e. $\gamma_{VS} \geq \gamma_{LS} + \gamma$, thanks to $C(0, 2) \geq C(1, 2) + C(0, 1) - C(1, 1)$

Interaction energies in e.u. morphological transitions of liquid columns	Gas, $X_i = 0$	Liquid, $X_i = 1$	Fibre, $X_i = 2$
Gas, $X_j = 0$	$C(0, 0) = -40$	$C(0, 1) = -20$	$C(0, 2) = -10$
Liquid, $X_j = 1$	$C(1, 0) = -20$	$C(1, 1) = -28$	$C(1, 2) = -20$
Fibre, $X_j = 2$	$C(2, 0) = -10$	$C(2, 1) = -20$	$C(2, 2) = 0$

values of C from the Hamiltonian [14.53] are given in Table 14.2. These values are so chosen to ensure almost negligible contact angles. The calculus for choosing C's follows.

Imagine a prismatic simulation box partially filled up by two unlike Materials 1 and 2, with a flat interface in-between; let a new configuration be created simply by moving a slab of Material 2 to a space originally occupied by Material 1. The substitution is supposed to obey a conservation of the total number of cells for both the materials so that the original configuration with two material slabs has one interface while the latter, consisting of four slabs, has three interfaces. Both the configurations are sketched in Fig. 14.26(b). The two-slab configuration has an interfacial energy per unit area [l.u.^{2}] of 1, corresponding to $C(X_1, X_2)$, while the four-slab configuration possesses three interfacial interaction energies of the same value. The first of them substitutes the interaction energy $C(X_1, X_1)$ in the layer made of Material 1 and the next substitutes the original interaction energy $C(X_2, X_2)$ in that made of Material 2 of the original configuration. Finally, the third interface boundary between 1 and 2 with the interaction energy $C(X_1, X_2)$ located somewhere in the middle of the simulation box remains unchanged. All the other corresponding horizontal layers of cell of both the configurations of the simulation box have equal contents of interaction energies. Subtracting the extra interfacial energy $3C(X_1, X_2)$ of the second configuration from the first one, i.e. $C(X_1, X_2) + C(X_1, X_1) + C(X_2, X_2)$, the increase of interaction energy per unit surface area, $2C(X_1, X_2) - [C(X_1, X_1) + C(X_2, X_2)]$, is obtained. This increase is due to the creation of the two new interfaces between Materials 1 and 2 and hence the surface energy $E_{1,2}$, numerically equal to the surface tension $\gamma_{1,2}$, is half the increment of the interaction energy per unit area, i.e. $E_{1,2} = C(X_1, X_2) - \frac{1}{2}[C(X_1, X_1) + C(X_2, X_2)]$ A more advanced and general but more complicated method to determine the interfacial tension can be found, for instance, in the work of Aloisi *et al.* (1987).

In Table 14.2 the interaction energies are expressed in e.u./l.u.^{2}, where

e.u. is the energy unit. There, the indices 0, 1, 2 denote the gas/vapour, the liquid, and the fibre, i.e. the triad (0,1,2) corresponding to the former (*V*, *L*, *S*). The interaction energies, i.e. $C(X_i, X_j)$'s are chosen to keep the contact angle between the liquid and the solid fibre negligible. Hence, the relations $E_{0,2} \geq E_{1,2} + E_{0,1}$, i.e. $\gamma_{VS} \geq \gamma_{LS} + \gamma$ are obtained, in agreement with the condition for a complete wetting given by Young's equation. One obtains the inequality $C(0, 2) - \frac{1}{2}\,[C(0, 0) + C(2, 2)] \geq C(1, 2) - \frac{1}{2}\,[C(1, 1) + C, (2, 2)] + C(0, 1) - \frac{1}{2}\,[C(0, 0) + C(1, 1)]$ after substituting the previously derived expression of $E_{1,2}$ into the aforementioned Young's condition for a zero contact angle. It is proper to point out that the inequality does not depend on $C(0, 0)$ and $C(2, 2)$. So, the final form of the inequality is $C(0, 2) \geq C(1, 2) + C(0, 1) - C(1, 1)$. For the particular $C(X_i, X_j)$ values of Table 14.2, the inequality gives -10 e.u./l.u.$^2 > -12$ e.u./l.u.^{2}, safeguarding the zero contact angle of the investigated system and maintaining the spreading coefficient *S* close to zero.

The appearance of long liquid columns and unduloids for various distances and fibre radii are depicted in Fig. 14.27. The threshold values of *d/r* estimated from the computer simulation are near to 1.414, the same as predicted by Princen in his approach.

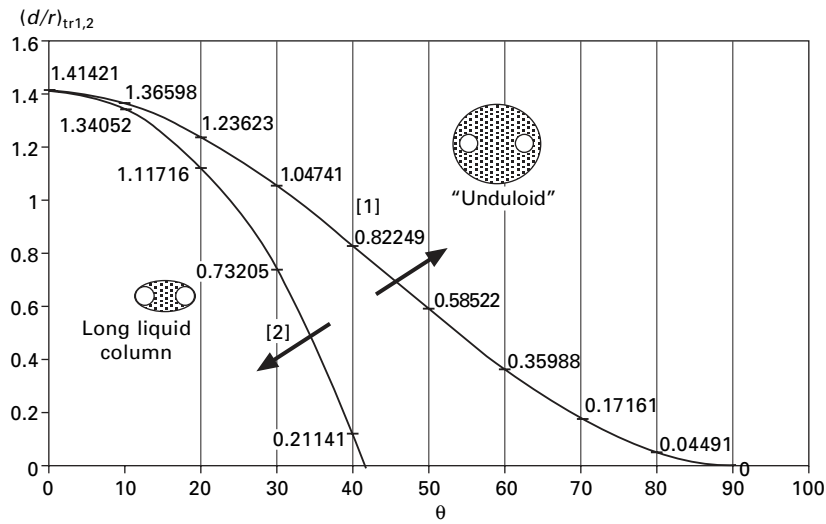

14.27 The dependence of the dimensionless distance *d*/*r*, (*r* is the fibre radius) between two parallel cylindrical fibres and the contact angle *θ*. The curve in the graph represents the transition boundary between long liquid columns and unduloids.

14.3.3 Computer simulation of three-dimensional liquid transport in fibrous materials

Liquid movement in three-dimensional fibrous materials is studied in this subsection by means of Monte Carlo simulation, based on the auto-model with Kawasaki kinetics. Related algorithms are developed in accordance with the standard liquid wicking rate tests from both the European Disposables and Nonwovens Association (EDANA), and the International Nonwovens and Disposables Association (INDA). The simulation provides information about liquid wicking into computer-generated fibre assemblies as a function of time. The analysis mainly focuses on the connection between the fibre orientation and the liquid wicked into computer-generated fibre assemblies, as a function of time. Factors such as the fibre orientation and the liquid wicking rate are varied, keeping other geometrical parameters of the fibrous material unaltered. This simulation also presents dynamic data of both the mass of drawn liquid and energy changes, i.e. the energy dissipation of the system. The results are in agreement with some known experimental evidence. More information about this kind of simulation is available in recent papers of the authors Lukas *et al*. (2004).

A flow involving more than a single phase is classified as a multiphase or inhomogeneous one – such as liquid flow in fibrous media. The dynamics of the evolved macroscopic interface of the distinct phases during such inhomogeneous flow through fibrous masses is of interest. The dynamics are qualified by surface tension, fibrous media anisotropy and inhomogeneity, fibre volume fraction, and fibre wetting behaviour. An uncertainty of structural conformation in fibrous media, accompanied by susceptibility to small loads, tortuous connectivity of their open pores and poorly defined boundaries, results in complex local inhomogeneous flows and interfacial evolution (Hentschel, 1994). This complexity becomes prohibitive for development of analytical theories describing these phenomena in many cases.

The wetting and wicking of fibrous materials constitute a class of flows that have critical scientific and practical significance, on which technologies such as fibre lubricating and processing, fibre-reinforced composite manufacturing, and fibre web bonding and dyeing are based. Wetting and wicking behaviours of many consumer products, such as baby diapers, female hygiene products, and sport and other protective garments, are vital in determining their commercial success.

The chosen method makes it possible to investigate the wetting and wicking phenomena, as well as to predict the system parameters that are comparable with experimental ones at a macroscopic level. One such parameter is the wicking rate, which can be measured, simulated, and theoretically derived from the Lucas–Washburn theory. The wicking rate in fibrous systems is heavily influenced by several complex geometrical parameters, as mentioned

previously. Hence, at present, exclusively one aspect of the effect of fibre orientation is attended to here. Other morphological features, such as heterogeneity, fibre volume fraction, fibre aspect ratio, fibre curl and fibre surface geometry, are kept constant in the bulk of the modelled specimens. All fibres are represented strictly by their linear geometry. In other words, the main subject in this subsection is a detailed study of the relationship between the wicking rate and fibre orientation.

Wicking and absorption rate in fibrous media are conveniently described using the Lucas (1918) and Washburn (1921) approach. The simple theory of Lucas and Washburn deals with the rate at which a liquid is drawn into a circular tube by capillary action. Such a capillary is, in reality, a grossly simplified model of a pore in a fibrous medium with a highly complex structure. The derivation of the following equation may be found in a recent work of Lukas *et al*. (2004).

$$\frac{dh}{dt} = \frac{r\gamma\cos\theta}{4\mu h} - \frac{r^2\rho g\cos\beta}{8\mu} \qquad [14.57]$$

Parameters and quantities visible in the Lucas and Washburn equation are introduced further. A newtonian liquid with viscosity μ wets a tube of radius r. The contact angle of the liquid against the tube wall is denoted as θ, and the parameter β is the angle between the tube axis and the vertical direction, as shown in Fig. 14.28. The symbol γ stands for the liquid surface tension, ρ for the liquid density, g for the gravitational acceleration, and h for the distance travelled by the liquid, as measured from the reservoir along the tube axis. The distance, obviously, is a function of time, i.e. $h = h(t)$. For a given system, as is shown in Fig. 14.28, parameters r, γ, θ, μ, ρ, g, and β remain constant. The following two constants may be introduced

$$K' = \frac{r\gamma\cos\theta}{4\mu} \quad \text{and} \quad L' = \frac{r\rho g\cos\beta}{8\mu} \qquad [14.58]$$

to simplify the Lucas–Washburn Equation [14.58] to get

$$\frac{dh}{dt} = \frac{K'}{h} = L' \qquad [14.59]$$

The above relation is an ordinary non-linear differential equation that is solvable in terms of function $h(t)$ after ignoring the parameter L' physically by considering either of the cases when liquid penetration is horizontal (β = 90°), or r is small to render $L' \to 0$. L' is also comparatively negligible when the rising liquid height h is low, so that $\frac{K'}{h} >> L'$. It also becomes insignificant with a diminishing effect of the acceleration due to gravity g. The Lucas–Washburn Equation [14.59] thus reduces to:

$$h = \sqrt{2K't} \qquad [14.60]$$

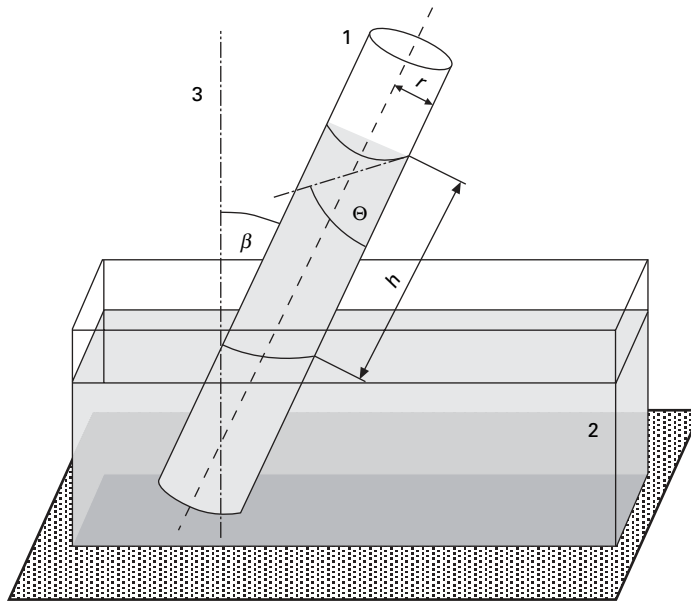

14.28 A tube (1) of a radius r is suspended in a liquid source (2). The distance traveled by the liquid along the capillary axis is h. The angle θ is the contact angle between the liquid surface and the capillary wall, while β denotes the angle between the tube and the vertical axis (3).

The result satisfies an initial condition $h = 0$ for $t = 0$. Gupta's approach (Gupta, 1997) concerns a similar work pertaining to a study of the wicking rate of a fluid spreading radially outward from a point source at the centre of a substrate instead of a vertical movement of the liquid in which the fibrous substrate is partially immersed. This is illustrated in Fig. 14.29.

It is now time to speak about modifying the Lucas–Washburn equation by expressing the distance h in terms of the liquid mass uptake m. Such an alteration is detailed in some recent literature (Ford, 1933; Hsieh, 1995; Lukas *et al.*, 2004). The applied manipulation does not affect the fundamental shape of the Equation [14.59] as h and m are linearly related for a circular tube with a fixed cross-section. Furthermore, for radial spreading, the liquid mass m_R is expressed as $\pi r^2 T\rho VL$, and for an ascending movement the mass m_A becomes $whT\rho V_L$, where T is the thickness of the substrate and V_L is the liquid volume fraction inside the substrate of width w.

For a radial liquid spreading in a flat textile specimen, the following equation may be written using Equation [14.60]:

$$Q = \frac{m_R}{t} = 2\pi K' T\rho V_L \qquad [14.61]$$

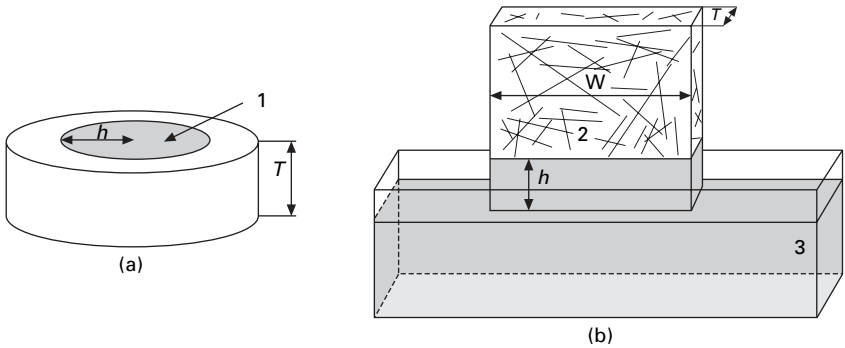

14.29 Two different experimental arrangements for wicking (absorbency) rate measurement: (a) Liquid source initiates in the centre of a flat specimen and is spread radially outward, and (b) Liquid ascends in a specimen perpendicular to the reservoir liquid surface.

where Q is the liquid wicking (absorbency) rate used by Gupta (1997). It is independent of time during the spreading process. Now, let liquid mass uptake m_A be substituted into the original Lucas–Washburn Equation [14.59], resulting in:

$$\frac{dm_A}{dt} = \frac{K}{m_A} - L \qquad [14.62]$$

The new constants K and L are

$$K = (wT\rho V_L)^2 K', \; L = wT\rho V_L L' \qquad [14.63]$$

It is obvious that the constant K in the modified Lucas–Washburn Equation [14.62] is proportional to the wicking/absorption rate Q, defined in [14.61]. From [14.61] and [14.63], it follows that $Q = \dfrac{2\pi}{w^2 T\rho V_L} K$. Hence the parameter K can be used as a measure of the wicking spread rate Q in those experiments where a fabric is hung vertically in a liquid. The values of K and L may be derived from the slope and intercept of the dm_A/dt versus $1/m_A$ graph, as mentioned by Miller and Jansen (1982). On the other hand, Equations [14.59] and [14.62] are solvable in terms of functions $t(h)$ or $t(m_A)$ without dropping the gravity term, g, as shown in some earlier works (Lucas, 1918; Washburn, 1921; Lukas and Soukupova, 1999). For the liquid mass uptake, i.e. for the ascending liquid movement, the Lucas–Washburn Equation [14.62] yields:

$$t(m_A) = -\frac{m_A}{K} - \frac{K}{L^2} \ln\left(1 - \frac{L}{K} m_A\right) \qquad [14.64]$$

However, a theory like that of Lucas–Washburn has innumerable limitations.

Firstly, the assumed cylindrical capillary tubes are far from the reality from the standpoint of open porous structures of fibrous masses. Also, because of the increasing mass of ascending liquid in a vertical sample, the wicking rate is, in fact, a variable and not a constant, as assumed theoretically. Furthermore, this kind of theory is unable to deal with the effects of several fundamental system parameters, including fibre orientation and fibre volume fraction. Therefore, development of a more robust technique is desirable in this field, and the following is such an attempt. A three-dimensional stochastic method, based on the auto-model with Kawasaki dynamics on a cubic lattice, is presented to obtain the shape of a liquid body wicked into a fibrous material with known fibre orientations.

The auto-model used here consists of a rectangular simulation box of size $n_W * n_H * n_L = W \times H \times L$ (width × height × length), subdivided into numerous lattice cells. Each cell is occupied by only one type of media: gas, liquid, or fibre. The cells interact with their neighbours through an energy exchange. A neighbourhood of order, o, of 2 is formed of 26 cells, arranged into a super-cube, surrounding a cell at the centre, as seen in Fig. 14.17. The energy exchange values of C in the Hamiltonian [14.65] depend on the types of interactions.

To make the description concise and the notations appropriate for computer processing, the lattice cells may be located using indices i and j and designated with an entity, such as the random variable value x_i. Indices i and j may vary in the range $i, j \in \{1, 2,\ldots, n\}$, where n is the total number of cells. The variable value x assumes a value of 0 when occupied by a gas, a value of 1 when occupied by a liquid, and a value of 2 when occupied by a fibre. The exchange energies, C, are then symmetrical functions of two variables, i.e. $C(x_i, x_j) = C(x_i, x_j)$. The possible energy values assigned to two interacting cells are shown in Table 14.3.

There are nine possible combinations for pairs of the three variables. However, the allowable combinations reduce to six due to symmetry. Furthermore, as the fibre structure or the fibre cells are immovable during the simulation, the interaction energy value $C(2,2)$ does not play a role in the model and hence is set to 0.

Table 14.3 Interaction energy values $C(x_i, x_j)$ used for the simulation of three-dimensional liquid transport in fibrous materials

Interaction energies in e.u., Liquid transport in fibrous materials	Gas, $X_i = 0$	Liquid, $X_i = 1$	Fibre, $X_i = 2$
Gas, $X_j = 0$	C(0, 0) = –40	C(0, 1) = 5	C(0, 2) = 20
Liquid, $X_j = 1$	C(1, 0) = 5	C(1, 1) = –26	C(1, 2) = –30
Fibre, $X_j = 2$	C(2, 0) = 20	C(2, 1) = –30	C(2, 2) = 0

Generally, systems tend to minimise their total internal energy. This leads to an expectation, that an attractive intercellular interaction corresponds to a low-exchange energy while a repulsive one corresponds to a high-exchange energy. Chosen values of $C(x_i, x_j)$ ensure such interactions by encouraging aggregation of gas and liquid cells. Commonly, the liquid cells will have higher preference than gas cells to adhere to the fibres, due to the assigned interaction energy values, thus reflecting the physics behind spontaneous imbibition of a liquid into a fibrous material. As an assumption, the interaction with the gravitational field is considered significant only for liquid cells; the influence of gravity on the mass of the gas is small enough to be neglected. The presence of gravity is represented by a uniform field C_g. The gravitational potential of a liquid particle of mass m in a cell s_i, located at the h_i-th level of the lattice along the vertical axis H, is mgh_i. With this information, the system Hamiltonian $U(\vec{x})$ may be written as

$$U(\vec{x}) = \sum_{1 \le i \le n} C_g h(x_i) + \sum_{1 \le i < j \le n} C(x_i, x_j) \qquad [14.65]$$

where the first sum applies to liquid cells only, with m having a value of 1 and C_g equivalent to acceleration due to gravity, g. Each couple of cells is counted once in the second sum term of the right-hand side of Eq. [14.65]. It may be recollected, that this Hamiltonian was introduced earlier in Eq. [14.40] while examining auto-models in Section 14.2.4.

A simple cuboid lattice of size $37 \times 300 \times 150$ ($n_W \times n_H \times n_L$), having a total number of cells n of 1 665 000 under free boundary conditions, is conceived for the present simulation. To convey the initial spin cell configuration, it is proper to specify that the first ten bottom layers at $h_i \in \{0, 1, 2,\ldots, 9\}$ are immersed in a liquid pool, with variables, x_i , assigned values of 1, and the rest of the lattice space is filled by gas spins having variable values, x_i, of 0. The direction of a fibre inside the cuboid lattice is determined by a unit vector $\vec{a}$, making angles α and β with the perpendicular axes H and W of the three-dimensional cuboid lattice system, as shown in Fig. 14.30. The orientation of $\vec{a}$ can be chosen up or down the line, determined by the couple of angles (α, β). A vertical cross-section of each fibre consists of one fibre cell only. The entire fibrous mass is, then, simulated through generation of individual random lattice cells, acting as origins of the fibres. Consequently, the vector $\vec{a}$, as described above, is used to generate the fibre directions through a random-number generator related to the angle α and fibre origin, along with a chosen constant value β. Each fibre is defined by an abscissa, having an equal probability in upwards or downwards directions along the vector $\vec{a}$, starting from the fibre origin. The fibre length is equal to 50 lattice units, and the diameter is equal to 1 lattice unit. The total number of fibres is 10 000 (M = 10 000). Fibres thus generated are arranged throughout the cubic lattice and can be considered as chains of cells that are occupied by them (i.e. the

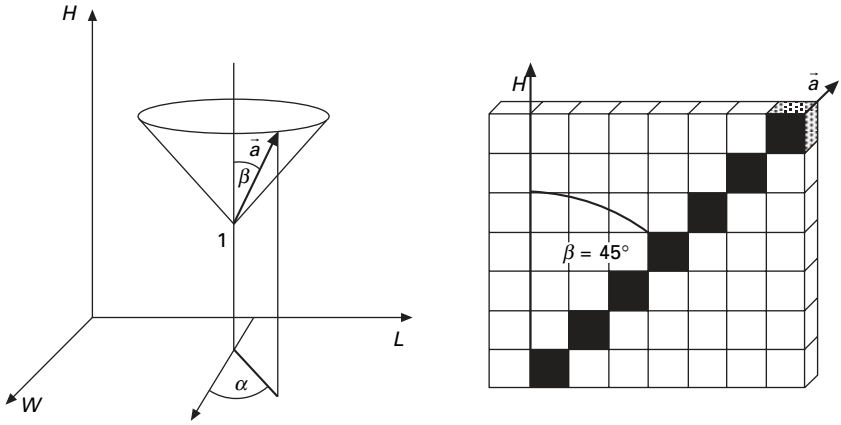

14.30 A fibre system is generated via the location of its origin *o* of a fibre containing a unit vector *a* inside the simulation box $W \times H \times L$. On the right-hand side is a thin section of the simulation box (one cell thick) with a part of a fibre with the deflection angle β =45°.

fibre cells). The average fibre volume density V_f (Wiebel,1979), hence equals the proportion of fibre cells out of the total number of cells, n. Simulations are carried out for $V_f = 0.22$.

After creating the initial configuration, the simulation is carried out following all the steps other than the fifth one of the algorithm, previously described in Section 14.3. This conditional step is substituted with the one stating that as soon as a liquid particle is moved from the initial liquid layer, i.e. $h_i \in \{0, 1, 2, \ldots, 9\}$, its position is always refilled with other liquid particles. This simulates the liquid absorbing from an inexhaustible liquid reservoir.

The described computer simulation model delineates the dynamic behaviour. Apparently, the evolving configurations $\vec{x}_m \rightarrow \vec{x}_{m+1}$ in the algorithm differ only by an exchange of a couple of cells. That is the reason behind a strong correlation between the physical properties of the sequential configurations of the system. This correlation forms the theoretical basis for the application of Kawasaki dynamics in simulating dynamic processes (Manna *et al.*, 1992; Lukkarinen, 1995; Binder, 1997). The dynamic interpretation of the method lies in the association of a time, t, with a subsequent configuration $\vec{x}_m \rightarrow \vec{x}(t)$ in a Markov chain. The time scale is often normalised to a relative unit, during which exchange, trials of n variable values are performed. The time unit is 1 MCSPS, as was introduced in Section 14.3.1.

For the joint probability distribution function, $P(\vec{x}, t)$ at a time t, a configuration $\vec{x}$ occurs in the Monte Carlo process, satisfying the Markovian master equation (Binder, 1997):

$$\frac{dP(\vec{x})}{dt} = -\sum_{\vec{x}} W(\vec{x} \rightarrow \vec{y}) P(\vec{x}, t) + \sum_{\vec{y}} W(\vec{y} \rightarrow \vec{x}) P(\vec{y}, t) \qquad [14.66]$$

In the above equation, the first term on the right-hand side represents all the processes that push the system away from the configuration $\vec{x}$. The second term contains all the reverse events that lead to an enhancement of the joint probability $P(\vec{x})$, corresponding to the configuration $\vec{x}$. In the case of thermal equilibrium, the two sums cancel each other because the system is supposed to fulfil the principle of detailed balance. Therefore, $P_{eq}(\vec{x}, t)/dt = 0$, where $P_{eq}(\vec{x}, t)$ is the steady-state distribution of the master Equation [14.66].

In general, the time associated with the variable exchange procedure cannot be related to the physical time through which a real system evolves. The fact that the time evolution in a real system is governed by a deterministic equation, not by a stochastic master Equation [14.66], accounts for the disparity. But for an Ising-like Hamiltonian [14.65], the stochastic kinetics provided by Eq. [14.66] may be explained physically in terms of a very weak coupling of the spins in a heat bath, which induces random spin exchanges in the system (Binder, 1997).

In the simulation, an initial investigation is done to study the influence of the fibre orientation on the dynamics of liquid wetting and wicking in a fibrous mass. Thereafter, the fibre declination β from the vertical axis H is varied by steps of 10°, so that the simulation is carried out for 11 different fibrous systems with β ranging between the inclusive limits of angles 0° and 90°, in addition to $\beta = 45°$. After each Monte Carlo step per site/cell (MCSPS), the outputs recorded are: the number or the mass m_A of the wicked liquid particles, the liquid particles above the original liquid surface, and the changes of the total system energy U. The simulation is terminated after 600 MCS, and information from each subsequent configuration is preserved for further analysis.

The results of this process are provided in Fig. 14.31, where side views and top views of wetting patterns of cross-sections of the fibrous mass at different values of β are paired. The horizontal cross-sections are all cut at a distance of 100 cells from the liquid surface.

The pictures present two extreme situations. The first one is vertical to the (WL) plane or $\beta = 0°$, where the ascending liquid moves at the highest rate but is mostly scattered. The other one is parallel to the ($W\,L$) plane or $\beta = 90°$, with the lowest wetting rate but the liquid pattern is highly aggregated, as evident from Fig. 14.32(a). From Fig. 14.31, one can intuitively evaluate the volume of the liquid wicked into the fibrous mass. Yet from Fig. 14.32(a), it is clear that, at initial periods (i.e. MCSPS < 200), the absorbed liquid body is generally more voluminous as angle β reduces, because the fibre assemblies with smaller β values apparently start with greater wicking rates as the liquid climbs faster. Nevertheless, such trend in the calculation remains true only for $\beta \geq 20°$, whereas for $\beta < 20°$ the climbing of the liquid stagnates and become independent of the time; the smaller the β value, the earlier the climbing stops. The above discussions reveal that there will be either one or

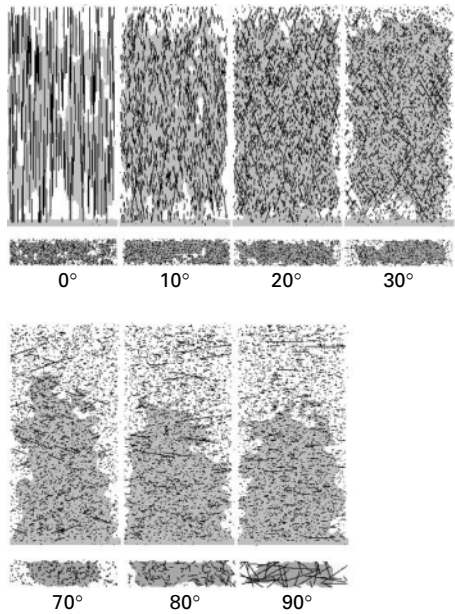

14.31 Wetting patterns from both vertical and horizontal cross-sections of a fibre mass at different orientation angles β after 600 MCSPS (Monte Carlo step per site particle). The fibres in the individual samples have strictly identical declination β. From the left- to the right-hand side, the β values are 0, 10, 20, 30, 70, 80, and 90, as denoted in each sample. Only those fibres that lie in the cross-section plane are depicted in full length with the corresponding declination angle β. The fibre system is uniformly random.

a range of optimal combinations of β and MCSPS at which the fibre mass will absorb a maximum amount of liquid, resulting from an optimal wicking rate and wicking duration, as illustrated in Fig. 14.32(b). It is apparent from the figure that, at a value of β equalling 20°, the greater the MCSPS value, the more the liquid is absorbed into the specimen.

To evaluate the wicking rate K, the time derivation of the wicked liquid mass, dm_A/dt, is plotted against the reciprocal value of the mass $1/m_A$ at different values of β, as given in Fig. 14.33. As mentioned earlier, the value of K may be determined from the slope of the plot. In general, a wicking rate may be defined as $K = tg\alpha$, where α is, presently, the slope of the $dm_A/dt - 1/m_A$ plot.

It is clear from Fig. 14.33 that a fibrous mass with a smaller value of β does yield a higher slope or a greater wicking rate K. However, according to Equation [14.62], when the other parameters are given, the dm_A/dt versus $1/m_A$ characteristic is expected to be linear. The results of the simulation, consistent with experimental practice, demonstrate otherwise. This is clear

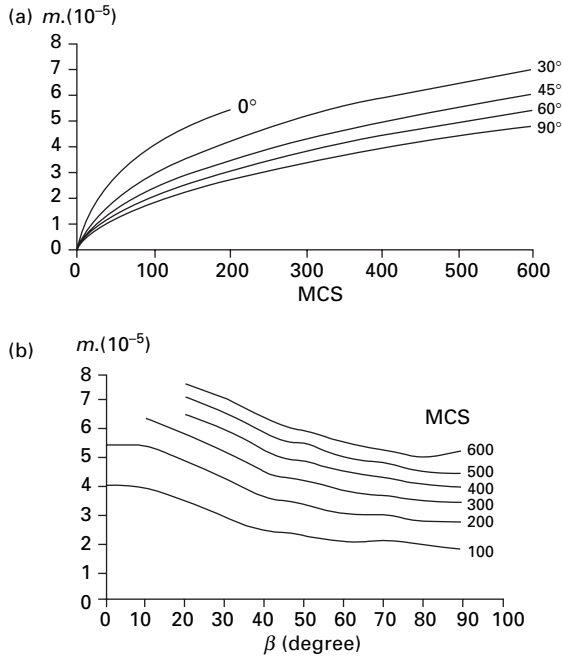

14.32 (a) The dependency of a liquid mass wicked into a specimen on MCS (Monte Carlo step per particle) at different fibre orientation angles β. (b) The dependency of a liquid mass wicked into a specimen on orientation angle β after different MCS values.

from Fig. 14.33. In reality, the rate dm_A/dt cannot maintain a linear relationship as the liquid weight will slow down and eventually stop the wicking process (i.e. the wicking rate dm_A/dt decreases gradually with time until zero). This, on the other hand, provides strong evidence for validating the simulation methodology. A detailed analysis of the relationship between the wicking rate K and the fibre orientation angle β based on the simulated data is summarised in Fig. 14.34. It may be observed that the dependence between the two is also non-linear, showing a rapid decrease of the wicking rate K in the interval $\beta \in \langle 0, 30° \rangle$, while for the rest of the graph, i.e. $\beta > 30°$, there is, rather, a constant or even a slight increase of K.

Computer simulations based on this method, realistically and quantitatively depict the dynamic ascending liquid wicking process. Moreover, a parametric study has been conducted in this article to examine the influences of the important factors involved in the simulation.

The simulated results indicate that the relationship between the fibre orientation β and the generalised wicking rate K is non-linear, and a greater wicking rate K is achieved for the structures with fibre orientation with respect to the axis perpendicular to the original liquid surface, i.e. β smaller than 30°.

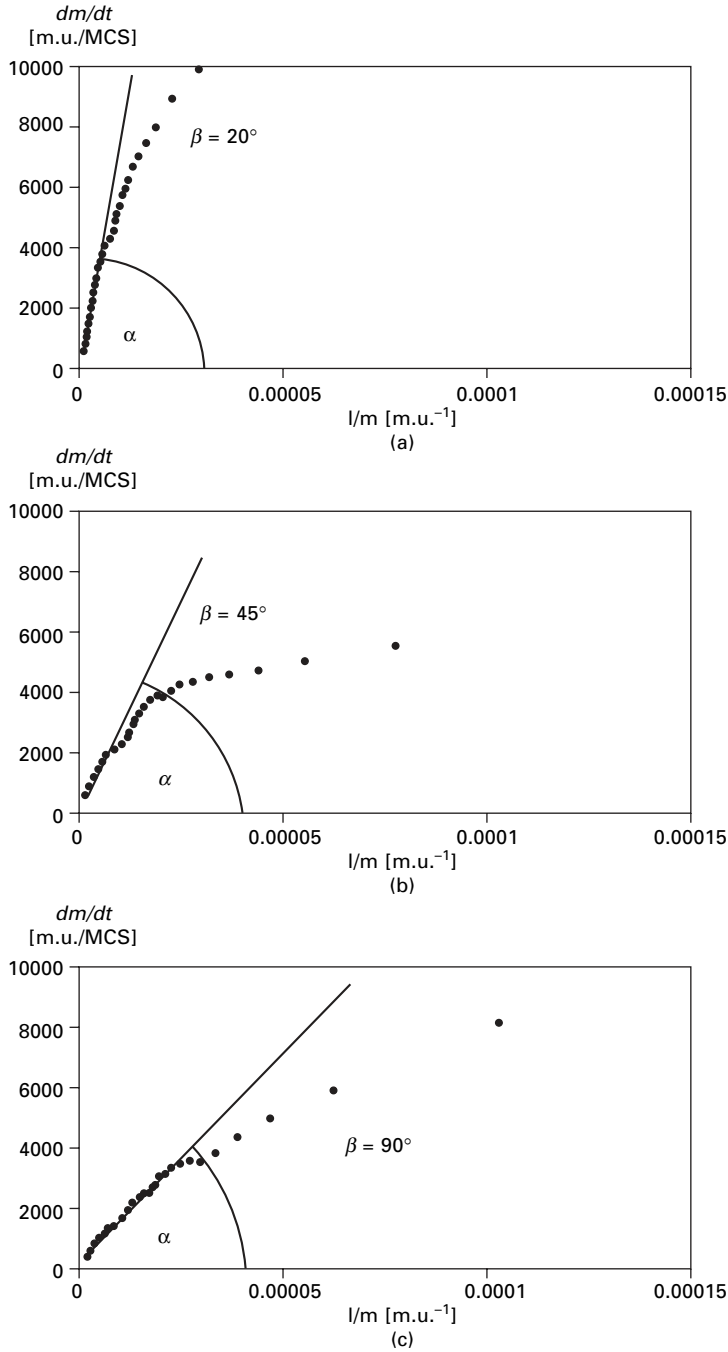

14.33 Time derivation of wicked liquid mass dmA/dt against the reciprocal mass $1/mA$: (a) fibre orientation $\beta = 20°$, (b) fibre orientation $\beta = 45°$, and (c) fibre orientation $\beta = 90°$.

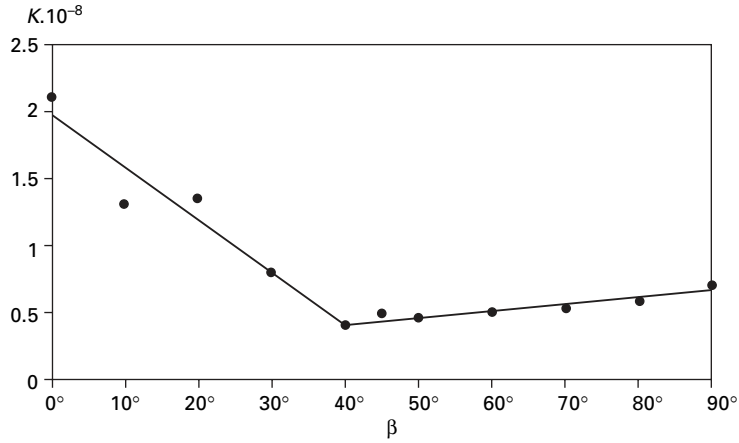

14.34 The generalised wicking rate K versus fibre orientation angle β.

The effects of β on the total liquid absorption are not monotonic; a smaller β leads to a greater wicking rate K or a quicker liquid wicking process, as stated above. The wicking process, however, stagnates as time increases. Although a greater β results in a slower wicking rate, the wicking process can prolong further. An optimal condition can be explored.

Anisotropy of liquid transport in fibrous layers is of great interest for producers of disposable items such as diapers and feminine hygiene products. The liquid distribution in such commodities has to be selective so as to protect consumers against lateral outflow. This is achieved by the so-called acquisition layers, whose function may be controlled by using the wicking rate–fibre orientation relationship.

14.4 Sources of further information and advice

The field of inhomogeneous flows, i.e. flows described in Section 14.3, has been an active area for systematic research since the mid-nineteenth century. The basic theory was the equation of capillarity, given by Young (1972) and De Laplace (1806). One of the earliest works is that of Lamb (1879), dealing with the motion of solids through liquids. In the 1970s, some pioneering works on the dynamics of liquid spreading on solids were published; Huh and Scriven (1971) suggested a singularity in the dissipation for such flows. A useful distinction was revealed between simple fluids, e.g. liquids that were found to spread through a 'rolling motion' (Dussan and Davis, 1974), and polymeric melts, which often tended to slip on a solid surface (Brochard and de Gennes, 1984). More recently, de Gennes (1985) published a review of wetting research.

The first attempt to understand capillary-driven inhomogeneous flows for

practical applications was made by Lucas (1918) and Washburn (1921). Lucas–Washburn theory had been used and developed further for the textile area by few authors. Chatterjee (1985) dealt with these kinds of flows in dyeing. Pillai and Advani (1996) conducted an experimental study of the capillarity-driven flow of viscous liquids across a bank (a container filled by a fibrous mass) of aligned fibres. Hsieh (1995) discussed theories and applications of wetting and capillary principles to analyse liquid wetting and transport in fibrous materials. Several techniques employing fluid flow to characterise the structure of fibrous materials were also presented by Hirt *et al*. (1987). Lukas and Soukupova (1999) carried out data analysis to test the validity of the Lucas–Washburn approach for some fibrous materials.

Inhomogeneous flows have also been studied using stochastic simulation. Manna *et al*. (1992) presented a stochastic simulation that generated the shape of a two-dimensional liquid drop, subjected to gravity, on a wall. The system was based on the modified Ising model, i.e. the auto-model in the context of the present chapter, with Kawasaki dynamics. They located a phase transition between a hanging and a sliding droplet. Lukkarinen (1995) studied mechanisms of a fluid droplet spreading on flat solids and found, that the spreading initially behaved almost linearly with time, and the spreading of the liquid precursor film was dominated by a surface flow on the bulk of a solid. Afterwards, however, such dynamics of spreading depended on the square root of time. A similar study of a fluid droplet spreading on a porous surface was recently reported by Starov *et al*. (2003). The first attempt to simulate the liquid wetting dynamics in fibre structures using the auto-model was done by Lukas *et al*. (1997) and Lukas and Pan (2003) followed by Zhong, Ding and Tang (2001, 2002), although the simulation was restricted to two-dimensional systems only.

EDANA, the European Disposables and Nonwovens Association, and INDA, the International Nonwovens and Disposables Association have formulated tests (ERT Absorption 10.2-96 and IST Absorption 10.1-92) to measure the vertical speed at which liquid moves upwards in a fabric, i.e. the capillarity of the test material.

Gupta (1997) defined absorption rate as the quantity that was characterised by modifying the Lucas–Washburn equation, and then applied it to a flat, thin circular fabric on which fluid diffused radially outwards.

Berg (1989) dealt also with the Lucas and Washburn theory. The theory was actually a special form of the Hagen–Poiseuille law (Landau and Lifschitz, 1988) for laminar viscous flows. It was shown that the Lucas and Washburn equation was valid for a variety of fibrous media, including paper and textile materials (Berg, 1989; Evert *et al*., 1978).

Finally, a brief discussion to compare the Monte Carlo-based simulation of auto-models, and final element analysis may be added. One may also refer to Section 10.5 of Chapter 10 for more information about the relationship

between lattice gas cellular automata and auto-models. The finite element method (Nicholson, 2003), also referred to as finite element analysis, is a computational technique for approximate solutions of boundary value problems, which is preferably used in engineering. A boundary value problem is, generally, a mathematical problem in which one or more dependent variables must satisfy a differential equation everywhere within a known domain of independent variables and should satisfy specific boundary conditions at the boundary of this domain. Depending on the type of physical problem being analysed, the dependent variables may include physical displacement, temperature, heat flux, fluid velocity, and so on. Thus, the basic difference between the auto-model approach and finite element analysis is that auto-models are based on discrete structures, statistical physics and simulated through Monte Carlo algorithms, while finite element analysis is governed by continuum mechanics framed with differential equations. Auto-models are governed totally by Hamiltonians with interaction energies and are not able to reflect easily mass inertial effects. On the other hand, the extremely simple ones involve manifold and complex boundary conditions and can tackle systems composed of fluid mixtures. Finite element methods are much more widespread in application and are employed more frequently as compared to the alternative approach.

14.5 References

Adamson A W and Gast A P (1997), *Physical Chemistry of Surfaces*, John Wiley & Sons, New York.

Aloisi G, Guidelli R, Jackson R A and Barnes P (1987), 'A new method to determine the interfacial tension in Monte Carlo simulations', *Chemical Physics Letters*, **133**, 343–345.

Berg J C (1989), 'The use of single-fibre wetting measurements in the assessment of absorbency', *Nonwovens Advanced Tutorial*, edited by F. T. Albin and L.V. Tyrone. Atlanta, GA: TAPPI Press.

Besag J E (1972) 'Nearest neighbour systems and the auto-logistic model for binary data', *J. R. Statist. Soc. B*, **34**, 75–83.

Besag J (1974), 'Spatial interaction and statistical analysis of lattice systems', *J. R. Statist. Soc. B*, **36**, 192–236.

Binder K and Heermenn D W (1997), *Monte Carlo Simulation in Statistical Physics; An Introduction*, Berlin, Heidelberg, New York, Springer Verlag.

Binder K (1986), *Monte Carlo Methods in Statistical Physics*, *Topics Curr. Phys*., Berlin Heidelberg, Springer Verlag.

Brochard F and de Gennes P G (1984), 'Spreading laws for liquid polymer droplets – interpretation of the foot', *Journal de Physique (Paris) Lettres,* **45**, L597–L602.

Brush S (1967), 'History of the Lenz–Ising model', *Review of Modern Physics*, **39**, 883–893.

Chatterjee, P K (1985) *Absorbency*. Amsterdam: Elsevier.

Chen C C and Dubes R C (1989), 'Experiments in fitting discrete Markov random fields to textures', *CVPR'89 IEEE Computer Society Conference on Computer Vision and Pattern Recognition*, San Diego, IEEE Comput. Soc. Press.

Cochran W G (1936), 'The statistical analysis of the distribution of field counts of diseased plants', *J. R. Statist. Soc. Suppl*., **3**, 49–67.

Cox D R (1970), *Analysis of Binary Data*, London, Meuthen.

Cross G C and Jain A K (1983), 'Markov random field texture models', *IEEE Trasactions on Pattern Analysis and Machine Intelligence*, **5**, 25–39.

Derin H and Elliott H (1987), ' Modelling and segmentation of noisy textured images using Gibbs random fields', *IEEE Transactions on Pattern Analysis and Machine Intelligence*, Vol. PAMI–9(1), 39–55.

Dobrushin R L, Kryukov V I and Toom A L (1978), 'Locally interacting systems and their applications in biology', *Lecture Notes in Mathematics*, 653.

Dubes R C and Jain A K (1989), 'Random field models in image analysis', *Journal of Applied Statistics*, **16**(2), 131–164.

Dussan V E and Davis S (1974) 'On the motion of a fluid–fluid interface along a solid surface', *Journal of Fluid Mechanics*, **65**, 71–95.

de Gennes P G (1985), 'Wetting: statics and dynamics, *Reviews of Modern Physics,* **57**(3, pt. 1), 826–863.

de Gennes P-G, Wyart-Brochard F and Quere D (2003), *Capillarity and Wetting Phenomena; Drops, Bubbles, Pearls, Waves*, New York, Berlin, Springer-Verlag.

De Laplace P S (1806), *Mechanique Celeste*. Supplement to Book 10. Paris, Durat.

Ermakov S M and Nekrutkin V V (1989), *Random Processes for Classical Equations of Mathematical Physics*, Dordrecht, Boston, London, Kluwer Academic Publishers.

Everet D H, Haynes J M and Miller R J (1978), 'Kinetics of capillarity imbibition by fibrous materials' *Fibre–Water Interactions in Papermaking*, edited by the Fundamental Research Committee. London, Clowes.

Ford L R (1933), *Differential Equations,* NewYork, McGraw-Hill.

Fricot J (1985), *'Champs aleatoires de renouvellement'*, thesis, University of Grenoble

Geman S and Geman D (1984), 'Stochastic relaxation, Gibbs distributions, and the Bayesian restoration of images', *IEEE Transaction of Pattern Analysis and Machine Intelligence*, **6**(6), 721–741.

Geman D (1991), 'Random fields and inverse problems in imaging', *Lecture Notes in Mathematics*, **1427**, 113–193.

Glauber R J (1963), 'Time development statistics of the Ising model', *J. Math. Phys.*, **4**, 294–307.

Gupta B S (1997), 'Some recent studies of absorbency in fibrous nonwovens', *XXV International Nonwovens Colloquium*, Brno, Czech Republic.

Hammersley J M and Clifford P (1971), Markov fields on finite graphs and lattices (unpublished).

Hentschel, H G E (1994), *Encyclopaedia of Applied Physics: Inhomogeneous Flows*. Vol. 11. New York, VCH Publishers.

Hirt D G, Adams K L, Prud'Hommer R K and Rebenfeld L (1987), 'In-plane radial fluid flow characterization of fibrous materials', *Journal of Thermal Insulation*, **10**, 153–172.

Hsieh Y L (1995), 'Liquid transport in fibrous assemblies', *Textile Research Journal,* **65**, 299–307.

Huh C and Scriven L E (1971), 'Hydrodynamic model of steady movement of a solid/liquid/fluid contact line', *Journal of Colloid and Interface Science,* **35**, 85–101.

Ising E (1925), 'Beitrag zur Theorie des Ferromagnetismus', *Z. fur Phys.*, **31**, 253–58.

Kawasaki K (1972), *Phase Transitions and Critical Phenomena*, ed. By C. Domb and M.S. Green, 5b(2), New York, Academic.

Kittel C (1980), *Thermal Physics*, San Fransisco, W.H. Freeman.
Korolyuk V and Swishchuk A (1995), *Semi-Markov Random Evolutions*, Dordrecht, Boston, London, Kluwer Academic Publishers.
Lamb H (1945) [1879], *Hydrodynamics*. Reprint, NewYork: Dover.
Landau L D and Lifshitz E M (1988), *Theoretical Physics: Vol. 6. Hydrodynamics*, Moscow, Nauka.
Lenz W (1920), 'Baitrag zur Verstandnis der magnetischen Erscheinung in festen Korpern', *Z. fur Phys.*, 21, 613–15.
Liggett T M (1985), *Interacting Particles Systems*, Berlin, New York, Springer Verlag.
Lucas R (1918), 'Uber das Zeitgesetz des kapillaren Aufsteigs von Fussigkeiten', *Kolloidn Zhurnal,* **23**, 15–22.
Lukas D, Glazirina E and Pan N (1997), 'Computer simulation of liquid wetting dznamics in fibre structures using the Ising model', *Journal of the Textile Institute,* **88**, 149–161.
Lukas D and Soukupova V (1999), 'Recent studies of fibrous material wetting dynamics', *INDEX 99 Congress*, Geneva, Switzerland.
Lukas D and Pan N (2003), 'Wetting of a fibre bundle in fibrous structures', *Polymer Composites,* **24**, 314–322.
Lukas D and Chaloupek J (2003a), 'Wetting between parallel fibres; column-unduloid and column disintegration transitions', *Journal of Engineering in Medicine*, **217**, 273–277.
Lukas D, Pan N, Soukupova V and Parikh D V (2004), 'Computer simulation of 3/D liquid transport in fibrous materials', *SIMULATION*, **80**, 547–557.
Lukkarinen A (1995), 'Mechanisms of fluid spreading: Ising model simulations', *Physical Review E: Statistical Physics, Plasma, Fluids, and Related Interdisciplinary Topics,* **51**, 2199–2202.
Manna S S, Herrmann H J and Landau D P (1992), 'A stochastic method to determine a shape of a drop on a wall, *Statistical Physics*, **66**, 1155–1163.
Meister B J and Scheele G F (1967), 'Generalized Solution of the Tomotika Stability Analysis for a Cylindrical Jet', *AICHE J.*, **13**, 682.
Metropolis N, Rosenbluth A W, Rosenbluth M N, Teller A and Teller E (1953), 'Equation of state calculation by fast computing machines', *Journal of Chemical Physics,* **21**, 1087–1092.
Miller B and Jansen S H (1982), 'Wicking of liquid in nonwoven fibre assemblies: Advances in nonwoven technology', *10th Technical Symposium*, New York, 216–226.
Moussouris J (1973), 'Gibbs and Markov random systems with constraints', *Journal of Statistical Physics*, **10**(1), 11–33.
Neimark A V (1999), 'Thermodynamic equilibrium and stability of liquid films and droplets on fibres', *J. Adhesion Sci. Technol.,* **13**, 1137–1154.
Nicholson D W (2003), *Finite Element Analysis: Thermodynamics of Solids*, London, New York, CRC Press.
Paget R D (1999), '*Nonparametric Markov random field models for natural texture images'*, Doctoral thesis, Queensland, Australia, The University of Queensland.
Pillai K M and Advani S G (1996), 'Wicking across a fibre-bank, *Journal of Colloid and Interface Science*, **183**, 100–110.
Plateau J (1873), *Statique Experimentale et Theoretique des Liquids Soumis aux Seriles Forces Molecularies*, Paris, Gauthier-Villars.
Preston C (1976), 'Random fields', *Lecture Notes in Mathematics*, 534.
Princen H M (1969), 'Capillary phenomena in assemblies of parallel cylinders: Capillary rise between two cylinders', *J. Colloid Interface Sci.*, **30**, 69–75.

Princen H M (1969a), 'Capillary phenomena in assemblies of parallel cylinders: II. Capillary rise in systems with more than two cylinders', *J. Colloid Interface Sci*., **30**, 359–371.

Princen H M (1970), 'Capillary phenomena in assemblies of parallel cylinders: III. Liquid columns between horizontal parallel cylinders, *J. Colloid Interface Sci*., **34**, 171–184.

Prum B and Fort J C (1991), *Stochastic Processes on a Lattice and Gibbs Measures*, Dordrecht, Boston, London, Kluwer Academic Publishers.

Rayleigh L (1878), On the Instability of Jets, *Proc. London Math. Soc*., **10**(4).

Roe R-J (1957), 'Wetting of fine wires and films by a liquid film', *Journal of Colloid and Interface Science*, **50**, 70–79.

Rowlinson J S (2002), *Cohesion, A Scientific History of Intermolecular Forces*, Cambridge University Press.

Ruelle D (1969), *Statistical Mechanics; Rigorous Results*, New York, Benjamin.

Seymour L (1993), *'Parameter Estimation and Model Selection in Image Analysis Using Gibbs-Markov Random Fields'*, PhD thesis, The University of Carolina, Chapel Hill.

Spitzer F (1971) 'Markov random fields and Gibbs ensembles', *Amer. Math. Monthly.*, **78**, 142–154.

Starov V M, Zhdannov S A, Kosvinstev S R, Sobolev V D and Velarde M G (2003), 'Effect of interfacial phenomena on dewetting in dropwise condensation', *Advances in Colloid and Interface Science*, **104**, 123–190.

Swishchuk A (1997), *Random Evolutions and Their Applications*, Dordrecht, Boston, London, Kluwer Academic Publishers.

Tomotika S (1935), 'On the instability of a cylindrical thread of a viscous liquid surrounded by another viscous fluid', *Proc. Roy. Soc*., A **150**, 322–337.

van Kampen N G (1992), *Stochastic Processes in Physics and Chemistry*, Amsterdam, New York, North-Holland.

Washburn E W (1921), 'The dynamics of capillary flow', *Physical Review,* **17**, 273–283.

White C F (2001), 'Driving innovation', *Nonwovens Report International*, November, 368, 8.

White P (1963), 'Stochastic processes in several dimensions', *Bull. Int. Statist. Inst.*, **40**, 974–994.

Young T (1972), *Miscellaneous Works. Vol. 1*. Edited by G. Peacock. NewYork: Johnson Reprint Corporation.

Zhong W, Ding X and Tang Z L (2001), 'Modeling and analyzing liquid wetting in fibrous assemblies', *Textile Research Journal,* **71**, 762–766.

Zhong W, Ding X and Tang Y L (2002), 'Analysis of fluid flow through fibrous structures', *Textile Research Journal,* **72**, 751–755.

15

Computational modeling of clothing performance

P. GIBSON, U.S. Army Soldier Systems Center, USA
J. BARRY and R. HILL, Creare Inc., USA
P. BRASSER, TNO Prins Maurits Laboratory, The Netherlands, M. SOBERA and C. KLEIJN, Delft University of Technology, The Netherlands

15.1 Introduction

Protective clothing provides laboratory and hazardous materials workers, fire fighters, military personnel, and others with the means to control their exposure to chemicals, biological materials, and heat sources. Depending on the specific application, the textile materials used in protective clothing must provide high performance in a number of areas, including impermeability to hazardous chemicals, breathability, light weight, low cost, and ruggedness. Models based on computational fluid dynamics (CFD) have been developed to predict the performance of protective clothing materials. Such models complement testing by enabling property data from laboratory material testing to be used in predictions of integrated multilayer garments under varying environmental conditions.

Advances in computational fluid dynamics (CFD) have made it possible to create accurate engineering models which can include the irregular shapes of a clothed human, as well as the extremely different length and time scales present in a typical computation (e.g. thin clothing layers over a relatively large human body and irregular air spaces). Body-fitted coordinates or unstructured grids are used to model shapes such as a clothed human arm covered by a permeable clothing layer, or simpler geometries such as a fabric-covered cylinder. This capability can help to design more comfortable and effective protective clothing. Modern chemical protective garments provide high levels of protection against battlefield chemical threats, but also cause debilitating heat stress under certain environmental conditions. Accurate modeling and analysis techniques for heat and mass transfer aid in designing more comfortable protective clothing systems.

Air flow, heat transfer, and mass transfer through clothing can be studied on different scales: (i) macroscale of the whole human body in protective clothing, (ii) mesoscale of a single limb covered by clothing material and (iii) microscale, focusing on transport phenomena in the clothing material at the scale of individual fibers. Clothing material properties are important at

all of these scales. Transport through the clothing system involves diffusion of heat and moisture, convective airflow, and liquid water capillary wicking. Hygroscopic fibers absorb water in vapor or liquid form and release the heat of sorption within the clothing. Water can condense or evaporate in outer layers of clothing. Many modern protective clothing systems include polymeric membranes, which may be a microporous hydrophobic polymer or a very thin solid layer of a hydrophilic polymer. Modeling the sorption of liquid water or vapor into the membrane, diffusion through the structure, and desorption from the other side, are complicated by the polymer's concentration-dependent permeation properties. Nearly all transport phenomena in clothing systems are time dependent. Equilibrium does not take place within a matter of seconds, but may require time scales of minutes to hours. Since humans rarely work at a sustained constant level for hours on end, the use of steady-state approximations to determine quantities such as total moisture accumulation within the clothing, or total heat and mass transferred through the clothing, are often inaccurate. Steady-state heat and mass transfer properties do not describe the true situation. With the appropriate assumptions, CFD is useful at both the material and system level in clothing design. CFD provides a framework to model the diffusive and convective transport of heat and gases/vapors; capillary transport of liquids; vapor and liquid sorption phenomena and phase change; and the variable properties of the various clothing layers. It can also model the effects of sweating and humidity transport on the thermal stress imposed upon the wearer of the clothing.

15.2 Material modeling

A porous material may be described as a mixture of a solid phase, a liquid phase, and a gaseous phase (Fig. 15.1(a)). In protective clothing the solid phase consists of several materials (usually polymers and carbonaceous adsorbents), plus any bound liquid absorbed in the solid matrix, or on the surface of a solid absorbent (such as activated carbon). Hence, the solid phase density is dependent on the amount of liquid contained in the solid phase. Solid polymer layers, such those present in laminates and membranes, are treated by assuming the gas phase volume fraction for that layer is zero.

The liquid phase consists of the free liquid that may exist within the porous medium. The liquid phase is a pure component, and its density is assumed to be constant. In protective clothing, the liquid phases are liquid water (sweat or rain) and liquid chemical agents.

The gaseous phase consists of vapor plus the non-condensable gas (e.g. air). The gas phase density is a function of temperature, pressure, and vapor concentration.

The general governing equations for energy, mass, and momentum transport

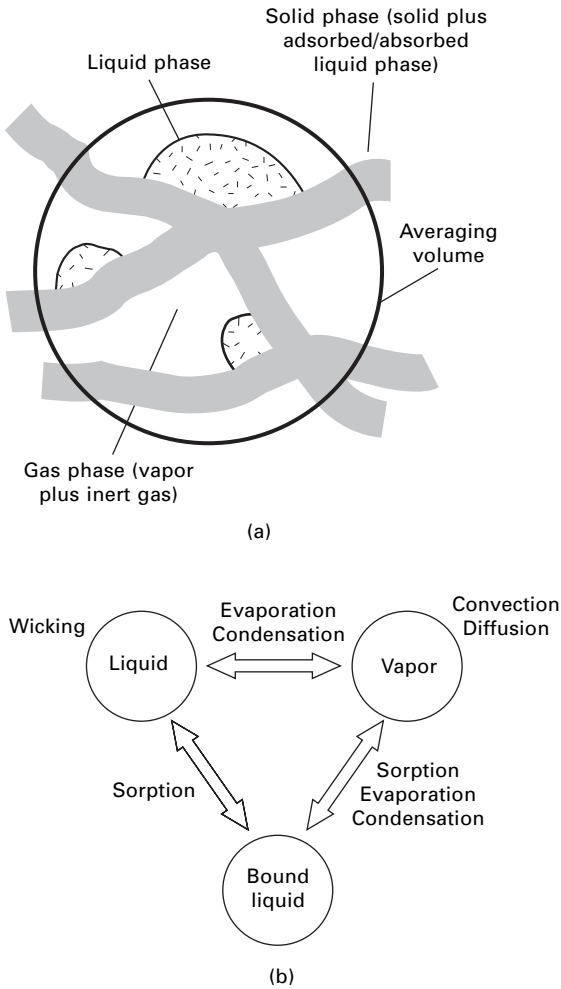

15.1 (a) Material model and (b) Mass transport interactions.

in porous media are obtained by volume-averaging techniques,[1,2] using definitions for intrinsic phase average, phase average, and spatial average for porous media given by Whitaker.[3,4] Material models must account for vapor phase transport (convection and diffusion), liquid phase transport (wicking), heat transfer (convection, conduction, and radiation), liquid evaporation and condensation, and sorption/diffusion of vapor and liquid through the solid phase (Fig. 15.1(b)). Complications due to variable porosity caused by swelling or shrinkage of the porous matrix are accounted for by various source terms in the transport equations.

15.3 Material modeling example

The system of governing equations may be solved to simulate the case of transient diffusion/sorption. Heat is released as water vapor diffuses through and is absorbed by a bed of hygroscopic fibers. The heat released can be physiologically significant for clothing layers incorporating hygroscopic fibers such as cotton or wool, or polymer membranes such as polyurethane, which are often components in protective clothing systems. This sorption process can also buffer the effect of rapid changes in environmental humidity. CFD methods have been used to model this transient sorption process for a variety of hygroscopic clothing materials,[5] and an example is given as follows.

Experimental results for the transient diffusion/sorption case were obtained using two layers of fabric instrumented with three thermocouples sandwiched between the two layers, to record temperature changes as the fibers absorb or desorb water vapor from a gas stream flowing on the two sides of the fabrics. The sample was initially equilibrated with a dry gas flow on both sides under constant nitrogen flow. The relative humidity was then changed to 100% on both sides, and the temperature rise and fall due to vapor sorption was recorded as a benchmark for the computer simulations. Figure 15.2 shows the computed temperatures and the experimentally measured temperatures of three fabrics as a function of time. The numerical results match the experimental results, illustrating that the coupled diffusion of heat and moisture in hygroscopic materials can be successfully modeled using these computational techniques.

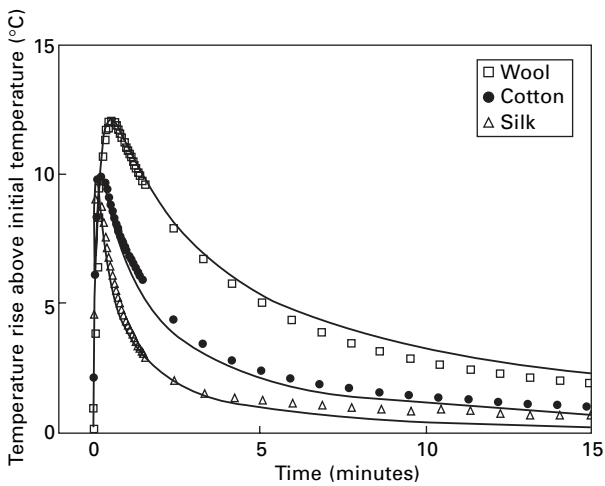

15.2 Numerical (solid lines) and experimentally measured (symbols) temperature transients for hygroscopic fabrics subjected to a step change in relative humidity.

15.4 Modeling of fabric-covered cylinders

Fabric-covered cylinders provide a convenient geometry to study some of the system-level effects important for clothing systems. The effects of variable air spacing between fabric layers, or between the fabric and the human skin surface, can be important in determining how much heat and mass is transferred into or out of the clothing. In many cases, approximating the human body as an assemblage of fabric-covered cylinders provides sufficiently accurate results for engineering purposes. In general, an external air flow due to wind or body motion impinges on the clothed human, and some air flows around the body, while some air penetrates through the clothing system and into the gap between the clothing and body. This is illustrated in Fig. 15.3, which is a typical CFD simulation of flow over a cylinder covered by a permeable fabric. For a given external air velocity, the amount of air which flows around the body, and the amount which penetrates through the clothing layer is determined by the air-flow resistance (air permeability) of the clothing layer. Materials with a low air-flow resistance allow a relatively high flow-rate through the fabric, with a correspondingly low pressure drop. Materials with a high air-flow resistance allow less flow through the fabric, and have a higher pressure drop across the fabric layer (up to the limit of the stagnation pressure for the particular environmental flow conditions).

The simple flow geometry shown in Fig. 15.3 is useful for answering some very basic questions about the interaction of the different transport properties characterized individually by laboratory test methods, but which all operate simultaneously in a clothing system. For example, protective clothing systems can be designed to protect from aerosol particles present in the environment. But clothing aerosol barrier performance cannot be measured in the same way as industrial filters are evaluated. Aerosol particle filters are

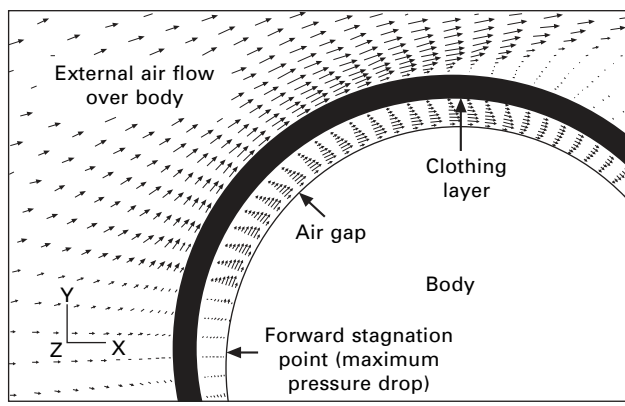

15.3 Flow conditions for a fabric-covered body.

commonly placed in systems that have a well-defined flow rate or pressure drop across the filter material. In clothing systems, however, the aerosol barrier is incorporated into a clothing system covering the human body, and the actual flow rates and pressure drops for a particular set of conditions are dependent on the air-flow resistance properties of the fabric layer itself.

For a truly valid comparison between aerosol barrier materials which differ in their air permeability properties, it would be desirable to test at a unique volumetric flow rate/filter velocity and pressure drop which corresponds to that produced by a given external air velocity on a typical clothing system. A simple cylinder model is useful in defining a reasonable set of laboratory test conditions for comparing different material candidates for new protective clothing systems.[6–11]

Similar questions arise for interactions between the convective properties of air permeability, or convective air flow resistance, and the diffusive property of thermal conductivity/thermal resistance. Laboratory evaluations of individual transport properties yield a variety of material responses due to a wide range of thermal resistance and air permeability properties. A CFD simulation of the performance of the materials in the fabric-covered cylinder geometry can help to determine how the total heat and mass transfer coefficients are influenced by a particular combination of fabric properties.

An illustration of typical CFD modeling results for fabric-covered cylinders is shown in Fig. 15.4. A body-fitted mesh is created for a cylindrical geometry. A thermal insulation layer, and an air space, is placed around the cylinder. The air-flow resistance property of the insulation layer is varied (while keeping thermal insulation constant). In this particular case the cylinder diameter was 0.187 m (corresponding to the diameter of a human thigh), and the air

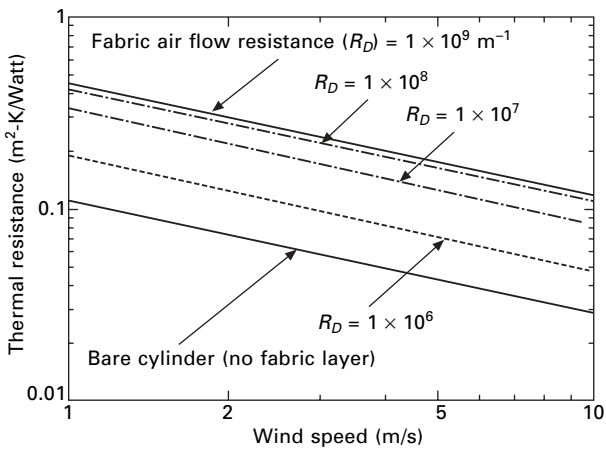

15.4 Overall heat transfer resistance of fabric-covered cylinders in cross-flow conditions at various wind speeds.

space between the fabric and the cylinder surface was 0.01 m. The cylinder surface temperature was 35 °C (nominal human skin temperature) and the air temperature was 5 °C. Simulations were carried out over a range of air-flow velocities from 1 to 40 m/s, although only the results up to 10 m/s are shown in Fig 15.4. The curve for the bare cylinder case in this figure agrees with heat transfer correlation experiments for gas flow over heated cylinders. Figure 15.4 shows that the effect of fabric air flow resistance on heat transfer is non-linear in nature; above a certain value of resistance, the fabric-covered cylinder behaves like a solid cylinder, with little air penetration of the system. These types of simulations are useful in efforts to design the proper mix of fabric transport properties to maximize comfort while still providing adequate protection from the environment, and from chemical/biological warfare agents.

These modeling techniques were applied to commercially available knit fleece layers that were under consideration for cold-weather applications. Considerable effort is expended to develop clothing that is 'breathable' to sweat vapor, yet that will also retain heat even in windy conditions. Modeling simulations were carried out for a variety of new insulating fleece fabrics produced for the outdoor clothing market that address the need for materials which breathe well, but which also keep out enough wind in cold conditions to keep people warm. These fabrics are becoming available in a wide variety of material properties, and it is difficult to rank or evaluate them based on material properties alone. CFD modeling of the behavior of these materials in a simple clothing analog of a fabric-covered cylinder can be helpful in distinguishing significant differences between some of these fabrics.

Thermal resistance, water vapor diffusion resistance, and air permeability were determined on flat samples using laboratory test methods. The material properties were then input into a CFD model of a fabric-covered cylinder, with an air space, under conditions of several different wind speeds. The CFD model provides the ability to go directly from laboratory tests of material properties to a system simulation that approximates real-world conditions. An example comparison for three of the fabrics is shown in Fig. 15.5.

The baseline bare cylinder results are essentially the cooling effect and evaporative heat loss due to 'wind chill.' The presence of a clothing layer modifies the wind chill effect significantly, depending on the air permeability, thermal resistance, and water vapor diffusion resistance of the clothing layer, and the air space between the cylinder surface and the clothing layer. The air permeability of the fabric layer was found to be the most significant parameter affecting the performance of the various materials evaluated. Differences in thermal resistance that seemed important under the stagnant test conditions present in the laboratory tests were much less significant when the materials were compared under moderate wind speeds which produced significant air flow through the model fabric-covered cylinder system.

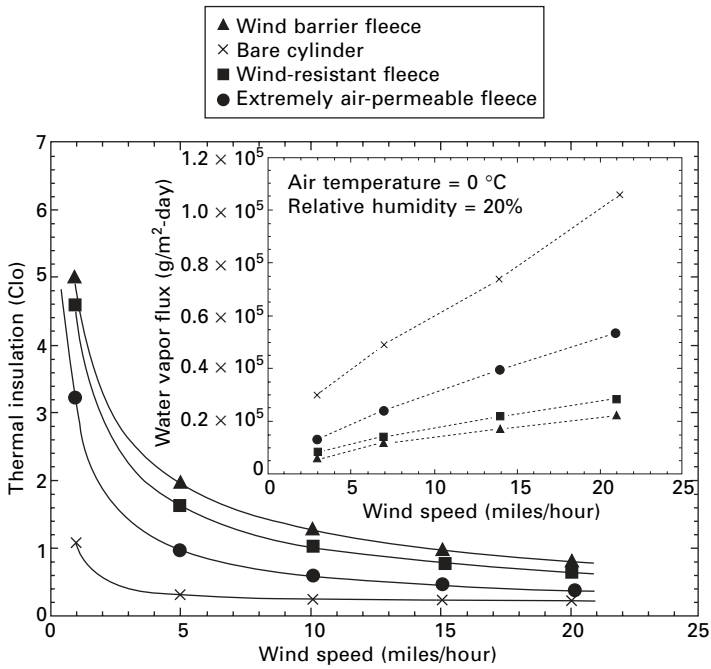

15.5 Comparison of heat transfer and water vapor flux for three varieties of insulating fleece.

Of equal importance for military protective clothing systems is the transport of chemical and biological warfare agents into a clothing system. The cylinder model is useful as a starting point for looking at the importance of a property such as fabric air flow resistance on the performance of a particular protective clothing system design.

More systematic studies of flow around fabric-covered cylinders use sophisticated turbulence models incorporating vortex shedding in the wake of the cylinder.[12,13] Experimental measurements conducted in parallel with CFD computations developed single correlations which predict heat and mass transfer properties based on nondimensional scaling relations between fluid flow rate, fabric air-flow resistance, and the inner gap between the fabric and the cylinder surface. Scaling rules have been deduced as a function of the Reynolds number, the Darcy number and the Damkohler number, representing the wind speed, clothing permeability, and adsorptivity of poisonous trace gases, respectively. The range of values of the studied parameters was based on applications in heat and mass transfer to a clothed human limb in outdoor wind. For a wide range of conditions, air was found to penetrate the outer porous cylinder in the upstream region, down to an angle of approximately 50 degrees from the front stagnation point. In this region, heat and mass transfer are high. Further downstream, heat and mass

transfer are dictated by conduction/diffusion through the air layer in-between the two cylinders. For large Reynolds numbers and high fabric air permeability, the flow easily penetrates the porous sheath and heat transfer approaches that of a bare cylinder. For low Reynolds numbers, on the other hand, the boundary layer around the pair of concentric cylinders becomes very thick and limiting for heat transfer, and again heat transfer approaches that of a bare cylinder. The dimensionless parameters for heat transfer and mass transfer can be summarized in a single correlation under a wide range of conditions. Within its range of validity, this correlation is accurate within 5%, compared to the numerical simulations.

A battlefield hazard for the soldier is the presence of droplets of liquid chemical agents that have contaminated the outer surfaces of protective clothing. These droplets evaporate and the vapor can diffuse into the clothing system. The droplets can also be carried into the clothing system by convective air flow due to body motion or an external wind.

Figure 15.6 is an example of a CFD simulation of a liquid droplet placed onto the outer surface of the fabric-covered cylinder model. All fabric properties are constant with the exception of the fabric air flow resistance. What is interesting about this particular example is that the fabric with the highest air flow resistance does not produce the lowest total exposure to the chemical vapor. The fabric with low air-flow resistance provides a standoff of the

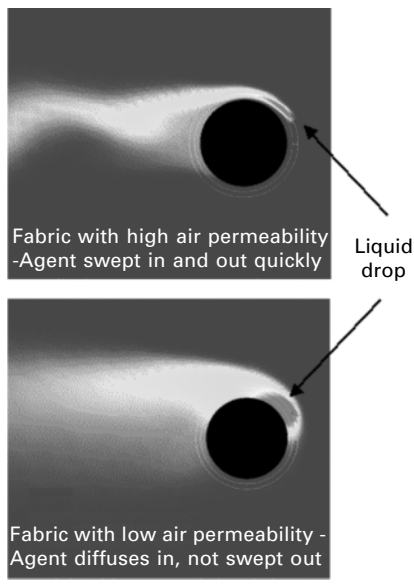

15.6 CFD simulation of liquid droplet evaporating on outside surface of an air-permeable fabric layer covering a cylinder (shade contours refer to vapor concentration, scale not shown).

droplet from the cylinder surface, while the ventilating air flow carries vapor quickly through the system and away from the cylinder. For the case of the fabric with a high air-flow resistance, the total vapor exposure is higher. This is due to the fact that, although there is little convective flow into the air space under the fabric layer, the vapor is able to diffuse through the clothing and build up to higher concentrations. In this case there is no ventilating air flow to sweep the vapor out of the system, and the total exposure to the vapor is much higher than for the well-ventilated system.

Modeling fabric properties in this simple cylindrical geometry provides much of the information required for system-level decisions about various transport property trade-offs between different material candidates for protective clothing materials. However, there are some situations, particularly those having to do with body movement and motion, as well as interfaces and closures between different clothing system components, where more detailed models are desirable.

A variety of geometric parameters affect the transport of agent vapor from a liquid surface drop.[14,15] These parameters include orientation of the drop relative to the flow direction, gap size between the cylinder and the clothing layer, non-uniform gap size, and multiple clothing layers. The variation in parameters was assessed at two imposed wind speeds: 5 and 20 mph.

Figure 15.7 shows the base geometry assumed for these two-dimensional transient simulations. The model is that of a cross-section of a 10 cm diameter

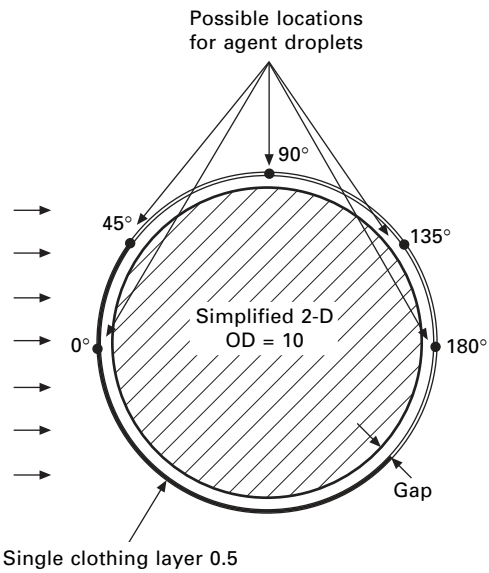

15.7 Schematic of base geometry for two-dimensional simulations of evaporating surface agent (with droplet locations shown).

arm covered with a single 0.5 mm thick clothing layer having a 1.1 cm gap between the surface of the arm and the clothing layer. Fabric permeability was assumed to be a cotton shell (permeability approximately 2.4×10^{-12} m^2). Vapor properties correspond to GB (Sarin) (molecular weight of 140.1 kg/kg mol, vapor pressure of 2.9 mm Hg, and vapor diffusivity of 7.5×10^{-6} m^2/s). The transient simulations were performed with a time step chosen to resolve the shedding frequency of the vortex street for flow over a circular cylinder.

The following sets of geometric parameters were considered:

(i) Base geometry with an incident wind direction of 0°, 45°, 90°, 135°, and 180° relative to the droplet. A condition of 0° corresponds to the droplet located at stagnation point.
(ii) Wind direction at 0° relative to droplet with single clothing layer having uniform gap spacing of 0.2, 0.6, 1.1, and 2.1 cm.
(iii) Wind direction at 0° relative to the droplet with single clothing layer eccentric to the arm with non-uniform gap spacing of 4.1:1, and 6.8:1 (maximum/minimum of 1.767 cm/0.433 cm and 1.918 cm/0.282 cm, respectively with minimum thickness located at the stagnation point).
(iv) Wind direction at 0° relative to the droplet with two clothing layers having uniform gap spacing. First case: inner surface of inner and outer layers located 0.55 cm and 1.1 cm from arm surface, respectively. Second case: inner surface of inner and outer layers located 1.1 cm and 2.1 cm from arm surface, respectively.

All simulations were run until they reached a stationary oscillatory state in which the solution variables varied with time around a constant asymptotic mean (physical times of approximately 80 seconds and 20 seconds for 5 mph and 20 mph, respectively). Once this condition was reached, the agent concentration was assessed at the arm to determine the maximum concentration (mg/cm^3) as a function of time. The area-averaged concentration over the arm surface as a function of time was also computed. For the conditions under consideration here, the amplitudes of the time varying concentrations at the arm were typically small relative to the time average values once the stationary state was reached.

Table 15.1 provides a summary of the maximum and area averaged agent concentrations observed at the surface of the arm for these simulations. Note that the saturation concentration imposed at the droplet is 2.19×10^4 mg/m^3. The trends are generally consistent with expectations.

Droplets located at the stagnation point produce higher exposure than when located at other angles relative to the wind direction. For the 5 mph wind speed, maximum and average concentrations are the same order of magnitude for all orientations. The lowest maximum is observed for the 45° orientation with an increase in maximum concentration as the droplet is

Table 15.1 Summary of maximum and area average agent concentration (mg/m^3) at the arm surface for various 2-D arm cases

Simulation	Case	5 Mph		20 Mph	
		Maximum	Average	Maximum	Average
Droplet orientation	0°	9386	1769	12 850	5379
	45°	3238	545	135	29
	90°	3778	449	101	15
	135°	4914	542	69	6
	180°	5641	519	51	3
Non-uniform gap width	4:1:1 offset	14 428	1582	16 058	4899
	6:8:1 offset	16 900	1512	17 925	4679
Uniform gap width	0.2 cm gap	16 867	1200	14 814	3339
	0.6 cm gap	11 867	1464	13 871	4601
	1.1 cm gap	9379	1765	12 842	5374
	2.1 cm gap	7417	2173	11 626	6243
Multiple clothing layers	1.1 cm and 0.55 cm	8787	1357	11 816	4299
	2.1 cm and 1.1 cm	6735	1512	10 858	5014

moved around to the back of the arm (180°). The average concentration is similar for all orientations other than the stagnation point droplet location, indicating that diffusion of agent from the droplet location is of primary importance for these wind and fabric conditions. For the 20 mph wind speed, the maximum and average concentrations are several orders of magnitude higher for the stagnation point location, with asymptotically decreasing concentrations as the droplet is moved away from this location. For the fabric conditions considered here, the higher velocity increases exposure for stagnation point conditions, but assists in sweeping agent away when the droplet is located away from the stagnation point. There is an increase in maximum concentration as the droplet is moved around to the back of the arm (180°). The average concentration is similar for all orientations other than the stagnation point droplet location, indicating that diffusion of agent from the droplet location is of primary importance for these wind and fabric conditions.

For droplets located at the stagnation point, increased gap widths and multiple clothing layers reduce the observed maximum agent concentration at the arm surface. For this flow configuration, the maximum concentration is always directly under the droplet location.

Increasing the distance from the droplet or adding additional resistance to agent transport in the form of an additional clothing layer allows the surrounding air to dilute the agent concentration before reaching the arm surface. The results in Table 15.1 also indicate that increased gap widths tend to increase

area-averaged agent concentrations at the arm surface. Increasing the distance between the arm and the outer clothing layer has the effect of increasing the resistance to agent diffusion transport out of the gap region and allowing higher concentrations to be reached within the gap away from the droplet location.

As an example of the agent concentration results, Fig. 15.8 shows the agent concentration at the surface of the arm for different uniform gap thicknesses with a droplet located at the stagnation point. The larger gaps show a lower peak concentration. However, the larger gaps show higher concentrations over most of the arm surface.

15.5 Full-body modeling

Detailed computational simulations of clothing systems are not necessary at all steps of an analysis. Use of a body that is a solid geometric shape (no porous clothing layers or air spaces) can be useful to define the air flow pattern and pressure field developed over a human form. This information may then be used with the simpler body segment models (such as an arm or torso) to define exposure levels.

Figure 15.9 shows the geometry of a soldier modeled as a solid body (no porous clothing layers). Two calculations were performed with the model, both for a 4.5 m/s headwind. Figure 15.9(a) shows the calculated steady-state flow field around the soldier. The recirculation region immediately behind the soldier is readily visible. In the second calculation (transient), a

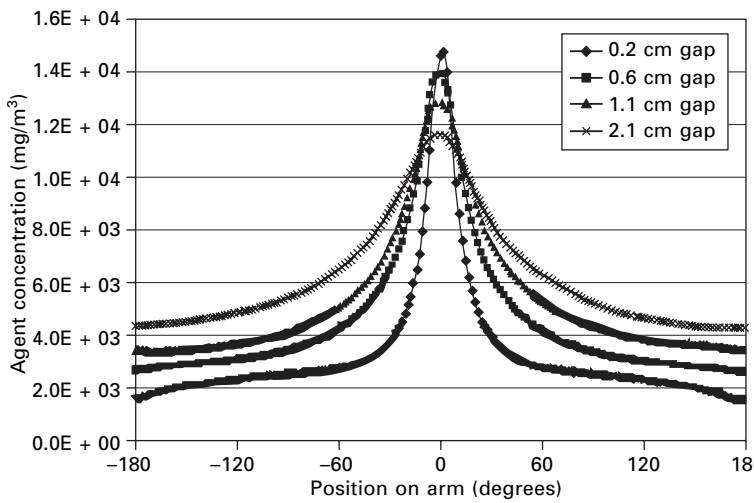

15.8 Agent concentration at the surface of the arm using different uniform gap thicknesses (wind speed 20 mph).

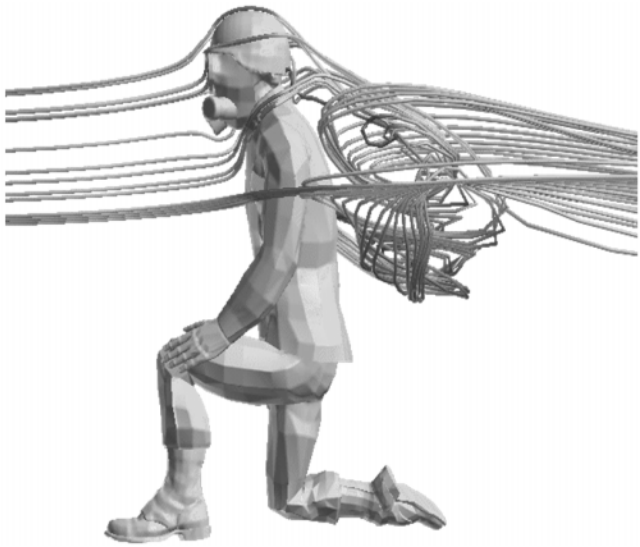

(a)

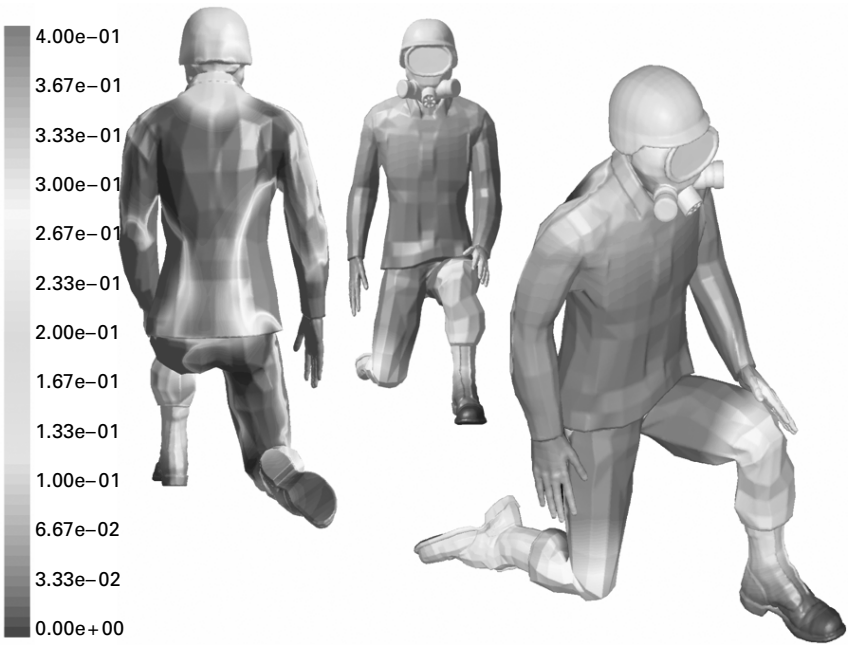

(b)

15.9 (a) Streaklines for 4.5 m/s headwind (b) Surface concentrations of tracer gas: 0.5 s after release of 1 m spherical cloud at location 2 m in front of soldier.

spherical cloud of tracer gas 1 m in diameter is released at a location 2 m in front of the soldier. Figure 15.9(b) displays surface concentrations of gas at 0.5 seconds after release. The results show high concentrations of gas in the soldier's midsection where the cloud is centered.

Figures 15.10(a) and 15.10(b) depict more complex 3-D models of an arm and torso, respectively. Two layers of fabric clothe the arm. The undulations

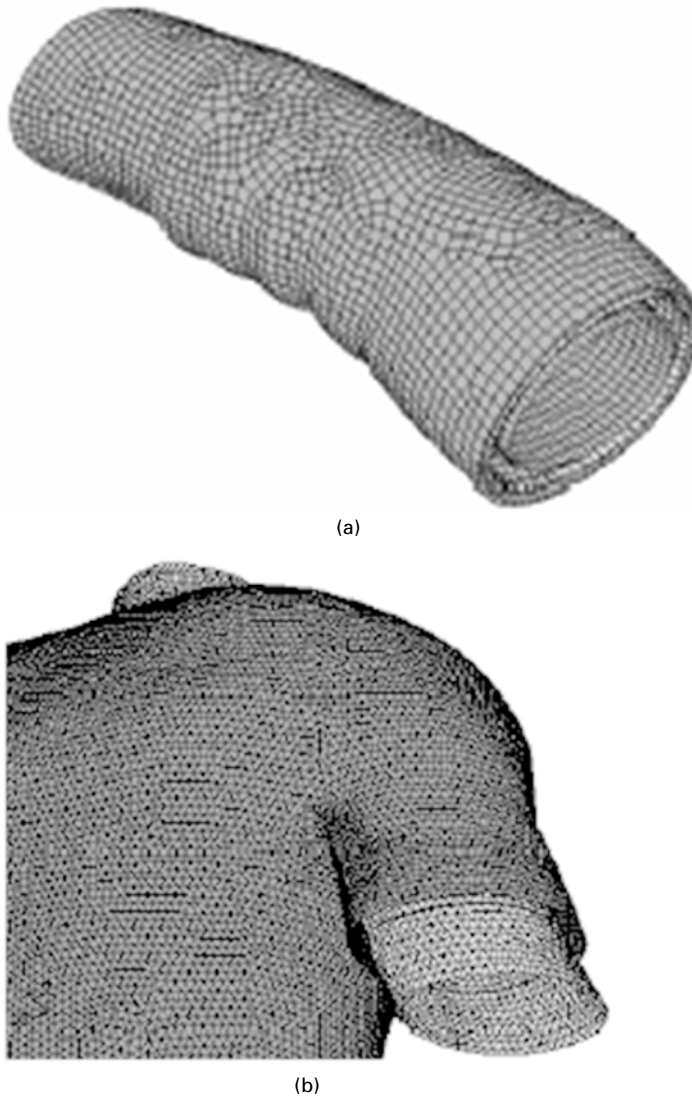

15.10 (a) 3-D Model of arm with two clothing layers. (b) Model of torso (clad in T-shirt).

visible on the inner arm near the elbow are in the outer layer of fabric only. The torso model here is clad in a single fabric layer, a crew-neck T-shirt. Both arm and torso models are based on laser scans of humans. Scanned points are brought into computer-aided design software for creation of the body surface and generation of clothing layers. The geometry is then exported to the CFD software's preprocessor for grid generation. 3-D simulations are generally similar to the 2-D fabric-covered cylinder studies, particularly for the fabric-covered arm segment. Problems arise in the computational requirements for the large number of grid points for a human body, the irregular geometry, and the differences in scale between the size of the human body and the thickness of the mesh required for thin clothing layers.

Three-dimensional models of a human torso having one or more layers of clothing have been developed.[14,15] Results from a simulation using the computational mesh of Fig. 15.10(b) were performed under steady-state conditions of a 5 mph wind imposed on the front of the torso. Skin conditions are assumed to be a sweat flux of 3×10^{-5} kg/m^2 s and heat flux of 100 W/m^2, with the shirt modeled as a 1 mm thick cotton fabric.

Figure 15.11 shows the temperature at the skin surface and velocity vectors in a plane around the torso for conditions of full closure between the layer of clothing and skin at the bottom of the shirt, ends of the sleeves, and at the

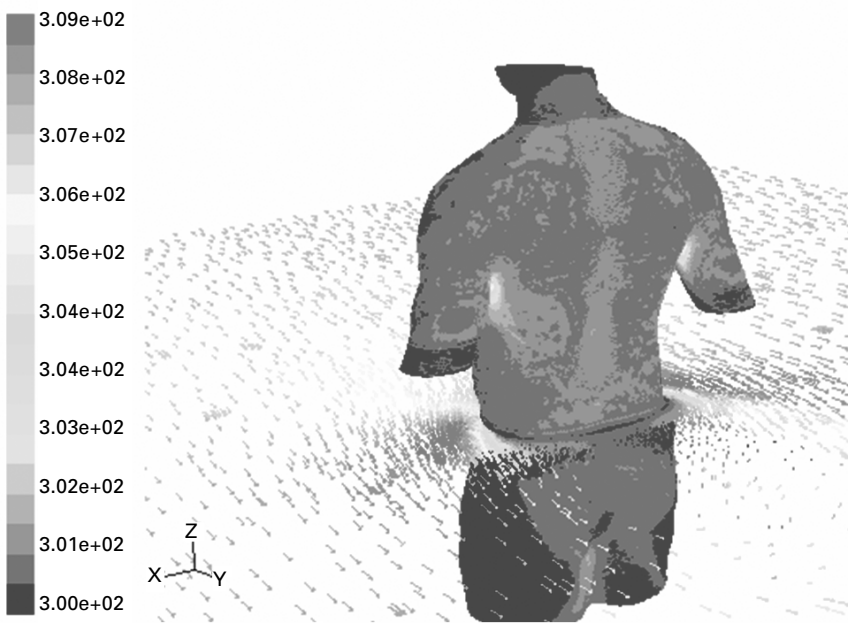

15.11 Simulation results of clothed 3-D human torso: Temperatures at skin surface and flow around torso with complete closure (snug fit) at neck, sleeves, and waist.

neck (i.e. snug fit at neck, sleeves, and waist). As might be expected, the highest temperatures are in the vicinity of under the arm. Furthermore, the presence of the closures and their effect of limiting the ability of flow from the environment to enter the area under the shirt results in higher temperatures. These results represent a first step in performing simulations of thermal and agent transport in protective clothing on a 3-D human torso model.

15.6 Conclusions

Modeling offers a powerful companion to experiments and testing in the development of protective clothing materials and other textiles. Detailed material models for vapor and liquid phase transport within textile fabrics have been developed and integrated with CFD software. Material-level modeling can account for transient processes such as aerosol transport and deposition, liquid wicking, and phase changes due to evaporation, condensation, and sorption/desorption. It is desirable to include these more complicated phenomena in the system-level three-dimensional body modeling efforts.

General non-dimensional scaling correlations of heat and mass transfer from cylinders covered with a porous layer are very valuable for application to the problems of clothing comfort and protection from chemical agents. Modeling and experiments for fabric-covered cylinders will continue to be an efficient pathway to understanding the interactions between materials properties and their performance in a protective clothing system. Modeling applications involve assessment of thermal comfort/stress on wearers of protective clothing, effects of layering on protective performance, and sensitivity to textile permeability and wicking properties.

15.7 References

1. P.W. Gibson, *Governing Equations for Multiphase Heat and Mass Transfer in Hygroscopic Porous Media with Applications to Clothing Materials*, Technical Report Natick/TR-95/004 (U.S. Army Natick Research, Development and Engineering Center, Natick, MA, 1994).
2. P.W. Gibson, *Multiphase Heat and Mass Transfer Through Hygroscopic Porous Media With Applications to Clothing Materials*, Technical Report Natick/TR-97/005 (U.S. Army Natick Research, Development, and Engineering Center, Natick, MA, 1996).
3. S. Whitaker, in *Advances in Heat Transfer* 13 (Academic Press, New York, 1977) p. 119.
4. S. Whitaker, in *Advances in Heat Transfer* 31 (Academic Press, New York, 1998) p. 1.
5. P.W. Gibson, M. Charmchi (1997) *Journal of Applied Polymer Science* 64, p. 493.
6. P. Brasser and J. Kaajik, *Modelling of the Protective Performance of NBC-Clothing 1: Profile Between Clothing and Skin*, Technical Report PML 1998-A107 (TNO Prins Maurits Laboratory (The Netherlands) June, 1999).

7. P. Fedele, W. Bergman, R. McCallen and S. Sutton (1986) *Proceedings of the 1986 Army Science Conference, Vol. I* p. 279.
8. J. Hanley and P. Fedele (1988) *Proceedings of the 1987 U.S. Army Chemical Research, Development, and Engineering Center Scientific Conference on Chemical Defense Research*, p. 444.
9. J. Hanley, D. Van Osdell and P. Fedele (1989) *Proceedings of the 1988 U.S. Army Chemical Research, Development, and Engineering Center Scientific Conference on Chemical Defense Research*, p. 347.
10. R. Kind and C. Broughton, *Textile Research Journal* 70 (2000), p. 171.
11. R. Kind, J. Jenkins and F. Seddigh (1991) *Cold Regions Science and Technology* 20 p. 39.
12. M.P. Sobera, C.R. Kleijn and P. Brasser, H.E.A. Van den Akker, presented at the *2002 ASME Pressure Vessel and Piping Conference*, Vancouver, British Columbia, Canada, August 4-8, 2002, preprint.
13. M.P. Sobera, C.R. Kleijn and P. Brasser, H.E.A. (2002) Van den Akker, 'Convective Heat and Mass Transfer to a Cylinder Sheathed by a Porous Layer,' unpublished manuscript.
14. J.J. Barry and R.W. Hill 2002, presented at the *International Nonwoven Technical Conference INTC 2002*, Atlanta, GA, September 24-26, preprint.
15. J.J. Barry and R.W. Hill (2002) in *Proc. Fall 2002 Fiber Society Annual Technical Conference*, Natick, MA, October 16-18, 2002 [CD-ROM] (The Fiber Society, Raleigh, NC, p. 124.

16

The skin's role in human thermoregulation and comfort

E. ARENS and H. ZHANG, University of California, Berkeley, USA

16.1 Introduction

This chapter is intended to explain those aspects of human thermal physiology, heat and moisture transfer from the skin surface, and human thermal comfort, that could be useful for designing clothing and other types of skin covering.

Humans maintain their core temperatures within a small range, between 36 and 38°C. The skin is the major organ that controls heat and moisture flow to and from the surrounding environment. The human environment occurs naturally across very wide range of temperatures (100 K) and water vapor pressures (4.7 kPa), and in addition to this, solar radiation may impose heat loads of as much as 0.8 kW per square meter of exposed skin surface. The skin exercises its control of heat and moisture across a 14-fold range of metabolisms, from a person's basal metabolism (seated at rest) to a trained bicycle racer at maximum exertion. The skin also contains thermal sensors that participate in the thermoregulatory control, and that affect the person's thermal sensation and comfort.

The body's heat exchange mechanisms include sensible heat transfer at the skin surface (via conduction, convection, and radiation (long-wave and short-wave)), latent heat transfer (via moisture evaporating and diffusing through the skin, and through sweat evaporation on the surface), and sensible plus latent exchange via respiration from the lungs. Dripping of liquid sweat from the body or discharge of bodily fluids cause relatively small amounts of heat exchange, but exposure to rain and other liquids in the environment can cause high rates of heat loss and gain.

Clothing is used outside the skin to extend the body's range of thermoregulatory control and reduce the metabolic cost of thermoregulation. It reduces sensible heat transfer, while in most cases permitting evaporated moisture (latent heat) to escape. Some clothing resists rain penetration, both to prevent the rain from directly cooling the skin, and to prevent the loss of insulation effectiveness within the clothing. Wet clothing will have a higher heat transfer than dry: depending on design, it can range from almost no

difference to a 20-fold increase. Clothing is nearly always designed to allow the wearer's breath to enter and exit freely in order to keep the temperature and humidity of inhaled air low, and to avoid moisture condensation within the clothing.

Bedclothes are a form of clothing used for sleeping. Because the metabolic rate during sleep (0.7 met) is lower than the basal rate, and the body's skin temperature tends to be higher during sleep, bedclothes typically have a higher insulation value than clothing.

Bandages and other medical coverings may also be a special case of clothing, controlling the heat, moisture, and biotic transfer above a damaged skin.

This chapter gives a brief description of the body's skin structure and thermoregulatory system, followed by a more detailed description of how heat and moisture are transferred at the skin's outer boundary, and finally, the comfort implications of skin temperature and humidity. Since skin characteristics are not evenly distributed across the surface of the entire body, it is useful for clothing design to have this information presented by individual body part, wherever possible.

16.2 Body–environment exchange

Over time, heat gains and losses must balance to maintain homeothermy – maintaining the body's core temperature within its narrow range. Figure 16.1 illustrates the full range of core temperatures and environmental temperatures encountered by humans.

16.2.1 Heat gains

Most of the body's heat production is in the liver, brain, and heart, and in the skeletal muscles during exercise. This heat is transferred, through the network

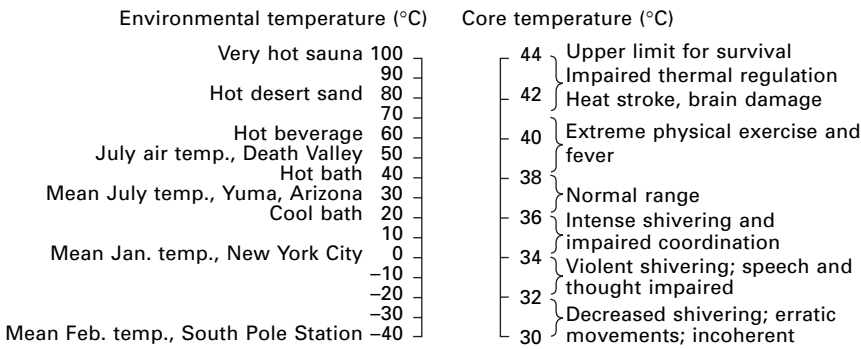

16.1 Ranges of environmental and human body temperatures (adapted from Brooks *et al.*, 1996).

of blood vessels and tissue, to the skin, from whence it is lost to the environment. The amount of metabolic heat generation depends on the level of muscular exercise, and to a lesser degree on factors such as illness and time in the menstrual cycle. A base level of metabolism has been defined as the metabolism of a seated person resting quietly. For a man of typical height and surface area, this amount is about 100 W.

To normalize among people of different sizes, metabolism is typically expressed in per unit skin surface area. A specialized unit, the 'met', has been defined in terms of multiples of basal metabolism: 1 met is 58.15 W/m^2. A sleeping person has a rate of 0.7 met, and reclining awake is 0.8 met. Office work is 1.2 met: a mostly seated activity but one that involves occasional moving about. Walking slowly (0.9 m/s, or 2 mph) is 2 met, moderate walking (1.2 m/s or 2.7 mph) is 2.6 met, and fast walking (1.8 m/s or 4 mph) is 3.8 met (*ASHRAE Handbook of Fundamentals*, 2005). Swimming ranges from 4 to 8 met, and jogging 8 to 12 met (Brooks *et al.*, 1996). The work efficiency of muscles is about 15%, with 85% of total energy released as heat.

Brain metabolism consists mostly of the energy required to pump ions through neuron cell membranes (Guyton and Hall, 2000). This takes place at a rate per unit mass that is 7.5 times that of non-nervous system tissues. Although the brain only comprises 2% of the body mass, it produces about 15% of the body's total metabolism. During high mental activity, this neuron metabolism can more than double. The head has specialized thermoregulatory physiology to assure the high rates of heat loss needed to keep the brain temperature constant.

Heat may also be gained from the environment through the skin. Solar radiation, and long-wave radiation from surfaces warmer than skin temperature, warm the skin as a function of its color and surface emissivity. Although in most conditions convection and evaporation carry metabolic heat away from the body, hot winds may cause the skin to warm, when the body's sweat supply rate is insufficient to keep up with evaporation, and sensible gains exceed evaporative losses.

16.2.2 Heat losses

The body's heat losses are through radiation, convection, conduction, evaporation, and through respiration. Figure 16.2 shows heat transfers above and below the skin surface. In a neutral environment, where the body does not need to take thermoregulatory action to preserve its balance, evaporation provides about 25% of total heat loss, and sensible heat loss provides 75%. During exercise, these percentages could be reversed. In general, the heat transfer by conduction through the soles of the feet or to a chair is small, around 3%. In normal indoor environments with still air, the convective and radiation heat transfer are about equal (McIntyre and Griffiths, 1972). In the

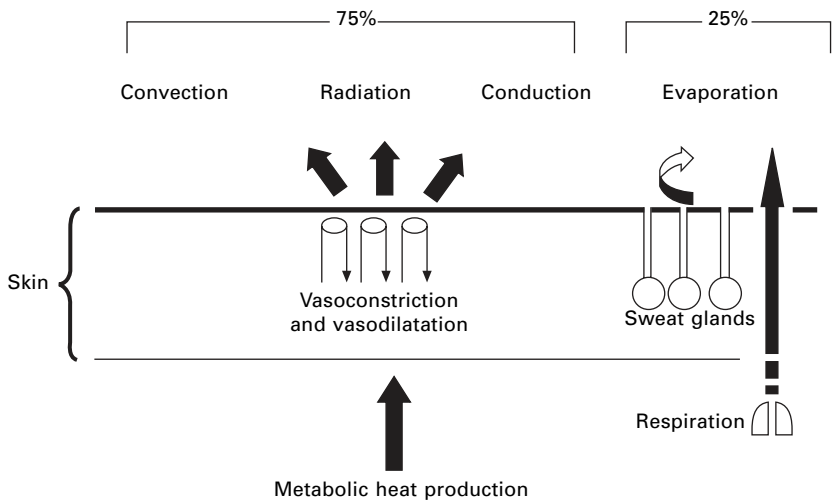

16.2 Heat transfer through and above the skin.

outdoors, wind strongly affects convective heat loss or gain, and radiation (solar and long-wave) can also cause large losses and gains. These forces act asymmetrically on the body, affecting some parts more than others.

16.2.3 Thermal regulation

Thermoregulation generally refers to four mechanisms: sweating, shivering, vasodilatation, and vasoconstriction. Sweating increases body heat loss by increasing sweat evaporation. Shivering produces heat by involuntary movement of muscle. Vasodilatation and vasoconstriction refer to changes in blood vessel diameter, which affect skin temperature by changing the rate of blood exchange with the interior. In the heat, increased conductance below the skin surface (due to increased blood flow) facilitates heat transfer from body interior to the skin. Then convection and evaporation of sweat carries the heat away from the surface of the body to the environment. In the cold, muscle tensing and shivering increase heat production and body temperature. Decreased conductance (due to decreased blood flow) keeps the heat from escaping to the cold environment. This combination of heat loss and heat gain control mechanisms is able to maintain human body core temperature within a very small range in spite of variation in metabolic output that can exceed an order of magnitude above the base value, and similar variation in the heat loss rate from body to the environment.

A comprehensive overview of the thermoregulatory control system is found in Guyton and Hall (2000) and Gagge and Gonzalez (1996). The control system senses the body's thermal state with sensory organs in the hypothalamus (within the brain), within the skin, and in the spine and some

abdominal organs. The thermal sensors within the anterior hypothalamus sense the core temperature of the body, especially that of the brain, by measuring the temperature of blood passing through it. The anterior hypothalamus's warm sensors outnumber its cold sensors by three to one, and are most active when the body core is too hot. The anterior hypothalamus primarily acts as a controller of the body's heat loss; any rise in hypothalamus temperature above its set point causes it to send out nerve impulses to activate vasodilatation and sweating, the body's heat loss mechanisms. The mechanism is precise: the setpoint for vasodilatation and sweating is only a couple of tenths of a degrees higher than the set point for vasoconstriction, and the setpoint for shivering is just below 36 °C (Sessler, 2006). These setpoints are raised during exercise or fever. The skin temperature also plays a secondary role in controlling cooling in the heat: at the same core temperature, a warmer skin temperature enhances the sweat rate, and a colder skin inhibits it (Stolwijk *et al*., 1971; Nadel *et al*., 1971).

Cold- and warm-sensitive nerve endings located in the skin send signals, through the sympathetic nerve system to the anterior hypothalamus, that are passed on to the posterior hypothalamus, which acts a controller of body temperature during cold. The skin has many (ten times) more cold sensors than warm, and the cold sensors are closer to the surface than the warm, so these peripheral sensors are more dedicated to the rapid detection of cold than of warmth. There are some cold-sensitive temperature sensors in the anterior hypothalamus, and in the spine and abdomen, that also alert the posterior hypothalamus to body cooling. The posterior hypothalamus emits nerve signals to the periphery, stimulating vasoconstriction and shivering, and it also initiates the release from the medulla of hormonal messengers such as norepinephrine that rapidly initiate vascular contraction throughout the body.

If a local part of the body is warmed or cooled, sweating or vasoconstriction can be locally initiated and controlled for that particular area, even if the rest of the body is being centrally controlled for a different temperature. The relative contributions to sweating from core and skin temperatures are about 10 to 1 (Nadel and Stolwijk, 1973; Nadel *at al*., 1971; Benzinger *et al*., 1961). The core threshold for sweating decreases by 0.6 °C as the skin temperature is warmed from 29 °C to 33 °C. Similarly, with the hypothalamus temperature constant, heating a local body part can induce local sweating (Nadel *et al*., 1971; Randall, 1946).

16.3 Skin

16.3.1 Skin surface area

The area of skin on the body can be estimated from the body's height and weight, using a relationship developed by DuBois and DuBois (1915):

$$A_{Dubois} = 0.202\ M^{0.425}\ L^{0.725} \mathrm{m}^2 \quad [16.1]$$

where A_{Dubois} is the skin area in m^2, M is the mass in kg, and L the person's height in m. A 1.65 m person weighing 73 kg will have a skin surface area of 1.8 m^2, a commonly used figure for 'standard' men. The range of surface areas from school-age children through large adults is 0.8 through 2.4 m^2.

The surface areas of local body segments vary among individuals, but it can be useful to know the relative percentages of total surface area that they cover. Table 16.1 presents such percentages for a detailed female thermal manikin with a total surface area of 1.588 m^2.

16.3.2 Skin structure

The skin provides a first barrier between the organism and its environment. It keeps the uncontrolled loss or gain of water through the skin at a low constant level. In addition to that, it contains complex vascular systems and sweat glands that allow it to change its conductance in response to thermoregulatory demands of the body. It also contains four types of thermally-sensitive nerve endings (to cold, warmth, and hot and cold pain) that sense the skin's temperature and transmit the information to the brain.

Although there are some regional variations in skin thickness, in most places the skin is about 2 mm thick. It includes two main layers, the epidermis and dermis (Fig. 16.3).

The epidermis is thin, mostly about 0.075–0.15 mm (except for the soles and palms, which are thicker). The outermost layer of the epidermis is the

Table 16.1 Body surface areas for a detailed female thermal manikin

Body part	Area (m^2)	Percentage (%)
Head	0.117	7.5
Chest	0.143	9.2
Back	0.135	8.6
Pelvis	0.143	9.2
L-Upper arm	0.093	5.9
R-Upper arm	0.093	5.9
L-Lower arm	0.063	4.1
R-Lower arm	0.063	4.1
L-Hand	0.039	2.5
R-Hand	0.039	2.5
L-Thigh	0.143	9.2
R-Thigh	0.143	9.2
L-Calf	0.125	8.0
R-Calf	0.125	8.0
L-Foot	0.048	3.1
R-Foot	0.048	3.1
Whole-body	1.588	100

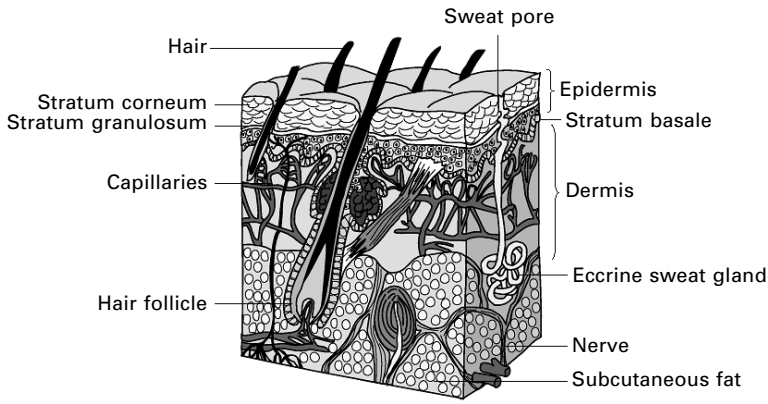

16.3 Cross-sectional view of the skin (Image courtesy of LifeART.com).

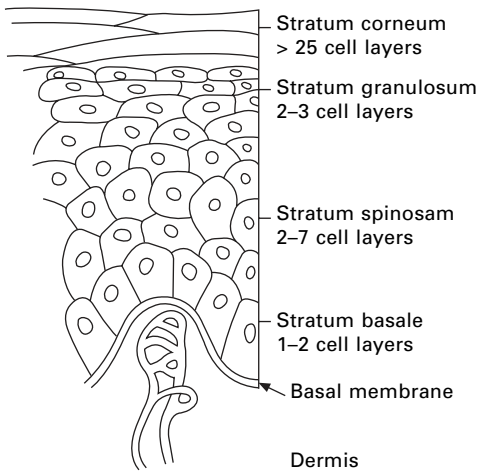

16.4 Layers of the epidermis (Copyright (2004) from *Skin, Hair and Nails: Structure and Function* by Forslind and Lindberg, Reproduced by permission of Routledge, Taylor and Francis Group LLC).

stratum corneum (Fig. 16.4), an assemblage of overlapping plate-like cells (corneocytes), interleaved with hydrophobic layers of lipids. The stratum corneum is 0.01 to 0.1 mm thick, and serves as the skin's primary barrier to water diffusion. Because the corneocytes are impervious to water transmission, whatever moisture passes the stratum corneum barrier has to travel around them through the lipids, following a long tortuous path back and forth among the plates. The stratum corneum is well described in Forslind and Lindberg (2004), who make the memorable point in their introduction that this waterproof

barrier protecting our bodies is thinner than the plastic cling wrap used to protect our sandwiches.

The corneocytes are non-viable, having lost their nucleus and organelles. They are continuously shed from the surface as they are replaced from below. The shedding is accomplished by the dissolution of small rivetlike structures called desmosomes that hold the plates together. The dissolution is mediated by enzymes controlled by the moisture gradient in the stratum corneum layer. Corneocytes consist of a protein cell wall and a matrix of keratinous fibrils within, which stiffen the structure. When immersed in water or exposed to high levels of atmospheric humidity, they absorb moisture and thicken by as much as 25%; this is thought to smooth the outer skin surface and protect it from tearing when wet (Forslind and Lindberg, 2004).

Below the stratum corneum, at the bottom of the epidermis, is a basal layer of stem cells ('stratum basale'), which generates epidermal cells continuously. Above it are two layers in which the upward-migrating cells transform themselves into the interleaved plates and lipids of the stratum corneum. The basal level has an undulating lower contour to provide mechanical shear resistance, connecting the epidermis to the dermis layer below it.

The dermis is much thicker than the epidermis, varying by body part (Fig. 16.5, Rushmer *et al*., 1966). It contains vascular systems, sweat glands, and thermoregulatory nerves at different depths in the layer. These will be described in the following sections. The dermis also houses nail and hair follicles, which produce keratinized structures physiologically related to the stratum corneum. Sebaceous glands within the dermis serve the functions of smoothing and moisture-proofing the outer surface of the skin, and coating hair to reduce tangling.

Beneath the dermis lies the subcutaneous or fat layer, whose thickness is highly variable among individuals (for a normal person, it is, on average,

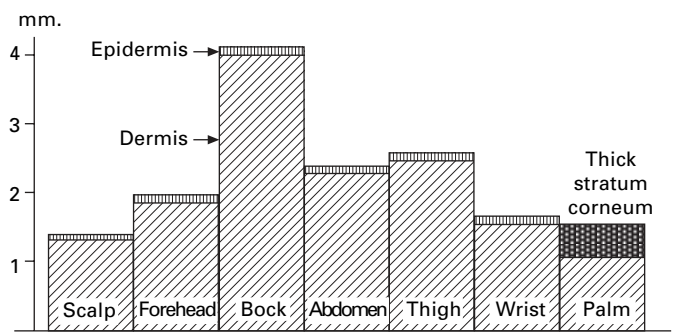

16.5 Regional variations in thickness of skin (From Rushmer *et al.*, 1966, with permission from the American Association for Advancement of Science, Washington, D.C.).

about 17 times the thickness of the dermis – Stolwijk and Hardy, 1965). It serves the functions of insulating the underlying musculature against conductive heat transfer to the outer skin, as well as of storing food energy for the body.

16.3.3 Thermoreceptors

Human beings can perceive different levels of cold and warmth (including pain) through four discrete types of sensory organs – cold, warmth, and cold and hot pain receptors (Guyton and Hall, 2000; Craig, 2003). The relative degrees of stimulation of the nerve endings determine the person's perception of the intensity of thermal sensation.

The discovery of discrete thermoreceptors was made independently in 1884/1885 by Blix in Sweden, Goldscheider in Germany, and Donaldson in America. All three investigators, and many since, have reported that, when touched with small (punctate) warm and cold stimulators, some spots on the skin feel warm and/or cold, others do not. Each receptor is activated in a specific range (Fig. 16.6). At high temperatures perceived as painfully hot, warmth receptors are inactive, and pain receptors are simulated. The same is true for painfully cold temperatures. If a warm stimulus is applied to a cold thermoreceptor, no signal is produced. Thermoreceptors are located mainly in the skin and in the hypothalamus, but are also found in places such as the spinal cord, abdominal viscera, and in or around the great veins in the upper abdomen and thorax.

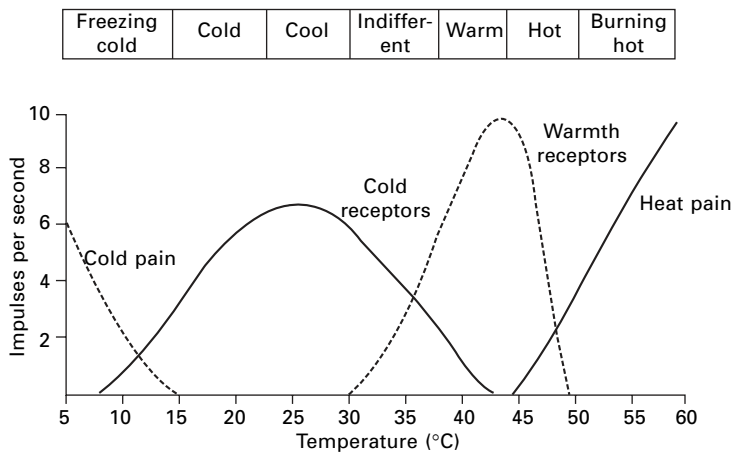

16.6 Discharge frequencies of a cold receptor, a warmth receptor, and cold and hot pain nerve fibers at different temperatures (From Guyton and Hall, 2000: *Textbook of Medical Physiology*, with permission from W.B. Saunders Company, Philadelphia).

The thermoreceptors are located in the dermis at an average depth of 0.15 to 0.17 mm for cold receptors and 0.3 to 0.6 mm for warmth receptors (Bazett and McGlone, 1930; Bazett *et al.*, 1930; Hensel, 1982). These depths indicate that the layer of cold receptors is immediately beneath the epidermis, and the site of warmth receptors is within the upper layer of the dermis. The number of cold thermoreceptors far exceeds the number of warmth receptors. In general, there are about ten times more cold receptors than warmth receptors in skin (Guyton and Hall 2000). The distribution of the cold and warm receptors is shown in Table 16.2. Figure 16.7 displays examples from classic studies: the warm and cold receptors on the dorsal forearm (Strughold and Porz, 1931), and warm receptors on the fingers (Rein, 1925).

The preponderance of cold spots over warm spots, and the shallower depth of cold spots relative to the skin surface, suggest that humans are more sensitive to danger from cold than from heat.

The dynamic characteristics of thermoreceptors determine thermal sensation and comfort responses. A thermoreceptor is capable of a great deal of adaptation. When it is subjected to an abrupt change in temperature, it is strongly stimulated at first, sending impulses at a high frequency, but this stimulation fades rapidly during the first minute following the temperature change, and then progressively more slowly until it reaches a steady level (Fig. 16.8 – Hensel, 1982). Thermoreceptors respond to steady temperature states at this lower rate. A person feels much colder or warmer when the temperature of the skin is actively falling or rising than when the temperature remains at the same

Table 16.2 Number of cold and warm spots per cm^2 in human skin

Body parts	Cold spots (Strughold and Porz 1931)	Warm spots (Rein 1925)
Forehead	5.5–8	
Nose	8	1
Lips	16–19	
Other parts of face	8.5–9	1.7
Chest	9–10.2	0.3
Abdomen	8–12.5	
Back	7.8	
Upper arm	5–6.5	
Forearm	6–7.5	0.3–0.4
Back of hand	7.4	0.5
Palm of hand	1–5	0.4
Finger dorsal	7–9	1.7
Finger volar	2–4	1.6
Thigh	4.5–5.2	0.4
Calf	4.3–5.7	
Back of foot	5.6	
Sole of foot	3.4	

Adapted from Hensel, 1982

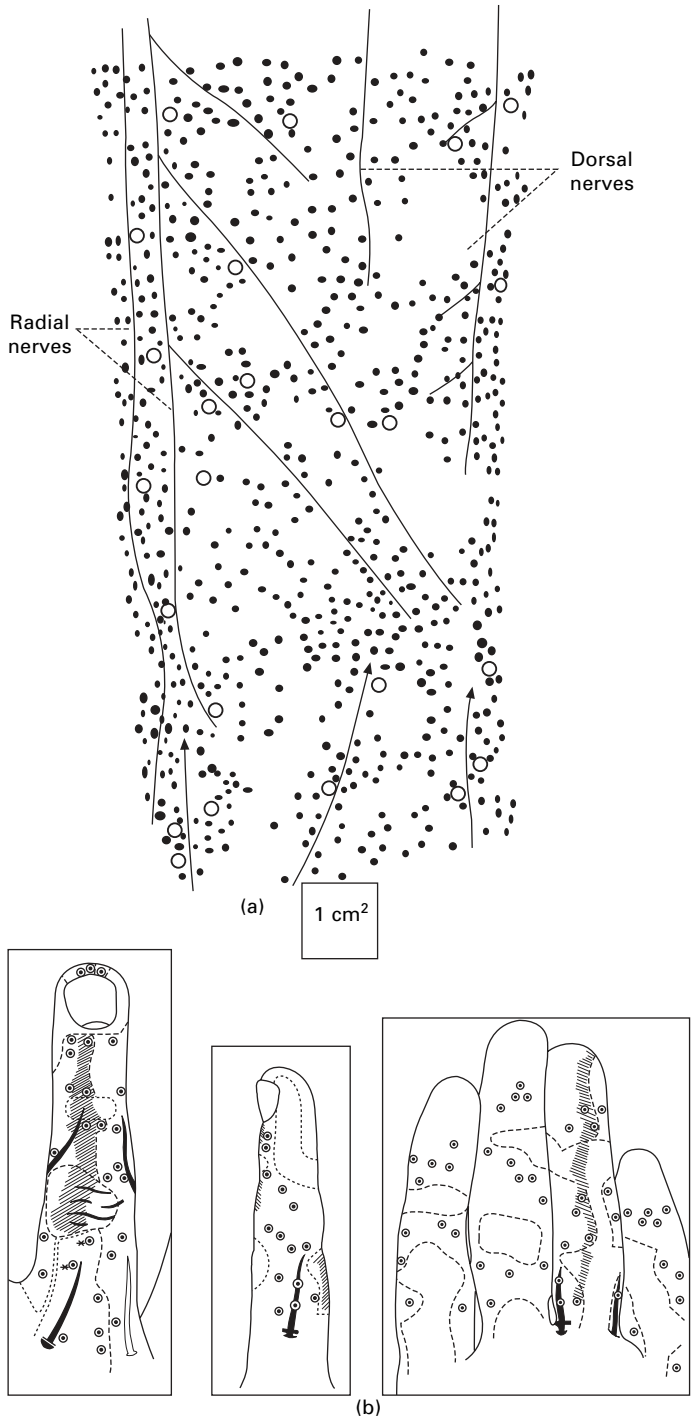

16.7 (a) Warm and cold receptors on the dorsal forearm, and (b) warm receptors on the fingers.

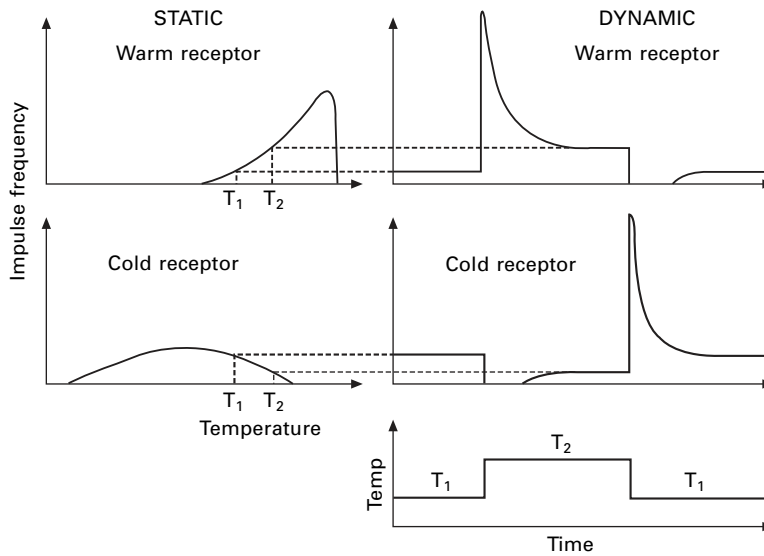

16.8 General properties of thermoreceptors. Static and dynamic responses of warm and cold receptors to constant temperature and temperature changes (From Hensel, 1982: *Thermal Sensation and Thermal Receptors in Man*, courtesy of Charles C Thomas Publishers, Springfield, Illinois.).

level. This explains the stronger sensation of coolth or warmth felt upon entering a cold pool or a hot tub. The overreaction during transient exposures has been termed 'overshoot' (deDear *et al*., 1993; Gagge *et al*., 1967; Zhang, 2003). The dynamic response of thermoreceptors to changes in temperature in essence predicts the body's steady-state response to a new thermal environment well before the body's heat content has had time to alter significantly. Such a capability has clear adaptive value for survival.

16.3.4 Vascular system

Figure 16.9 illustrates the vascular system in the skin. The primary function of blood circulation is to deliver nutrients and oxygen to tissues and organs. In addition to that, blood circulation assists the principal mechanisms of thermal homeostasis. It keeps the heat within the body when it is cold by reducing blood circulation (vasoconstriction) to the skin, or enhances the outward flow of heat to the skin by vasodilatation.

In the outer region of the skin (epidermis and outer dermis), the thermal resistance of the tissues determine heat flow, and the variation of blood flow within the small dermal capillaries is not thermally important. Below these, however, the subcutaneous region contains the venous plexus, a dense vascular network that strongly affects skin temperature and heat transfer from the

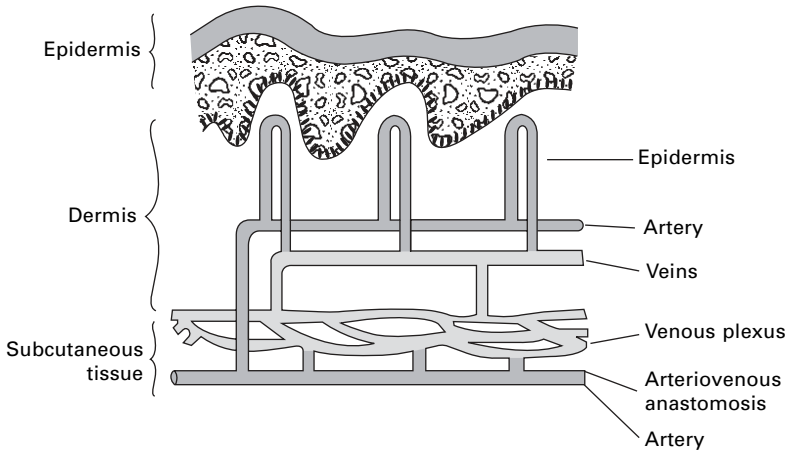

16.9 Vascular system in the skin (From Guyton and Hall, 2000: *Textbook of Medical Physiology*, with permission from W.B. Saunders Company, Philadelphia, p 823, with permission from Elsevier).

skin to the environment. Blood flow into the venous plexus is fed by arterioles, which vasodilatate and vasoconstrict significantly. Since blood flow varies to the fourth power of vessel diameter, a doubling in diameter corresponds to a 16-fold increase in the blood supply volume. In cold, the blood supply to the venous plexus can be effectively as low as zero, resulting in a local gradient across the skin of 10 K. In heat, dilatation can cause an eight-fold increase in the skin conductance, producing a gradient from the body's central core temperature to skin surface temperature that is less than 1 K.

Vascular control takes place through the sympathetic nervous system. When stimulated in the posterior hypothalamus or skin, the rate of nerve impulses transferred to the periphery activates vasoconstriction or vasodilatation. The relative contributions to the control signal from the hypothalamus (core) temperature and from the skin temperature are in the order of 10:1, so the system is heavily weighted toward representing the overall body thermal state.

Highly exposed areas of the body, such as the fingers, hands, feet, and ears, have an additional vascular control mechanism that can vary their temperature and heat loss across a wide range. Arterio-venous anastamoses (AVAs) (Sherman, 1963) are present in these areas in large numbers. These are valves that, when open, shortcut the normal route of the blood from the arterioles to the venous plexus. The diameters of AVA are 20–150 μm, about 20 times larger than that of capillaries (1–8 μm) and five times larger than that of arterioles (15–30 μm) (Hales, 1984, 1985). When the body is hot, AVAs are stimulated by sympathetic nerves to open and rapidly supply arterial blood to the venous plexus, which acts as a warm reservoir close to the skin

surface. This promotes heat loss by conduction through the overlying tissues to the surroundings.

Warm-blooded animals keep their core temperature fairly constant using another important vascular feature: counter-current heat exchange between arteries and veins, where the warm outbound arterial blood transfers heat to the cold inbound venous blood. The counter-current vascular structures can be categorized into three types. The first has one artery and one vein in parallel, as exist down the lengths of our arms and legs, and in most birds' legs. The second has one artery surrounded by many veins, as in human fingers and relatively uninsulated body parts such as whales' fins and some animals' tails. The third consists of a net where 20–40, or sometimes several hundred, small arteries and veins run parallel and are intermingled (Schmidt-Nielsen, 1972). An example of this is the *rete mirabile*, found between the nasal passages and the brain of non-sweating animals like dogs, which rely on panting for keeping their brains cool.

Unlike tissues in other body parts, the brain stores very small amounts of energy and oxygen. Due to the high level of metabolic rate of neurons, the brain needs second-by-second delivery of glucose and oxygen from the blood (Guyton and Hall, 2000), a relatively constant blood flow, 750 ml/min, about 13–15% of the total cardiac output. Since this amount cannot be reduced, the head does not have a vasoconstriction mechanism. If the body is cooling in a cold environment, the head should be wrapped in order to protect it from excessive heat loss. In heat, selective brain cooling (SBC, discussed below under evaporative cooling systems) is able to keep the brain temperature lower than the nearby core temperatures measured in the esophagus (Cabanac, 1993).

16.3.5 Evaporative control systems

Because the temperature gradient between the skin surface and the environment diminishes in hot weather, sensible heat transfer becomes insufficient to remove the body's metabolic heat. Evaporation of body moisture is a highly efficient heat removal process, and therefore complex physiological mechanisms have evolved to encourage evaporation under conditions of heat stress, and to minimize it when not, both to avoid overcooling and to minimize the amount of water lost by the body.

Insensible evaporative heat losses

There is always a constant amount of trans-epidermal loss of water vapor directly diffused through the skin, resulting in heat loss by 'insensible evaporation'. In addition, the breathing cycle involves humidifying exhaled air, producing another evaporative heat loss. The transdermal moisture diffusion

is about 100 to 150 mL per day per m^2 of skin surface, representing a heat loss 6% as great as the evaporation from a fully wetted surface. The respiratory portion of the body's total heat loss is estimated as 8%, depending on the metabolic rate. Although both these modes of evaporation contribute to heat loss from the body, neither is controlled for the purpose of temperature regulation.

Thermoregulatory sweating mechanism

The body's eccrine sweat glands primarily serve the purpose of thermoregulation, although emotions can also stimulate them. Figure 16.3 shows an eccrine sweat gland and its opening onto the skin surface. When the body becomes overheated, sweat is secreted onto the surface of the skin and is evaporated by the heat supplied by the skin surface. If the atmosphere is dry, evaporation is effective, and high sweat rates can occur without wetting much of the skin around the sweat gland opening, so sweating may not be perceived. If the atmosphere is moist, the sweat-covered area around the sweat gland must increase in order to evaporate the quantity of sweat coming out of the gland. The term 'skin wettedness' alludes to this area. It is the fraction of the skin covered with water that would account for a total amount of observed evaporation (ASHRAE Fundamentals, 2005). Perspiration as secreted has a lower salt concentration than interstitial body fluid or blood plasma. Over short intervals of sweating, sweat evaporates indistinguishably from water (Kerslake, 1972; Berglund and McNall, 1973). With extended sweat evaporation, salt may accumulate on the skin, reducing the sweat's vapor pressure and evaporative efficiency. However, this is somewhat offset by the sweat glands reducing the salt concentration of sweat after prolonged heat exposure, presumably to conserve salt.

Eccrine sweat glands are regulated by the autonomic nervous system. For thermoregulation, they are activated through nerve fibers that stimulate the release of the neurotransmitter acetylcholine. Warming in the anterior area of the hypothalamus excites sweating through the whole body. However, as mentioned in Section 16.2.3, the threshold of the hypothalamus temperature for sweating is somewhat modified by skin temperature (Nadel *et al*., 1971; Benzinger, 1961).

An increase in sweat production is brought about by both increasing the number of participating sweat glands and by increasing the output of each active gland. The primary response to heating a local skin area is to increase the output of individual glands, rather than stimulating a larger number of glands to sweat (Randall, 1946, 1947). Sweat does not begin simultaneously all over the body. On the onset of sweating, the first area is generally the forehead, followed in order by the upper arms, hands, thighs, feet, and back and abdomen (Houdas and Ring, 1982); a little different order is presented

by McIntyre (1980) after Kuno (1956) and Randall (1946). The high skin temperature and small number of sweat glands on the zygomatic and buccal regions of the face have been hypothesized to help the evaporation of sweating droplets running down over these regions from the forehead (Randall, 1946).

With repeated intermittent heat exposure, the set point for the onset of sweating decreases and the proportional gain or temperature sensitivity of the sweating system increases (Hensel, 1982). This is acclimatization, and it takes place over a time period of about a week. However, under long-term exposure to hot conditions, the sweating set point increases, perhaps to reduce the physiological effort of sweating.

Sweat gland distribution

The distribution of eccrine sweat production across the body is described in Kuno (1956) and is shown in Table 16.3.

The average density of active glands is around 125–200 glands/cm^2, depending on the individual (Kuno, 1938; Randall, 1946), although considerable variation exists in different areas of the body (Randall, 1946). Table 16.4 gives the sweat gland distribution in various areas.

Table 16.3 Distribution of eccrine sweat production

	Body parts
Greatest	Forehead, neck, back of hand and forearm, back and front of trunk
Middle	Cheeks, arms and legs, lateral surface of trunk
Least	Inside of thighs, soles, palms, armpits

Kuno, 1956

Table 16.4 Sweat gland distribution

Segment	Sweat glands (functional pores/cm^2)
Forearm, extensor surface	213
Upper arm, over biceps	177
Dorsum of hand	377
Trunk – anterior chest	151
Trunk – scapular region of back	30
Leg (over gastrocnemius)	99
Thenar eminence	284
Face – forehead	167
Face – zygomatic arch (temple)	21
Face – buccal (cheek, jaw)	16

Adapted from Randall, 1946

Acclimatization and sweat dripping

People are born with a considerable excess of sweat glands, but if they do not spend their early years in a hot climate, many of the glands become permanently inactive. Whether or not people live in hot climates, accumulated exposure to heat or exercise (acclimatization) will cause more of their available sweating glands to be active, so that their sweat more evenly covers their bodies, making their evaporative heat loss more effective (Kuno, 1956; Guyton and Hall, 2000). In the heat, if sweat beads up and drops off the skin, it normally means that the person is not well acclimatized. An acclimatized person, in fact, looks drier, even though the sweat rate may be greater. Dripping sweat is adaptively undesirable because it provides no evaporative cooling to the skin while dehydrating the body.

The maximum sweat rate for an unacclimatized person seldom reaches 1 liter/hour. However, a well-acclimatized person can sweat as much as 2–3 liter/hour, which, when evaporated, removes about ten times the basal body heat production. It is equivalent to a 4–6 pounds of body weight loss per hour (Guyton and Hall, 2000). The concentration of sodium chloride in the sweat is also smaller for an acclimatized person.

Hidromeiosis

When a local area of skin is thoroughly wet for periods exceeding two hours, the sweat rate abruptly drops off, an effect called 'hidromeiosis' (Sargent, 1961; Hertig *et al*., 1961; Candas *et al*., 1980). It can be brought on by a large amount of unevaporated sweat on the skin surface, or by exposure to very high ambient humidities (such as produced by waterproof coverings over the skin). If the skin is dried (by a towel, wicking fabric, or by convection), the sweat-rate dropoff is rapidly reversed. The causal mechanism has been the subject of debate for many years and has not yet been resolved. Proposed mechanisms include squeezing the sweat pores by swelling in the epidermal cells, changes in the water/salt balance around the sweat glands affecting the secretion rate, and changes in the transmission of nerve impulses at the junction between nerve and gland. Because a fully wetted skin surface cannot further increase its evaporative heat removal rate, and is likely to be experiencing sweat drip, the hidromeiosis mechanism has adaptive benefit to the body by reducing unproductive (in heat removal terms) water loss (Ogawa *et al*., 1984).

Salt will accumulate on the surface of the skin as the water in sweat evaporates. Salt lowers the vapor pressure of water and thereby reduces its evaporation rate. Accumulated salt therefore results in increased skin wettedness for a given rate of evaporative cooling. The *ASHRAE Handbook* (2005) suggests that some of the pleasure of washing after a warm day comes from the restoration of a hypotonic sweat film and decreased skin wettedness.

Emotional sweating

The palms of hands and soles of feet have a large number of eccrine sweat glands, but these do not respond during thermal stimulation or play a substantial role in thermoregulation. They do, however, sweat profusely as a result of emotional excitement and strong mental activity (Kuno, 1956). The sweat glands on palms and soles are stimulated by epinephrine or norepinephrine circulation in the blood. This emotional sweat starts and stops very rapidly, and the resulting changes to electrical resistance of the skin (galvanic skin response) are exploited by lie detectors to detect psychological stress.

Apocrine sweat glands

There is another type of sweat gland, the apocrine. The apocrine glands in humans are mainly located in the armpits and pubic region, always exiting to the skin surface via hair follicles. They are stimulated by adrenergic nerves, part of the sympathetic nervous system. Apocrine sweat contains a mixture of substances unlike that of the more watery eccrine sweat (Goldsmith, 1991); the decomposition this mixture by bacteria in the skin creates its odour (McIntyre, 1980). Due to their locations on the body, apocrine sweat glands serve little thermoregulation purpose. Guyton and Hall (2000) suggests that apocrine sweat, together with sebum exiting from the hair follicles, serves a lubrication function in these areas of the body where skin surfaces touch each other.

Selective brain cooling

The brain, with its high rate of internal heat production, needs to be kept cool within a narrow range to avoid damage. The lack of vasoconstriction in the scalp blood vessels has already been noted. Brain temperature, as measured on the tympanum (inner ear), is typically higher than or equal to other core temperatures in the cold, but in the heat, a mechanism called selective brain cooling (SBC) keeps it lower than the other core temperatures (Caputa and Cabanac, 1988). SBC cooling occurs through upper airway respiration and high heat losses from the surfaces of the head, via convection, radiation, and sweating. Sweating from the surface of the head is maintained at the expense of warming the rest of the body: in mild hyperthermia with the body mildly dehydrated, the sweat rate on the trunk will be depressed while remaining constant on the head (Cabanac, 1993).

16.3.6 Shivering

In cold environments, the body first conserves its internal temperature by vasoconstricting its blood vessels. If this passive insulative measure proves

insufficient, the body begins to actively generate additional metabolic heat through tensioning its muscles, starting with 'muscle tone' in the skin, and then leading to involuntary shivering. Shivering can raise metabolic heat production by as much as three times the normal sedentary value. It begins in the trunk region and spreads to the limbs (Spurr *et al.*, 1957).

In the cold, skin temperature has a more important role in thermoregulation than it does in the heat. The relative contribution from core and skin temperatures in eliciting shivering is between 4 and 5 to 1 when the skin is cold (Tikuisis and Giesbrecht, 1999; Stolwijk, 1971), compared to the 10 to 1 ratio seen for sweating. When the core becomes very cold, below 30 °C, the metabolic heat produced by shivering diminishes (Bristow and Giesbrecht, 1988); it is thought that the body does this in order to conserve energy for survival. Shivering onset requires simultaneous cold signals from both the skin and core. Shivering is not activated when a person is exercising in a cold environment with a cold skin temperature but high core temperature.

People with higher body fat shiver less at a given temperature due to the insulation provided by the fat. Shivering heat production is inversely proportional to the square root of body fat (Tikuisis and Giesbrecht, 1999). In addition, fatter people tend shiver less because they produce more metabolic heat by carrying the additional mass.

16.4 Heat exchange at the skin surface

16.4.1 Conduction

Conduction takes place primarily to solid surfaces in the environment, since conduction from the skin surface to fluid or gaseous surroundings is rapidly replaced by convective processes. A standing person has roughly 3% of his/her body surface area in contact with the floor. For a seated or reclining person, the surface contact area to the seat or bed is in the order of 8 to 12% of total body surface area, depending on how yielding the contact surface is. The overall heat transfer from the body via conduction is usually less than these percentages suggest, because the conductivity of bedding and seating materials tends to be small. However, if the contact surface conductivity is high (such as the earth), conduction can be a dominant path of heat exchange with the environment:

$$K = h_k\,(T_{skin} - T_{surface}) \quad (\mathrm{W/m^2}) \qquad [16.2]$$

where K is conductive heat transfer from the skin surface to a contacting surface.

In a transient state, the heat flux to and from a contacting environmental material will depend on the thermal inertia of that material, quantified as its volumetric heat capacity multiplied by its conductivity. The thermal inertia determines the amount of heat that the skin will gain or lose from contact with

Table 16.5 Values of thermal inertia of, and sensation of heat or cold given by, various substances

Material	Thermal Inertia ($J/m^4\ K^2\ sec$)	Threshold of pain (cold)	Temperature (°C) range of comfort	Threshold of pain (hot)
Steel	0.5×10^{-2}	14	29–32	45
Concrete	1×10^{-2}	4	27–34	54
Rubber	1.2×10^{-3}	–12	24–35	67
Oak	7.3×10^{-4}	–20	22–35	74
Pine	2.4×10^{-4}	–53	17–39	84
Cork	6.0×10^{-5}	–140	5–42	150

Houdas and Ring, 1982

that material over short-term periods. Houdas and Ring (1982) present a table of common materials, and the temperature ranges at which contact with them is comfortable, or produces hot or cold discomfort or pain (Table 16.5). For comparison, the thermal inertias of the body tissues themselves are: skin, $30–80 \times 10^{-4}$, fat $10–15 \times 10^{-4}$, muscle $30–60 \times 10^{-4}$, and bone $25–40 \times 10^{-4}$. Each of these is temperature dependent, reflecting blood flow and content.

16.4.2 Convection

Convective heat loss from the body surface is often expressed as a heat transfer coefficent and the difference between the mean temperature of the outer surface of the body and that of the surrounding air:

$$C = h_c\ (T_{\text{skin}} - T_a) \quad (\text{W/m}^2) \qquad [16.3]$$

where h_c = convective heat transfer coefficient ($\text{W/m}^2 \cdot \text{K}$)

Still-air convective heat transfer coefficients

If there is no air motion over the skin surface, a relatively thick layer of heated air will lie adjacent to the surface, and the temperature gradient across this layer is determined by the conductivity of air ($k = 0.024$ W/m K). However, in nature, the thermal gradient produces a buoyancy gradient in the air, which, depending on the air's viscosity and the orientation of the surface relative to gravity, will cause bulk motion that decreases the conductance of this boundary layer. The heat transfer through such a naturally convecting boundary layer is governed by the Nusselt, Prandtl, and Grashof numbers, which take into account the diffusion and bulk convection of heat.

Still-air convective heat exchange from the human body is dominated inevitably by a slow-moving buoyant plume of air that develops adjacent to the heated body surfaces, and rises along the body carrying heat, water

vapor, and bioeffluents with it. The plume usually envelops the head, and affects the subject's breathing and olfactory senses, giving it an important effect on thermal sensation. The convective heat transfer to the plume depends on posture, clothing, and the local temperature of the air at various points in the plume. This has recently become the subject of computerized fluid dynamics (CFD) simulations (Murakami, 2004), and detailed laboratory visualizations using particle-tracing anemometry.

Since the free-convection process is complex, still-air convective dry heat loss coefficients have been obtained empirically. deDear *et al*. (1997) used a detailed thermal manikin whose individual body segments were electrically heated to maintain realistic skin temperatures, measuring the required wattage to obtain the heat transfer coefficient for each segment. Radiant losses were decoupled by varying the surface emissivity of the manikin. (This manikin's surface areas are shown in Table 16.1, Section 16.3.1.)

Table 16.6 gives some natural convective heat transfer coefficients (*hc*) for a nude thermal manikin standing and sitting in still air (velocity < 0.1 m/s), from deDear *et al*. (1997). These were obtained at a fixed skin-to-air temperature gradient of 12 K.

Using the same manikin, Oguru *et al*. (2002a) found the still-air coefficients to vary with the temperature difference between air and skin. He presents power functions for calculating them for each body part. For the overall body, seated, the coefficient is

$$hc = 0.78\ (T_{skin} - T_a)^{0.56} \qquad [16.4]$$

and for the standing body,

$$hc = 1.21\ (T_{skin} - T_a)^{0.43} \qquad [16.5]$$

Table 16.6 Natural convective heat transfer coefficients (hc) for a nude thermal manikin standing and sitting in still air (velocity < 0.1 m/s), Obtained at a fixed skin-to-air temperature gradient of 12K

Manikin segment	Seated natural convective coefficients (W/m^2 K)	Standing natural convective coefficients (W/m^2 K)
Foot (L and R)	4.2	5.1
Lower leg (L and R)	4.0	4.1
Thigh (L and R)	3.7	4.1
Pelvis region	2.8	3.4
Head	3.7	3.6
Hand (L and R)	4.5	4.1
Forearm (L and R)	3.8	3.7
Upper arm (L and R)	3.4	2.9
Chest	3.0	3.0
Back	2.6	2.9
Whole body	3.3	3.4

From deDear *et al.* (1997).

Moving-air convective heat transfer coefficients

Moving air increases heat transfer from the skin surface by reducing the thickness of the heated layer adjacent to the skin, and thereby increasing its conductance (W/m^2 K). The body's boundary layers are fundamentally characterized by the properties of air and the dimensions of the body's surfaces (Nusselt, Prandtl, and Reynolds numbers), with body segments represented with empirical values for cylinders. However, with the complexities of the human shape, such values are usually empirically determined on human-shaped manikins.

With the manikin in a wind tunnel, deDear (1997) and Oguro *et al*. (2002b) separately developed expressions for heat transfer coefficients as a function of air velocity. For the overall body, their values are close, as shown in Table 16.7.

They also obtained expressions for each body part, repeated for upwind, downwind, and sideways wind orientations. In general, the expressions are quite similar, regardless of direction, unless a given body part passes into the wind shadow of another body part (e.g. the arm and its adjacent torso, or the lower limbs while seated). The insensitivity to direction can be explained to some extent by the fact that most body segments are cylindrical and vertically oriented.

Air motion across the skin surface can also be caused by the motion of the body itself. For a walking or running person, the limbs experience higher and lower air velocities than the mean speed of the body as they swing back and forth. Chang *et al*. (1988) quantified values for various body parts using an articulated moving manikin mounted on a treadmill in a wind tunnel. They found that the convective coefficients for the outer limbs were lower than those for body parts closer to the trunk. This could be due to the non-linear relationship of convection to velocity; if for half of the swing cycle the arm or calf is almost stationary relative to the ground and the surrounding air, the reduction in convective loss will be great, and the doubled velocity during the other half of the cycle will not make up for it.

In the outdoors, it is common to express forced-convective heat transfer in terms of an ambient temperature at which equivalent heat transfer would occur; this is termed a 'wind-chill index' or 'wind-chill equivalent temperature' (WCET):

Table 16.7 Moving air convective heat transfer coefficients

Standing		Seated	
deDear	Oguro	deDear	Oguro
$hc = 10.4\ V^{0.56}$	$hc = 9.41\ V^{0.61}$	$hc = 10.1\ V^{0.61}$	$hc = 9.43\ V^{0.63}$

$$\text{WCET} = T_{skin} - h_{actual}/h_{calm} \times (T_{skin} - T_a) \quad [16.6]$$

Shitzer (2005) has reviewed the historical formulations of the wind chill index. The index is usually developed for a simple geometrical shape such as a cylinder.

In cold weather, the skin develops bumps (gooseflesh) around hair follicles, and the hair itself 'stands on end' – pilo-erection. For fur-bearing animals, this serves to insulate the skin. For humans, the hair density on most of the skin has become thin, and both the hair and the muscular apparatus that erects it have evolved to be insignificant for thermoregulatory purposes. The hair on the head, however, is often thick enough to form a substantial insulative layer.

16.4.3 Long-wave radiant exchange

The radiation emitted from a surface is proportional to the fourth power of absolute temperature, but it is possible to approximate radiant exchange with a linear coefficient when the surfaces are within a limited range of temperatures.

$$R = h_r \times \varepsilon\,(T_{skin} - T_r) \quad (\text{W/m}^2) \quad [16.7]$$

where h_r = radiative heat transfer coefficient (W/m^2 K), ε = emissivity, and T_r = the temperature of the surrounding surfaces. T_r is also represented by the 'mean radiant temperature' (MRT).

The linearized radiative heat transfer coefficient can be calculated by:

$$hr = 4\varepsilon\sigma \frac{A_r}{A_D}\left[273.2 + \frac{T_{skin} + T_r}{2}\right]^3 \quad [16.8]$$

where σ = Stefan–Boltzmann constant, 5.67×10^{-8} W/m^2 K^4 A_r = effective radiation area of the body A_D = total area of the body (Dubois area)

The ratio A/A_D is 0.70 for a sitting person and 0.73 for a standing person (Fanger, 1967). Emissivity is close to unity for the skin surface (typically 0.95). The coefficient h_r is nearly constant for typical indoor temperatures, and a value of 4.7 W/m^2 · K suffices for most calculations (Fanger, 1972).

Using the thermal manikin with its radiative and convective loss fractions separated, deDear *et al*. (1997) obtained h_r values for each segment of the unclothed body (Table 16.8). These apply to uniform radiant surroundings. Although the individual segment values differ substantially, the whole-body values are close to the Fanger value of 4.7 W/m^2 K.

When exposed to an asymmetric radiant environment, where the surfaces surrounding the body have different temperatures from each other, e.g. a cold or hot window in an otherwise neutral room, it is necessary to know the angle factors between the body and the surrounding surfaces to determine the radiative heat exchange with them. Angle factors require knowledge of

Table 16.8 Body segment radiative heat transfer coefficients (hr) for a nude thermal manikin standing and sitting in still air

Manikin segment	Seated radiative coefficients (W/m^2 K)	Standing radiative coefficients (W/m^2 K)
Foot (L and R)	4.2	3.9
Lower leg (L and R)	5.4	5.3
Thigh (L and R)	4.6	4.3
Pelvis region	4.8	4.2
Head	3.9	4.1
Hand (L and R)	3.9	4.1
Forearm (L and R)	5.2	4.9
Upper arm (L and R)	4.8	5.2
Chest	3.4	4.5
Back	4.6	4.4
Whole body	4.5	4.5

From deDear *et al.* (1997).

the projected area of the body from the direction of the surface with which the body is exchanging radiation. The whole body's projected areas were measured by Fanger (1967, 1972) for the full spherical surroundings of standing and seated persons. From these he calculated angle factors for a wide range of window sizes at varying distances from standing and seated occupants; these are universally used in standards and design (ASHRAE, 2005). Oguro *et al.* (2001b,c) extended this to measuring projected areas for each individual body part, again using the manikin in both standing and seated postures.

16.4.4 Short-wave (solar) gain to skin

The absorptivity of skin to solar radiation varies with skin color in the visible and the near-infrared spectra. For visible wavelengths (0.4–0.7 μm), white skin is about 0.5 absorptive, while black skin has been measured at 0.74 (Houdas and Ring, 1982). In the near infrared from 0.8 to 1.4 μm, white skin is 0.6 and black 0.7, while from 1.4 to 2 μm they are almost the same at 0.82, and above 2 μm, they both approach unity. For ultraviolet (<0.4 μm), both skin colors absorb at 0.85. Narita *et al.* (2001) tested subjective thermal sensations from equal radiation intensities at different wavelengths, and found that human skin is more sensitive to the visible (0.3–0.8 μm) and middle-infrared (1.7–2.3 μm) than to near-infrared (0.8–1.35 μm) wavelengths. This difference is attributed to the wavelengths' variable depth of penetration into the skin, relative to where the sensory nerves are located.

In the heat, light breathable clothing may be cooler for the wearer than exposing bare skin, if the clothing is pervious to evaporated sweat but shields

the radiant heat from the sun. Offsetting the shading effect, clothing reduces convective exchange with the atmosphere, but this can be beneficial when T_{air} is greater than T_{skin}.

16.5 Moisture exchange at the skin surface

The heat lost to the environment by evaporation (E) is calculated using an evaporative heat exchange coefficient and the water vapor pressure difference between the skin and the ambient air. The equation is analogous to the convective heat transfer equation.

$$E = h_e\, w\, (P_{skin,\, saturated} - P_a) \quad (\mathrm{W/m^2}) \qquad [16.9]$$

where h_e = evaporative heat transfer coefficient ($\mathrm{W/m^2}$ kPa), w = skin wettedness (dimensionless), $P_{skin,saturated}$ = water vapor pressure at the skin surface, assumed to be the pressure of saturated air at the skin temperature (kPa), and P_a = water vapor pressure of the ambient air (kPa).

The evaporative heat transfer coefficient h_e for the outer air layer of a nude person can be estimated from the convective heat transfer coefficient h_c using the Lewis ratio, which describes the relationship between convective heat transfer and mass transfer coefficients for a surface:

$$LR = h_e/h_c \qquad [16.10]$$

The Lewis ratio equals approximately 16.5 K/kPa for typical indoor conditions.

Evaporative heat loss from the skin depends on the amount of moisture on the skin and the difference between the water vapor pressure at the skin and in the ambient environment.

Skin wettedness is the ratio of the actual evaporative heat loss to the maximum possible evaporative heat loss, *Emax*, under the same environmental conditions and a completely wet skin ($w = 1$). Evaporative heat loss from the skin is a combination of the evaporation of sweat secreted because of thermoregulatory control mechanisms and the natural diffusion of water through the skin. With no regulatory sweating, skin wettedness caused by diffusion is approximately 0.06 for normal conditions. For large values of *Emax* or long exposures to low humidities, the value may drop to as little as 0.02, because dehydration of the outer skin layers alters its diffusive characteristics.

Skin wettedness is strongly correlated with warm discomfort. For clothed subjects, $w > 0.2$ is perceived as uncomfortable. Skin wettedness can theoretically approach 1.0 while the body still maintains thermoregulatory control, but in practice it is difficult to exceed 0.8 (Berglund and Gonzalez, 1977).

16.5.1 Control of evaporation from damaged skin

Wounds (burns and scrapes) that remove the stratum corneum expose a fully wetted saturated surface. Evaporation from a wounded surface may cause heat loss 3 times that of dry heat loss and equivalent to vigorous sweating (Maglinger *et al*., 2005). This creates a serious problem in cool operating theaters because anesthetic-induced inhibition of normal thermoregulation is likely to cause patient hypothermia. Surgical drapes and bandages are used to reduce moisture and heat loss.

Ordinary surgical drapes reduce cutaneous dry heat loss by 30% during operations and prior skin preparation (Sessler *et al*., 1991). Making the surgical drapes impervious to moisture may reduce evaporative heat loss, as well as preventing contamination of the surgical sites from fluid passing through the drape.

Bandages were traditionally cotton and polyester but have expanded into numerous types of porous and nonporous fabrics, foams, and films (van Rijswijk and Beitz, 1998) including bioactive dressings that accelerate healing and grow with the skin (Bhowmick *et al*., 2003). They provide a moisturized microenvironment, reduce fluid loss, wick away bacteria and exudates, and prevent bacteria from penetrating. Bandages help to fulfil the functions of the natural skin.

16.6 Typical skin temperatures

The core temperature is maintained within a small range, about 36–38 °C (Fig. 16.1). The skin temperature may change significantly in order to keep the core temperature in that range, and its temperature will be sensed by the thermoreceptors in the skin (Fig. 16.6). However, the skin temperature is not uniform across the different segments of the body, due to a variety of physiological factors. The inter-segment temperature variation has entirely different patterns in the cold versus in the heat, when the body is either attempting to conserve or reject metabolic heat. Skin temperature distributions are described below for three conditions: neutral, cold, and warm.

Skin temperature distribution under conditions perceived by the subjects as neutral are provided in Table 16.9. The UC Berkeley data were taken with the subject wearing a thin leotard over the temperature sensor (Zhang, 2003). The data provided by Olesen and Fanger (1973) were taken with subjects wearing office clothing. It is unclear why the Berkeley data are consistently about 1K higher than the Olesen and Fanger data, but the distribution patterns are consistent.

In cold environments, skin temperature varies widely across the body as a whole, and even within many individual body parts, due to the effects of vasoconstriction. In the cold, the fingers and nose are the coldest, and finger

Table 16.9 Local skin temperatures (°C) in neutral stable condition

Segment	Skin temperature (°C) – UC Berkeley	Skin temperature (°C) – Olesen and Fanger
Forehead	35.8	34.2
Cheek	35.2	
Front neck	35.8	
Back neck	35.4	
Chest	35.1	34.5
Back	35.3	34.4
Abdomen	35.3	34.9
Upper arm	34.2	33.5
Lower arm	34.6	32.7
Hand	34.4	33.5
Left finger	35.3	
Thigh	34.3	33.7
Shin	32.9	32.6
Calf	32.7	32.2
Foot	33.3	32.2
Average	34.45	33.38

Table 16.10 Local skin temperatures in a cold stable condition (°C)

Segment	Skin temperature (°C)
Forehead	30.7
Cheek	27.7
Front neck	33.5
Back neck	34.5
Chest	30.9
Back	32.4
Abdomen	28.7
Upper arm	24.7
Lower arm	27.3
Hand	23.1
Left finger	21.1
Thigh	27.0
Shin	26.5
Calf	24.3
Foot	21.4
Average	26.8

temperature is 9 K colder than the forehead temperature. The neck temperature is the warmest and can represent a significant source of heat loss (Table 16.10).

In warm environments, skin temperatures are more uniform than in cold. The skin temperatures are evenly distributed, with only a small variation of 2.7 K (Table 16.11). Unlike the cold, the fingers and feet are dilated, and

Table 16.11 Local skin temperatures in a warm stable condition

Segment	Skin temperature (°C)
Forehead	36.5
Cheek	36.3
Front neck	36.8
Back neck	36.1
Chest	36.1
Back	36.3
Abdomen	36.2
Upper arm	36.4
Lower arm	36.1
Hand	36
Left finger	36.7
Thigh	35.6
Shin	34.4
Calf	34.1
Foot	36.4
Average	35.8

have some of the warmest surface temperatures on the body. The upper torso and extremities are very uniform. The lower extremities (thigh, lower leg) are colder than the areas above the pelvis, because in sitting they have not moved as frequently as the hands and arms. A following section describes how movement increases finger and hand skin temperatures.

16.6.1 Finger skin temperature in extreme cold environments

Finger dexterity is decreased when the finger skin temperature is below 15 °C. If finger tissue temperature reaches freezing, frostbite occurs, which can cause permanent damage to the tissue and permanently impair circulation. The body has a defense mechanism in cold-induced vasodilatation, which periodically delivers warm blood to the freezing tissue. The vasodilatation occurs because the smooth muscle in the blood vessel walls becomes fatigued or paralyzed and cannot continue the vasoconstriction. A similar effect can be obtained by heating the chest or torso, which increases hand and finger skin temperatures by triggering increased circulation of blood to the extremities (Bader and Macht, 1948; Brajkovic *et al.*, 1998, 2003).

16.6.2 Neck

The neck has the highest skin temperature of any body part when a person is cold. In the IR images taken in a cold environment, the warm neck is very

noticeable, like a bright collar. This justifies turning up jacket collars or putting on a scarf in cold weather. (Zipping up the collar of a jacket also restricts the pumping effect of the air through the opening of the collar, which removes heat from the larger torso area).

16.6.3 Hand

The hand is probably the most active body part in responding to the body's thermoregulation requirements. In warm conditions, the hand is fully vasodilated and the fingertips are the warmest areas of the hand. This pattern is reversed when cooling. Constriction of the hand blood vessels causes the skin temperature of the hand to vary on the order of 8 °C. When the hand is cold, it ceases to transfer much body heat to the environment.

The hand is very sensitive to the body's overall thermal state. An IR image taken a few minutes after the subject moved from a warm environment (30 °C) to a slightly cool (22.6 °C) environment, showed that, although the rest of the upper body temperature has not changed much yet, the blood vessels of the hand were already well constricted. A 3 K difference in finger skin temperature has been observed in slightly cool environments, caused by the difference in muscular exertion between typing *vs* holding the computer mouse (Table 16.12 – Huizenga *et al*., 2004).

16.6.4 Skin temperature during sleep

Skin temperature increases, and core temperature decreases, prior to and during sleep onset (Van Someren, 2004; van den Heuvel, *et al*., 1998; Gilbert *et al*., 2000). To preserve heat, people normally would cover themselves with blankets to create a microclimate of 34 °C (Muzet *et al*., 1984), which is much warmer than the normal environment for comfort when awake (28–30 °C for a nude person). Measures that increase skin temperature may also help people fall asleep (Van Someren, 2004), as long as the high skin temperature does not evoke warm discomfort. Warming the extremities (feet) is especially effective (Krauchi *et al*., 1999).

Table 16.12 Effect of using a computer mouse on fourth finger temperature (°C) in cold, neutral, and warm environments. Skin temperatures were measured at the end of a two-hour test

	T_{air}: 15.6	T_{air}: 19	Neutral	T_{air}: 30
Left	21.1	21.1	35.4	36.4
Right (using mouse)	17.8	19.3	34.7	36.2

16.7 Sensation and comfort

16.7.1 The distribution of thermal sensitivity

Much research exists on how thermal sensitivity is distributed across the body, and across specific areas of the body. We will focus here on sensitivity differences found across the body as a whole.

Regional sensitivity to warmth (Stevens *et al*. 1974) and cold (Stevens 1979) has been examined. For warmth, thermal stimulation was provided by heat lamps, which eliminated any touch stimulation. The skin surfaces measured are shown in Fig. 16.10. The subjects judged the degree of warmth sensation using the method of magnitude estimation, i.e. the assignment of numbers to match sensation. The forehead and cheek are the most sensitive, followed by: chest, abdomen, back, thigh, and calf. At the higher levels of radiation, the differences were less pronounced.

In the cold sensitivity test, an aluminum contact stimulator was used on the same body surface locations (Fig. 15.11). For cold, the trunk region (including the thighs is the most sensitive, followed by the limbs; the forehead and cheek are the least sensitive.

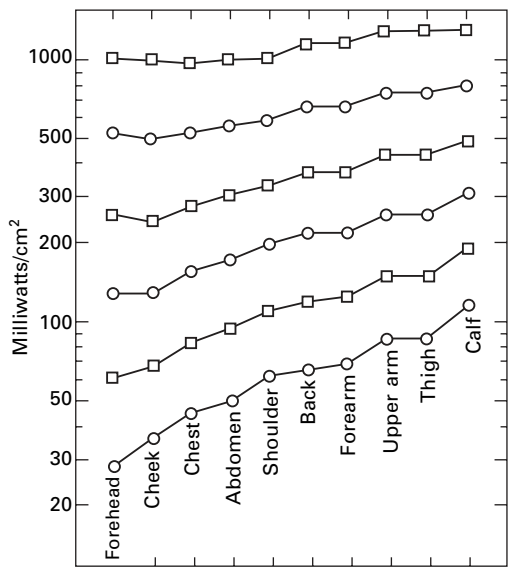

16.10 Equal-warmth profile. Each contour shows the irradiance level needed to produce a given constant level of warmth (From Stevens *et al.*, 1974 with permission from Elsevier).

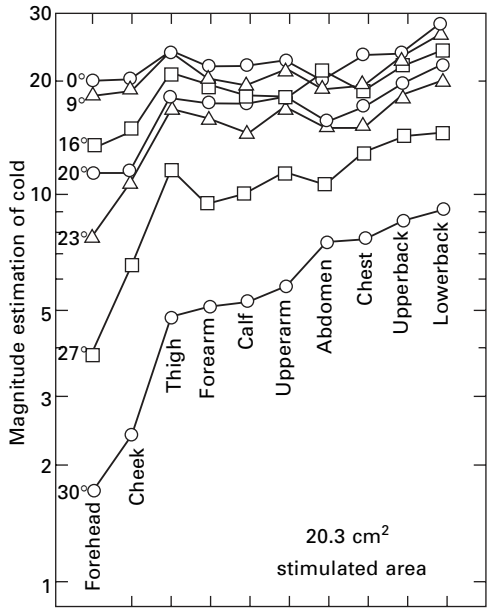

16.11 Magnitude estimation of cold sensation, arranged in order from the least sensitive (forehead) to the most sensitive (lower back), for different levels of cold stimulation (From Stevens, 1979, with permission from Elsevier).

16.7.2 Thermal sensation and comfort distributions under uniform environments

Sensation and comfort for local body parts vary greatly in subjects exposed to uniform environments (Arens *et al.*, 2006a,b; Zhang, 2003). In cool environments, the sensation difference from the least cold sensation (breathing zone, 'slightly cool') to the coldest (hand, 'very cold') is more than 2.5 units on the sensation scale. The hands and feet feel colder than other body parts (Fig. 16.12), and their skin temperatures are also the lowest. A local skin temperature distribution in a cold room (15.6 °C, Table 16.10) shows hand and feet skin temperatures to be about 9 °C lower than the forehead skin temperature. The head, insensitive to cold but sensitive to warm, feels warmer than the rest of the body in cold environments. The subjects' overall sensation follows that of the coldest (hands and feet) in cool environments.

The comfort for all body parts varies considerably – almost four comfort scale units (from 'very uncomfortable' to 'comfortable'. Although the whole-body sensation is cold and the local sensations for the head region (head, face, breathing zone, neck) are also cool, the local comfort for all the head parts is on the comfortable side. The comfort for the remaining body parts is all uncomfortable. The overall comfort follows the worst local comfortable

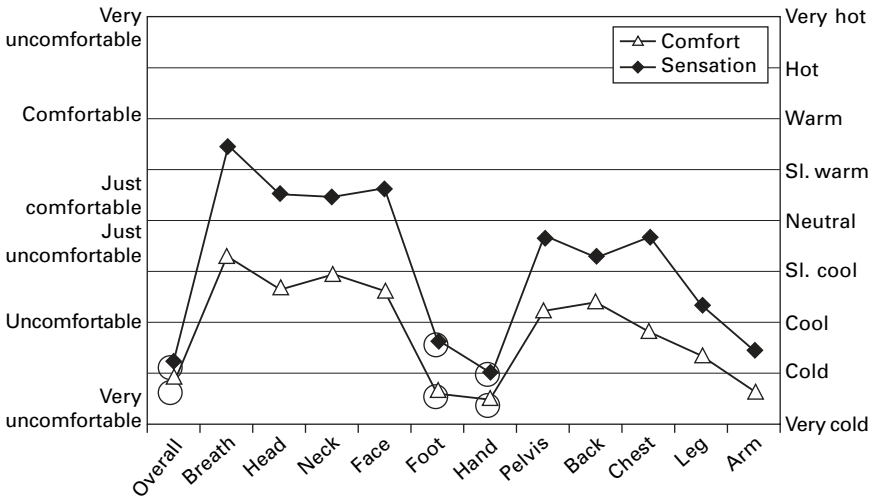

16.12 Local and overall thermal sensation and comfort in a uniform/cold environment.

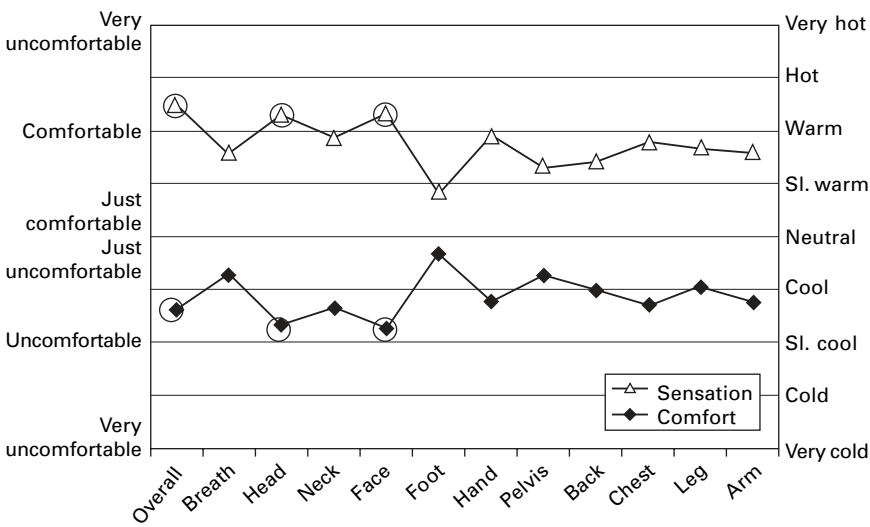

16.13 Local and overall thermal sensation and comfort in a uniform/warm environment.

votes closely (marked by circles), the head region comfort exerting little apparent influence.

In the warm environment, there is still a considerable variation in sensation between body parts. The sensation distribution (Fig. 16.13) shows the variation to be about 1.5 scale units from the head or face (sensation above 'warm' at

2.3) to the feet (sensation 'slightly warm' at 0.8). The variation in skin temperature is much smaller (2.7 °C, Table 16.11) than in the cold environment, and the sensation distribution does not follow the skin temperature as closely. Unlike in the cold environment, where the overall sensation is driven by the vasoconstricted extremities, in the warm environment the overall sensation follows the head region sensation (the warmest local sensation) closely.

Unlike the distribution of local comfort seen in the cold environment, all the local comfort levels are uncomfortable, with the head region perceived as the most uncomfortable. Again, the overall discomfort value is close to the level of the head region discomfort, and could be predicted by the worst one or two local comfort values.

The sensation of the head – insensitive to cold but sensitive to warm – matches the thermal sensitivity presented by Stevens (1974, 1979) described earlier. From the above two figures, we see that head is not only relatively insensitive to cold, but comfortable with the cool sensation.

16.7.3 Sensation and comfort related to skin temperature

Although the contribution of core temperature to the body's thermoregulation is much stronger than the contribution of skin temperature (e.g. about 10:1 for sweating, 4:1 for shivering), for determining subjective thermal sensation, skin and core temperatures have equal importance (Frank *et al*., 1999).

Within a small range of skin temperatures around neutral, thermal sensation does not change. In this range the setpoint for sensation adapts to the current skin temperature, and people are comfortable (McIntyre, 1980). The range is considerably greater for the extremities than the torso (Zhang, 2003). This is shown in Table 16.13. The set point adaptation occurs over periods of time,

Table 16.13 Ranges of comfortable skin temperatures by body part

Body part	T_{low}	T_{high}
Head	33.8	35.8
Face	32	36.2
Breath	31.7	35.2
Front neck	36.0	36.6
Chest	33.8	35.4
Back	33.8	35.8
Pelvis	32.6	34.8
Upper arm	31	34.6
Lower arm	31	36.5
Hand	30	36
Thigh	31.6	34.8
Lower leg	31.8	35.1
Foot	30.8	35

varying from seconds for small surface areas, to minutes when the areas are larger.

16.7.4 Thermal sensation related to finger skin temperature

Figure 16.14 presents subjects' overall thermal sensation votes and corresponding finger temperatures obtained during the final 10 minutes of hour-long stable condition tests, in chamber air temperatures from 15.6–31.5 °C (Wang *et al.*, 2006). Each subject registered 6 votes. When subjects felt warm or hot (their overall sensation between 0.5 and 2.8), their finger temperatures were closely bunched around 37 °C, close to the core temperature. On the cool to cold side (overall sensation less than –0.5), finger temperature ranged widely between 20–30 °C.

Whenever finger temperature was above 30 °C, the overall sensation was above –0.5 (the lower boundary of the neutral sensation zone), and there was therefore no cool discomfort ($p < 0.001$). When finger temperature was below 30 °C, whole-body sensation was (with the exception of a few data points) always below –0.5 ($p < 0.001$), and therefore, cool discomfort was a possibility. 30°C is a clear threshold, separating warm from cool. All the actual discomfort votes occurred below 28 °C (overall thermal sensation < –1.5).

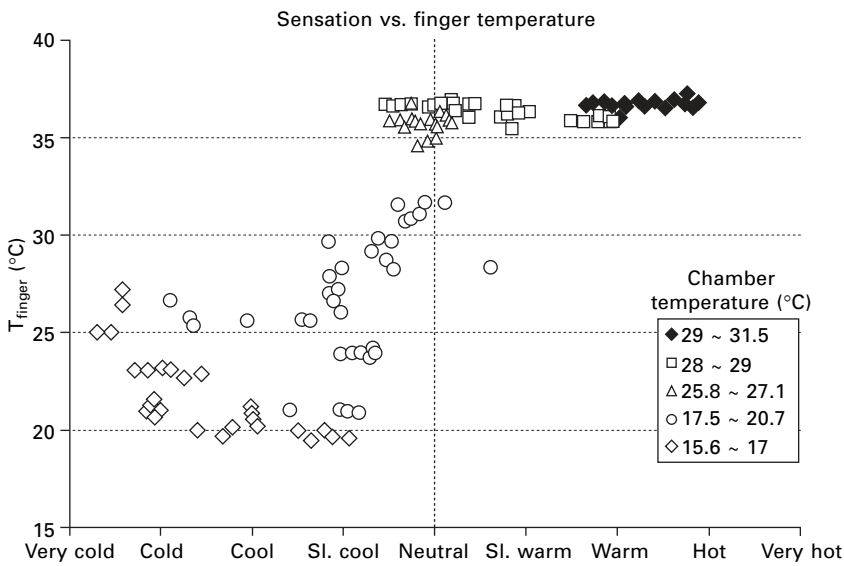

16.14 Whole-body sensation *vs* finger skin temperature.

16.7.5 Upper and lower back

Figure 16.15 compares upper back and lower back thermal sensations. The thermal sensation for the upper back is warmer than for the lower back (Arens *et al*., 2006a). When the lower back sensation is neutral (scale value 0), the upper back feels warm (scale value 0.3). When the upper back is neutral, the lower back is already cool. This is also consistent with the thermal sensitivities which show the lower back to be more sensitive to cold than the upper back (Section 16.7.1). These sensation results apply also to comfort (not shown here). In warm environments, the upper back feels warmer (and more uncomfortable) than the lower back. In cool environments, the lower back feels colder (and more uncomfortable) than the upper back. A heated chair (Knudsen and Melikov, 2005) can be an effective solution to this thermal sensitivity.

16.7.6 Neck, face, ankles

In cold, the neck always has a high skin temperature. Consequently, people feel particularly susceptible to drafts impinging on the back of the neck. Yet air movement from the side of the head is generally regarded as pleasant and effective at cooling in warm environments. This directional asymmetry suggests that lightweight clothing designed to shield the back of the neck (with a relatively high collar) could be very adaptable for thermoregulation, especially in environments such as offices, where people tend to be oriented in a fixed direction for long periods of time.

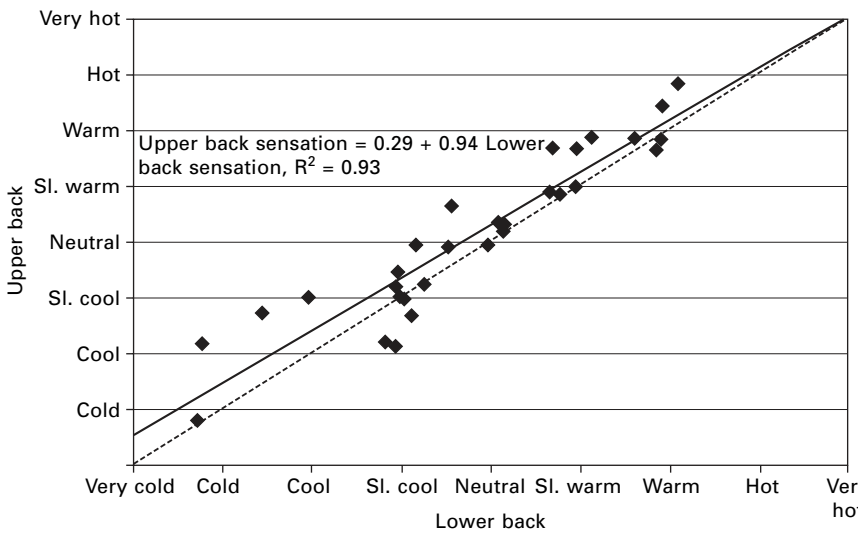

16.15 Comparison between upper and lower back thermal sensations.

16.7.7 Moisture effects on comfort

Wet skin discomfort

Humans have no known sensors that directly detect humidity, but they are sensitive to skin moisture caused by perspiration, and skin moisture is known to correlate with warm discomfort and unpleasantness (Berglund and Cunningham, 1986). It is rare for a sedentary or slightly active person to be comfortable with a skin wettedness greater than 25%. The proposed mechanisms for discomfort are related to the swelling of the epidermis as it absorbs moisture (Kerslake, 1972). Berglund (1995) suggested that the skin's swelling may stimulate the skin's tactile mechanoreceptors in some way and be perceived as uncomfortable.

In addition, mechanoreceptors are clearly stimulated by the friction of clothing moving across the skin surface. With moisture absorption, the stratum corneum outer layer softens, allowing clothing fibers to dig in and increase friction. The additional friction is perceived as fabric coarseness and cling (Gwosdow *et al*., 1986). Moisture-induced cling effect also occurs with architectural and furniture surfaces, particularly smooth, non-hygroscopic materials (ASHRAE, 2005).

Fabrics with different moisture absorbance properties are potentially perceived differently, but there is little experimental evidence for this at present. Toftum *et al*. (1998a) studied knitted and woven cotton and polyester clothes under controlled levels of skin relative humidity ranging from 10 to 70%, and found that fabric type had no effect on comfort, or on perceived humidity of skin or fabric. He found the acceptance of skin humidity decreases as the skin's relative humidity increases, and produced a predictive model of this. It should be noted that, for normal environments where air temperature is less than skin temperature, the effect of the *air's* relative humidity is much less than that of the skin's relative humidity. For cool environments, very high air relative humidity produces almost no perceived skin comfort effect; even at the warm limit of the comfort zone, 70% air relative humidity causes less than 15% of subjects to perceive discomfort due to skin humidity.

Dry eye syndrome

Dry eye discomfort is caused by thinning or sometimes rupturing of the precorneal tear film (PTF) which defends the ocular surface from exposure to the environment. Dry eye can be caused by high temperature, low relative humidity, and indoor pollutants affecting the PTF (Wolkoff *et al*., 2003, 2005). The body's thermal plume, clinging to the face, acts to protect the PTF from excessive heat and moisture losses, but air movement across the face can disrupt the plume and hasten PTF evaporation (Murakami, 2004). Dry eye stimulates eye blinking in order to restore the moisture on the PTF;

indeed eye-blinking frequency is used as a measure to investigate dry eye discomfort (Nojgaard *et al*. 2005).

Respiratory tract comfort

Insufficient evaporative and convective cooling of the mucous membranes in the upper respiratory tract may cause local warm discomfort and a sense of stuffiness and staleness when temperature and humidity are high. This effect is many times more noticeable immediately after a step-change in humidity than after a period of exposure to the humidity. In determining the sensation of staleness, 1K drybulb temperature is equivalent to 1K dewpoint temperature after 15 sec exposure, whereas 1K drybulb is equivalent to 6K dewpoint after 60 minutes of exposure (Berglund and Cain, 1989; Toftum, 1998b).

16.8 Modeling human thermal regulation and comfort

There are numerous models of human thermoregulation and of the resulting perceived thermal sensation and comfort. They can be divided into whether they are static or dynamic, whole-body or multisegment, physical or empirical.

The most commonly used comfort model is the Fanger Comfort Equation, or 'predicted mean vote' (PMV) model, which now forms the basis of the ASHRAE and ISO indoor environmental comfort standards (Fanger, 1972). The model predicts the mean thermal sensation (PMV) and the 'predicted percentage dissatisfied' (PPD) of a large population. It bases the PMV and PPD on a physical prediction of the heat flow from the body to the surrounding environment, relative to the heat flow required for comfort (this is a function of metabolic rate). The prediction is applicable only in steady-state conditions, and the whole body and its clothing are treated as a uniform object. The thermal sensation and discomfort outcomes are empirically based on data from chamber studies of a large number of subjects.

A model capable of dynamically simulating transient conditions was developed by Gagge *et al*. (1971, 1986). This 'two-node model' treats the body as a core and a skin shell, with the whole body surface treated uniformly. Skin and core temperatures are simulated by a physiological model of the heat transfers between core, skin and the environment, using dynamic thermoregulatory control functions for sweating, vasodilatation and constriction, and shivering. The skin and core temperatures are then the basis for a prediction of thermal sensation, which in turn is combined with skin wettedness to predict comfort.

The *ASHRAE Handbook of Fundamentals* provides the underlying equations for the PMV and the two-node models, and the models are compared in

detail in Doherty and Arens (1988). Both models are incorporated in user-friendly software available from ASHRAE.

Multi-segment models have been developed to account for the differences in clothing, heat transfer, and thermal sensitivity that occur on a real body, especially when the body is exposed to a non-uniform environment. Like the two-node model, they are dynamic and are based on simulations of the physiology in the body. Most multi-segment models originated with Stolwijk and Wissler in the early 1970s (Wissler, 1964; Stolwijk, 1971). The body is divided into segments (e.g. head, trunk, leg, foot, arm, hand), and each segments into four layers (core, muscle, fat, skin). The models vary in their detail and treatment of the thermophysiology, but most of them (Smith, 1991; Wang, 1992; Tanabe, 2002; Fiala, 1998) calculate the thermal sensation outcome on a whole-body basis.

The University of California at Berkeley developed a multiple-segment physiology and comfort model (Huizenga *et al.*, 2001; Zhang *et al.*, 2003) that calculates thermal sensation and comfort for each body segment, based on segment-specific human subject tests. It predicts whole-body sensation and comfort by integrating the sensations from all the body parts.

In addition to the physical models above, deDear and Brager (2002) developed an entirely empirical model of human adaptation to the environment. It is based on extensive studies of thermal sensation and comfort carried out in office buildings around the world, in which the range of acceptable environments varied widely, especially for buildings without air conditioning. The concept of the adaptive model is that when people are subjected to a given thermal environment over time, they adapt physiologically, psychologically, and behaviorally. The comfort ranges for these people are different from people who have not adapted to the environment. This model is now incorporated in the ASHRAE (2004) comfort standard, applicable for buildings with openable windows.

16.9 References

Arens E, Zhang H and Huizenga C (2006a), 'Partial and whole body thermal sensation and comfort. Part I: Uniform environmental conditions', *Journal of Thermal Biology*, *31*, 53–59, Also presented in *The 2nd Symposium on Physiology and Pharmacology of Thermal Biology and Temperature Regulation*, Phoenix US, March, 2006.

Arens E, Zhang H and Huizenga C (2006b), 'Partial and whole body thermal sensation and comfort. Part II: Non-uniform environmental conditions', *Journal of Thermal Biology, 31,* 60-66, Also presented in *The 2nd Symposium on Physiology and Pharmacology of Thermal Biology and Temperature Regulation*, Phoenix US, March, 2006.

ASHRAE (American Society of Heating, Refrigerating, and Air Conditioning Engineers) (2004), *ANSI/ASHRAE Standard 55–2004, Thermal Environmental Conditions for Human Occupancy.* Atlanta, ASHRAE, Inc.

ASHRAE (American Society of Heating, Refrigerating, and Air Conditioning Engineers) (2005), *Handbook of Fundamentals*, Atlanta, ASHRAE, Inc.

Bader M E and Macht M B (1948), 'Indirect peripheral vasodilation produced by the warming of various body areas', *Journal of Applied Physiology*, **1**, 215–226.

Bazett C and McGlone B (1930), 'Experiments on the mechanism of stimulation of end-organs for cold', *American Journal of Physiology* **93**, 632.

Bazett C, McGlone B. *et al*. (1930), 'The temperature in the tissue which accompanies temperature sensations', *Journal of Physiology (London)*, **69**, 88–112.

Benzinger T H (1961), 'The diminution of thermoregulatory sweating during cold-reception at the skin', *Proc. Natl. Acad. Sci.*, **47**, 1683.

Benzinger T H, Pratt A W *et al*. (1961), 'The thermostatic control of human metabolic heat production', *Proc. Natl. Acad. Sci.*, **47**, 730–738.

Berglund L (1995), 'Comfort criteria – humidity and standards', *Proceedings of the Pan Pacific Symposium on Building and Urban Environmental Conditioning in Asia*, Nagoya Japan, March 16–18 Vol **2**, 369–382.

Berglund L G and Cain W (1989), 'Perceived air quality and the thermal environment', *Proceedings of IAQ '89*, San Diego CA, 93–99.

Berglund L G and Cunningham D J (1986), 'Parameters of human discomfort in warm environments', *ASHRAE Transactions*, **92** (2b), 732–746.

Berglund L G and Gonzalez R R (1977), 'Evaporation of sweat from sedentary man in humid environments', *Journal of Applied Physiology*, **42** (5), 767–772.

Berglund L G and McNall P E (1973), 'Human sweat film area and composition during prolonged sweating', *Journal of Applied Physiology*, **35**, 714–718.

Bhowmick S., Fowler A, Warner S B, Toner M, Chen M and Sitaula R (2003), 'Bio-active bandages', *National Textile Center Annual Report.*

Brajkovic D, Ducharme M B and Frim J (1998), 'Influence of localized auxiliary heating on hand comfort during cold exposure', *Journal of Applied Physiology*, **85**, 2054–2065.

Brajkovic D and Ducharme M B (2003), 'Finger dexterity, skin temperature, and blood flow during auxiliary heating in the cold', *Journal of Applied Physiology*, **95** (2), 758–770.

Bristow G K and Giesbrech G G (1988), 'Contribution of exercise and shivering to recovery from induced hypothermia (31.2°C) in one subject', *Aviation Space Environmental Medicine*, **59**, 549–552.

Brooks G A, Fahey T D and White T P (1996), *Exercise Physiology, Human Bioenergetics and Its Applications*, Mountain View, Ca, Mayfield.

Cabanac M (1993), 'Selective brain cooling in humans: "Fancy" or fact?', *FASEB Journal*, **7**, 1143–1147.

Candas V, Libert J P and Vogt J J (1980), 'Effect of hidromeiosis on sweat drippage during acclimatisation to humid heat', *European Journal of Applied Physiology*, **44**, 123–133.

Caputa M and Cabanac M (1988), 'Precedence of head homeothermia over trunk in dehydrated men', *European Journal of Applied Physiology*, **57**, 611–615.

Chang S, Arens E and Gonzalez R (1988), 'Determination of the effect of walking on the forced convective heat transfer coefficient using an articulated manikin', *ASHRAE Transactions*, **94** (1), 71–81.

Craig A D. (2003), 'Pain mechanism: Labeled lines versus convergence in central processing', *Annual Review of Neuroscience*, **26**, 1–30.

deDear, R J and Brager G S (2002), 'Thermal comfort in naturally ventilated buildings: Revisions to ASHRAE Standard 55', *Energy and Buildings*, **34**, 549–561.

deDear R, Ring J W and Fanger P O (1993), 'Thermal sensation resulting from sudden ambient temperature changes', *Indoor Air*, **3**.

deDear R J, Arens E, Zhang H and Oguro M (1997), 'Convective and radiative heat transfer coefficients for individual human body segments', *International Journal of Bio-Meteorology*, **40** (3), 141–156.

Doherty T and Arens E (1988), 'Evaluation of the physiological bases of thermal comfort models', *ASHRAE Transactions*, **94** (1), 1371–1385.

DuBois D and DuBois E F (1915), 'The measurement of the surface area of man', *Archives of Internal Medicine*, **15**, 868–881.

Fanger P O (1967), 'Calculation of thermal comfort: Introduction of a basic comfort equation', *ASHRAE Transactions*, **73** (2), III 4.1–III 4.20.

Fanger P O (1972), *Thermal Comfort*, New York, McGraw–Hill.

Fiala D (1998), *Dynamic simulation of human heat transfer and thermal comfort*, Ph. D. thesis, Institute of Energy and Sustainable Development, De Montfort University, Leicester.

Forslind B and Lindberg M (2004), *Skin, Hair, and Nails, Structure and Function,* New York, Basel, Marcel Dekker.

Frank S M, Raja S N *et al*. (1999), 'Relative contribution of core and cutaneous temperatures to thermal comfort and autonomic responses in humans', *Journal of Applied Physiology*, **86**(5), 1588–1593.

Gagge A P and Gonzalez R R (1996), 'Mechanisms of heat exchange: Biophysics and physiology'. In Fregly M J and Blatteis C M, *Handbook of Physiology, Section 4, Environmental Physiology*, New York, Oxford University Press, 45–84.

Gagge A P, Stolwijk J A J and Hardy J D (1967), 'Comfort and thermal sensation and associated physiological responses at various ambient temperatures', *Environmental Research*, **1**, 1–20.

Gagge A P, Fobelets A P and Berglund L G (1986), 'A standard predictive index of human response to the thermal environment', *ASHRAE Transactions*, **92** (2), 709–731.

Gagge A P, Stolwijk J A J and Nishi Y (1971), 'An effective temperature scale based on a simple model of human physiological regulatory response', *ASHRAE Transactions*, **77** (1), 247–262.

Gilbert S, Burgess H, Kennaway D and Dawson D (2000), 'Attenuation of sleep propensity, core hypothermia and peripheral heat loss after temazepam tolerance', *American Journal of Physiology – Regulatory, Integrative and Comparative Physiology*, **279** (6), R1980–R1987.

Goldsmith L (1991), *Physiology, Biochemistry, and Molecular Biology of the Skin*, Oxford, New York, Oxford University Press.

Guyton A C and Hall J E (2000), *Textbook of Medical Physiology*, London, New York, W.B. Saunders Company.

Gwosdow A R, Stevens J C, Berglund L G and Stolwijk J A J (1986), 'Skin friction and fabric sensations in neutral and warm environments', *Textile Research Journal*, **56**, 574.

Hales J R S (1984), 'Skin arteriovenous anastomoses, their control and role in thermoregulation cardiovascular shunts', *Alfred Benzon Symposium 21,* Munksgaad, Copenhagen.

Hales J R S (1985), 'Skin AVA and capillary and constriction induced by local skin heating', *Pflugers Archiv*, **404**, 203–207.

Hensel H (1982), *Thermoreception and Temperature Regulation*. London, Academic Press.

Hertig B A, Riedesel M L and Belding H S (1961), 'Sweating in hot baths', *Journal of Applied Physiology*, **16**, 647–651.

Houdas Y and Ring E F J (1982), *Human Body Temperature, its Measurement and Regulation*, New York, London, Plenum Press.

Huizenga C, Zhang H, Arens E and Duan YT (2001), 'A Model of Human Physiology and Comfort for Assessing Complex Thermal Environments', *Building and Environment*, **36**(6), 691–699.

Huizenga C, Zhang H, Arens E and Wang D (2004), 'Skin and core temperature responses in uniform and non-uniform, steady-state and transient thermal environments', *Journal of Thermal Biology*, **29**, 549–558.

Kerslake D McK (1972), *The Stress of Hot Environments*, Cambridge, UK, Cambridge University Press.

Knudsen G L and Melikov A K (2005), 'Human response to an individually controlled environment', *Proceedings of Indoor Air 2005*, Beijing, China, 421–425.

Krauchi K *et al*. (1999), 'Warm feet promote the rapid onset of sleep', *Nature*, **401**, 36–37.

Kuno Y (1956), *Human Perspiration,* Springfield, Ill., Charles C. Thomas.

Kuno Y (1938), 'Variation in secretory activity of human sweat glands', *Lancet*, p 299.

Maglinger P E, Sessler D I and Lenhardt R (2005), 'Cutaneous heat loss with three surgical drapes, one impervious to moisture', *Anesth. Analg*, **100**, 738–742.

McIntyre D A (1980), *Indoor Climate*. London, Applied Science Publishers.

McIntyre D A and Griffiths I S (1972), 'Radiant temperature and thermal comfort', *Symposium*; *Thermal Comfort and Moderate Heat Stress*, CIB Commission W45, BRE, Watford, England.

Murakami S (2004), 'Analysis and design of micro-climate around the human body with respiration by CFD', *Indoor Air*, **14** (Suppl. 7), 144–156.

Muzet A, Libert J P and Candas V (1984), 'Ambient temperature and human sleep', *Experientia*, **40**, 425–429.

Nadel E R, Bullard R W *et al*. (1971), 'Importance of skin temperature in the regulation of sweating', *Journal of Applied Physiology*, **31**, 80–87.

Nadel E R and Stolwijk J A J (1973). 'Effect of Skin Wettedness on Sweat Gland Response.' *Journal of Applied Physiology*, **35** (5), 689–694.

Narita C, Tanabe S, Ozeki Y and Konishi M (2001), 'Effects of spectral property of solar radiation on thermal sensation at back of hands', *Moving Thermal Comfort Standards into the 21st Century*, *Conference Proceedings*, 393–400.

Nojgaard J K, Christensen K B and Wolkoff P (2005), 'The effect on human eye blinking frequency by exposure to limonene oxidation products and methacrolein', *Toxicology Letters*, **156**, 241–251.

Ogawa T, Asayama M, Sugenoya J, Fujimatsu H, Miyagawa T and Terai Y (1984), 'Temperature regulation in hot–humid environments, with special reference to the significance of hidromeiosis', *Journal of Thermal Biology*, **9** (1/2), 121–125.

Oguro M, Arens E *et al*. (2002a), 'Convective heat transfer coefficients and clothing insulation for each part of the clothed human body under calm conditions', *Journal of Architectural Planning and Environmental Engineering*, AIJ, **561**, 21–29.

Oguro M, Arens E *et al*. (2002b), 'Convective heat transfer coefficients and clothing insulation for each part of the clothed human body under air flow conditions', *Journal of Architectural Planning and Environmental Engineering*, AIJ, **561**, 31–39.

Oguro M, Arens E *et al*. (2001a), 'Evaluation of the effect of air flow on clothing insulation and on dry heat transfer coefficient for each part of the clothed human body', *Journal of Architectural Planning and Environmental Engineering*, AIJ, **549**, 13–21.

Oguro M, Arens E *et al*. (2001b), 'Measurement of projected area factors for each part of a sitting person', *Engineering Science Report, Kyushu University*, **23** (2), 97–206, September.

Oguro M, Arens E *et al*. (2001c), 'Measurement of projected area factors for thermal radiation analysis on each part of the human body', *Journal of Architectural Planning and Environmental Engineering*, AIJ, **547**, 17–25.

Olesen B W and Fanger P O (1973), 'The skin temperature distribution for resting man in comfort', *Arch. Sci. Physiology*, **27**, A385–A393.

Randall W C (1946), 'Quantitation and regional distribution of sweat glands in man', *Journal of Clin Invest*, **25**, 761–767.

Randall W C (1947), 'Local sweat gland activity due to direct effects of radiant heat', *American Journal of Physiology*, **150**, 365–371.

Rein F H (1925), 'Uber die Topographie der Warmempfindung, Beziehungen zwischen Innervation und receptorischen Endorganen', *Zeitschrift fur Biologie*, **82**, 515–535.

Rushmer R F, Buettner K J K, Short J M and Odland G F (1966), 'The skin', *Science*, 154, 343–348.

Sargent F (1961), 'The mechanism of hidromeiosis', *International Journal of Biometeorology*, **5** (1), 37–40.

Schmidt-Nielsen K (1972), *How Animals Work*, Oxford University Press, oxford.

Sessler D I, McGuire J and Sessler A M (1991), 'Perioperative thermal insulation', *Anesthesiology*, **74**, 875–879.

Sessler D I (2006), 'Perioperative thermoregulation, heat balance, and clinical outcomes', *Presentation at the 2nd International Meeting on Physiology and Pharmacology of Temperature Regulation*, Phoenix, Arizona.

Sherman J L (1963), 'Normal arteriovenous anastomoses', *Medicine Baltimore*, **42**, 247–267.

Shitzer A (2005), 'Wind chill equivalent temperatures – regarding the impact due to the variability of the environmental convective heat transfer coefficients', *International Journal of Bio-Meteorology*, **50** (4), 224–232.

Smith C E (1991), *A Transient, Three-dimensional Model of the Human Thermal System*, Ph. D. thesis, Kansas State University.

Spurr G B, Hutt B K and Horvath S M (1957), 'Shivering, oxygen consumption and body temperature in acute exposure of men to two different cold environments', *Journal of Applied Physiology*, **11**, 58–64.

Stevens J C, Marks L E *et al*. (1974), 'Regional sensitivity and spatial summation in the warmth sense', *Physiology and Behavior*, **13**, 825–836.

Stevens J C (1979), 'Variation of cold sensitivity over the body surface', *Sensory Processes*, **3**, 317–326.

Strughold H and Porz R (1931), 'Die Dichte der Kaltpunkte auf der Haut des menschlichen Korpers', *Zeitschrift fur Biologie*, **91**, 563–571.

Stolwijk J A J and Hardy J D (1965), 'Skin and subcutaneous temperature changes during exposure to intense thermal radiation', *Journal of Applied Physiology*, **20**, 1006–1013.

Stolwijk J A J, Nadel E R *et al*. (1971), 'Modification of central sweating drive at the periphery', *International Journal of Biometeorology*, **15**, 268–272.

Stolwijk J A J (1971), *NASA Contractor Report. A Mathematical Model of Physiological Temperature Regulation in Man,* Yale University School of Medicine.

Tanabe S, Kobayashi K, Nakano J, Ozeki Y and Konishi M (2002), 'Evaluation of thermal comfort using combined multi-node thermoregulation (65MN) and radiation models and computational fluid dynamics (CFD)', *Energy and Buildings*, **34**, 637–646.

Tikuisis P and Giesbrecht G G (1999), 'Prediction of shivering heat production from core and mean skin temperatures', *European Journal of Applied Physiology*, **79**, 221–229.

Toftum J, Jorgersen A S and Fanger P O (1998a), 'Upper limits for indoor air humidity to avoid uncomfortable humid skin', *Energy and Building*, **28**, 1–13.

Toftum J, Jorgersen A S and Fanger P O (1998b), 'Upper limits of air humidity for preventing warm respiratory discomfort', *Energy and Building*, **28**, 15–23.

van den Heuvel C J, Noone J, Lushington K and Dawson D (1998), 'Changes in sleepiness and body temperature precede nocturnal sleep onset: Evidence from a polysomnographic study in young men', *Journal of Sleep Research*, **7** (3), 159–166.

Van Rijswijk L and Beitz J (1998), 'The traditions and terminology of wound dressing: Food for thought', *Journal of Wound, Ostomy, and Continence Nursing*, **25** (3), 116–122.

Van Someren E J W (2004), 'Sleep propensity is modulated by circadian and behavior-induced changes in cutaneous temperature', *Journal of Thermal Biology*, 29, 437–444.

Wang D, Zhang H, Arens E and Huizenga C (2006), 'Observations of upper-extremity skin temperature and corresponding overall-body thermal sensations and comfort', *Building and Environment* (in press).

Wang X L (1992), 'Estimating Thermal Transient Comfort', *ASHRAE Transactions*, **98** (1), 7 pp.

Wissler E (1964), 'A mathematical model of the human thermal system', *Bulletin of Mathematical Biophysics*, **26**, 147–167.

Wolkoff P, Skov P, Frand C and Pedersen L N (2003), 'Eye irritation and environmental factors in the office environment: Hypotheses, causes, and a physiological model', *Scand J Work Environ Health*, **29**, 411–430.

Wolkoff P, Nojgaard J K, Troiano P and Piccoli B (2005), 'Eye complaints in the office environment: Precorneal tear film integrity influenced by eye blinking efficiency', *Occupational and Environmental Medicine*, **62**, 4–12.

Zhang H (2003), *Human Thermal Sensation and Comfort in Transient and Non-Uniform Thermal Environments*, Ph. D. thesis, CEDR, University of California at Berkeley.